DEVELOPMENT OF ROLL-TO-ROLL SLOT DIE COATED PEROVSKITE SOLAR CELLS

Rahul Patidar

Dissertation submitted to Swansea University
in fulfilment of the requirements for the PhD

Swansea University

Department of Materials Engineering

2022

Acknowledgments

To begin, I would like to thank Professor Trystan Watson for supervising and advising me throughout the entirety of my project. Your knowledge and support have been invaluable, and I am grateful for the opportunity to have learned from you.

I would also like to extend my gratitude to my co-workers at SPECIFIC for the consistent encouragement and support they have provided. Your contributions have been extremely helpful, and I am extremely grateful to have had the opportunity to collaborate with such a skilled group of individuals. Sincere gratitude goes out to everyone involved in the European Union project MAESTRO, which provided financial support for me to carry out this research.

I would also like to express my gratitude to my parents for the unwavering love and support they have shown me not only throughout this project but also throughout my entire life. Your faith in me has meant everything to me.

I would also like to thank my wife Diksha for her unwavering support and understanding during the busy and sometimes stressful times of completing this project. Your love and encouragement have meant so much to me, and I am grateful to have you by my side.

Finally, I would like to thank my friends for their encouragement and support during this process. Your kindness and understanding have meant a lot to me, and I am grateful to have such wonderful friends.

Thank you all again for your help and support.

Declarations

This work has not previously been accepted in substance for any degree and is not being concurrently submitted in candidature for any degree.

Signed 

Date 30-12-2022

This thesis is the result of my own investigations, except where otherwise stated. Other sources are acknowledged by footnotes giving explicit references. A bibliography is appended.

Signed 

Date 30-12-2022

I hereby give consent for my thesis, if accepted, to be available for electronic sharing **after expiry of a bar on access approved by the Swansea University.**

Signed 

Date 30-12-2022

The University's ethical procedures have been followed and, where appropriate, that ethical approval has been granted.

Signed 

Date 30-12-2022

Summary

Perovskite solar cells (PSCs) have gained a lot of attention in recent years because of their outstanding optoelectronic properties and ability to tolerate defects. Additionally, they can be produced at high throughput using solution processing techniques. It is this feature of perovskite that is leveraged in this work to show their scale up potential by R2R slot die coating.

Slot die coating is a highly precise and controllable technique that can be used to coat a wide range of materials onto a variety of substrates, including flexible and rigid materials. Slot die coating is commonly used in the production of electronic devices, solar cells, and other products that require thin, uniform films of materials.

First a P-I-N architecture of PSCs was developed and optimised with 4 layers slot die coated. This included the hole transport layer (PEDOT:PSS), active layer ($MAPbI_3$), electron transport layer (PCBM), buffer layer (BCP). With 4 R2R slot die coated layer, a stabilised PCE of 12% is achieved. Further, a low toxic solvent system was used to coat the $MAPbI_3$ and its economic benefits are discussed.

Next, in efforts to replace PEDOT:PSS, PTAA hole transport layer was explored. Due to thin coating of PTAA on rough surfaces of PET-ITO, PTAA based devices resulted in high shorting. To avoid this a thin buffer layer of PEDOT:PSS on PET-ITO was slot die coated before coating PTAA. This improved the performance of the PSCs to 15.2%. Further, the role of PEDOT:PSS is characterised using AFM and XPS.

Additionally, the optimization of a R2R slot die coating process for $MAPbI_3$ was carried out on a PTAA surface. The loss of performance that occurred during the transfer from spin coating to R2R slot die coating was characterized, and multiple theories were tested to understand the cause. It was found that the poor interface between $MAPbI_3$ and PTAA was responsible for the drop in performance. Finally, the addition of dimethyl sulfoxide (DMSO) helped to reduce the gap in performance between R2R and spin-coated $MAPbI_3$ on PTAA hole transport layers. The presence of DMSO slowed the growth of crystal formation, leading to improved crystal orientation and improved performance of the PSCs.

Table of Contents

List of Figures

List of Tables

Abbreviations

OPV: Organic Photovoltaics

DSC: Dye Sensitised Solar Cells

PSCs: Perovskite Solar Cells

OHP: Organic Inorganic halide perovskite

PCE: Power Conversion Efficiency

J_{sc}: Current Density

V_{oc}: Open Circuit Voltage

FF: Fill Factor

TCO: Transparent Conducting Oxide

FTO: Fluorine doped Tin Oxide

ITO: Tin doped Indium Oxide

ETL: Electron Transport Layer

HTL: Hole Transport Layer

R2R: Roll-to-Roll

S2S: Sheet-to-Sheet

WFT: Wet Film Thickness

DFT: Dry Film Thickness

MAI: Methylammonium Iodide

PbI_2: Lead Iodide

DMSO: Dimethyl Sulfoxide

DMF: Dimethyl Formamide

ACN: Acetonitrile

MA: Methyl Ammine

THF: Tetrahydrofuran

PEDOT:PSS Poly(3,4-ethylenedioxythiophene)-poly(styrenesulfonate)

PCBM: [6,6]-Phenyl C_{61} butyric acid methyl ester

PTAA: Poly(triaryl amine), Poly[bis(4-phenyl)(2,4,6-trimethylphenyl)amine]

Chapter 1
Introduction

''I'd put my money on the sun and solar energy. I hope we don't wait until oil and coal run out''

Thomas A. Edison

A well-put sentence to describe the potential solar energy holds and compelling need for alternatives to burning oil and coal. After the industrial revolution, fossil fuels have been heavily relied upon to meet the energy demand. Only about 11% of the world's primary energy consumption as of 2019 came from renewable sources.[1] The rest 89% led to over 35 billion tons of CO_2 emission.[2] The air pollution caused as a result takes at least 7 million premature lives each year.[3] To solve this problem, greater effort needs to be made towards developing renewable technologies. Solar energy, photovoltaics in particular is very interesting as it can be integrated into buildings with less space and low cost.

Even though French physicist Alexandre-Edmond Becquerel first noted the photovoltaic effect in 1839, it wasn't until 1954 that Bell Labs researchers showed the first usable solar cell. Silicon solar cells since then have a come a long way and now can be seen on residential and commercial roofs. Whilst silicon technology has reached a state of maturity suitable for commercial applications, its low throughput poses a significant challenge to the production of solar cells in quantities large enough to supplant non-renewable energy sources. Consequently, it is expected to require a substantial amount of time before the requisite quantity of solar cells can be manufactured for widespread use as a replacement for non-renewable energy sources. Also, its non-compatibility with curved surfaces increases the cost of installation. However, emerging technologies like Organic Photovoltaics (OPV), Dye-sensitised Solar Cells (DSCs) and Perovskite Solar Cells (PSCs) have shown a lot of promise as a solution-processable alternative. Solution processing allows cost reduction in many numbers of ways. It reduces the need of high vacuum systems thus saving operations cost along with increased throughput. This work will discuss the challenges and solutions in the development of scalable coating techniques for the manufacturing of PSCs. This is done by taking step by step approach to the current challenges in scaling the PSCs. Specifically, the

work will explore the deposition vis roll-to-roll integrated slot die coating for high through put production.

1.1 The Working of a Solar Cell

The process of light to electricity conversion is covered in the following section. In-depth discussion will be done on understanding the process followed by a discussion on PSCs and their current development status.

1.1.1 Band Structure

According to the Pauli exclusion principle, no two electrons in an atom can have the same four quantum numbers and hence when two atoms are brought together, they form two distinct molecular orbitals. When N such atoms in a solid, usually of the order of 10^{22} combine to form N discrete energy levels we see a continuum of energy levels or 'bands'. A schematic of a band is shown in Figure 1. 1.

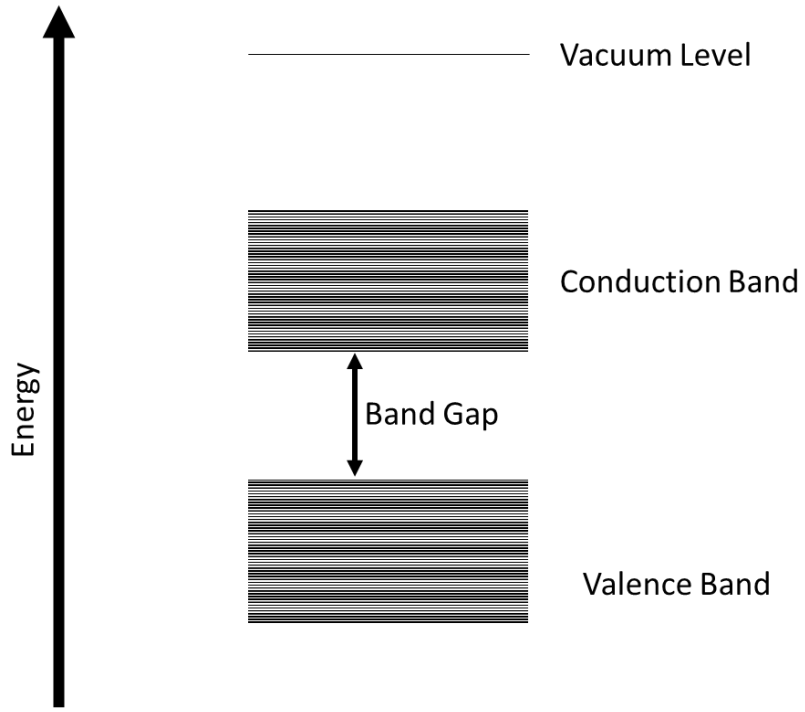

Figure 1. 1: A representative example of a band structure

The band gap can now be simply defined as a forbidden energy space between two adjacent bands. The occupied band with the highest energy level is called a valence band and the lowest unoccupied is called a conduction band. These bands have sharp and well-defined

band edges for uniform and highly ordered material. Any occurrence of intrinsic or extrinsic disorder may have energies in forbidden regions and are generally referred as defects or trap states.

The band gap can further be classified as “direct” and “indirect”. Indirect band gap materials are those that do not have the same electron momentum in the conduction and valence bands. While for direct band gap material there is no difference in electron momentum of the two bands. For the energy transition in an indirect band gap material, an electron, a phonon and a photon need to interact at the same time reducing the likelihood of this transition and is much less efficient than the direct band gap material. Hence for an ideal photovoltaic active material a direct band gap is an added advantage.

For the conduction of electricity, an electron must jump to another state as no two electrons can occupy the same quantum states. In metals or conductors, the two bands overlap, meaning the ‘one band’ is not entirely filled hence electrons can access the vacant energy levels at room temperature and conduct electricity. For the insulator, the valence band is filled and the gap to the next band (conduction band) is way too high for the electron to make this transition and hence are poor conductors of electricity. On the other hand, we have a semiconductor where the valence band is fully filled same as an insulator, but the bandgap is not as high as that of insulators and the electrons can be excited by external energy in form of the heat or light which then conducts electricity.

1.1.2 P-N Junction

It is important to understand Fermi Level before diving deep into a p-n junction. The electron distribution in an orbit is described by Fermi-Dirac distribution as follows:

$$f(E) = \frac{1}{1 + e^{\frac{(E-Ef)}{kT}}} \qquad 1$$

$f(E)$ represents the probability of an electron occupancy at an energy level E at a certain temperature T with the Fermi energy Ef. Fermi level can now be defined as the energy level at which the probability of electron occupancy is 50%.

The function dictates that at normal temperature the probability of electrons existing above Ef goes down and most of the electrons occupy the levels below Fermi level.

The characteristics of the semiconductor affect the Fermi level of the semiconductor. The Fermi level is located between the valence band and conduction band in an intrinsic semiconductor. For an n-type material, wherein the material is doped with impurities having higher electrons in the valence shell than the material, leaving extra free non-bonded electrons, the Fermi energy moves slightly up. In p-type semiconductors, the doping impurities have fewer electrons than the material creating extra electron vacancies or 'holes', the Fermi level, in this case, moves down and closer to the valence band. Figure 1. 2 shows the schematic representation of all three scenarios.

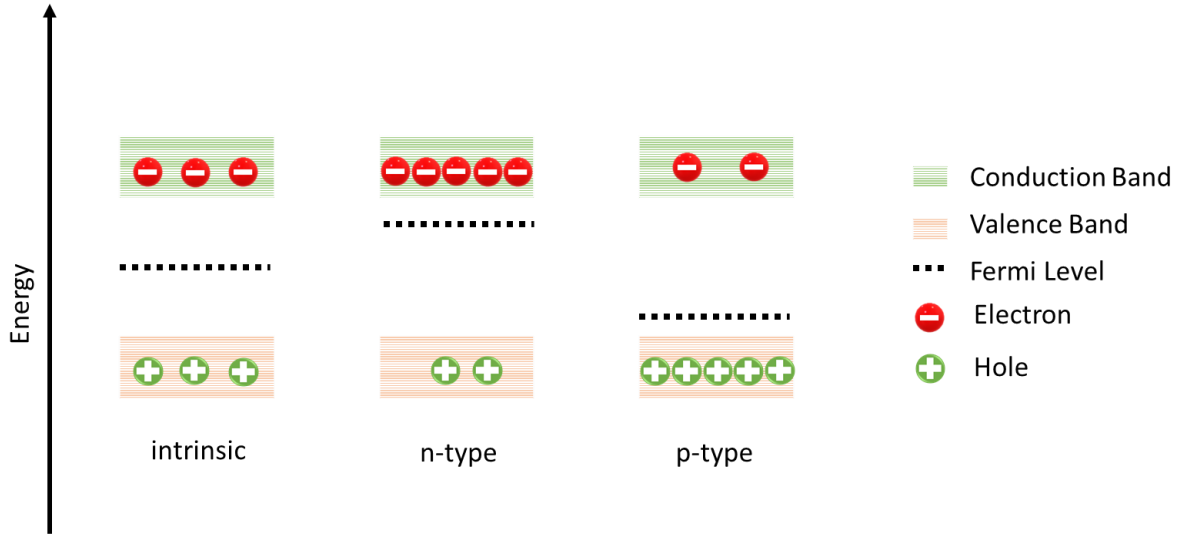

Figure 1. 2: Schematic of charge distribution in different types of semiconductors.

P-N junction is formed when a p-type semiconductor is placed next to an n-type semiconductor. As discussed above, p-type semiconductors have a greater density of positive charges (holes) therefore the majority charge carriers are holes while n-type would have majority charge carriers as electrons. Because of this concentration difference when the junction is made of these two materials, diffusion of charge carriers take place. The diffusion of electrons will take place into p-type material and holes into n-type material. This continues till equilibrium is established. At equilibrium, the n-type material near the junction has lost few of its majority charge carriers (electrons) and is depleted of the same thus termed as depletion region. This happens to the p-type as well where holes move across the junction

and the material near the junction gets depleted of its majority carrier forming a depletion region at the junction on both the sides as shown in Figure 1. 3.

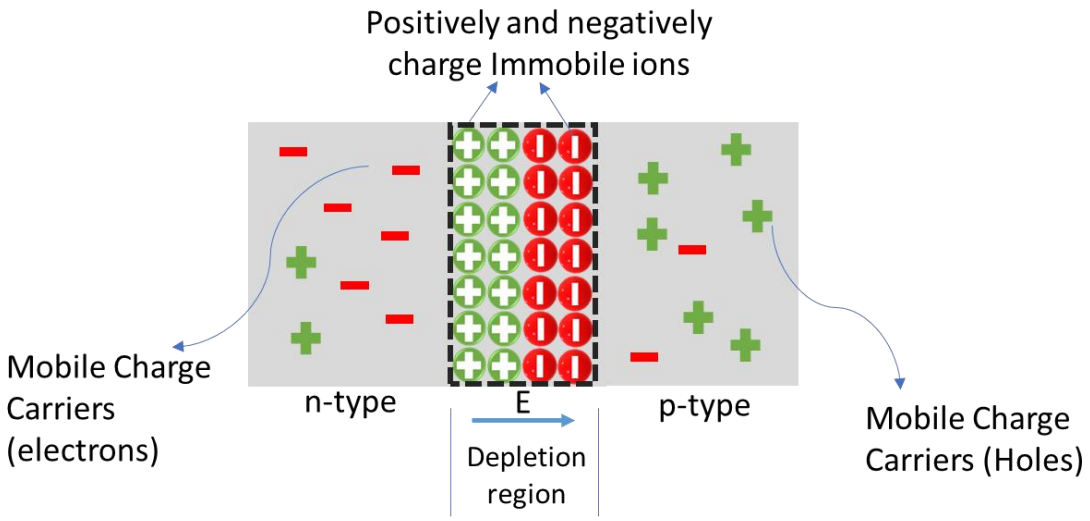

Figure 1. 3: Schematic of P-N junction

Due to this separation of charges, an electric field is generated, known as 'built in' electric field, and represented as E in Figure 3. Statistically, there is a slight probability of a few majority charge carriers having enough velocity to cross the depletion region and once it does it becomes a minority charge carrier on the other side and will travel an average distance equivalent to the diffusion length of the respective charge carrier before recombining. This movement generates a current known as diffusion current. On the other side minority charge carrier near to the depletion region (up to the diffusion length of the minority charge carrier) or in the depletion region are carried across by the in-built electric field E. Since the movement of these charges happens because of the electric field, the generated current due to this movement is called drift current. And the velocity of the charges under the influence of electric field E is called drift velocity.

The current density can be expressed as the summation of both the currents:

$$\overrightarrow{J_n} = J_n\, drift + J_n\, diffusion \qquad 2$$

At equilibrium, the net current flow across the junction is zero meaning both the currents balance each other.

When the external bias is applied such that, the effective electric field is reduced, it is called a forward bias p-n junction. A lower effective electric field reduces the width of the depletion region increasing the probability of majority charge carriers crossing the junction. These carriers diffuse away and recombine with the majority charge carriers on the other side of the junction. Thus, diffusion current in the state of forward bias is a recombination current. Moreover, drift current largely remains unchanged as it is limited by the number of the minority charge carriers that are close to the depletion region or in the depletion region. Due to this imbalance, we now have a net current flowing across the junction in a forward bias p-n junction.

In the reverse bias p-n junction, the external field is applied in the same direction of the in-built field. This increases the depletion region width. As a result, diffusion current goes down but a small increase in drift current can be seen because of the increment of the depletion region, more minority charge carriers can be swept across the junction to generate drift current. However, it is a second-order effect and does not contribute to the large current flow and hence no current in reverse bias p-n junction. The device (in this case p-n junction) which only allows current flow in one direction is the backbone of modern electronics and is commonly known as a diode.

1.1.3 Diode

Understanding the characteristics of the diode is critical to understanding the light-generated current in the photovoltaic solar cell. Current flowing through a diode is represented by the diode equation:

$$I = I_0 \left(e^{\frac{qv}{nkT}} - 1 \right) \quad 3$$

Where I is the net current flowing across the diode, I_0 is the dark saturation current, v is the applied voltage across the diode, T is the absolute temperature, n is the ideality factor, q is the absolute electron charge and k is the Boltzmann's constant.

I_0 is perhaps the most important factor, it's a measure of the quality of the diode material and has an inverse relation. I_0 represent the recombination current in absence of light, a low dark saturation current is indicative of a high-quality diode with good performance characteristics, such as low leakage current, high blocking voltage, and high efficiency. Conversely, a diode with a high dark saturation current is likely to have a high level of leakage current, which can reduce the overall efficiency and performance of the device. Figure 1. 4 represents a graphical version of the diode equation at T = 300K and n = 1 of two different materials with different dark saturation currents. The low turn-on voltage in the case of lower I_0 is an example of inferior quality of material which has higher recombination.

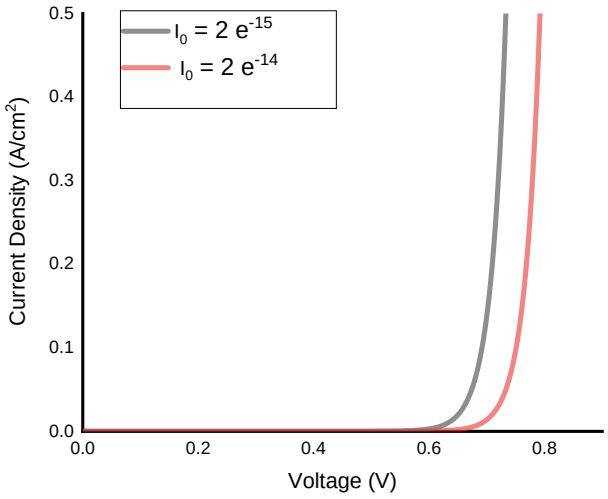

Figure 1. 4: Current profile of a diode at varying bias for two materials having different dark saturation current (I_0).

1.1.4 Generation of Light Current

To understand the current generation in a photovoltaic cell, it is useful to consider the solar spectrum incident on a photovoltaic cell. As electromagnetic radiation travels through Earth's atmosphere, it can undergo scattering as it interacts with particles in the atmosphere. The spectrum in the space outside the earth's atmosphere is referred to as AM0 and is relevant for space applications.

The spectral distribution and intensity will vary depending on the location and its angle to the sun. Air mass coefficient AM1 is the spectrum at the sea level calculated considering the sun is directly overhead and is useful for the characterization of photovoltaic cells near the equator region. However, most of the world's population lives in the middle latitudes and

hence AM1 would not be the best standard for performance characterization. Therefore AM1.5 which represents the yearly average solar radiation in the middle latitude region is used as the standard for photovoltaic testing. Figure 1. 5 compares the different spectra plotted from NREL data.[4]

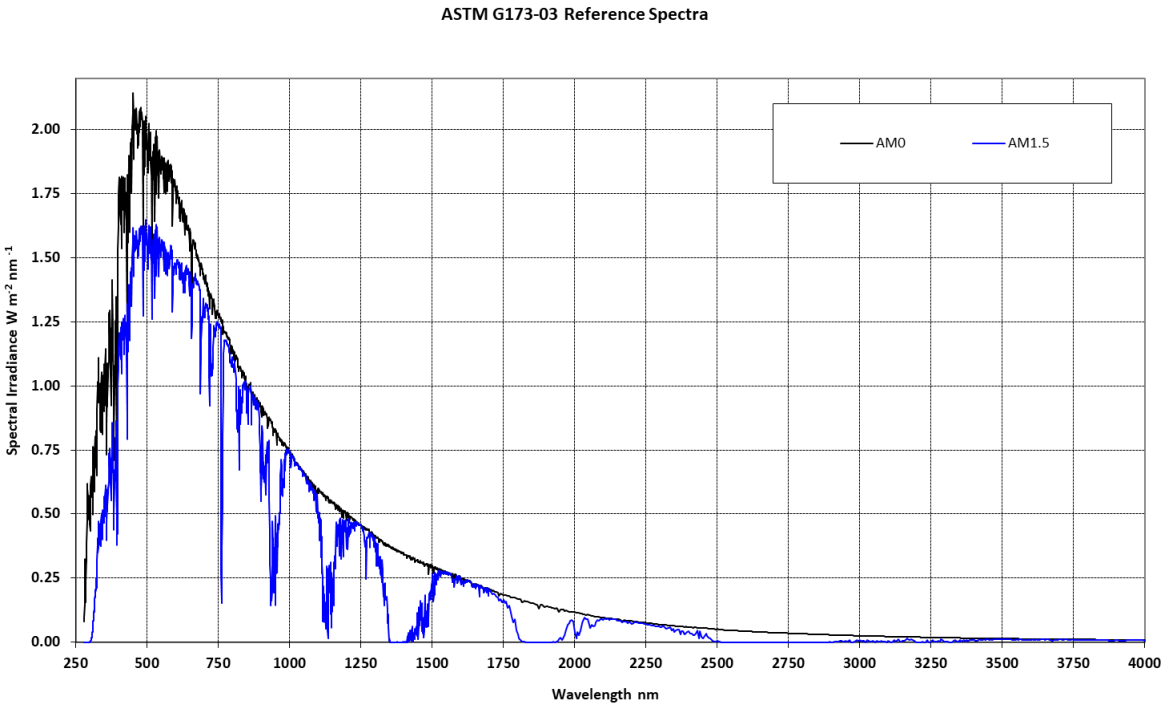

Figure 1. 5: Comparison between AM0 and AM1.5

For solar cell operation, there are two key processes, charge generation, and charge separation. A combination of these two processes generates a 'light current'. When an electron in a material absorbs a photon with sufficient energy (more than the bandgap of the material) to transition from the valence band to the conduction band, an electron-hole pair is created, as shown in Figure 1. 6. However, this electron-hole pair only remains for short time and that depends on the carrier mobility of the material, which is a function of several factors including its crystal structure, impurities, defects, and doping. For the generation of light current, this electron-hole pair needs to be separated and collected at different ends. This separation happens when a minority charge carrier is generated near the depletion region it is taken across the junction by inbuilt electric field E which then becomes a majority charge carrier on the other side. Current flows when these two sides are shorted and the current in this state is also known as short circuit current.

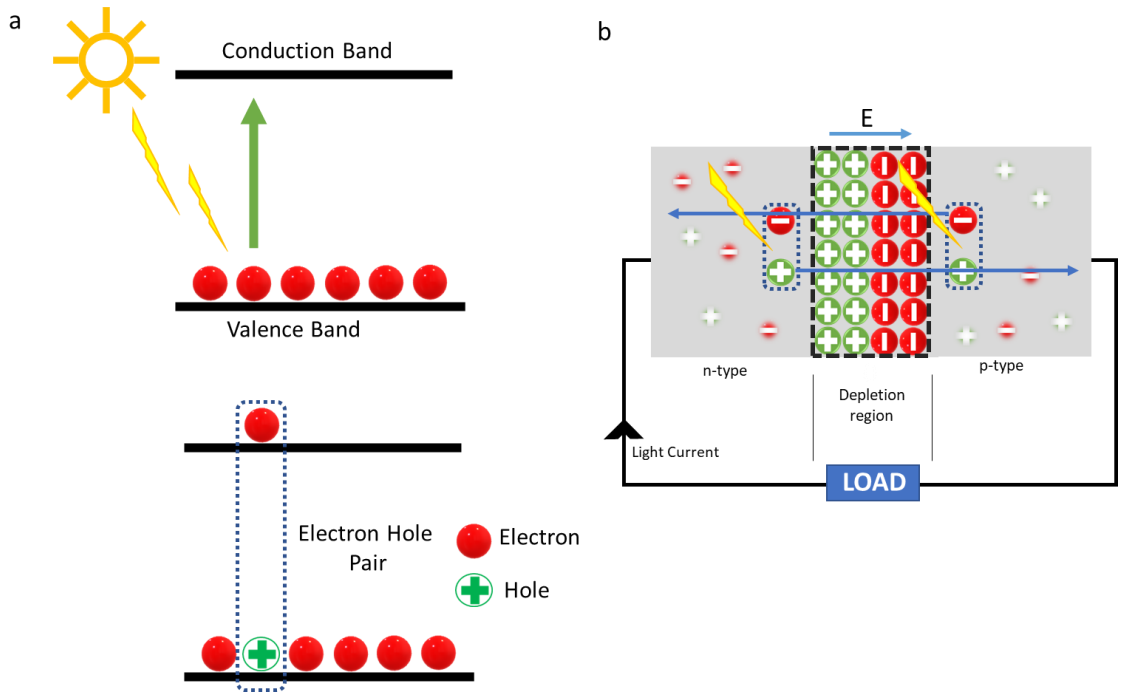

Figure 1. 6: a) Electron hole pair generation. b) Charge separation and collection in a p-n junction diode

1.1.5 Recombination in Solar Cells

Recombination in solar cells refers to the loss of charge carriers (electrons and holes) within the device, which reduces the overall efficiency of the cell. It occurs when electrons and holes recombine instead of participating in the desired process of generating electrical current. There are three main types of recombination in solar cells, radiative recombination, non-radiative recombination, and Auger recombination.

In radiative recombination, a photon is emitted when electrons and holes are recombined. This emitted photon with similar energy to the bandgap can be absorbed back by the material, allowing it to contribute to current generation. Techniques like photoluminescence and electroluminescence rely on measuring radiative recombination.

On the other hand, non-radiative recombination transpires when electrons and holes recombine without emitting photons. Instead, the excess energy is dissipated as heat. This type of recombination is generally undesirable in solar cells as it diminishes the efficiency of the device. Non-radiative recombination can be induced by various factors such as defects in the semiconductor material, impurities, and surface recombination.

Auger recombination, the third and less common recombination mechanism, involves three carriers. For instance, the recombination of an electron and a hole leads to the emission of energy, which is subsequently absorbed by a second electron. This absorption causes the second electron to transition to a higher energy state and subsequently lose the excess energy through heat dissipation or other mechanisms. However, Auger recombination is typically observed under conditions of high carrier concentrations, such as intense light or heavy doping.

1.1.6 Characterisation of Solar Cells by IV Measurement

IV measurement, short for current-voltage measurement, is a fundamental technique used to characterize the electrical behaviour of a solar cell. It involves applying a range of voltage biases to the solar cell and measuring the resulting current flowing through the device. The data obtained from the IV measurement can then be used to calculate important parameters such as the open-circuit voltage (V_{oc}), short-circuit current (I_{sc}), fill factor (FF) and power conversion efficiency.

To perform an IV measurement, a solar cell is connected to a voltage source and a current-measuring device, such as a source meter or a digital multimeter. The voltage source sweeps across a range of voltages while the current-measuring device records the corresponding current values. These values are then utilised to plot IV curve. (see Figure 1. 7)

The open-circuit voltage (V_{oc}) is the voltage at which no current flows through the solar cell, meaning the current is zero (I = 0). In the IV curve, it corresponds to the point on the x-axis (voltage axis) where the current is zero. V_{oc} represents the maximum voltage that the solar cell can generate when there is no external load connected.

The short-circuit current (I_{sc}) is the current that flows through the solar cell when the voltage across its terminals is zero (V = 0). In the IV curve, I_{sc} is the value on the y-axis (current axis) where the voltage is zero. I_{sc} represents the maximum current that the solar cell can deliver.

The fill factor (FF) is a parameter that characterizes the quality of a solar cell and indicates how well it utilizes the available power. It is calculated by dividing the maximum power output (P_{max}) of the solar cell by the product of V_{oc} and I_{sc}.

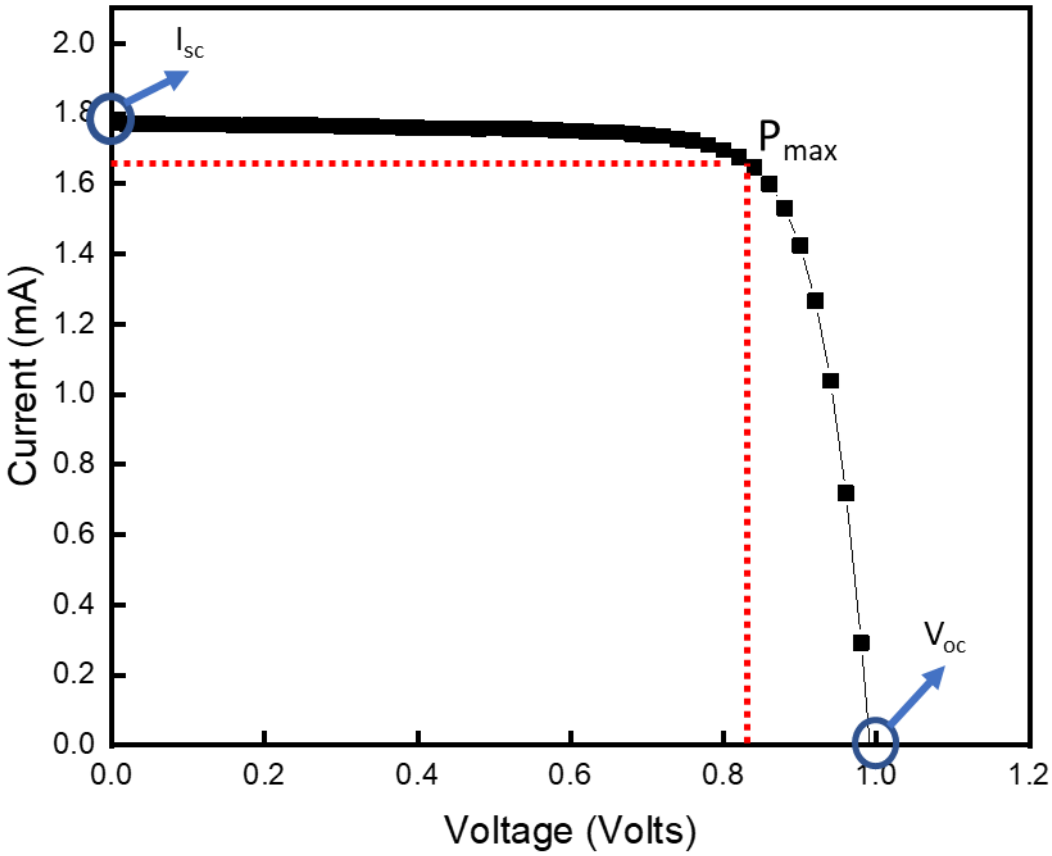

Figure 1. 7: A typical IV curve of a solar cell

The efficiency of the solar cell (η) is estimated by dividing the maximum power output of the solar cell with incident power and can be described as:

$$\eta = \frac{P_{max}}{P_{in}} \qquad 4$$

where P_{max} is the maximum power output of the solar cell and P_{in} is the incident power on the device.

The IV curve can also serve as a means to calculate the series resistance (Rs) and shunt resistance (Rsh) of the device, both in dark conditions and under illumination. The slope of the IV curve around zero current (Voc), can provide an estimation of the series resistance. Similarly, the slope of the curve around zero voltage (Isc), can be utilized to estimate the shunt resistance.

1.2 Perovskite Solar Cells

1.2.1 Organic-Inorganic Halide Perovskites

Perovskite, named after Russian mineralogist Perovski are material with the same crystal structure as that of $CaTiO_3$. Amongst the family of perovskites, Organic Inorganic halide perovskite (OHP) was first reported by Weber in 1978 and were later studied in 1994 for their optoelectronic applications.[5,6] However not until, 2009, it was first used for a photovoltaic application in DSCs reporting over 3% power conversion efficiency (PCE).[7] Yet, due to the low performance and low stability in polar liquid electrolytes, they did not attract much interest among the scientific community. Later in 2012, two groups reported solid-state perovskite solar cells (PSCs) with PCE of 9.7% and 10.9%.[8,9] Properties like the ease of fabrication, strong absorption coefficient, band gap tunability, and high defect tolerance made PSCs highly interesting to explore. Plus, the advantage of over 20 years worth of research and development in related DSCs and OPVs aided to their exponential growth in PCE to over 26% in just a decade time. [10]

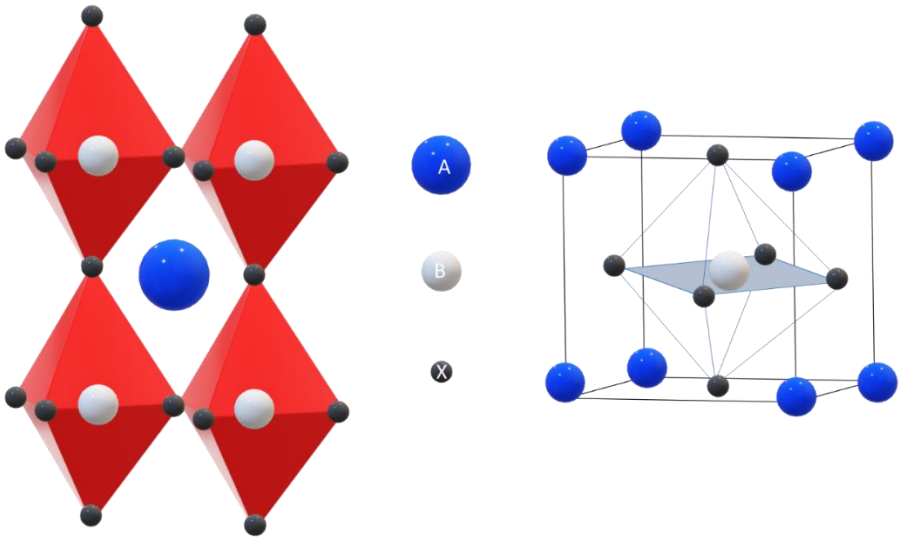

Figure 1. 8: Schematic of ABX_3 Crystal Structure

The formula ABX_3 can be used to describe OHPs, where X is a halide anion, B is a metal cation, and A is a large organic cation. A schematic representation is shown in Figure 1. 8. The Goldschmidt tolerance factor (t) can be used to describe the stability of the perovskite structure.

$$t = \frac{R_A + R_x}{\sqrt{2(R_B + R_x)}} \quad 5$$

Where radius of cation A is represented by R_A and that of B by R_B. R_x represent ionic radius X anion. Cubic structure would have tolerance factor in the range of 0.9-1 whereas octahedral would have lower in the range 0.71-0.9. When the tolerance factor is above or below these values, a non-perovskite structure is said to be formed.[11]

1.2.2 Perovskite Solar Cell Architectures

PSCs consist of a stack of various layers. This stack is typically built on a rigid or flexible transparent substrate. But it can also be made on opaque metal foils provided the top contact does not block the light. Out of the two contacts at least one of the two needs to be transparent and conductive to maximise the light absorption by the photoactive layer. The contacts must also have an aligned energy band to not form the Schottky barrier. Transparent conductive oxides (TCO), such as Fluorine doped Tin oxide (FTO) or Tin doped Indium oxide, are frequently used for this purpose (ITO).

OHP are an intrinsic semiconductor. To extract charge from an intrinsic material, it needs to be sandwiched between an n-type and p-type material. For an n-type or p-type light absorber a p-n junction is needed, the charge extraction of which was discussed in section 1.1.4. The first perovskite solar cells were developed using a DSC architecture, in which a perovskite material was used as the sensitizer dye on a layer of TiO_2. This was then improved to solid-state PSCs. Since this was still an extended version of DSCs it also used mesoporous TiO_2. By replacing TiO_2 with an insulator Al_2O_3 it was confirmed that meso-TiO_2 does not play a role in charge extraction instead it just acts as a scaffold layer for perovskite crystal growth. The architecture that has a scaffold layer is commonly referred to as mesoporous structure.

In the early days of PSCs, the use of scaffold layers was very common. However, this layer was a bottleneck to the deployment of perovskite on flexible substrates because of its high-temperature processing. With the development of better perovskite thin films and processing conditions, the PCEs without scaffold layer gradually got better. Since the architecture does not use any mesoporous layer, it's commonly referred to as a planar architecture. Typical

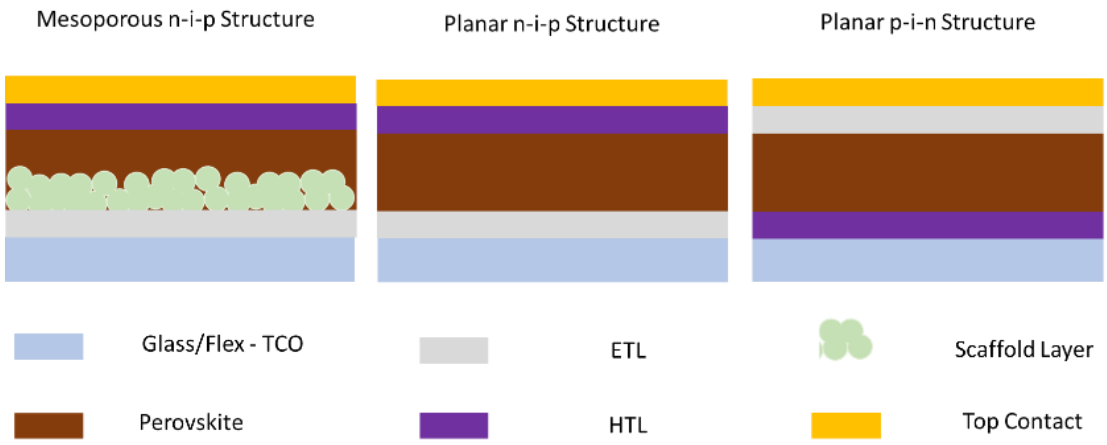

Figure 1. 9: Schematic representation of Mesoporous n-i-p, planar n-i-p, planar p-i-n

planar PSC is made up of the following components: transparent conductive oxide, electron transport layer (ETL), perovskite, hole transport layer (HTL), and metal contact. The architecture with the layers deposited in this sequence is known as n-i-p structure. Along with the planar n-i-p structure and mesoporous structure, taking a leaf from the OPV books planar p-i-n structure was also developed for PSCs. This configuration is often called an inverted structure because it contains an opposite sequence of ETLs and HTLs compared to the planar n-i-p structure. All three architectures are represented in Figure 1. 9. Within this work p-i-n architecture is used as a starting point for scaling up PSCs and will be discussed in detail in chapter 3.

Figure 1. 10 depicts the energy band alignment of the layers in a P-I-N perovskite solar cell. The principle behind its operation is as follows: when the perovskite layer absorbs light with an energy equal to or greater than its band gap, the electrons residing in the valence band, make a transition to the higher energy state, which is the conduction band, leaving behind a corresponding hole. Guided by the built-in electric field, the electron and hole then migrate towards their respective electrodes through the ETL and HTL. These two layers are carefully aligned with the perovskite absorber, ensuring the charge selectivity. For example, ETL conduction band matches well with that of the absorber layer to facilitate the transfer of excited electrons from perovskite to ETL. While the HTL band aligns with the absorber's valence band to facilitate the transfer of holes to HTL. Subsequently, the electron and hole enter the electrode materials and are connected in a circuit, generating power.

To prevent recombination charge selectivity is introduced by having deep high conduction band for HTL and deep valence band for ETL as shown in Figure 1. 10. The "top electrode" in these device stacks is typically an opaque metal like gold, silver, or aluminium, known for their low sheet resistances. However, materials with lower conductivity such as carbon black can also be used successfully, offering cost advantages over gold, for instance.

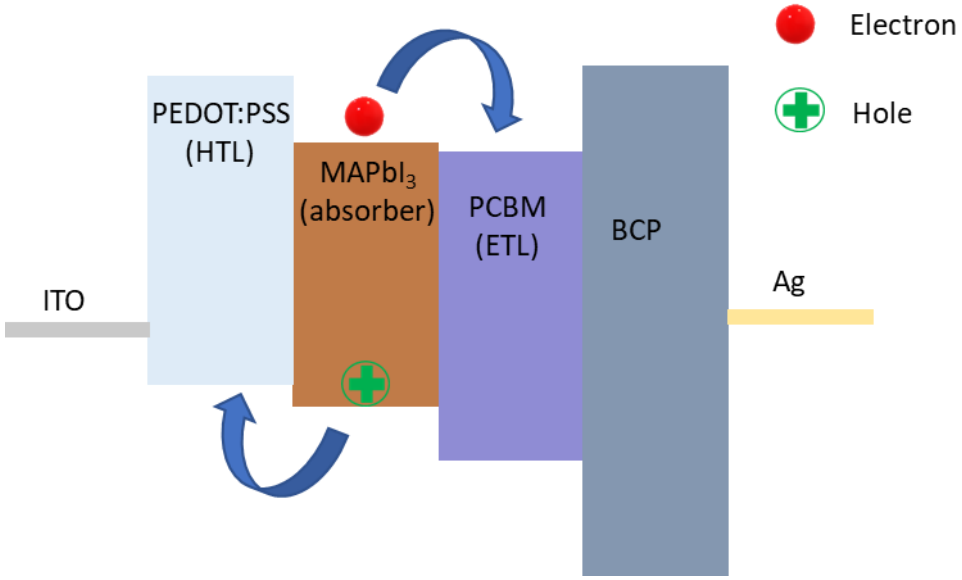

Figure 1. 10: Typical band diagram of a p-i-n perovskite solar cell

As can be noticed in Figure 1. 10 a layer of BCP was included in the architecture. Bathocuproine (BCP) is widely used as an interface modifier between PCBM and silver electrodes in PIN PSCs. It improves the charge collection by reducing recombination losses by forming an ohmic contact between PCBM and silver top electrode helping improve the overall performance of the PSCs.[12] BCP has also been reported to form a complex with Ag and it was found that the LUMO of this complex aligns with the Fermi level of Ag which assist in the charge transfer.[13] BCP has been used both as a solution-processed layer and also as a thermally evaporated interlayer. A solution processed BCP layer was introduced in 2015 and was found to be more effective over rougher perovskite morphology as it could help planarize the surface.[14] The optimisation of this layer along with others will be carried out in chapter 3.

1.3 Slot-Die Coating

A wide range of methods have been used for PSCs fabrication from solution-based spin coating to vacuum thermal deposition. Quite often, for the lab-scale studies, spin coating is used. It is ideal for prototyping and rapid research because of its simplicity and ease. Also,

dynamic drying helps achieve uniform thin films. In this work we used spin coating for the same reason, as it sets a reference for optimisation of other deposition techniques.

A deposition method must be scalable and cost-effective in order to be used for industrial-scale manufacturing. Spin coating, for example, is not an attractive option for scalable manufacturing because it limits the area that can be coated on a single substrate in one go. Spin coating also is highly inefficient as a lot of the solution used during the coating process is lost. It is also possible to use techniques like thermal evaporation, but this lowers throughput as it requires high vacuum and temperature, which also increases the cost of the deposition. Inkjet printing, screen printing, gravure printing, blade coating, and slot die coating are some other deposition techniques that have demonstrated a lot of promise as scale-up low-cost deposition alternatives. For Roll to Roll (R2R) deposition, however, only slot die coating and gravure printing have been used. In this work, we have chosen slot die coating for the fabrication of PSCs, the merits of which are discussed in the next section.

Slot-die coating is an effective technique for low viscosity inks like perovskite and other layers used in PSCs device stacks. Compared to techniques like spin coating, spray, and screen printing, slot die coating is highly effective in terms of materials usage and produces very little to no waste. Slot-die coating is a technique in which a solution is passed onto a substrate through a narrow slot created by a shim sandwiched between the two halves of a slot-die head. Through the inlet, ink is delivered to the reservoir, which is a channel on one side of the slot-die head. The reservoir is used to allow the ink to spread across the width of the head. The coating width is defined by a shim sandwiched between the heads and can also be used to print stripes of material. At the slot die lips, the ink touches the substrate and forms a meniscus between the substrate and the lips. At times, an extra layer or a plate in between the heads termed a meniscus guide is used next to the shim to make the meniscus more stable for low viscosity inks.[15] The meniscus guide extends out from the head to stabilise the meniscus and support it while delivering ink to the substrate. The protrusion could be of various lengths depending on the rheological properties of the ink being used. The stability of the meniscus, however, can also be controlled by adjusting the gap height, thickness of shim and meniscus guide, ink pumping rate etc. A typical slot die coating setup is shown in Figure 1. 11.

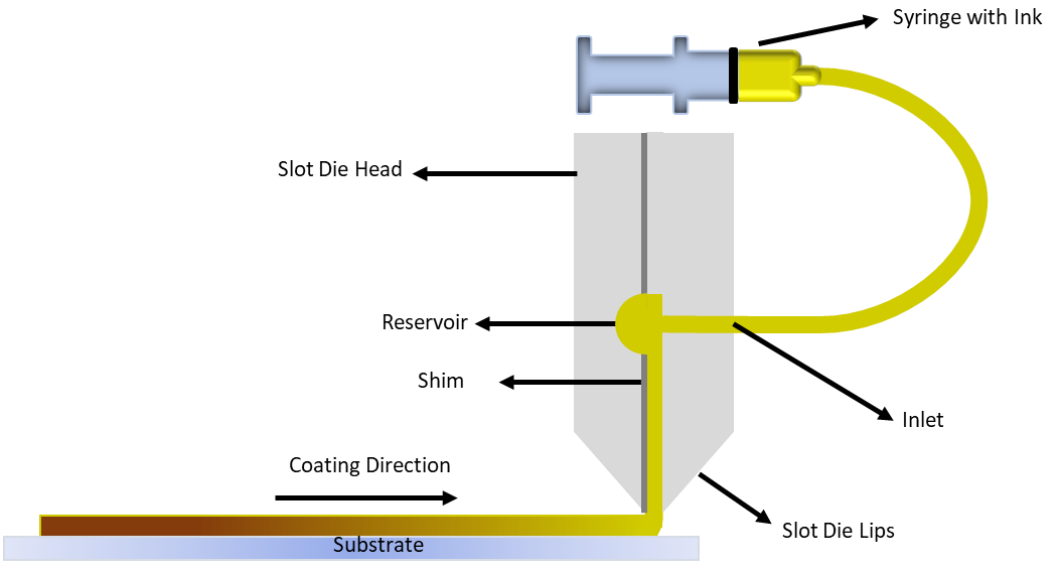

Figure 1. 11: Slot Die Coating Setup

Since all the ink that is fed into head goes on to the substrate, the thickness of the coated wet film can be controlled by controlling the flow of ink onto the substrate. This type of controlled flow coating is referred as pre-metered coating technique. This means it is easy to determine the relationship between the thickness of the wet-film coating, the flow rate, and the speed at which the substrate is moving relative to the head. This relation can be expressed by Eq 6.

$$WFT = \frac{r}{vw} \qquad 6$$

Where WFT is wet film thickness, r is pump rate in ml/min, v is coating speed in m/min and w is coating width in m. Further from WFT dry film thickness (DFT) can also be determined given the density of solid film (ρ) and concentration of the ink (c) are known. The relation can be expressed by Eq 7.

$$DFT = WFT\frac{c}{\rho} \qquad 7$$

Along with predetermined wet and dry film thickness, it is also possible to determine the coating window for slot die coating using the visco-capillary model.[16] Visco-capillary model

relates the properties of the ink and coating speed which is represented by the capillary number (Eq 8), to that with the dimensionless gap (Eq 9) by Eq 10

$$C_a = \frac{\mu\vartheta}{\sigma} \quad (8)$$

$$Dimensionless\ Gap = \frac{H_0}{t} \quad (9)$$

$$C_a = \frac{\mu v}{\sigma} = 0.65\left(\frac{2}{\left(\frac{H_0}{t}\right) - 1}\right)^{3/2} \quad (10)$$

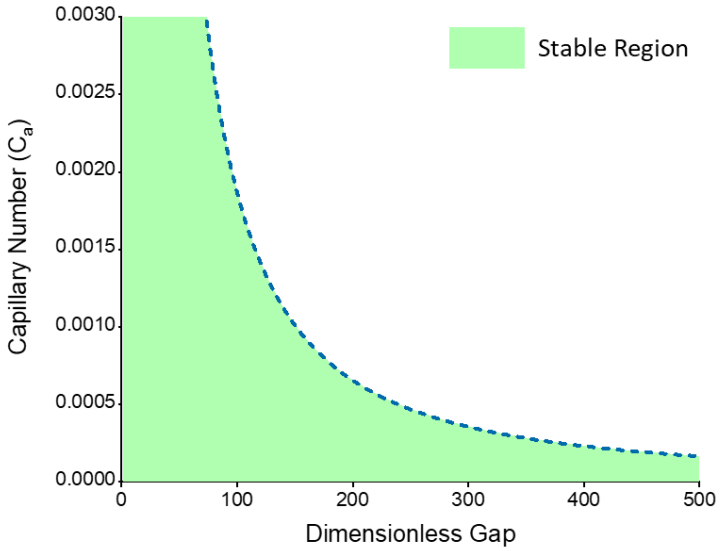

Figure 1. 12 Stable and unstable region plotted using Eq. 9

where t is the wet film thickness and H_0 is the distance between the head and substrate. The model helps determine the stability of the meniscus in various conditions for stable defect-free films. It states, that for a given ink with known surface tension (σ), viscosity (μ) and coating speed (υ), the meniscus will become unstable below a minimum wet film thickness. This limit also referred as a low-flow limit can be represented graphically by plotting Eq 10 for various capillary number as shown in Figure 1. 12. Above the dotted line the meniscus becomes unstable which leads to coated and uncoated areas also referred as rivulets.

However, at higher capillary numbers that is at higher coating speed or with higher viscosity inks the model breaks. At a higher capillary number an extended coating window is found when inertial effects are considered meaning thinner films can be coated by elevating the coating speed which the visco-capillary model would otherwise predict to be unstable. Meaning, for a given thickness a higher production rate can be achieved at higher capillary number. But the inks and coating speed used in this work is within C_a< 0.1 hence low flow limit would be a valid indicator for predetermination of the coating window.

1.4 Roll to Roll Manufacturing

Roll-to-roll manufacturing is a production method that performs a variety of processes and operations onto flexible rolled substrate materials while the material is being continuously fed from one roller to the next. Roll-to-roll manufacturing also goes by the acronym R2R. A standard configuration includes both an unwinder and a winder roll. After that, the web path or web is formed by connecting these two rolls to each other through a number of additional rolls. In the space between these two rolls, a wide range of operations, including those involving subtractive and additive processes, can be carried out in order to produce the final product. For example, the R2R coater from Coatema that was utilised in this project includes a corona treatment station, a coating station, and a drying area. Figure 1. 13 illustrates the R2R system's schematic that was used for this work.

Manufacturers prefer R2R over sheet-to-sheet (S2S), also referred as batch processing, because of its scale and economic benefits. Continuous R2R processing allows for higher production speeds while S2S processing has the disadvantage of having to stop at certain points leading to low throughput production. For these reason, R2R manufacturing is widely used across the industries for e.g., flexible electronics, textile manufacturing, metal foil and sheet manufacturing, batteries etc. As PSCs are compatible with flexible substrates, R2R unlocks a high potential for rapid throughput low-cost flexible photovoltaic manufacturing. However, high speed coating brings several challenges. One being limited oven residence time. Ideally the oven length can be increased if needed by increasing the overall length of the coating line but due to space constraint its usually limited. This impedes the use of high boiling point or low volatile solvents for ink formulations.

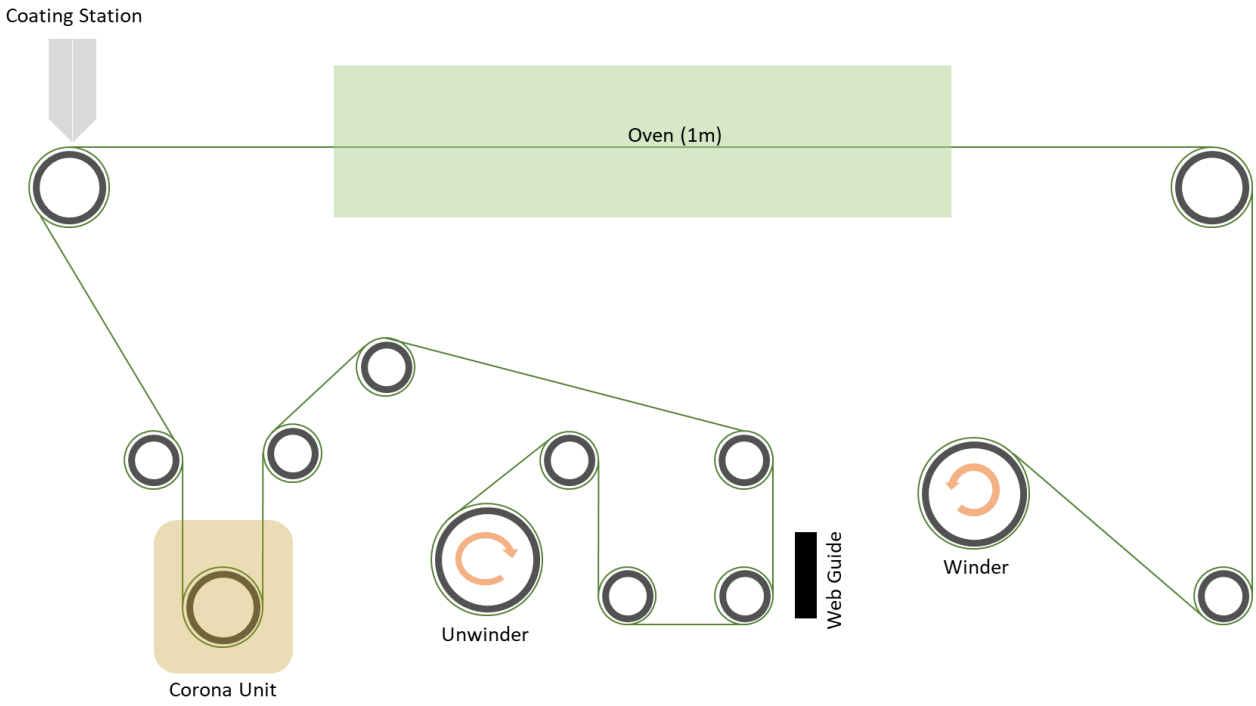

Figure 1. 13: Roll- to-Roll setup used for this work.

1.5 Literature Review

To build upon and address the next set of challenges, it is important to summarize developments in this field. The different methods developed in the literature to slot-die coat perovskite and other layers of the device stack will be discussed in detail. Along with discussion on the fundamental understanding of nucleation and crystallisation of slot-die coated perovskite films, the effects of various coating procedures, additives, and drying conditions are also discussed. This will include a thorough analysis of how slot-die coated perovskite solar cells have improved in terms of performance. The work in this section is published in Material today Communications and has been reprinted with permission from ref [17]

Patidar, R., Burkitt D., Hooper, K., Richards, D. & Watson, T. Slot-die coating of perovskite solar cells: An overview. Materials Today Communications 22, 100808 (2020).

(The author of this thesis led this work and Dr. Daniel Burkitt edited the article. Dr. Dave Richards wrote the interlayer section (therefor it has been rewritten for this thesis) and the other co-authors helped with figures, suggestions and reviewing.)

1.5.1 Perovskite Film Formation

The most critical layer of the PSCs is the perovskite layer and therefore It is important to have high-quality films with large grain sizes, pure crystal phases, and good coverage to improve photovoltaic performance and stability. In the following sections, different methods for improving the quality of slot-die coated perovskite layers will be discussed, all of which are focused on controlling the crystallization process of the perovskite material.

1.5.1.1 Two Step

The two-step method was first introduced by Mitzi et al, for coating of perovskite[18]. Following this, Burschka et al used the same method for the coating of the active layer of perovskite in PSCs.[19] During this process, a pre-deposited lead halide film is reacted with a cation and halide source, such as methylammonium iodide (MAI) or caesium iodide. This reaction causes the formation of the perovskite phase. To accomplish this, lead iodide (PbI_2) is first spin coated. The coated films are then exposed to a solution of MAI. This can be accomplished in a couple of different ways, the first of which is to spin coat the MAI solution onto the PbI_2 film, and the second way is to dip the PbI_2 film into MAI bath. This when dried results in the final perovskite phase.

In a one step process the perovskite film is coated using the mixed precursor of PbI_2 and MAI. While in the two step these two materials are coated separately, this divides the perovskite film formation in two parts which can be controlled to achieve improved perovskite film morphology. When coating the perovskite film, it is essential to consider the nucleation and crystal growth of the perovskite from the wet film of the precursor solution. This is done in order to achieve high quality film formation with no pin holes resulting in good film coverage. When using many of the strongly polar aprotic solvents that are commonly used for perovskite precursor inks, this presents a particularly difficult challenge. These inks have poor wetting properties on many of the common interlayers such as SnO_2 and TiO_2. This causes the growth of large crystals with large voids, which, when fabricated into devices, can cause shunt leakages and shorts, both of which are detrimental to performance.

For overcoming the difficulties associated with producing high-quality spin-coated layers of perovskite, the two-step method was a common strategy that was adopted by the research community in the early development of PSCs. In later years, a technique known as "solvent quenching" or "anti-solvent" was developed,[20] which involved rapidly exposing the precursor

film to a solvent that is orthogonal to the precursor's solvent. This causes a rapid nuclei generation in high numbers resulting in high film coverage and small crystal size. Although this technique yields outstanding film characteristics, integrating it into a typical slot-die coating process is challenging. Therefore, the two-step approach, was employed in many of the early reports involving slot-die coating of perovskite layer.

Schmidt et al. conducted a study comparing the effects of one-step and two-step deposition on slot-die coated films.[21] They found that the performance of the two approaches varied depending on the architectures and the underlying layer on which the precursor solutions was deposited. On an ITO/PEDOT:PSS (P-I-N stack) geometry, one-step deposition worked better, but the same did not work well on an ITO/ZnO/PCBM (N-I-P stack) geometry. It was believed that the ineffectiveness of one-step deposition on an N-I-P stack was due to the poor morphology of the perovskite film when coated on electron transport layer (ETL). This led to lower photocurrent and hence low PCE.[22] In contrast, two step deposition led to perovskite formation in P-I-N as well as N-I-P stacks, however, P-I-N stack performance was lower. This indicates that the coating method, i.e, either one step or two step, the substrate layer properties, and the nucleation and crystallization of the different precursor solutions all play a role and interact with each other and are dependent on the substrate surface.

For the two-step coating method to be effective, PbI_2 films must be uniformly coated with high surface coverage for the next reaction to occur. However, the static drying process involved in slot-die coating unlike spin coating gives enough time for the solvent and mass to flow resulting in uneven coating.[23] Hwang et al. investigated the effects of delayed drying on of PbI_2 films upon slot die coating in the context of depositing the perovskite layer in a sequential manner.[24] When the films were slow-dried, highly non-uniform films were observed. To mitigate this undesired flow of the ink, a new method was used to simulate the spin coating dynamic drying by using an external gas jet to quench the films. A second slot-die coating head was positioned next to the first slot die head. The second slot die head was used to flow compressed nitrogen onto the wet film to quench the films by rapid removal of

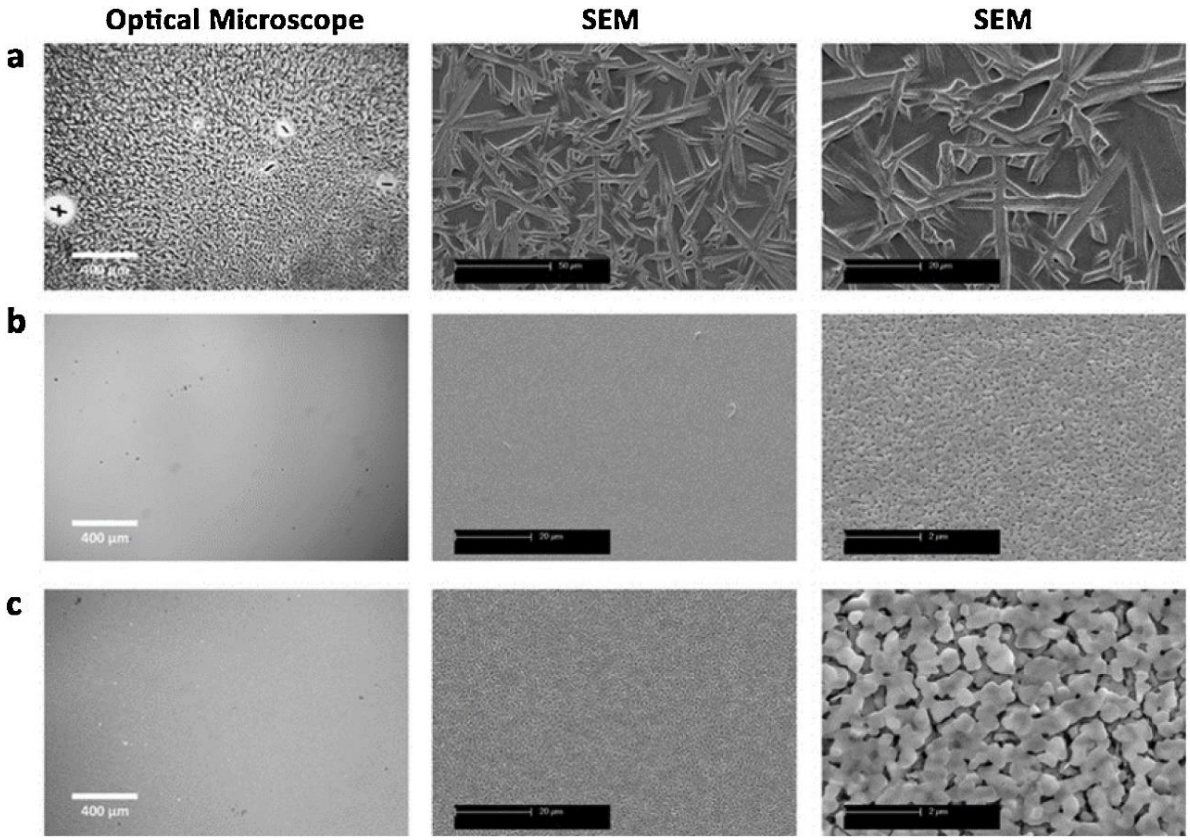

Figure 1. 14 Optical microscopy and SEM images of the slot-die coated PbI_2 films by (a) ambient drying (b) gas-quenching and air storage (c) by gas quenching and enclosed space storage. Reproduced with permission from Ref [17]

the solvent. The resulting "gas-quenched" PbI_2 films were highly dense and had high film uniformity. Figure 1. 14 demonstrates the change in the morphology of the PbI_2 film between those dried using gas quenching method and those that were dried under normal conditions. When exposed to MAI, the dense lead iodide films produced by the gas quenching approach poorly converted to perovskite. To enhance the reactivity of the PbI_2 films with MAI and achieve higher conversion to perovskite phase, a solvent vapor soaking technique was used. Following the drying of the gas quenched PbI_2 films, a closed chamber was used to store them. This resulted in a highly porous PbI_2 films which when exposed to MAI showed a high level conversion to perovskite. PSCs with slot die coated ETL, HTL and the perovskite layer resulted in PCE of 11.96%. However, storing the PbI_2 films for extended period to increase its reactivity is not a practical method, particularly in a large scale manufacturing setup. This would significantly reduce production time and hence low throughput. Additionally, this method impedes the transfer to continuous R2R manufacturing.

To create a scalable process for producing reactive PbI_2 films, researchers from the same group developed a process involving an unstable perovskite intermediate. This method had previously been demonstrated for devices fabricated via spin coating. 22,23,[27]. To increase the reactivity of slot die coated PbI_2 films and improve the conversion to the final perovskite, a non-stoichiometric quantity of MAI was mixed with PbI_2 precursor formulation. This slowed the crystallization rate of PbI_2 during the first stage of coating, which made it more reactive in the next deposition step. Consequently, there was a higher conversion into the perovskite phase. Figure 1. 15 illustrates the method schematically. Using this method, 5.8% PCE was

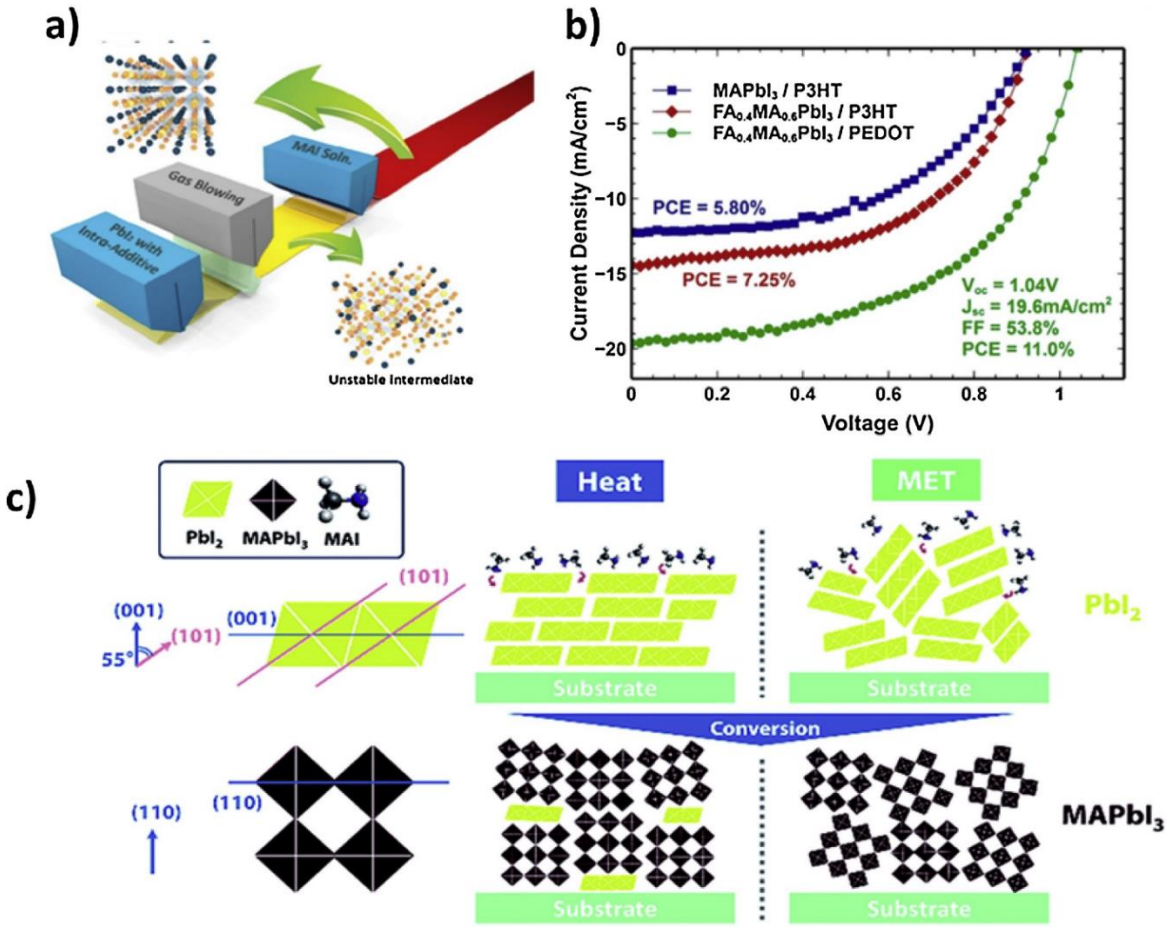

Figure 1. 15 (a) Schematic illustration of the coating procedure (b) JV curve of the R2R coated devices. (c) A schematic illustration showcasing the different PbI_2 crystal orientation made by MET and heat treatment and subsequent $CH_3NH_3PbI_3$ films. Reproduced with permission from Ref [17]

reported with R2R coated PSCs with thermally evaporated metal contact. To further increase the performance, $CH_3NH_2PbI_3$ was replaced with $FA_{0.4}MA_{0.6}PbI_3$. This was achieved by mixing 40 mol% FAI with PbI_2 at the first step of deposition. This was followed by the deposition of MAI on top of PbI_2 films. The change of perovskite led to the increment in the performance to 7.3% in the same device architecture on the flexible substrate. A further improvement in

performance was made by changing the P3HT HTL with PEDOT:PSS which resulted in 11.0% PCE (see Figure 1.13). Gong et al. also used a similar approach to coat multi cation perovskite.[28]For this process, PbI_2/CsI films containing a small quantity of MAI/FAI were first coated on gravure coated SnO_2 using the micro gravure method. Following this the mixture of FAI/MAI was slot die coated to induce the reaction between the two layer for the complete conversion to perovskite phase. Additionally, the perovskite film's roughness was reduced by gas blowing, which further enhanced the performance of the PSCs. The combination of the intra-additive method and gas quenching resulted in the best performance of 10.57% PCE.

Kim et al. also reported a method called "mediator extraction treatment" (MET) for preparing PbI_2 films that leads to improved conversion of perovskite and consequently high-quality perovskite layers.[29] A PbI_2 formulation composed of lead iodide mixed in dimethylformamide (DMF) and 10% vol/vol dimethyl sulfoxide (DMSO) was first slot-die coated and then partially dried using an air knife. This led to the formation of the PbI_2-DMSO adduct. DMSO was then removed from the films by soaking it an antisolvent bath. The as prepared PbI_2 films, in the next step were submerged in a MAI bath containing 25 wt% methyl ammonium chloride. Upon drying, the films were transformed into perovskite. The MET method produced porous PbI_2 films with random crystal orientation, resulting in an extremely reactive PbI_2 film. This is schematically represented in Figure 1. 15. The disoriented PbI_2 crystals enhanced the rate at which MAI penetrated the PbI_2 films, causing the fast conversion within 100 seconds. This technique produced an active layer with 18.3% maximum PCE, which is equivalent to a spin-coated active layer. Furthermore, Yu-Ching Huang and colleagues used near infrared (NIR) heating to dry the films in the two-step deposition method. The process involved coating the lead iodide ink onto a preheated substrate to enhance the PbI_2 film formation, and the use of NIR heating reduced the drying time for the perovskite layer from 1500 to 30 seconds.[30]

In addition to good stability and efficiency of the PSCs, the safety during the manufacturing is also of great importance. In perovskite solar cells, the lead and solvent are the main toxicants. Several attempts have been undertaken to explore low toxic and environment friendly solvent for precursors dissolution . The two-step deposition method therefore has gained lot of traction because it allows the use of low-toxic solvents, when compared with the generally used slovents like DMF and NMP. Remeika et al. used DMSO for the dissolution of lead iodide to coat the perovskite layer using two step method, however low performance was reported.

[31] Burkitt et al. later reported a better coating method when DMSO is used for PbI_2 dissolution. This when compared to using DMF, led to superior films and device performance.[32] The preheated (to 100℃) m-TiO_2 coated substrate when coated with PbI_2, the films became more reactive to MAI and converted to perovskite more effectively. Further the solvent used for the dissolution of MAI to slot-die coat the MAI layer was also optimised and ethanol was found to be the best, resulting in devices with 11% average PCE and for the hero cell, PCE up to 13.2% was recorded. In another study, the potential of the same solvent system was explored in a R2R setup with a P-I-N PSC stack on an ITO-PET films. In this study PEDOT:PSS was used as an HTL while PCBM/BCP were used as ETL with a metal top contact. However, the slow drying of DMSO due to its low volatile nature, caused the PbI_2 film to retract when passed through the inline convection ovens. To address this the temperature of the oven was increased to speed up the DMSO removal which did improve the film morphology, but it also caused damage to the flexible ITO-PET films and resulted in a broad range of device efficiecny.[33]

Two-step method for the deposition of perovskite has been effective in producing highly efficient devices with up to 18.3% PCEs and its feasibility with R2R process was also demonstrated. The use of techniques to quicken the PbI_2 films' drying process in order to increase film uniformity has been crucial to these achievements along with the processes that led to highly reactive PbI_2 films for its easy conversion to perovskite. Methods such as storing the films in a closed chamber, mediator extraction treatment, carefully selecting the solvent and using an intra-additive approach. Among these methods, the intra-additive approach demonstrated the most promise for R2R manufacturing. Combining it with the development of safer solvents and rapid heating methods, such as mediator extraction treatment and near infrared heating, could lead to a good R2R slot-die coated perovskite films.

1.5.1.2 One Step

One-step method for the deposition of the perovskite layer is a more streamlined method for large-scale manufacturing. Most research in which perovskite was slot die coated using one step method has focused on the P-I-N architecture which has better perovskite film morphology when coated on organic layers like PEDOT:PSS. However, instability of the P-I-N architecture remains a challenge for its large scale use.[34] N-I-P architectures have not been as widely studied with one-step slot-die coating but have shown promise in some cases. The

most used HTL in a P-I-N device stack, that is PEDOT:PSS, is hygroscopic and therefore degrades at high humidity. Further the unstable organic/ITO interface and the acidity of PSS, contribute to the fast degradation of this stack.[35,36] However, P-I-N PSCs are made of polymer layers that do not require high temperature processing and therefore is compatible with flexible substrates, making it suitable for roll-to-roll manufacturing. In contrast, the N-I-P stack needs high temperature processing of metal oxide ETLs, which may not be compatible with flexible substrates or manufacturing processes. However, recent advancements in the development of nanoparticle dispersion of metal oxide ETLs like SnO_2, it has become possible to fabricate PSCs with N-I-P stacks on flexible substrates.[37] This will be discussed in further detail later on in the text.

2.1.2.1 Controlling film formation through drying conditions

Initially, the P-I-N PSCs was the preferred choice for one-step perovskite formulations due to its improved film quality. However, researchers have developed various techniques to enhance film formation by one step method when fabrication PSCs in an N-I-P stack. Cotella et al. demonstrated a method for depositing $CH_3NH_3PbI_3{-}xClx$ perovskite on a mesoporous titanium dioxide (m-TiO_2) metal oxide scaffold using a one-step process in DMF solvent, with the film quenched by an air-knife to imitate the dynamic drying in spin coating.[38] By creating a temperature difference between the bottom and top of the coated film, the researchers were able to suppress vertical growth of perovskite grains and promote horizontal grain growth. This led to the formation of uniform film with lower roughness (Figure 1. 16). When the air knife is used it further increased the temperature gradient and improved the film's flatness and smoothness. This method resulted in a PCE of 9.2%. After their initial work, the same research group published a study with four slot die coated layers of the same device stack, including a compact TiO_2, mesoporous TiO_2, perovskite, and Spiro-OMeTAD. This illustrates how slot-die coating might be used for this device stack.[39]

Kim et al. reported a similar method to that of Cotella et al. to make high-quality $CH_3NH_3PbI_3$ films using a one-step method on planar N-I-P device stack with ZnO as ETL and DMF solvent. By using a combination of blowing and heating to speed up nucleation and solvent evaporation, the researchers were able to avoid the formation of large grains of perovskite with spaces in between them, resulting in improved surface coverage and uniformity. This resulted in 12.7% PCE.[40] Ciro et al. made flexible planar P-I-N PSCs on ITO-PET films, using

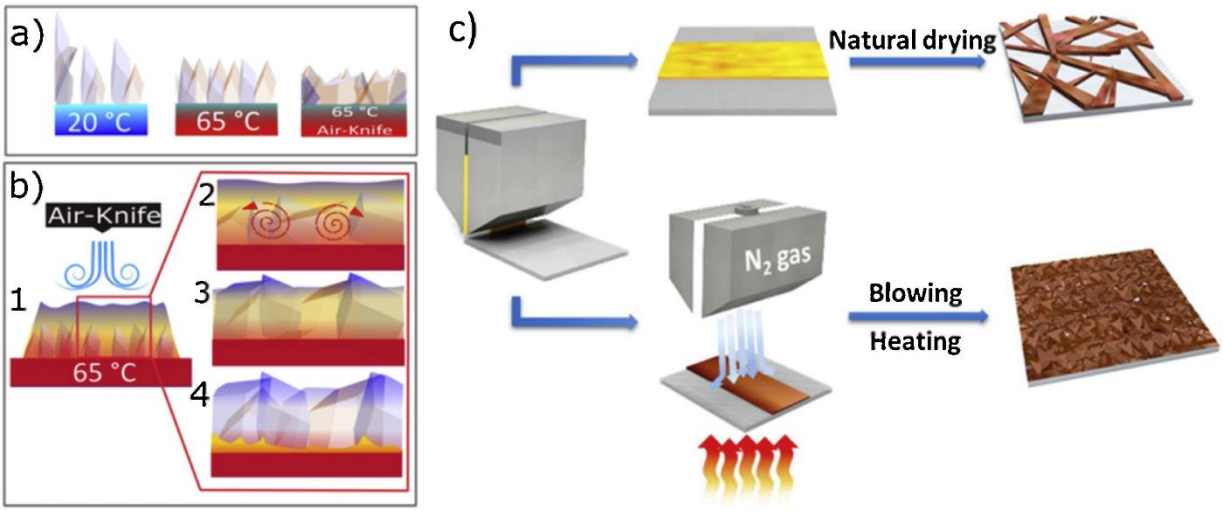

Figure 1. 16 (a) Illustration of layer differences with varying conditions (b) 1. Use of air knife following initial nucleation growth. 2. Convective motions and reduced viscosity boost the crystal growth at the interface with the substrate 3. Crystals approach the cooler region reducing the vertical growth rate in favour of lateral growth across the warm substrate. 4. Reduced thickness is achieved. (c) Schematic representation of the perovskite film formation via slot-die coating under the gas-blowing process combined with substrate heating. Reproduced with permission from ref [17].

PEDOT:PSS, $CH_3NH_3PbI_3$–xClx, and PCBM.[41] The perovskite formulation's solids content was tuned along with the substrate was heated to an ideal temperature (80°C) to enhance morphology of the film. This led to lower roughness and higher surface coverage. While the reported PCEs were low, it was demonstrated that the air knife along with heating of substrate is effective in controlling the perovskite morphology.

Studies have demonstrated that by speeding up the nucleation of the perovskite film and rapidly drying the solvent can help to high surface coverage and avoid the formation of large perovskite grains and voids between the film. These methods are demonstrated to be effective in controlling the growth of the perovskite film.

2.1.2.2 Controlling film formation through precursor choice

Lee et al. used rapid crystallization in order to fabricate PSCs with a P-I-N stack and PEDOT:PSS as HTL while C60/PCBM as the ETL. They used a solvent system with mixed lead precursors of lead chloride and lead acetate.[42] Lead acetate speeds up crystallization by forming methylammonium acetate which is an unstable byproduct.[43] But higher rate of crystallisation could also lead to solvent trapping and by-products within the film, resulting in voids. To prevent the formation of voids, lead chloride was also mixed into the perovskite ink to slow down the surface crystallization and prevent void formation, Figure 1. 17. The combination of

these two lead precursors and air knife enhanced the film coverage with improved grain size and morphology resulting in 13.3% PCE for 0.1cm^2 device and 8.3% for 10cm^2 module.

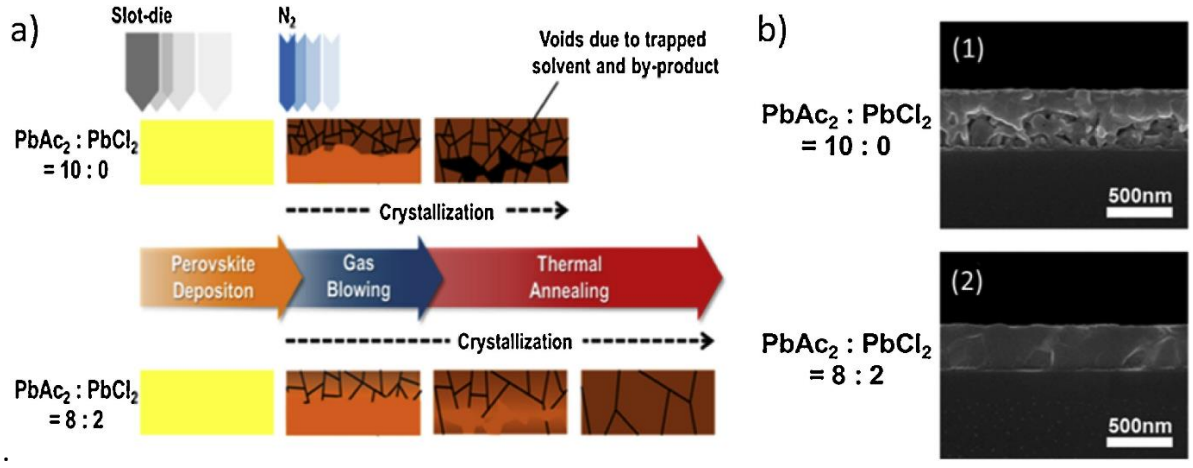

Figure 1. 17(a) Schematic representation of the crystallization of perovskite films. (b) SEM images showcasing the voids formed by rapid crystallization of perovskite and the same being mitigated by addition of $PbCl_2$. Reproduced with permission from Ref. [17]

Kamaraki et al. also used lead acetate as the only lead precursors in the DMF system for perovskite coating in PSCs on PET-ITO with a PEDOT:PSS and PCBM HTL and ETL respectively.[44] The solvent system with only lead acetate was optimized for the optimal deposition temperature of the perovskite formulation, which affected the films surface roughness similar to the observation made by Ciro et al. [41] Following the optimisation of the slot die coating parameters of all layers, PCE of 5% was recorded on average basis and with 6.5% PCE for hero cell. Giacomo et al. made use of a precursor solution in DMF with mixture of lead acetate and lead chloride. The as prepared formulation was then coated in a nitrogen filled glovebox to fabricate large-area high-performance modules.[45]

Selecting the appropriate perovskite precursors, which affects the film's surface coverage and morphology by regulating the nucleation and growth of the perovskite films. When paired with the techniques used to regulate the removal of the solvents, this can lead to the production of high-performance PSCs and modules.

2.1.2.3 Controlling film formation through solvent choice

Jung et al. showed that using solvent additives during the production of $CH_3NH_3PbI_3$ perovskite via one-step slot-die coating process can refine the morphology of the films. The films were used in a P-I-N device stack with PEDOT:PSS along with PCBM as HTL and ETL respectively.[46] 5% N-cyclohexyl-2-pyrrolidone (CHP) and 6% dimethyl sulfoxide (DMSO) was

mixed into the 0.75 M perovskite ink in DMF. It was demonstrated by Fourier-transform infrared spectroscopy (FTIR) that the PbI_2-DMSO adduct was more dominant over the DMF-CHP adduct, due to DMSO being highly polar and basic when compared to the other two solvents. The PbI_2-DMSO adduct slowed the crystallization rate of the perovskite. On the other hand, CHP due to its low vapour pressure and high boiling point was likely present in the drying film and played a role in uniform nucleation. The combination of these effects resulted in highly uniform and homogenous perovskite films with improved performance. The binary solvent additive was also found to contribute to the preferential orientation of the crystal growth of the perovskite films, improving charge transport.[47]

Using solvents like DMF and N-Methyl-2-Pyrrolidone (NMP) in a slot-die coating method has been demonstrated to produce PSCs with PCEs of around 18%.[29,48] However, the high toxicity of DMF and NMP has limited their use in the manufacturing process of PSCs. As a safer alternative, Noel et al. developed a mixture of acetonitrile (ACN) and methylamine gas for the dissolution of MAI and PbI_2.[49] ACN is a highly volatile with low boiling point, which allows for rapid removal of the solvent inducing the perovskite crystallisation at room temperature (98% crystallization was noted after approximately 110 seconds). The low toxicity of ACN as a solvent compared to DMF and its low viscosity fit well for high slot-die coating speeds. These properties make ACN a suitable choice for large-area fabrication of PSCs. Dou et al. used the ACN and methylamine gas composite solvent developed by Noel et al. for slot-die coating the perovskite layer with one step method for the fabrication of PSCs using R2R setup. The cells were made on a flexible glass coated with indium zinc oxide on which SnO_2 ETL was first slot die coated.[50] The optimized coating of $MAPbI_3$ via R2R slot die coating resulted in the film being highly crystaline which led to 14.12% PCE, while the best PCE for the S2S slot die coating was reported to be 17.31%, Figure 1. 18. While the ACN and methylamine gas composite solvent is great for large-area scalable deposition of perovskite film, its high flammability and toxicity may limit its commercial use. These properties may make it difficult to use this solvent in a manufacturing setting or may require additional safety measures to be taken.

Alternatively, DMSO is a less toxic solvent that has the potential to be used in the large-scale coatings. Even though DMSO is often thought of as low toxic solvent, it may readily permeate the skin along with any dissolved solute. As long as proper safety precautions are taken, DMSO could be a good option for PSC manufacturing. However, one issue with using DMSO

is that it has poor wetting properties on most substrates, which can make it difficult to coat films with high surface coverage. Galagan et al. showed that mixing 10% vol/vol of 2-Butoxyethanol with DMSO can reduce the surface tension of the mixed solvent system and improve its wetting properties. This resulted in improved film coverage and better PCE.[51] The best performing device in an R2R process had a 15.2% PCE on 0.09 cm^2 area and a stabilised 13.5% PCE. The architecture for the fabrication of this device was N-I-P and the perovskite ($Cs_{0.15}FA_{0.85}PbI_{2.85}Br_{0.15}$) layer was slot de coated on slot die coated SnO_2 layer.

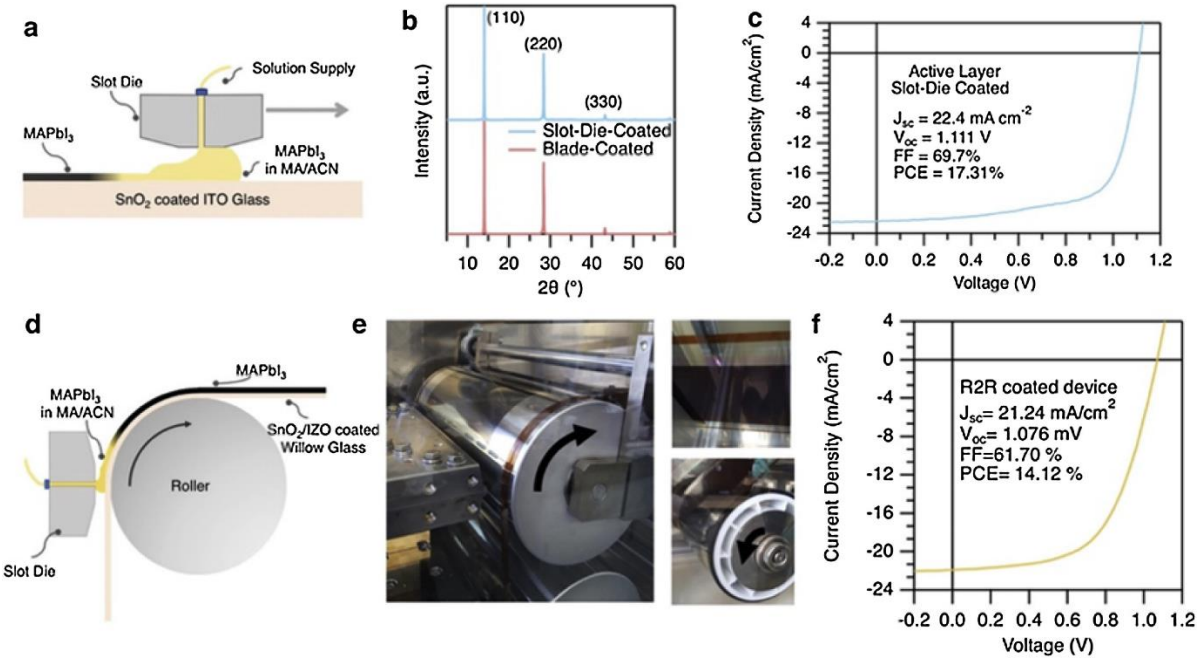

Figure 1. 18: (a–c) Schematic illustration of slot-die coating process on rigid substrate (a) XRD (b) JV data (c). (d) Schematic illustration of slot-die coating process on flexible glass substrate with R2R process. (e) Images showing R2R coating (f) JV curve of the best performing R2R-coated device. Reproduced with permission from Ref. [17]

Modifying the solvent system used in the production of PSCs can help regulate the morphology of the perovskite films and improve the performance of the cells. However, it is important to carefully consider the suitability of these solvent systems for industrial manufacture, considering factors such as toxicity, flammability, and wetting properties.

2.1.2.4 Controlling film formation through additives and surface modification

Due to their effect on grain growth which results in a change of morphology of perovskite films, additives have significantly contributed to increasing the stability and effectiveness of PSCs.[52] In a $CH_3NH_3PbI_3$ perovskite formulation in DMF, Zuo et al. made use of NH_4Cl along with perovskite precursors to enhance the quality of perovskite film in a P-I-N device stack

with PCBM and PEDOT:PSS as ETL and HTL respectively.[53] Absorption spectroscopy showed that the active layer of PSCs absorbs more light in the presence of NH_4Cl. The films also had higher photoluminescence intensity when NH_4Cl was present, indicating a increase in radiative recombination by lowering the defects in the film. Upon slot-die coating the perovskite precursors with NH_4Cl as an additive along with preheating substrate and air knife quenching, perovskite films of high quality was coated for S2S devices on glass substrates as well as for R2R devices on PET-ITO substrates. It should be noted that the fabrication was completed at 45% relative humidity yet demonstrated 15.57% PCE for the best cell fabricated via S2S coating and PCE of 11.16% was recorded for R2R coated devices.

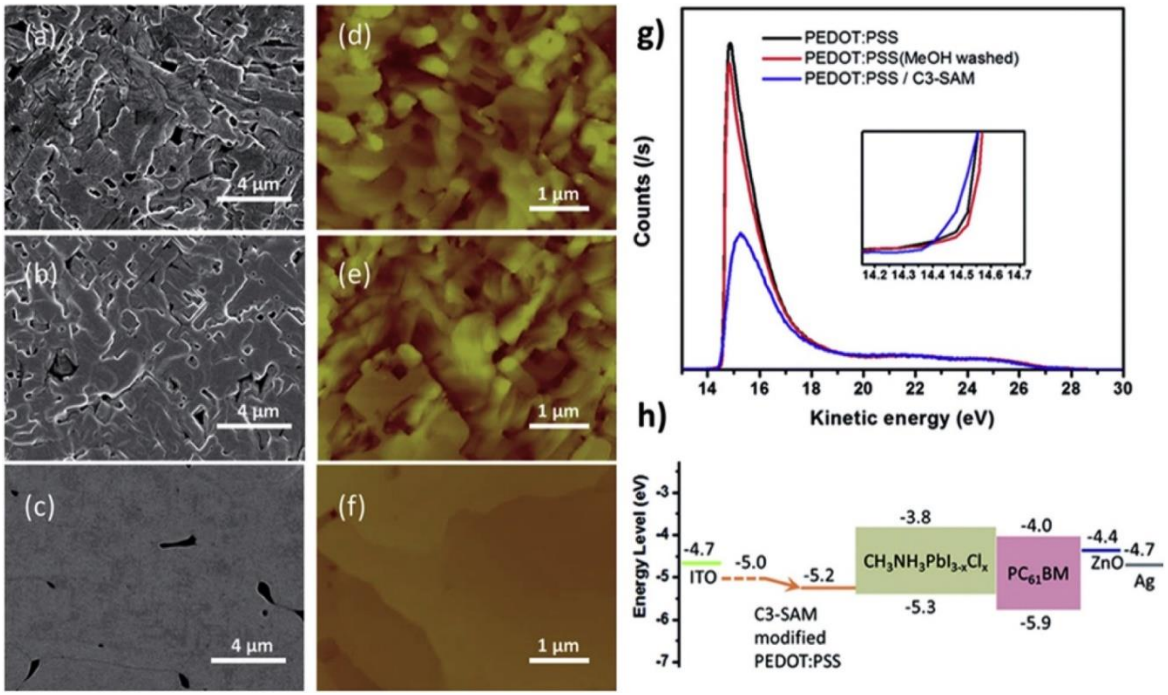

Figure 1. 19: SEM (a–c) and AFM (d–f) images of $CH_3NH_3PbI_3$–xClx films on the as-prepared PEDOT:PSS (a and d), methanol washed PEDOT:PSS (b and e) and C3-SAM modified PEDOT:PSS (c and f). (g) The ultraviolet photoelectron spectroscopy (UPS) spectra of the as-prepared PEDOT:PSS (black line), methanol washed PEDOT:PSS (red line) and C3-SAM modified PEDOT:PSS (blue line). (h) The energy band alignment of PSCs. Reproduced with permission from Ref. [17]

Surface treating interlayers is another method to enhance and regulate the perovskite morphology to reduce defects and increase homogeneity. In one such study, Gu et al. modified PEDOT:PSS surface by adding 3-aminopropanoic acid as an ambipolar self-assembled monolayer (C3-SAM).[54] In a P-I-N device with a $CH_3NH_3PbI_3$–xClx perovskite was coated along with PEDOT:PSS and PCBM/ZnO as HTL and ETL respectively. Applying a C3-SAM coating to the PEDOT:PSS film improved the growth of the perovskite film and also impacted

the energy band alignment by introducing a permanent dipole. UV photoelectron spectroscopy confirmed that the C3-SAM treatment reduced the work function of the PEDOT:PSS film by 0.2 eV, Figure 1. 19. The enhancement in charge transport and improved film morphology resulting from this treatment led to 5.1% PCE in flexible S2S roll coated devices.

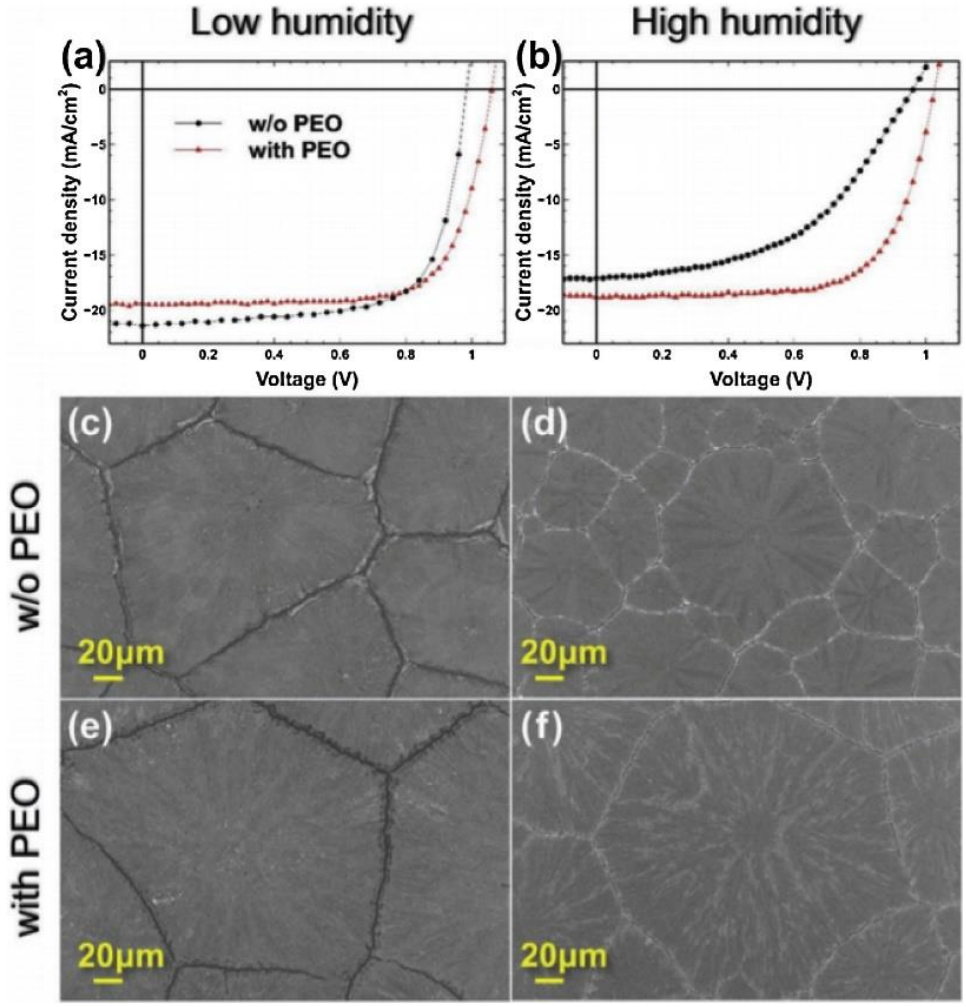

Figure 1. 20: Comparison of device performance and surface morphology with and without PEO at a low (30 ± 5% RH) and high (55 ± 5% RH) humidity. JV curves of the slot-die coated devices in (a) low and (b) high humidity, SEM images of perovskite films on glass/ITO/m-PEDOT:PSS substrates w/o PEO deposited in (c) low and (d) high humidity, and with PEO deposited at (e) low and (f) high humidity. Reproduced with permission from Ref.[17]

Kim et al. recently used polyethylene oxide (PEO) for slot-die coating of perovskite films used to fabricate a P-I-N device stack that included a modified PEDOT:PSS HTL, a $(CH_3NH_3)_{0.6}(HC(NH_2)_2)_{0.38}Cs_{0.2}PbI_{2.975}Br_{0.025}$ perovskite layer, and a PCBM/PEIE ETL.[55] The films were also made with $PbCl_2$ as the source of chloride and were deposited onto a preheated

substrate. Due to the addition of PEO into the perovskite precursors, it was found that the perovskite can be deposited in high humidity (around 55% relative humidity) conditions, Figure 1. 20. This method for fabricating PSCs in normal conditions could reduce the cost of manufacturing substantially. This is the only fully R2R (except for the top contact) processed perovskite solar cell reported at the time of writing and demonstrated an excellent efficiency of 11.7%.

1.5.2 2D Perovskite layer

Recently, two-dimensional (2D) perovskites have seen greater attention owing to their improved environmental stability compared to three-dimensional (3D) perovskites.[56] 2D perovskites are usually made by inserting a large organic cation, such as butylammonium, in between the layers of a 3D perovskite. While 2D perovskite solar cells have historically had lower performance as against 3D perovskite cells, they have meaningfully got better in recent years and have gone up to 14.1% PCE. The improved lifetime and performance of 2D PSCs has led to exploration of their potential with large-area printing and coating methods. R2R printing of PSCs with the active layer of 2D perovskite was first reported by Fu et al. 8% PCE on R2R coated PSCs on flexible substrate while 12.5% PCE was reported for S2S coated cells on a glass.[57] The lower PCE seen in the R2R coated cells as against S2S slot die coated cells was recognized due to the lower quality of the film produced by R2R slot-die coating on the less hydrophilic and rougher surface of ITO/PET. Despite the lower performance, this was an encouraging report as it demonstrated the potential for large area 2D perovskite solar cells.

1.5.3 Interlayers

The uniformity and quality of the perovskite film is crucial as discussed in the last section, but it is equally important to ensure uniformity in the charge transport layers as well. If the coatings are of poor quality, it can negatively affect a device's performance in various ways, such as causing short circuits or leakages due to pinholes or voids. If the charge blocking ability is inadequate, it can lead to an increase in recombination. It is also important to consider temperature limitations when coating the charge extraction layers on PET which is highly sensitive to temperatures above 140℃. This considerably restricts the use of PET as many charge extraction layers require high temperature processing. For example, the use of tin chloride ($SnCl_4.2H_2O$) for (SnO_2) [58] , nickel (II) acetate tetrahydrate for NiOx, and titanium

diisopropoxide bis (acetylacetonate) for TiO_2.[59] All these layers require annealing temperatures upwards of 300 °C to form the oxides from their respective precursor material.

1.5.3.1 Tin oxide electron transport layer

Due to its high electron mobility, improved band alignment compared to TiO_2, and lack of significant UV degradation, tin oxide (SnO_2) has seen significant interest in its use as an effective ETL for PSCs.[37] The use of SnO_2 in small area devices is well established, and most reports use a tin (IV) chloride precursor.[37,58] Although tin (IV) chloride requires to be annealed at a relatively low temperature of 180 °C for its conversion to SnO_2, the temperature is still high for its use on flexible substrates, such as PET, and a lengthy annealing period of about an hour is needed for the conversion.

SnO_2 formulations have recently been reported for low-temperature R2R slot die coating with excellent PCE. Galagan et al.[51] and Bu et al.[60] made use of a colloidal nanoparticle suspension of tin (IV) oxide 15 %wt./vol in H_2O (Alfa Aesar). When coated, these nanoparticles can be dried at 140-150 °C in a short period. Galagan et al. used this formulation to coat SnO_2 in an R2R N-I-P stack. The solution was first diluted with 10% 1-butanol to improve its wetting on the plastic substrate. This was then slot-die coated at 5 m min^{-1} and dried at 140 °C in a 20 m-long oven. Spiro-OMeTAD and gold contacts (post slot die coating perovskite) were then deposited offline, resulting in a PCE of 15.2% with stabilised efficiency of 13.5%. This SnO_2 solution was also used by Bu et al. to coat ETL for fabrication of PSCs and modules. In order to increase the wetting of ink on ITO-PET, the SnO_2 nanoparticle suspension was diluted using IPA in 1:1 ratio. To increase the film thickness and enhance uniformity, the ink was applied three times by slot-die coating before being dried at 140 °C for 60 minutes. High throughput R2R coating is unattractive with such a long drying time. Galagan et al. demonstrated, however, that this can be reduced to a few minutes. According to Bu et al., doping KOH as a stabilising chemical in the SnO_2 solution also helped passivate the SnO_2/perovskite interface, increasing stability and performance. Although the remaining layers in the device stack were spin-coated, it still demonstrates the suitability of the SnO_2 nanoparticle dispersion for its use in slot-die coating that can yield highly efficient PSCs at small scale (17.18% PCEs) as well as flexible modules of the size 5x6 cm^2 with 15% PCE.

1.5.3.2 Zinc oxide electron transport layer

Zinc Oxide (ZnO) ETL have been extensively studied in the organic photovoltaics field and its suitability with slot die coating is well explored.[61] Using this, Hwang et al. fabricated fully R2R slot die coated PSCs, except for thermally evaporated top electrode. For the ZnO deposition, they used an in house made ZnO nanoparticle solution.[24] When this was compared with the spin coated zinc oxide no differences were found. The compatibility of slot-die coated ZnO layer with R2R process on flexible substrates was demonstrated by the relatively quick drying at 120 °C for 10mins. However, it has frequently been reported that zinc oxide can cause instability of PSCs. Perovskite when annealed on top of ZnO post coating causes the perovskite to break down, which leads to the deprotonation of the methyl ammonium cations.[62]

Furthermore, Krebs et al. demonstrated a low temperature processed slot die coating of ZnO on flexible substrates in an N-I-P architecture. Along with ZnO, an interlayer of PCBM between the perovskite and ZnO was also used.[21] They as well discovered that perovskite formation was affected when drying it on top of the ZnO. To overcome this, they used a two-step method for the deposition of perovskite. This produced PCE of 2.6% for hero cell. This does show that ZnO is compatible with an R2R compatible process, despite the device performance being somewhat subpar which was attributed to the use of a printed top electrode.

1.5.3.3 Titanium dioxide electron transport layer

Burkitt et al. were able to show S2S slot die coating of the TiO_2 blocking layer, but this method is not compatible with low-temperature substrates because it required prolonged sintering at 550°C. To make a good blocking layer, the titanium diisopropoxide bis (acetylacetonate) precursor's solvent system was optimised. Also, the ink with the precursors were coated twice, in order to fill pinholes and reduce coating defects.[39] TiO_2 nanoparticles have recently been used by Hossain et al. to create a blocking layer which can be processed at 100 °C. They managed to avoid high temperature annealing because the nanoparticles used for the deposition were pre-synthesised in the anatase phase. With the help of these nanoparticles, Hossain et al. demonstrated the potential of low temperature processed TiO_2 ETL. 15.7% stabilised efficiency was reported when slot-die coating was used to deposit TIO_2. Moreover they also showed its compatibility with ink jet system by inkjet printing TiO_2 that resulted in similar efficiency.[63]

1.5.3.4 Hole transport layers

PSCs with both N-I-P and P-I-N architectures have been fabricated by slot-die coating various HTLs. PEDOT:PSS, however is the most commonly used HTL in P-I-N architecture, whose optimisation have been has been well understood in organic photovoltaics. PEDOT:PSS has been modified to improve efficiency by improving the energy alignment with perovskite[53,64], but it is still considered a poor HTL material due to its acidic nature which causes instability at the perovskite interface.[65] In place of PEDOT:PSS, reduced graphene oxide was explored by Zuo et al. for slot-die coating. This led to better performance and therefore might be a viable HTL for upscaling of PSCs.[53,66] Alternatives to PEDOT:PSS, a more stable metal oxide HTLs, such as nickel oxide (NiOx) have also been explored. Giacomo et al. successfully showed the slot-die coating of NiOx and presented it in a conference proceeding report, but complete explanation of the processing of this HTL was not provided.[67] In chapter 4 of this work, efforts have been made to replace PEDOT:PSS with PTAA for efficient R2R slot die coated PSCs.

Burkitt et al. slot die coated spiro-OMeTAD for its use in N-I-P stack of PSCs.[39] They also avoided the use of a highly toxic chlorobenzene solvent system for dissolution of spiro-OMeTAD by switching it out for the less toxic solvent toluene. However, the instability problems with spiro-OMeTAD still restricts its use for scalable processes. Qin et al switched spiro-OMeTAD with Bifluo-OmeTAD.[68] The performance of spiro-OMeTAD films was worsened by the formation of large crystallites, which by replacing it with bifluo-OMeTAD was avoided due to its amorphous nature. This led to devices with slot-die coated ETL, perovskite, and HTL achieving 14.7% PCE.

An alternative to spiro-OMeTAD, P3HT have also been explored for both S2S and R2R fabrication method. But P3HT devices typically have resulted in lower performance and has been combined with another thermally evaporated HTL for improving the performance.[24,27]HTL slot-die coating is a comparatively unexplored. There are very few reports available on the deposition of more stable HTL materials, therefore, a complete chapter (3) is dedicated to address this.

1.5.4 Contacts

Due to their high transparency and high electrical conductivity, transparent conductive oxides (TCOs) are often employed as transparent electrodes (hereinafter referred to as bottom electrode) in PSCs. TCOs are used in a variety of industries, including smart windows,

touchscreens, organic light emitting diodes, liquid crystal displays, and antistatic coatings. Although TCOs have been well developed for large-scale fabrication, they still contribute significantly to the overall cost of PSCs. To address this, Sears et al. developed a TCO-free transparent electrode for PSCs using a slot die printing method for replacing ITO with Ag/PEDOT:PSS. This resulted in a PCE of 11%.[69]

High vacuum thermal evaporation is a common method used for lab-scale fabrication of the top contact in PSCs, but it is not practical for high-throughput manufacturing. Solution processed top electrode is challenging to print due to the need for a high-conductivity material which must also be low temperature processable and must have a processing solvent that is compatible with all the layers beneath it. To achieve fully solution-processed PSCs, researchers have proposed solutions such as fully printed carbon-based mesoscopic PSCs [70] and printing friendly top electrodes.[71] At the moment of writing this, there are no reports of slot die coating being used to deposit the top electrode for PSCs. Other coating methods, such as ink-jet[72] and spray coating[71], have been explored for printing of silver nanowires as the top electrode.

1.5.5 Module representation

Although slot-die coated PSCs have been found to work well on small devices, it is crucial to also evaluate the performance of large-area slot die coated PSCs in order to determine their efficiency at manufacturing scale. Hwang et al. reported the first module with a 40 cm^2 active area where in perovskite was slot-die coated, but the performance was not fully reported and was poor.[24] In 2018, Lee et al. reported a method for fabricating large-area PSCs using mixed Pb precursors, as described in Section 2.2.2. This strategy was successful in fabricating a module with an 8.3% PCE on a 10 cm^2 area.[42] It is worth noting that only the perovskite layer was printed using slot-die coating in the report by Lee et al. Subsequently, Giacomo et al. reported a module with 168.75 cm^2 active area and a PCE of 10%. This was fabricated using slot-die coating to print both the perovskite and HTL, while the ETL deposition was done using electron beam technique (Figure 1. 21).[73]

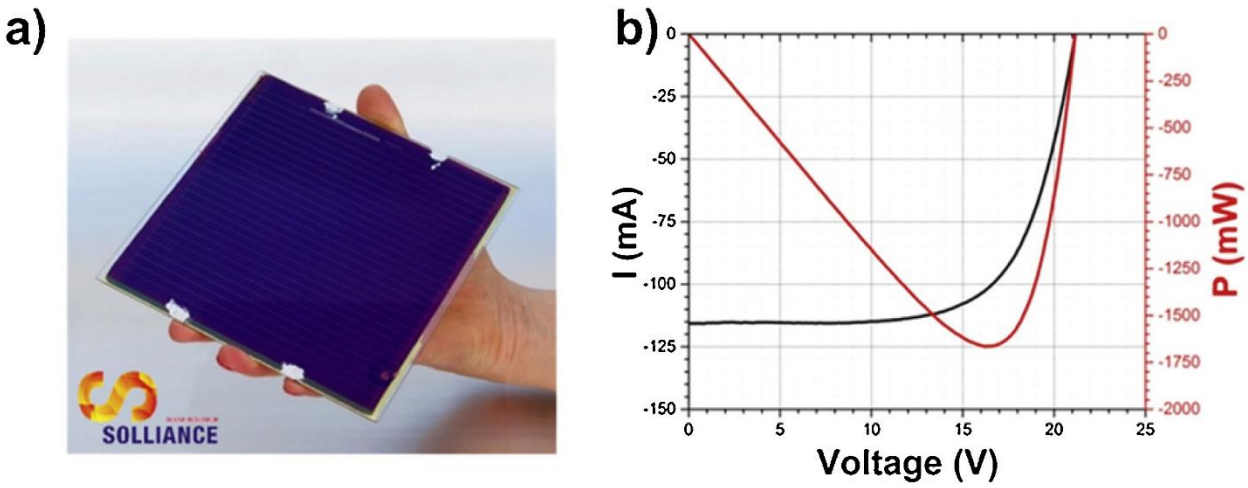

Figure 1. 21(a) 6 in.x6 in. perovskite module; (b) IV curve and power curve of the 6 in.x6 in. module, with the actual dimension of 168.75 cm^2 and 25 interconnected cells. Reproduced with permission from Ref.[17]

References

1. Hannah Ritchie & Max Roser. Renewable Energy. *OurWorldInData.org* https://ourworldindata.org/renewable-energy#citation (2020).
2. Hannah Ritchie & Max Roser. CO2 Emissions. *OurWorldInData.org* https://ourworldindata.org/co2-emissions (2020).
3. Air Pollution. *who.int* https://www.who.int/health-topics/air-pollution#tab=tab_1.
4. Reference Air Mass 1.5 Spectra | Grid Modernization | NREL. https://www.nrel.gov/grid/solar-resource/spectra-am1.5.html.
5. Weber, D. CH3NH3PbX3, ein Pb(II)-System mit kubischer Perowskitstruktur. *Zeitschrift fur Naturforschung - Section B Journal of Chemical Sciences* **33**, 1443–1445 (1978).
6. Mitzi, D. B., Feild, C. A., Harrison, W. T. A. & Guloy, A. M. Conducting tin halides with a layered organic-based perovskite structure. *Nature 1994 369:6480* **369**, 467–469 (1994).
7. Kojima, A., Teshima, K., Shirai, Y. & Miyasaka, T. Organometal halide perovskites as visible-light sensitizers for photovoltaic cells. *J Am Chem Soc* **131**, 6050–6051 (2009).
8. Lee, M. M., Teuscher, J., Miyasaka, T., Murakami, T. N. & Snaith, H. J. Efficient hybrid solar cells based on meso-superstructured organometal halide perovskites. *Science (1979)* **338**, 643–647 (2012).
9. Kim, H. S. *et al.* Lead Iodide Perovskite Sensitized All-Solid-State Submicron Thin Film Mesoscopic Solar Cell with Efficiency Exceeding 9%. *Scientific Reports 2012 2:1* **2**, 1–7 (2012).
10. Best Research-Cell Efficiency Chart | Photovoltaic Research | NREL. https://www.nrel.gov/pv/cell-efficiency.html.
11. Goldschmidt, V. M. Die Gesetze der Krystallochemie. *Naturwissenschaften 1926 14:21* **14**, 477–485 (1926).

12. Chen, C. *et al.* Effect of BCP buffer layer on eliminating charge accumulation for high performance of inverted perovskite solar cells. *RSC Adv* **7**, 35819–35826 (2017).

13. Yoshida, H. Electron Transport in Bathocuproine Interlayer in Organic Semiconductor Devices. *Journal of Physical Chemistry C* **119**, 24459–24464 (2015).

14. Yuan, D. X. *et al.* A solution-processed bathocuproine cathode interfacial layer for high-performance bromine–iodine perovskite solar cells. *Physical Chemistry Chemical Physics* **17**, 26653–26658 (2015).

15. Krebs, F. C. Polymer solar cell modules prepared using roll-to-roll methods: Knife-over-edge coating, slot-die coating and screen printing. *Solar Energy Materials and Solar Cells* **93**, 465–475 (2009).

16. Carvalho, M. S. & Kheshgi, H. S. Low-flow limit in slot coating: Theory and experiments. *AIChE Journal* **46**, 1907–1917 (2000).

17. Patidar, R., Burkitt, D., Hooper, K., Richards, D. & Watson, T. Slot-die coating of perovskite solar cells: An overview. *Mater Today Commun* **22**, 100808 (2020).

18. Liang, K., Mitzi, D. B. & Prikas, M. T. Synthesis and Characterization of Organic-Inorganic Perovskite Thin Films Prepared Using a Versatile Two-Step Dipping Technique. *Chemistry of Materials* **10**, 403–411 (1998).

19. Burschka, J. *et al.* Sequential deposition as a route to high-performance perovskite-sensitized solar cells. *Nature 2013 499:7458* **499**, 316–319 (2013).

20. Jeon, N. J. *et al.* Solvent engineering for high-performance inorganic–organic hybrid perovskite solar cells. *Nature Materials 2014 13:9* **13**, 897–903 (2014).

21. Schmidt, T. M., Larsen-Olsen, T. T., Carlé, J. E., Angmo, D. & Krebs, F. C. Upscaling of Perovskite Solar Cells: Fully Ambient Roll Processing of Flexible Perovskite Solar Cells with Printed Back Electrodes. *Adv Energy Mater* **5**, 1500569 (2015).

22. Im, J. H., Kim, H. S. & Park, N. G. Morphology-photovoltaic property correlation in perovskite solar cells: One-step versus two-step deposition of CH3NH3PbI3. *APL Mater* **2**, 081510 (2014).

23. Baker, J. A. *et al.* From spin coating to roll-to-roll: investigating the challenge of upscaling lead halide perovskite solar cells. *IET Renewable Power Generation* **11**, 546–549 (2017).

24. Hwang, K. *et al.* Toward Large Scale Roll-to-Roll Production of Fully Printed Perovskite Solar Cells. *Advanced Materials* **27**, 1241–1247 (2015).

25. Zhang, T., Yang, M., Zhao, Y. & Zhu, K. Controllable Sequential Deposition of Planar CH3NH3PbI3 Perovskite Films via Adjustable Volume Expansion. *Nano Lett* **15**, 3959–3963 (2015).

26. Xie, Y. *et al.* Enhanced Performance of Perovskite CH3NH3PbI3 Solar Cell by Using CH3NH3I as Additive in Sequential Deposition. *ACS Appl Mater Interfaces* **7**, 12937–12942 (2015).

27. Heo, Y. J. *et al.* Printing-friendly sequential deposition via intra-additive approach for roll-to-roll process of perovskite solar cells. *Nano Energy* **41**, 443–451 (2017).

28. Gong, C. *et al.* Flexible Planar Heterojunction Perovskite Solar Cells Fabricated via Sequential Roll-to-Roll Microgravure Printing and Slot-Die Coating Deposition. *Solar RRL* **4**, 1900204 (2020).

29. Kim, Y. Y. *et al.* Fast two-step deposition of perovskite via mediator extraction treatment for large-area, high-performance perovskite solar cells. *J Mater Chem A Mater* **6**, 12447–12454 (2018).

30. Huang, Y. C., Li, C. F., Huang, Z. H., Liu, P. H. & Tsao, C. S. Rapid and sheet-to-sheet slot-die coating manufacture of highly efficient perovskite solar cells processed under ambient air. *Solar Energy* **177**, 255–261 (2019).

31. Remeika, M., Ono, L. K., Maeda, M., Hu, Z. & Qi, Y. High-throughput surface preparation for flexible slot die coated perovskite solar cells. *Org Electron* **54**, 72–79 (2018).

32. Burkitt, D., Searle, J., A.Worsley, D. & Watson, T. Sequential Slot-Die Deposition of Perovskite Solar Cells Using Dimethylsulfoxide Lead Iodide Ink. *Materials 2018, Vol. 11, Page 2106* **11**, 2106 (2018).

33. Burkitt, D. *et al.* Meniscus Guide Slot-Die Coating for Roll-to-Roll Perovskite Solar Cells. *MRS Adv* **4**, 1399–1407 (2019).

34. Berhe, T. A. *et al.* Organometal halide perovskite solar cells: degradation and stability. *Energy Environ Sci* **9**, 323–356 (2016).

35. Tiep, N. H., Ku, Z. & Fan, H. J. Recent Advances in Improving the Stability of Perovskite Solar Cells. *Adv Energy Mater* **6**, 1501420 (2016).

36. de Jong, M. P., van Ijzendoorn, L. J. & de Voigt, M. J. A. Stability of the interface between indium-tin-oxide and poly(3,4-ethylenedioxythiophene)/poly(styrenesulfonate) in polymer light-emitting diodes. *Appl Phys Lett* **77**, 2255 (2000).

37. Jiang, Q. *et al.* SnO2: A Wonderful Electron Transport Layer for Perovskite Solar Cells. *Small* **14**, 1801154 (2018).

38. Cotella, G. *et al.* One-step deposition by slot-die coating of mixed lead halide perovskite for photovoltaic applications. *Solar Energy Materials and Solar Cells* **159**, 362–369 (2017).

39. Burkitt, D., Searle, J. & Watson, T. Perovskite solar cells in N-I-P structure with four slot-die-coated layers. *R Soc Open Sci* **5**, (2018).

40. Kim, J. E. *et al.* Slot die coated planar perovskite solar cells via blowing and heating assisted one step deposition. *Solar Energy Materials and Solar Cells* **179**, 80–86 (2018).

41. Ciro, J., Mejía-Escobar, M. A. & Jaramillo, F. Slot-die processing of flexible perovskite solar cells in ambient conditions. *Solar Energy* **150**, 570–576 (2017).

42. Lee, D. *et al.* Slot-Die Coated Perovskite Films Using Mixed Lead Precursors for Highly Reproducible and Large-Area Solar Cells. *ACS Appl Mater Interfaces* **10**, 16133–16139 (2018).

43. Zhang, W. *et al.* Ultrasmooth organic–inorganic perovskite thin-film formation and crystallization for efficient planar heterojunction solar cells. *Nature Communications 2015 6:1* **6**, 1–10 (2015).

44. Kamaraki, C. *et al.* Efficient flexible printed perovskite solar cells based on lead acetate precursor. *Solar Energy* **176**, 406–411 (2018).

45. di Giacomo, F. *et al.* Up-scalable sheet-to-sheet production of high efficiency perovskite module and solar cells on 6-in. substrate using slot die coating. *Solar Energy Materials and Solar Cells* **181**, 53–59 (2018).

46. Jung, Y. S. *et al.* One-Step Printable Perovskite Films Fabricated under Ambient Conditions for Efficient and Reproducible Solar Cells. *ACS Appl Mater Interfaces* **9**, 27832–27838 (2017).

47. Bae, S., Han, S. J., Shin, T. J. & Jo, W. H. Two different mechanisms of CH3NH3PbI3 film formation in one-step deposition and its effect on photovoltaic properties of OPV-type perovskite solar cells. *J Mater Chem A Mater* **3**, 23964–23972 (2015).

48. Whitaker, J. B. *et al.* Scalable slot-die coating of high performance perovskite solar cells. *Sustain Energy Fuels* **2**, 2442–2449 (2018).

49. Noel, N. K. *et al.* A low viscosity, low boiling point, clean solvent system for the rapid crystallisation of highly specular perovskite films. *Energy Environ Sci* **10**, 145–152 (2017).

50. Dou, B. *et al.* Roll-to-Roll Printing of Perovskite Solar Cells. *ACS Energy Lett* **3**, 2558–2565 (2018).

51. Galagan, Y. *et al.* Roll-to-Roll Slot Die Coated Perovskite for Efficient Flexible Solar Cells. *Adv Energy Mater* **8**, 1–7 (2018).

52. Li, T. *et al.* Additive engineering for highly efficient organic–inorganic halide perovskite solar cells: recent advances and perspectives. *J Mater Chem A Mater* **5**, 12602–12652 (2017).

53. Zuo, C., Vak, D., Angmo, D., Ding, L. & Gao, M. One-step roll-to-roll air processed high efficiency perovskite solar cells. *Nano Energy* **46**, 185–192 (2018).

54. Gu, Z. *et al.* Interfacial engineering of self-assembled monolayer modified semi-roll-to-roll planar heterojunction perovskite solar cells on flexible substrates. *J Mater Chem A Mater* **3**, 24254–24260 (2015).

55. Kim, J.-E. *et al.* Humidity-Tolerant Roll-to-Roll Fabrication of Perovskite Solar Cells via Polymer-Additive-Assisted Hot Slot Die Deposition. *Adv Funct Mater* **29**, 1809194 (2019).

56. Yan, J., Qiu, W., Wu, G., Heremans, P. & Chen, H. Recent progress in 2D/quasi-2D layered metal halide perovskites for solar cells. *J Mater Chem A Mater* **6**, 11063–11077 (2018).

57. Zuo, C. *et al.* Self-Assembled 2D Perovskite Layers for Efficient Printable Solar Cells. *Adv Energy Mater* **9**, 1803258 (2019).

58. Murugadoss, G. *et al.* An efficient electron transport material of tin oxide for planar structure perovskite solar cells. *J Power Sources* **307**, 891–897 (2016).

59. Supasai, T., Henjongchom, N., Tang, I. M., Deng, F. & Rujisamphan, N. Compact nanostructured TiO2 deposited by aerosol spray pyrolysis for the hole-blocking layer in a CH3NH3PbI3 perovskite solar cell. *Solar Energy* **136**, 515–524 (2016).

60. Bu, T. *et al.* Universal passivation strategy to slot-die printed SnO2 for hysteresis-free efficient flexible perovskite solar module. *Nature Communications 2018 9:1* **9**, 1–10 (2018).

61. Søndergaard, R. R., Hösel, M. & Krebs, F. C. Roll-to-Roll fabrication of large area functional organic materials. *J Polym Sci B Polym Phys* **51**, 16–34 (2013).

62. Zhang, P. *et al.* Perovskite Solar Cells with ZnO Electron-Transporting Materials. *Advanced Materials* **30**, 1703737 (2018).

63. Hossain, I. M. *et al.* Scalable processing of low-temperature TiO2 nanoparticles for high-efficiency perovskite solar cells. *ACS Appl Energy Mater* **2**, 47–58 (2019).

64. Zuo, C., Ding, L., Zuo, C. & Ding, L. Modified PEDOT Layer Makes a 1.52 V Voc for Perovskite/PCBM Solar Cells. *Adv Energy Mater* **7**, 1601193 (2017).

65. Cameron, J. & Skabara, P. J. The damaging effects of the acidity in PEDOT:PSS on semiconductor device performance and solutions based on non-acidic alternatives. *Mater Horiz* **7**, 1759–1772 (2020).

66. Yeo, J. S. *et al.* Reduced graphene oxide-assisted crystallization of perovskite via solution-process for efficient and stable planar solar cells with module-scales. *Nano Energy* **30**, 667–676 (2016).

67. Giacomo, F. di *et al.* Large area 140 cm2 perovskite solar modules made by sheet to sheet and roll to roll fabrication with 14.5% efficiency. *2018 IEEE 7th World Conference on Photovoltaic Energy Conversion, WCPEC 2018 - A Joint Conference of 45th IEEE PVSC, 28th PVSEC and 34th EU PVSEC* 2795–2798 (2018) doi:10.1109/PVSC.2018.8548157.

68. Qin, T. *et al.* Amorphous hole-transporting layer in slot-die coated perovskite solar cells. *Nano Energy* **31**, 210–217 (2017).

69. Sears, K. K. *et al.* ITO-Free Flexible Perovskite Solar Cells Based on Roll-to-Roll, Slot-Die Coated Silver Nanowire Electrodes. *Solar RRL* **1**, 1700059 (2017).

70. Mei, A. *et al.* A hole-conductor-free, fully printable mesoscopic perovskite solar cell with high stability. *Science (1979)* **345**, 295–298 (2014).

71. Guo, F. *et al.* High-performance semitransparent perovskite solar cells with solution-processed silver nanowires as top electrodes. *Nanoscale* **7**, 1642–1649 (2015).

72. Xie, M. *et al.* Fully Solution-Processed Semi-Transparent Perovskite Solar Cells With Ink-Jet Printed Silver Nanowires Top Electrode. *Solar RRL* **2**, 1700184 (2018).

73. di Giacomo, F. *et al.* Up-scalable sheet-to-sheet production of high efficiency perovskite module and solar cells on 6-in. substrate using slot die coating. *Solar Energy Materials and Solar Cells* **181**, 53–59 (2018).

Chapter 2
Experimental Methods

2.1 $MAPbI_3$ Ink Preparation

This experiment was done with the help from Dr. David Beynon.

For acetonitrile methylamine formulation (ACN-MA), lead iodide (PbI_2) and methylammonium iodide (MAI), were weighed in 1:1.06 ratio respectively. were added to a 50mL 2 neck Erlenmeyer flask. Solids were weighed in nitrogen glove box and was added to the flask along with ACN. A glass bubbler was then loaded with methylamine solution. Methylamine solution was then bubbled with dry nitrogen and the gas from bubbler was passed through desiccant column and to the precursor solution. During bubbling the perovskite precursor solution was kept on constant stir by stir bars. The colour of the solution would change from black (stage 1) to a yellow colloidal dispersion (stage 2) to a clear yellow solution (stage 3) as shown in Figure 2. 1. When the clear yellow solution was observed at stage 3 the gas was turned off. The prepared stock solution was stored at 5°C in a refrigerator and was taken out when needed for conducting experiments. A complete schematic of the process is presented in Figure 2. 1.

2.2 Coating Methods for Device Fabrication

The methods used for deposition of various layers making the perovskite solar cell stack will be discussed in the following section.

2.2.1 Spin Coating

Spin coating is a solution-based batch process used for depositing films with high reproducibility and uniform thickness. It is used for wide variety of solutions with a range of different rheological properties. A schematic representing the entire process is shown in Figure 2.1. Briefly, the substrate is held on a vacuum chuck, which stops it from falling when it is spun. Following this a fixed amount of solution is dropped on top of the substrate. In the next step, the spin programme is initiated, after which the spin chuck will rotate the substrate at a set acceleration up to a set speed for a period of time. The accelerations, spin speeds, and times determine the thickness of the film that a particular formulation will result in. As a

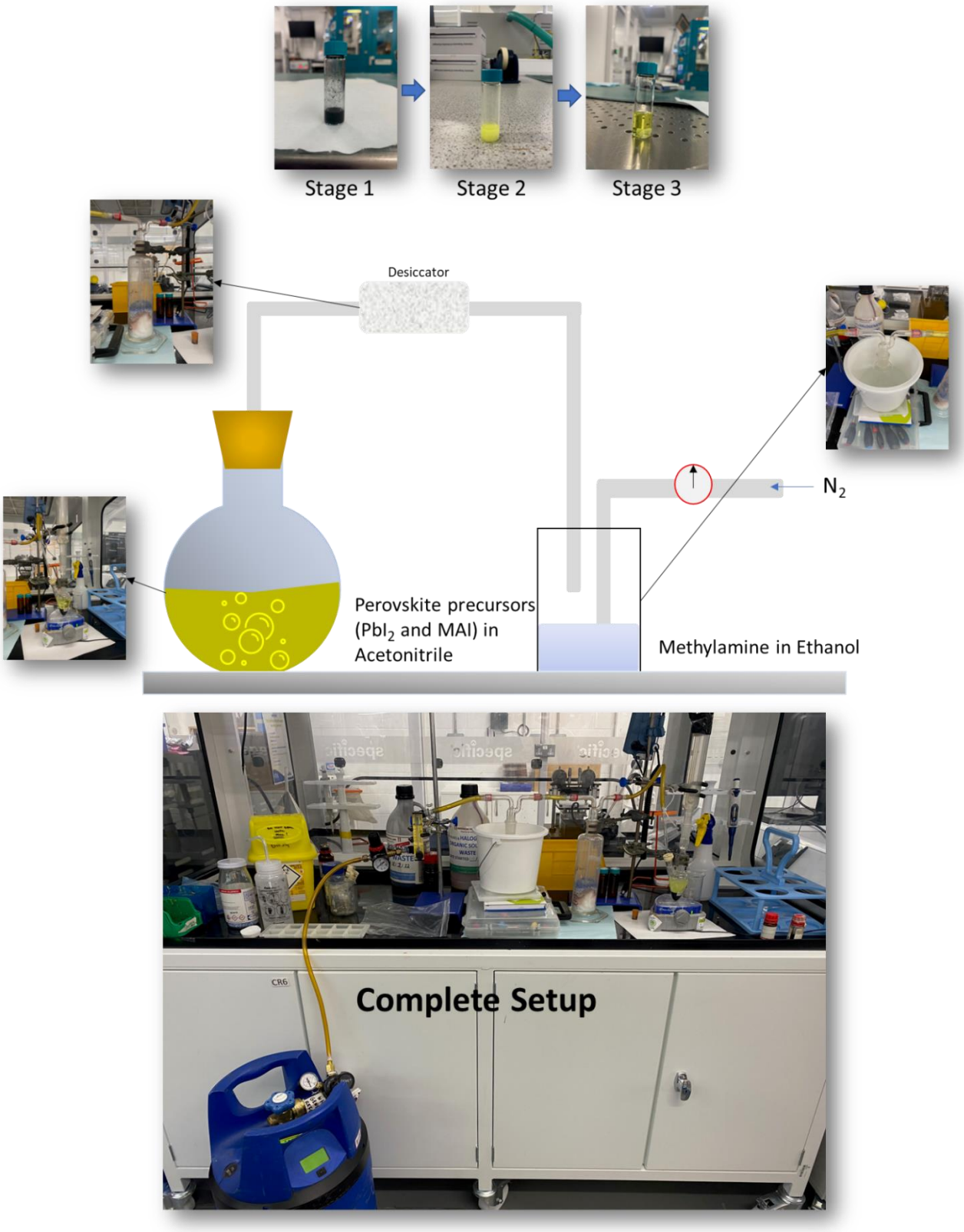

Figure 2. 1 Schematic representation of the $MAPbI_3$ ink formulation process.

result of the substrate being rotated; the solvent is forced out away from the substrate due to centripetal force. As the substrate continues to rotate, evaporation causes the film to lose

solvent, which leads to film drying. The combination of these factors results in the formation of a film that is evenly distributed across the substrate and has a thickness that can be very reproducibly controlled up to a few nanometres. Acceleration, spin speed, and spin time are all variables that can be changed in order to optimise the deposition of a uniform layer. In this work, a perf orated chuck was used to hold flexible substrate to prevent the substrate from bowing when it was placed under vacuum while a standard chuck was used for rigid substrates.

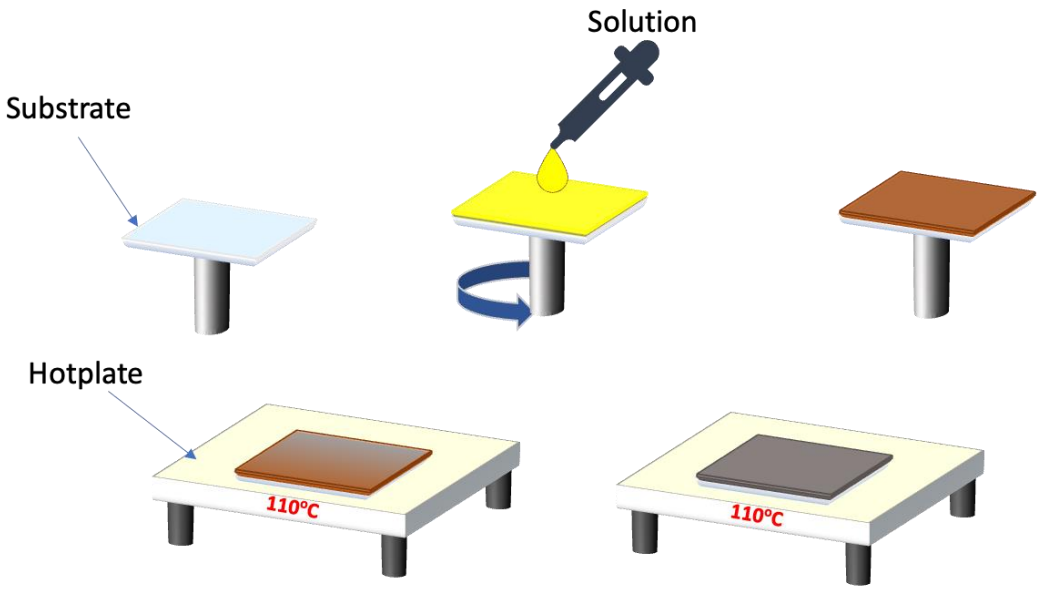

Figure 2. 2 Schematic representation of spin coating process

2.2.2 Thermal Evaporation

Because of its simplicity, thermal evaporation is a popular physical vapour deposition process. A substance (metal in this case) is placed in a resistive boat in a high-vacuum environment. It is heated to its evaporation point by passing high electric current through the resistive boat in which it is placed. The vaporised molecules then proceed from the source to the substrate, where they combine to form a thin film coating. The temperature of the resistive boat, which is controlled by the current, influence the rate of evaporation. The material can be rapidly evaporated in a "flash" with several hundred nm being deposited in one shot, or more slowly with the rate controlled to as low as a few A°/s which gives more control. Through this process a wide range of materials, including aluminium, silver, gold and copper can be deposited. This

technique can be used to deposit pure atomic elements such as metals and nonmetals, as well as molecules such as oxides and nitrides. It is equipped with a Quartz Crystal thickness monitor so that the evaporation process can be closely monitored.

2.2.3 Slot Die Coating

Slot die coating is a pre-metered coating method that has been widely employed in industrial settings for the manufacturing of thin films. Slot die coating is a highly scalable technology for uniformly coating thin films with minimal material waste and operational cost. The process can be described in multiple steps. First, a formulation sometimes also referred as ink is prepared of the material to be deposited. Then this solution is fed into slot-die head via a flow-controlled pump. The solution is then dispensed onto the substrate from the slot-die lip forming a meniscus. As the ink is pumped through the head to the substrate, the substrate is then moved and a uniform film is produced. The entire volume that is pumped via slot-die head goes into producing the coating and hence 100% material usage is ideally possible. This forms the basis for the premetering calculation of thickness. The volume dispensed (Vd) can be written in the following form:

$$Vd = r * t$$

Where r is the pump rate in ml min^{-1} and t is time in minutes. As the coating is done at a constant speed (s) by moving the substrate, in a time t the coated length will be:

$$coated\ length = s * t$$

Total volume coated ($Vcoated$) can now be described by multiplying the coating length with the width of coating (w) and thickness of coating (WFT), giving the following relation:

$$Vcoated = s * t * w * WFT$$

Since all the material that is dispensed and goes on to the substrate forming the entire volume of the thin film coated volume must be equal to dispensed volume, which gives us:

$$s * t * w * WFT = r * t$$

$$WFT = \frac{r}{s * w}$$

This relation effectively allows to control the coating wet film thickness during the coating process. However, the dry film thickness after the solvent has evaporated will be different then the WFT. And Dry film thickness can be calculated using the following relation:

$$dry\ film\ thickness = WFT * \frac{C}{\rho}$$

Where C is the concentration of the solution being coated and ρ is the density of the coated dry film.

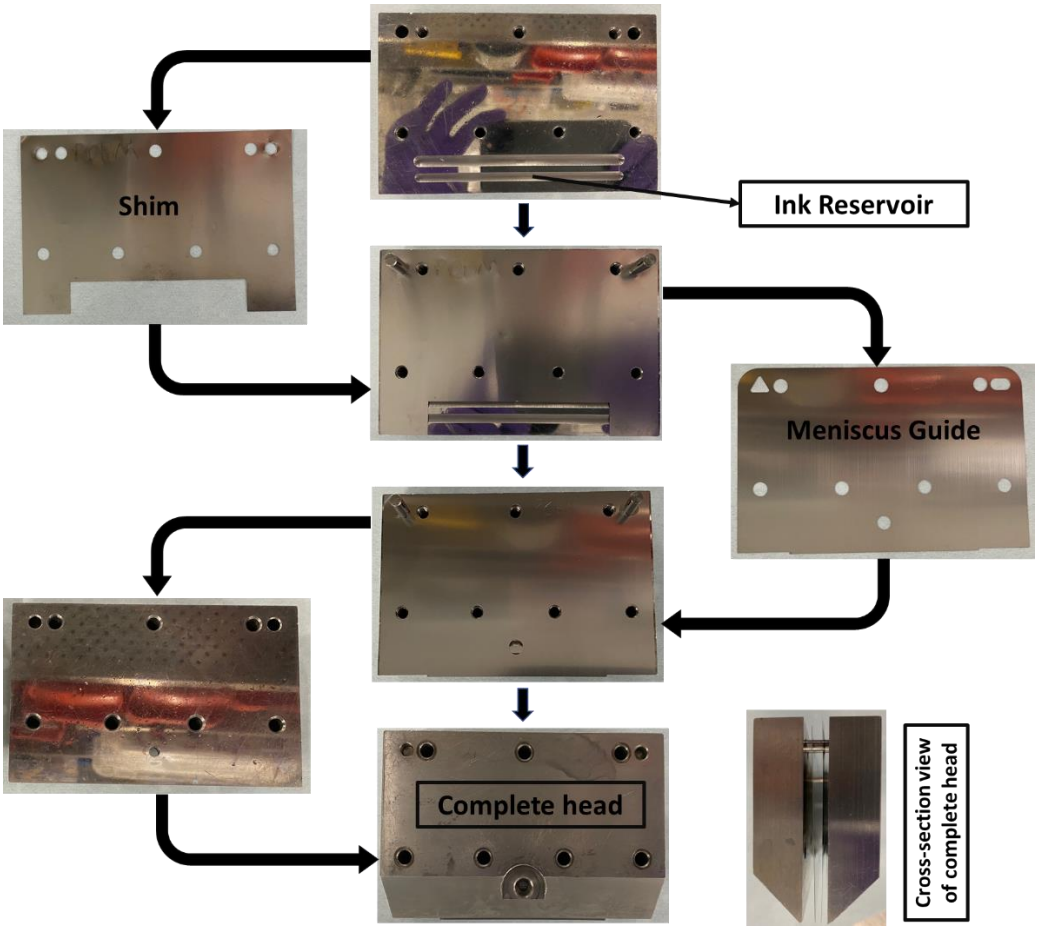

Figure 2. 3 Schematic representation of slot die head assembly.

The slot die head assembly is shown in Figure 2. 3. The meniscus guide and shim are sandwiched between the two halves of the head. One half contains the ink reservoir and the other the inlet for the ink.

S2S slot die coating was done using FOM technologies desktop coater. The instrument was placed inside a fume hood in a class 7 clean room with controlled humidity of approximately 25-30% RH. The S2S coater consisted of a coating station where slot die head was mounted

and a 30cm long convection oven (Figure 2. 4). The two stations (drying and coating) were connected by a conveyor belt. The substrate was placed on a conveyor belt was then moved with a set speed from the coating head to the convection oven. The speed of the belt can be set from 0.1 m min^{-1} to 10 m min^{-1} and the system could also be programmed to halt and change the speed in between the coating and the drying station. The slot die head was mounted at coating station and the height of the slot die lips from the substrate could be adjusted by height adjusting screws. A syringe pump was used to pump the ink into the slot die head and deliver it to the substrate.

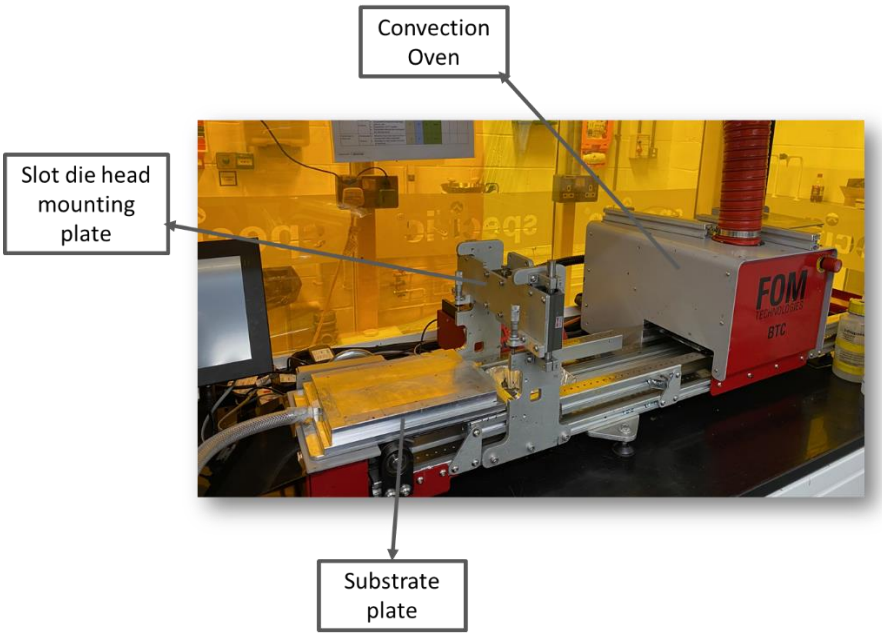

Figure 2. 4 Picture of the S2S FOM coater for all S2S coating in this work

R2R coating experiments was performed on Coatema Smartcoater (SC08) machine (Figure 2. 5) with an integrated corona unit and two stage convection ovens of approximately 1m length in total. This machine was housed in the same room as the S2S FOM coater with controlled humidity. The web path from unwinder to winder roll consisted of the web guide (to align the web with the coating head), corona unit (for surface treatment), coating station and a drying station with 2 convection ovens. The web path was modified for the work in chapter 3 to include a ACN bath before the coating head and after the corona unit. The assembled slot die head was mounted at the coating station and the height from the substrate was adjusted by height gauge and the gap between the two was monitored by the thickness gauge. All the coatings conducting in this work were applied at 1 m min^{-1}.

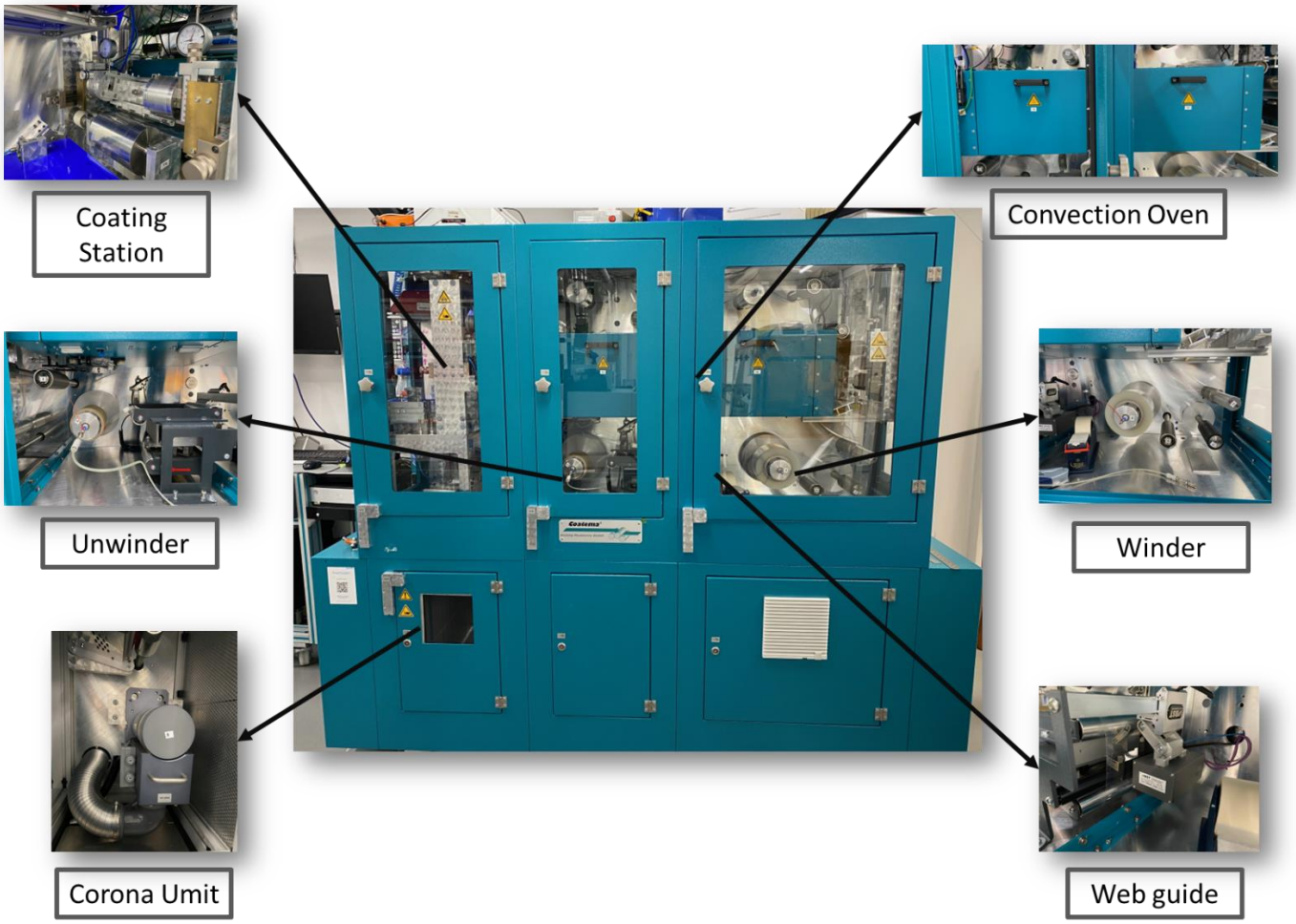

Figure 2. 5 Picture of R2R Coatema smart coater with all the parts.

2.3 Device Fabrication Process

In this work device fabrication is carried out using two deposition techniques that is spin coating and slot die coating while thermal evaporation was used to put metal contact on top. The following section will provide the detailed procedure carried out to fabricate device using small scale (spin coating) and large scale (slot die coating) deposition techniques.

2.3.1 Fabrication of P-I-N Perovskite Solar Cells via Spin Coating

Spin coating was done in a humidity-controlled class 7 cleanroom at 30% relative humidity. 15Ω/sq coated ITO substrates were cleaned stepwise with soap water, deionized water, 2-propanol, and dried using a nitrogen gun. While PET-ITO (50 Ω/sq) substrates were only rinsed with acetone before coating. PEDOT:PSS(AI4083) is used as an HTL in chapter 3. PEDOT:PSS diluted with 2- propanol in a 1:3vol/vol ratio was spun on the cleaned substrate at 1000RPM for 5s with an acceleration of 1000 $RPMs^{-1}$ and then at 5000 RPM for another

10s followed by drying on hot-plate at 120°C for 10 minutes. 0.5M ACN/methylamine perovskite formulation as prepared by bubbling method described in section 2.1 was doped with 20 µl ml^{-1} HCl (aq) before coating the $MAPbI_3$ layer. The prepared formulation was then spin-coated onto the PEDOT:PSS films at 2000 RPM for the 60s and was transferred directly to a hot-plate at 110°C. After drying for 10 minutes the films were cooled at room temperature. 40 mg ml^{-1} PCBM solution in chlorobenzene was spin-coated on the perovskite films at 3000RPM for 45s with an acceleration of 3000 $RPMs^{-1}$. This did not require extra hotplate drying. Following this, 0.5 mg ml^{-1} bathocuproine (BCP) was spin-coated on the PCBM films at 7000 RPM for 10s with an acceleration of 7000 $RPMs^{-1}$. Silver top contacts were then thermally evaporated in vacuum using a shadow mask for defining pixel areas.

For the fabrication of PTAA based P-I-N devices on glass in chapter 4, 2.5 mg ml^{-1} PTAA in toluene was deposited replacing PEDOT:PSS as HTL in the same architecture as fabricated in chapter 3. The PTAA was spun at 4000 RPM for 30 sec followed by hotplate drying at 100℃ for 10mins. 0.5M ACN/methylamine perovskite formulation as prepared by bubbling method described in section 2.1. was doped with 7 µl ml^{-1} HCl (aq) before coating the $MAPbI_3$ layer. The prepared formulation was then spin-coated onto the PTAA films at 2000 RPM for the 60s and was transferred directly to a hot-plate at 110°C. Remaining layers were coated flowing the same procedure as described in the previous paragraph.

For the deposition of PTAA HTL on PET-ITO an interlayer of PEDOT:PSS was need before the deposition of PTAA. For coating the interlayer, neat PEDOT:PSS was first diluted by 1:6 ratio (with IPA) and was spin coated at 5000 RPM for 15 sec and dried on a hotplate at 120℃ for 10mins. This was followed by the deposition of 2.5 mg ml^{-1} PTAA at 4000 RPM for 30 secs. The drying of PTAA was done at 100℃ for 10 mins on a hotplate. 0.5M ACN/methylamine perovskite formulation as prepared by bubbling method described in section 2.1. was doped with 7 µl ml^{-1} HCl(aq) before coating the $MAPbI_3$ layer. The prepared formulation was then spin-coated onto the PTAA films at 2000RPM for the 60s and was transferred directly to a hot-plate at 110°C. The remaining procedure for device fabrication was kept the same as glass devices with PTAA HTL.

2.3.2 Fabrication of P-I-N Perovskite Solar Cells via Slot-die Coating

A Coatema Smartcoater (SC08) machine with an integrated corona unit and two stage oven (total length approximately 1 m) was used to perform R2R coating. The machine was located in a humidity-controlled class 7 cleanroom environment A web guide system (BST ekr 500 Plus) was used to align the web with the coating head. For S2S coating a bench-top coating system from FOM was used. The same coating heads were used for both systems. A syringe pump from WPI Aladdin was used to pump the ink into the head. Pre-patterned ITO coated PET substrate with three stipes of 20 mm as received from Mekoprint (OC50), with conductivity of 50 Ω/sq and 100 mm web width was used. The optimised coating conditions of each slot die coated layer is summarised in Table 2. 1.

In chapter 3, the device architecture of 5 layers that consisted of PEDOT:PSS-$MAPbI_3$-PCBM-BCP-Ag on PET-ITO was coated via R2R slot die coating except the Ag electrode.

For slot-die coating, PEDOT:PSS from Heraeus Clevios was diluted with IPA (1:3vol/vol) and was deposited over a 90 mm coating width with a pump rate of 0.9 ml min^{-1} and web speed of 1 m min^{-1}. This resulted in a 10 µm wet film thickness. Throughout the coating a 200-300 µm gap between the meniscus guide and substrate was kept constant. The wet film was then passed through the two inline oven units set at 120 and 140℃ , with air flow set-points of 50% (45 m^3 hr^{-1}).

The perovskite was coated using the same 0.5M ink prepared for spin coating. An optimised 5 µm wet film thickness was coated by setting the pump rate at 0.45 ml min^{-1} for a 90 mm coating width at 1m min^{-1} coating speed. The gap between the head and substrate was kept at 1100-1200 µm including the 1000 µm tab width of meniscus guide used for the coating. The film was then passed through an Exair air knife set at 50 l min^{-1} air flow rate. The air knife was positioned at approximately 100 mm away from the coating head. The partially dried films were then fully dried using two convection ovens set at 150°C each.

A PCBM layer was coated using a 10 mg ml^{-1}solution in various blends of solvents. 5 µm wet film thickness was coated at 1m min^{-1} speed. An Ink flow rate of 0.45 ml min^{-1} was used to coat a 90mm width coating. A 1000 µm tab length meniscus guide was used with the total substrate to head height in the range of 200-300 µm. The wet film was then passed through the two convection ovens set at 90°C for drying. For S2S, since the oven length was only 0.3m,

a reduced speed of 0.3 m min^{-1} was used to have a similar residence time as R2R inline convection oven with 1m length. For the last layer of BCP, 0.5 mg of BCP per ml of Ethanol was used. The coating was done over a 90 mm width at a speed of 1 m min^{-1}. The wet film was then dried using the convection oven set at 60°C at the same air flow rate of 50% for both the ovens. For the coating of BCP, a meniscus guide with the tab width of 2000 µm was used. At last, the coated roll was taken offline and was diced into 28x28 mm^2 pieces. The small substrates were then transferred to bell jar for the thermal evaporation of silver contact of approximately 100 nm thickness.

Table 2. 1 Coating parameters of all the optimised layers used in this work.

Layer	Wet film thickness	Drying temperature Oven 1/Oven 2	Substrate to slot die head gap (including meniscus guide)	Meniscus guide tab width
PEDOT:PSS (chapter 3)	10 µm	120℃/140℃	200 µm	None
PEDOT:PSS (chapter 4)	8 µm	120℃/140℃	450 µm	250 µm
PTAA	10 µm	120℃/120℃	1500 µm	1000 µm
$MAPbI_3$	5 µm	150℃/150℃	1100 µm	1000 µm
PCBM	10 µm	90℃/90℃	1100 µm	1000 µm
BCP	7.5 µm	60℃/60℃	1100 µm	2000 µm

In chapter 4, PEDOT:PSS was replaced by PTAA as a HTL for the fabrication of efficient PSCs. However, a thin layer of PEDOT:PSS was still needed for the deposition of PTAA. This modified the device layer stack to 6 layers that consisted of PET-ITO-PEDOT:PSS-PTAA-$MAPbI_3$-PCBM-BCP-Ag.

For the R2R coating of PEDOT:PSS interlayer, PEDOT:PSS (AI4083) wad diluted by IPA in 1:6 (vol/vol) ratio. The diluted ink was then coated at 1 m min^{-1}. An optimised wet film thickness of 8 µm was achieved using an ink flow rate of 0.72 ml min^{-1} for 90 mm width coating. The wet films were dried inside two convection ovens set at 120 and 140°C, with air flow set-points of 50% (45 $m^3\ hr^{-1}$). After the PEDOT:PSS coating the roll was rewound for the PTAA

coating. 1 mg PTAA in 1ml of toluene was used for the deposition of PTAA layer. An optimised wet film thickness of 10 µm was coated at 1 m min^{-1} along 90 mm width. This was done by setting the pump rate at 0.9 ml min^{-1}. Due to low viscosity of PTAA ink formulation a meniscus guide of 1000 µm tab width was utilised and a gap of approx. 500 µm was kept between the meniscus guide and the substrate. The wet films were then dried in the convection ovens both set at 120°C with air flow set-points of 50% (45 m^3 hr^{-1}). The remaining layers of $MAPbI_3$-PCBM-BCP was coated by spin coating following the procedure discussed in the previous section. Finally, silver was thermally evaporated on top to complete the device.

In chapter 5, optimisation of R2R slot die coating of $MAPbI_3$ was carried out. $MAPbI_3$ was coated on top of the R2R slot die coated PEDOT:PSS-PTAA HTL as optimised in chapter 4. 0.5M $MAPbI_3$ ink was first doped with 5 µl ml^{-1} of HCl (aq) and 10 µl ml^{-1} DMSO. The prepared ink was then slot die coated at 1 m min^{-1}. For slot die coating 1000 µm tab width meniscus guide was used along with 90 mm wide shim. The flow rate of the $MAPbI_3$ ink to the substrate was controlled by a syringe pump set at 0.45 ml min^{-1} resulting in 5 µm WFT. The wet film was then dried by N_2 air knife at 50 l min^{-1} pressure, located roughly 100 mm after the coating head. The partially dried films were then fully dried using two inline convection ovens set at 150℃ each. To complete the device, the remaining layer of PCBM-BCP was spin coated following the procedure discussed in the previous section. Finally, silver was thermally evaporated on top.

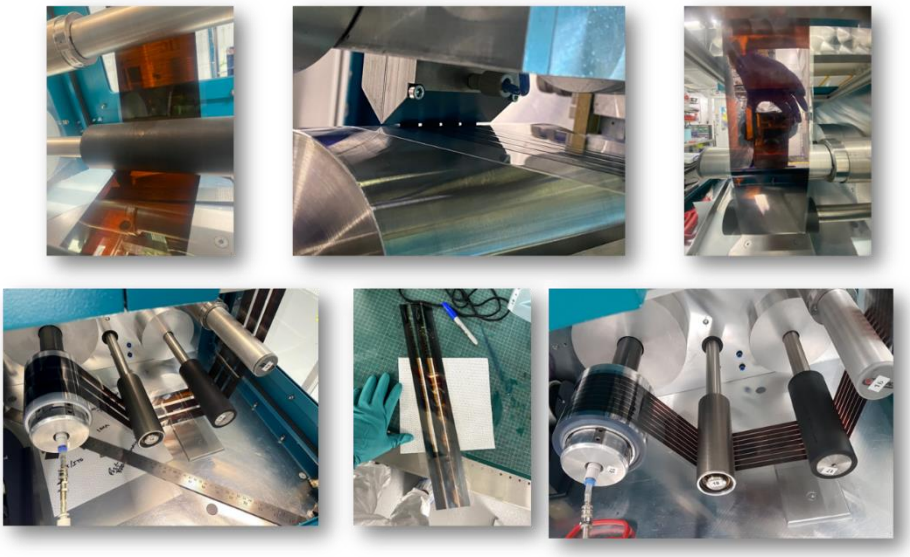

Figure 2. 6 Pictures taken during R2R slot die coating.

2.4 Characterisation Methods

The following section will discuss the various optical and electrical characterisation techniques that were employed in this work to characterise the ink formulations, thin films and devices.

2.4.1 Surface tension measurement

Measurements of surface and interfacial tension can be carried out optically through pendant drop shape analysis. The equilibrium of forces, which includes the surface tension of the liquid being investigated, determines the shape of the drop that is suspended from a needle. A determination of the surface tension helps predict the coating window according to the low flow limit for slot die coating. A FTA32 system was used for taking this measurement. A needle with a known width was utilised in order to calibrate the distances that were measured in the images, and a Pendant Drop Shape fitting routine was incorporated into the software in order to determine the surface tension of the liquids.

2.4.2 Contact Angle

To determine the contact angle, a small amount of the liquid was dropped onto the solid surface, and the shape of the drop was observed so that the contact angle could be calculated. After fitting a line to junction where the solid (the substrate), liquid (ink to be used for the coating on the substrate) and the gas phase (air) meet, the contact angle is calculated by measuring the angle between this line and the solid surface. The contact angle measurements were taken with an FTA32 system by dropping a small volume of ink with a micropipette onto a substrate and then measuring the angle the drop makes with the substrate. The Sessile Drop Profile programme that was included in the software was used to calculate the contact angle.

2.4.3 Viscosity Measurement

The measure of a fluid's resistance to flow is its viscosity. It is known as a fluid's internal flow resistance and can be viewed as a measurement of fluid friction. A fluid's flow rate is inversely correlated with its viscosity. Viscosity was measured in this work to calculate the capillary number which was useful to determine the coating window for slot die coating. The

Rheosense microVISC was used to take the viscosity measurement. The ink was injected at a constant rate through the flow channel inserted in the viscometer and an average of three reading was taken as the final value of the viscosity.

2.4.4 Thermogravimetric analysis and differential scanning calorimetry

This measurement was done with the help from Dr. Peter Greenwood.

Thermogravimetric analysis (TGA) is a method for calculating change in sample's weight in relation to temperature. It can reveal details about the chemical and physical changes that take place during heating and is frequently used to study the thermal stability and material decomposition. A sample is put in a sample pan and heated gradually during a TGA experiment. As the sample is heated, its weight is continuously measured. Any weight variations can be attributed to the sample going through physical or chemical changes like evaporation or decomposition. Differential scanning calorimetry (DSC) on the other hand is a method for measuring the heat flow into or out of a sample as a function of temperature. Typically, it is employed to investigate the thermal properties of materials, such as their melting and crystallisation temperatures, enthalpy changes, and heat capacity. TGA and DSC are frequently combined to give a more thorough understanding of a material's thermal behaviour.

The DSC and TGA measurement were done using a Simultaneous Thermal Analysis (STA) 6000 from Perkin Elmer.

2.4.5 Scanning Electron Microscopy

Scanning electron microscopy (SEM) is imaging technique used to generate high-resolution images of a sample's surface. In a SEM experiment, the sample is placed in a vacuum chamber, and a field-emission electron gun is used to produce an electron beam. Using a system of lenses and magnetic fields, the electron beam is then focused and bombarded on the surface of the sample. The scattered electrons from the surface of the samples are collected at the detector and analysed to generate the high-resolution image. For the images taken in this work, a JEOL JSM-7800F SEM system was used.

2.4.6 Atomic Force Microscopy

This measurement was carried out with help from Dr. Chris Griffiths

Atomic force microscopy (AFM) is a powerful imaging technique that can provide high resolution images as well as surface roughness properties. For AFM measurement, the sample is placed on a stage, and scanned using a sharp tip made of silicon or silicon nitride attached to a cantilever. Using a piezoelectric stage, the sample is scanned under the tip while the cantilever oscillates at a high frequency. As the probe interacts with the surface of the sample, it encounters van der Waals forces, electrostatic forces, and other interactions. These forces modify the cantilever's oscillation frequency, which can be measured with a laser and a detector. The resulting signal is utilised to generate a high-resolution image of the sample surface. For the purpose of this work an AFM machine from JPK (Nanowizard 3) was used to measure the surface roughness and morphology of the samples. The data gathered from the measurement was then analysed by Gwyddion software.

2.4.7 Photoluminescence measurement (PL) and Electroluminescence measurement (PL)

PL measurement is an important technique to probe the quality of the active material in solar cells. It provides the information about defects in the film. The PL emission is measured by exciting the electrons in the thin films with a monochromatic light. Excited electrons upon relaxing back to the ground state, release a mix of radiative and non-radiative energy which is used to probe the quality of the film.

For EL measurement, charges are injected externally into the full device. When the charges recombine in the active layer, they emit light. The intensity of this emission can be used to probe the charge recombination dynamics of the device.

A FS5 spectrofluorometer from Edinburgh Instruments was used for the PL and EL measurement in this work. For EL measurement a Keithley source meter was used to applied external voltage.

2.4.8 UV-Vis Spectroscopy

In a UV-Vis spectroscopy measurement light is sent through a sample and the measurement of absorbed light intensity is obtained. The sample absorbs the light because the energy of

the light is the same as the energy needed to move an electron from a lower energy level to a higher energy level in the sample. Only certain wavelengths of light are absorbed, so different materials will absorb light at different wavelengths.

In order to conduct a UV-Vis analysis (Perkin Elmer Lambda 750S), films are placed in front of the light source inside a spectrophotometer. It is then scanned to measure the sample's absorbance at various wavelengths. The resulting absorbance spectrum is a graph plotted showing sample absorbance as a function of wavelength. This spectrum can be utilised to determine the film thickness and band edge of an absorbing material.

2.4.9 X-Ray diffraction Spectroscopy (XRD)

X-ray diffraction (XRD) is a technique used to determine a material's crystalline structure. It operates by shining an X-ray beam onto a sample and analysing the resulting diffraction pattern. The diffraction pattern is the result of the interaction between the X-rays and the atoms in the sample, and it can provide information about the arrangement of the atoms, their size and shape. In this work a Bruker D8 discover with CuKα beam was used for diffraction pattern of $MAPbI_3$ films in a divergent slit setting.

2.4.10 X-ray photo electron spectroscopy (XPS)

XPS measurement was conducted with the help from Dr. James McGettrick

X-ray photoelectron spectroscopy (XPS) is a technique for analysing the surface chemistry of substances. It operates by bombarding a sample with an X-ray beam and measuring the energy and intensity of the photoelectrons emitted by the sample. XPS can provide information regarding the surface's elemental composition, chemical bonds, and electronic structure. It can be used to determine the types and quantities of elements present in a sample, as well as their chemical states. XPS is surface sensitive measurement, and it can only probe upto 10 nm deep into the film. This is because the non-elastic mean free path of the scattered electron is less than 10 nm and therefore electron scattered deeper than 10 nm in the sample do not come out of the sample to get detected by the detector.

In this work, point measurements as well as mapping was conducted. For mapping, multiple point measurements were done across the area to analyse the surface chemistry of the sample over an area. The measurement was conducted on a Kratos Axis Supra instrument.

With A1 Kα source at 225W 15mA and 20kV. For a typical measurement, a wide scan (@160eV) was conducted to identify the element on the surface of the samples. The spot of size of the incident Xrays was 300x750 μm^2. Analysis of the data is based on 20eV spectrum acquisition. CasaXPS software was used to analyse the spectra, with Shirley backgrounds and the default GL(30) lineshape.

2.4.11 Ultraviolet photoelectron spectroscopy (UPS)

UPS measurement was conducted with the help from Dr. James McGettrick

UPS measurements were carried out to understand the electronic structure of materials. It works by shining an ultraviolet (UV) light onto a sample and measuring the energy and intensity of the photoelectrons emitted as a result. It widely used to identify the position of the Fermi level and the valence band.

A He(I) plasma source was used to generate photoelectrons from the substrate using Kratos Axis Supra instrument. The samples were biased to 9.0 V and the integral charge neutraliser was turned off. C(1s) XPS spectra were collected in situ to confirm the absence of charging effects, and no charge correction was applied to the UPS spectra. Using CasaXPS software the secondary electron cutoff and valence band maximum were estimated at the x-axis intercept.

2.4.12 Current Density-Voltage (JV) Measurement

The JV measurement is one of the most fundamental methods that is used to characterise the efficiency of solar cells. It is a straightforward measurement in which a four-point probe (to remove contact resistance) is used to connect the solar cells to a source measuring unit (SMU). The solar cell is then placed under a standard light source (Xenon arc lamp) calibrated to AM1.5 spectrum. The current is then measured by the SMU across a range of voltages (usually between 0 and V_{oc}), which results in a "JV curve." For perovskite solar cells, this measurement is taken in both reverse (V_{oc} to 0) and forward (0 to V_{oc}) direction. The deviation of performance in between both the direction is termed as hysteresis and is not desirable for highly efficient solar cells. The measurement was done using Keithely source meter. A Newport Oriel Sol 3A class AAA fitted with xenon arc lamp was used as light source. A silicon reference cells with KG5 filter was used to calibrate the lamp at AM1.5G. The current voltage

sweep was taken from 1.2 to -0.1V and -0.1 to 1.2V at 10mVsec^{-1} scan rate. The data was thrn summarised by software made inhouse.

2.4.13. Intensity Dependent JV measurement

Intensity dependent JV measurements were conducted to calculate the ideality factor of the device. To do this a standard JV measurement protocol (as described in the last section) was followed but at different light intensity. Light intensity was controlled by putting a neutral density filter just above the device. To calculate the ideality factor, V_{oc} was plotted against light intensity and was fitted with a linear curve. The slope of the fitted linear curve was then used to calculate the ideality factor of the device using the following equation:

$$slope = \frac{q}{nkT}$$

where n is the ideality factor, T is the temperature, q is the elementary charge and k is the Boltzmann constant.

2.4.14 External quantum efficiency (EQE)

The external quantum efficiency (EQE) of a device is a measure of how efficiently the device converts incident photons into electrons. In this work, a PV Measurement QEX10 unit was used to measure external quantum efficiency over a wavelength between 270 - 850 nm. The EQE was then used to calculate the short circuit current density by multiplying the EQE with the photon flux at each wavelength.

Chapter 3
Roll to Roll Slot die Coating of P-I-N Perovskite Solar Cells

The work in this chapter was published in Sustainable Energy & Fuels (Burkitt, D., Patidar, R., Greenwood, P., Hooper, K., McGettrick, J., Dimitrov, S., ... & Watson, T. (2020). Roll-to-roll slot-die coated P–I–N perovskite solar cells using acetonitrile based single step perovskite solvent system. *Sustainable Energy & Fuels*, *4*(7), 3340-3351.)

This work was led by Dr Daniel Burkitt and Rahul Patidar. Unless otherwise specified, only the experiments where Rahul Patidar had an equivalent or full contribution have been used in the writing of this work.

Introduction:

The Power Conversion Efficiency (PCE) of perovskite solar cells (PSC) can now compete with conventional photovoltaic materials.[1] Although PSCs have grown rapidly in performance over the last decade, many of these accomplishments are at lab-scale fabrication. To realise the full potential of PSCs, significant efforts need to be made toward implementing scalable fabrication processes. Though relatively few, several research groups have used industry-compatible techniques like screen printing[2], slot-die coating[3], gravure printing[4], spray coating, [5] and inkjet printing[6]. Screen printing has attracted much attention due to the low capital requirements for the manufacturing infrastructure. Despite the low cost, it's been only used for triple mesoscopic architecture, which requires high-temperature treatment to remove the binder, making it porous for perovskite ink infiltration. This has significantly hindered their application in flexible solar cells and, therefore, cannot be integrated into R2R manufacturing. Only slot-die coating [7–11] and gravure[4] printing have been successfully used for R2R fabrication of PSCs. Among the two, slot-die coating is the most used method due to its capability to coat a wide range of inks, from highly viscous to low viscosity. Slot-die coating also allows the predetermination of coating thickness, commonly referred to as a pre-metering, and can achieve substantially fast speed.[12] The merits of slot die coating are discussed in detail in section 1.3.1.

Of the reported work on R2R slot die coated PSCs, only a few have been reported with all layers coated via R2R except the top electrode. This has been achieved on both N-I-P[13] and P-I-N[14,15] architecture. However, challenges like short annealing time, low cost, solvent toxicity,

and constant web speed are generally overlooked and this chapter aims to address some of these challenges. To maximise the benefits R2R offers, all fabrication steps should be done at the same rate. This will avoid bottlenecks and slow down the processing speed. This chapter will show the R2R slot die coating of P-I-N PSCs while demonstrating that all deposition steps can occur at the same web speed and detailed discussion will be done on challenges faced during the optimisation of individual layers.

3.1 Experimental Methods:

Spin coating was used to make control device for this work. A detailed description of the fabrication method has been mentioned in materials and methods section. Briefly, PEDOT:PSS diluted by IPA in 1:3 ratio was spin coated on glass/PET-ITO at 5000 RPM for 15 sec followed by drying at 120℃ on hotplate for 10 mins. 0.5M $MAPbI_3$ ink prepared by bubbling the methyl amine gas in $MAPbI_3$ precursors (PbI_2 and MAI) with ACN was spin coated at 2000 RPM for 60 sec and dried at 100℃ for 60 mins. PCBM (40 mg ml^{-1} in chlorobenzene) was spin coated on top of $MAPbI_3$ layer at 3000 RPM for 40 sec and no drying was required for this layer. Following PCBM deposition BCP was coated at 7000 RPM for 10 sec. Silver was evaporated on top to complete the device stack of glass/PET-ITO-PEDOT:PSS-$MAPbI_3$-PCBM-BCP-Ag.

For R2R slot die coating of PEDOT:PSS, the ink was diluted in 1:6 ratio by IPA. A 10 µm wet film thickness was coated directly on top of ITO-PET at a speed of 1 m min^{-1}. Approximately 200 µm gap between the substrate and slot die head was maintained and no meniscus guide was used. A 90 mm shim was used to define the coating width. The coated wet film of PEDOT:PSS was then dried with 2 inline convection ovens set at 120℃ and 140℃ respectively. The dried film was collected at the winder and was rewound back to coat $MAPbI_3$. For $MAPbI_3$ as prepared 0.5M $MAPbI_3$ ink was coated on top of PEDOT:PSS with 5 µm wet film thickness with 90mm coating width as defined by the shim. The slot die and the substrate gap was kept at approximately 1100 µm including 1000 µm tab width of the meniscus guide used. The wet film of $MAPbI_3$ was first dried using air knife at 50 l min^{-1} pressure and then was passed through two inline convection ovens both set at 150°C.

For slot die coating of PCBM, an ink with 10 mg ml^{-1} of PCBM was dissolved in different solvent blends as described in the main text. Coating width was defined by 90 mm shim and a meniscus guide of 1000 µm was used to coat films with variable thickness at 1 m min^{-1} coating

speed. R2R slot die coated films were dried through the two inline ovens both set at 90°C. For S2S slot die coated films, the wet film was passed through the oven at 0.3 m min^{-1} to achieve the same oven residence time as of R2R coated films.

For the deposition of BCP, ink with 0.5 mg ml^{-1} in ethanol was prepared. Films were coated at 1 m min^{-1} at variable thickness controlled by the ink pump rate. Slot die head was assembled using 2000 µm tab width meniscus guide and 90 mm width shim. The wet films were then dried in inline convection oven set at 60℃.

To complete the device, the roll was taken offline and diced into 28x28 mm^2 pieces. The substrates were then put in a bell jar and a top contact of silver was coated by thermal evaporation of silver metal.

3.2 Substrate and Device Architecture:

For R2R manufacturing, the main substrate requirements are flexibility and durability. Flexible substrates include metal foil and plastic. Recently, flexible glass has also been demonstrated for R2R manufacturing.[8] However, the technology is still in an early stage and not readily available. Metal foils can withstand high temperatures and can potentially be used for architectures requiring high-temperature processing, for instance, 'triple mesoscopic carbon cells' discussed earlier. Metal foils can also be an excellent barrier for moisture and oxygen which in theory would improve PSCs stability. Metal foils such as Titanium[16] and Steel[17] have been shown as substrates for PSCs and have achieved good performance. However, their opaque nature and surface roughness has been a challenge for their successful implementation for R2R fabrication. Transparent polymer flexible films however can be used in multiple solar cell architectures and are lightweight and cheap to produce. Because of its low cost and low roughness, polyethylene terephthalate (PET) has been the most popular material for flexible solar cell fabrication compared to other alternatives like polyethylene naphthalate (PEN)[18] and would be a substrate of choice in this work.

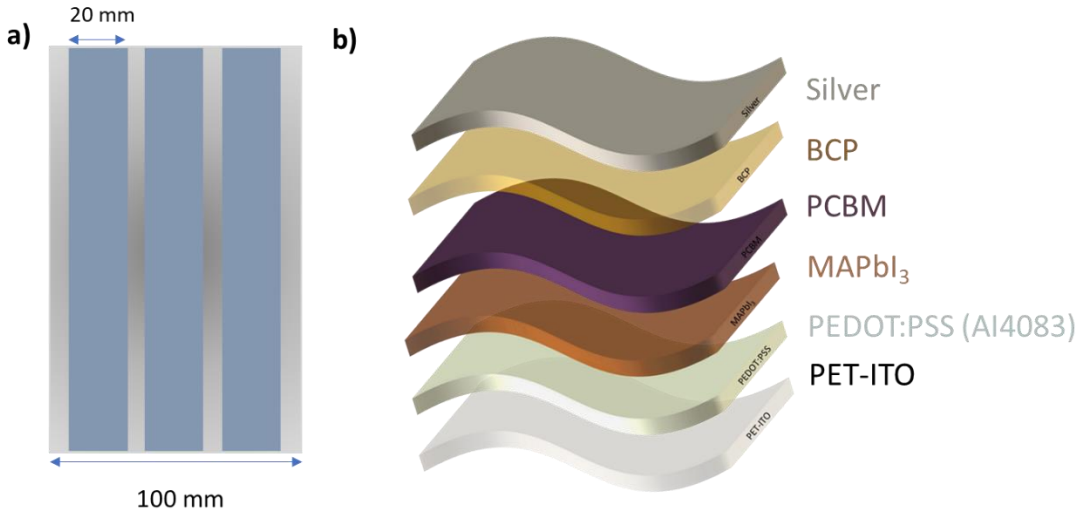

Figure 3. 1 Design of ITO-PET substrate with 28mm strips (a). P-I-N architecture of PSCs (b)

Pre patterned Tin doped indium oxide (ITO) coated PET substrates were sourced from a supplier in a three-strip design (Figure 3. 1a). Each stripe covers an area across the width of the coating thus covering the entire substrate. This helps test the uniformity of the coatings and variations in performance if any. Therefore, for every batch, the devices were taken from each stripe covering the coated area across length and width.

In the field of Organic Photovoltaics (OPV), R2R manufacturing has been well studied on several materials.[19,20] As OPV are structurally similar to PSCs, many of the materials used in OPV such as Poly(2,3-dihydrothieno1,4-dioxin)-poly(styrene sulfonate) (PEDOT: PSS) and [6,6]-phenyl-C61-butyric acid methyl ester (PCBM) have also been used quite extensively in PSCs fabrication.[21,22] PCBM and PEDOT:PSS generally do not require high-temperature processing making them favourable materials for use in R2R fabrication of PSCs. Hence for this work, the P-I-N architecture was chosen wherein the perovskite active layer is sandwiched between PEDOT:PSS and PCBM. The complete architecture is shown in Figure 3. 1b. This consists of PEDOT:PSS, used as hole transport layer (HTL) coated on top of PET-ITO, followed by perovskite active layer. PCBM, an electron transport layer (ETL) is coated on top of the active layer for electron extraction. Next, bathocuproine (BCP) is used as an interfacial layer to smoothen the perovskite/PCBM surface[23], while a recent study showed that it penetrates through the PCBM to perovskite and passivates the MA defect, leading to an improvement in performance[24]. A metal contact (silver in this work) is used to complete the architecture.

3.3 Optimisation of Hole Transport Layer

3.3.1 Ink Formulation

The conductive nature of PEDOT:PSS, low cost and its ability to smooth ITO resulted in wide adoption for applications across different electronics.[25] In PSCs particular, PEDOT:PSS has been extensively used as HTL[26] and transparent electrode[27]. PEDOT:PSS (Clevious AI:4083) used in this work was sourced from Heraeus. The as-received formulation of PEDOT:PSS is a water-based dispersion. Due to the high surface tension of water (72mN/m) the neat PEDOT: PSS does not wet well on PET-ITO and makes a very high contact angle of 61° with the substrate as can be seen in Figure 3. 2. The contact angle measurement is taken by dropping the neat PEDOT:PSS ink on top of ITO-PET. The poor wetting may lead to undesired defects and uneven coatings which may affect the device performance negatively. As a solution to this, neat PEDOT:PSS was diluted with isopropyl alcohol (IPA). IPA, due to its low surface tension (21.7 mN/m) reduces the contact angle of the diluted formulation. The neat

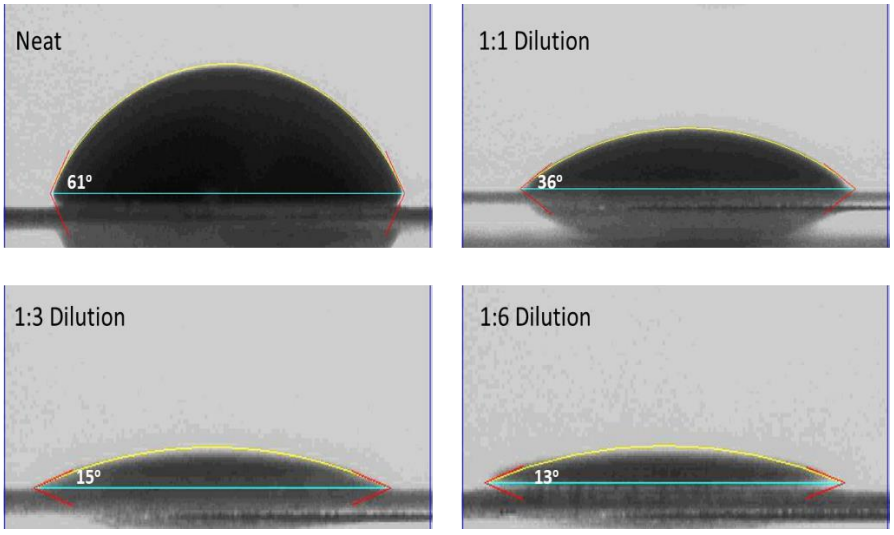

Figure 3. 2 Contact angle measurement of PEDOT:PSS and its diluted formulations.

PEDOT:PSS was diluted with IPA in the ratio 1:X, 1 part of PEDOT:PSS is mixed with x parts of IPA. (X= 1, 3 and 6). As anticipated, the diluted formulations significantly reduced the contact angle with the substrate compared to that of the neat formulation and decreased as the IPA (X) content increased. 1:1 made a contact angle of 36° which is 50% lower than that of neat and went down to 15° with formulation 1:3 and further down to 13° with formulation 1:6. This suggests the wetting was significantly improved as the ratio of IPA was increased with the neat PEDOT:PSS. To assess the uniformity and quality of the coatings, diluted formulations

were slot die coated onto acetone and IPA rinsed ITO-PET substrate using the desktop S2S system. Slot-die coating was done using a head fitted with a 90mm shim to define the coating width. No meniscus guide was needed for this formulation due to the high viscosity of PEDOT:PSS dispersion. A meniscus guide was first used by Krebs in 2009 and has been found

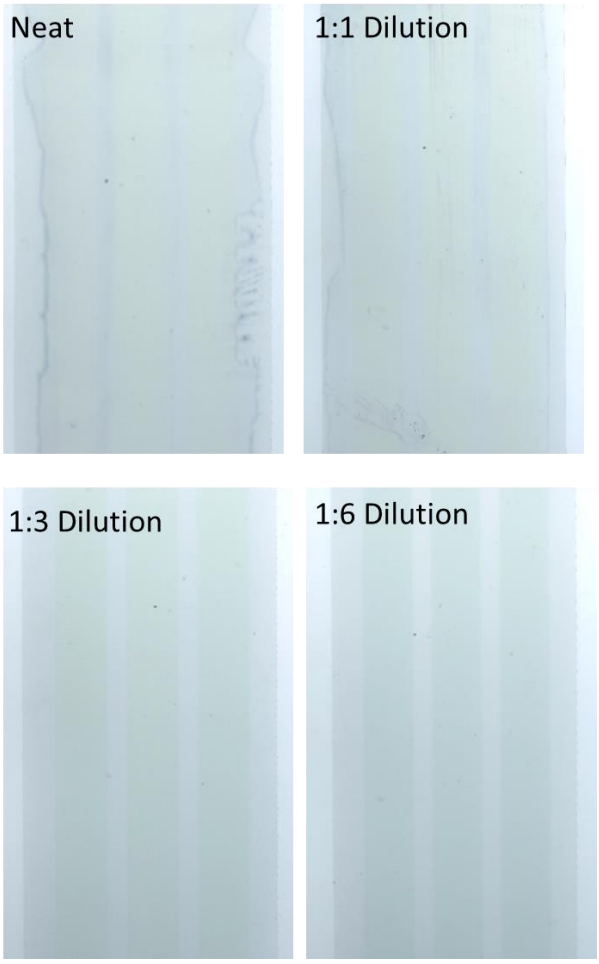

Figure 3. 3 Optical image of slot-die Coated films of PEDOT:PSS and the diluted formulation with IPA.

to be very useful for low-speed coating. Its merits are explained in more detail in the materials and methods section of slot die coating. The substrate to gap height was kept at 200 µm while coating 10 µm wet film thickness. The films were then dried at 120℃ for 10mins on a hotplate. The optical image of all four coatings after drying is presented in Figure 3. 3. The edge of the coating with neat PEDOT:PSS can be clearly seen to be uneven and not sharp. This is because the neat PEDOT:PSS being high surface tension dispersion has strong liquid-liquid forces which pull the liquid towards the centre and shrink the coating leading to irregular edges. This force decreases as the surface tension decreases with the addition of IPA and hence the coatings become sharper and maintain their width with no shrinking observed.

Especially with 1:3 and 1:6 dilution, the coatings are even, and the edges were very sharp, although not very visible in the optical images. The films were then chopped into 28x28 mm^2 pieces and spin coated rest of the layers to complete the device. The current density–voltage (JV) results are presented in Figure 3. 4. Though neat PEDOT:PSS films looked visibly poor they performed in a similar way to that of their diluted counterpart except for the 1:6 formulation which looked optically better but did not perform as well. The low V_{oc} and low FF suggest poor

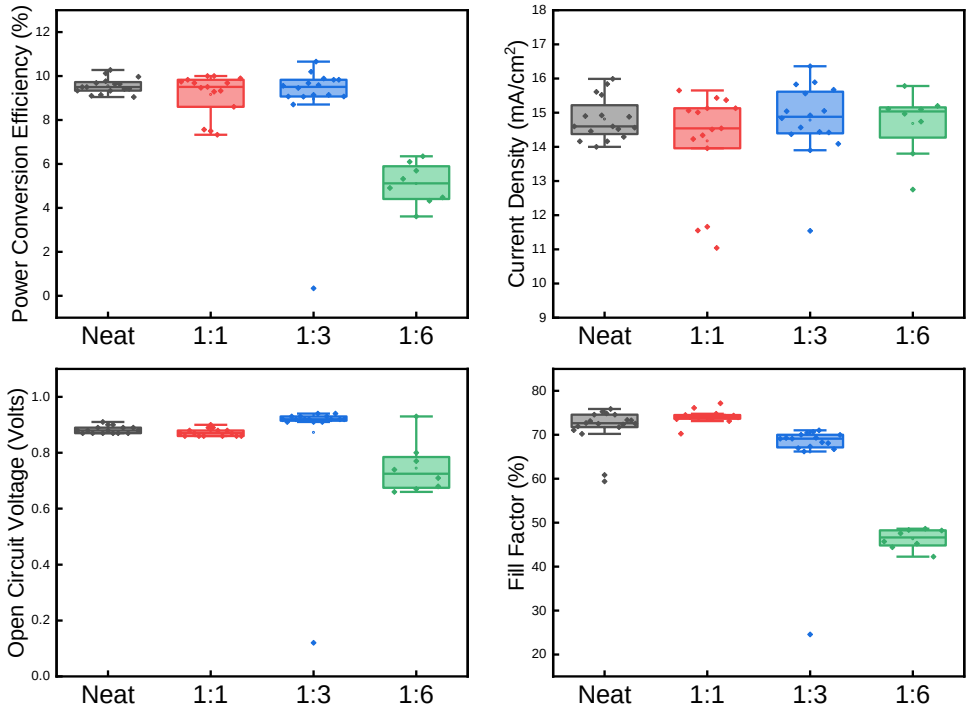

Figure 3. 4 Statistics of JV forward scan parameters from devices made with S2S slot die coating of neat, 1:1, 1:3 and 1:6 PEDOT:PSS formulations. Rest of the device was completed by spin coating all the layers followed by thermal evaporation of silver contact on top.

shunt resistance which could be due to low coverage of ITO upon extreme dilution of PEDOT:PSS neat formulation resulting in an extremely thin film. Though complete coverage of bottom contact can be achieved with thicker contact layers, it may also lead to parasitic absorption which could have damaging effects on the overall performance of PSCs. However, upon reducing the thickness of PEDOT:PSS HTL via diluting the neat PEDOT:PSS formulation, no improvement in current density was observed and it remained consistent across the various diluted formulations. This shows that its likely no parasitic absorption losses took place in the PEDOT:PSS layer despite the change in thickness. However, due to lack of the required absorption data this was not confirmed to be the case. High thickness (with low

dilution of neat PEDOT:PSS) rather led to a high fill factor which could possibly be the result of higher coverage of ITO in thicker films. However, the shrinkage of the coating width observed with thicker PEDOT:PSS films is not desirable for module production, especially for stripe coatings. The stripes uneven width may lead to shorts between the bottom contact and the layer coated on top of PEDOT:PSS, essentially increasing the recombination pathways. Therefore, for the rest of the optimisation of the stack 1:3 diluted formulation of PEDOT:PSS was chosen to coat the bottom layer which performed on par with that of neat PEDOT:PSS and did not show any coating width shrinkage.

3.3.2 R2R deposition of PEDOT:PSS

Having shown good performance on S2S slot die coated PEDOT:PSS in the previous section, R2R deposition was explored. However before directly coating PEDOT:PSS on PET-ITO via R2R, surface treatment of ITO-PET using inline corona unit was tested. It is very critical to remove contaminants from the surface and increase further surface wettability to ensure uniform defect-free films to achieve high performance. Previous studies have shown that surface treatment like corona discharge results in fewer shunt defects in photovoltaic devices.

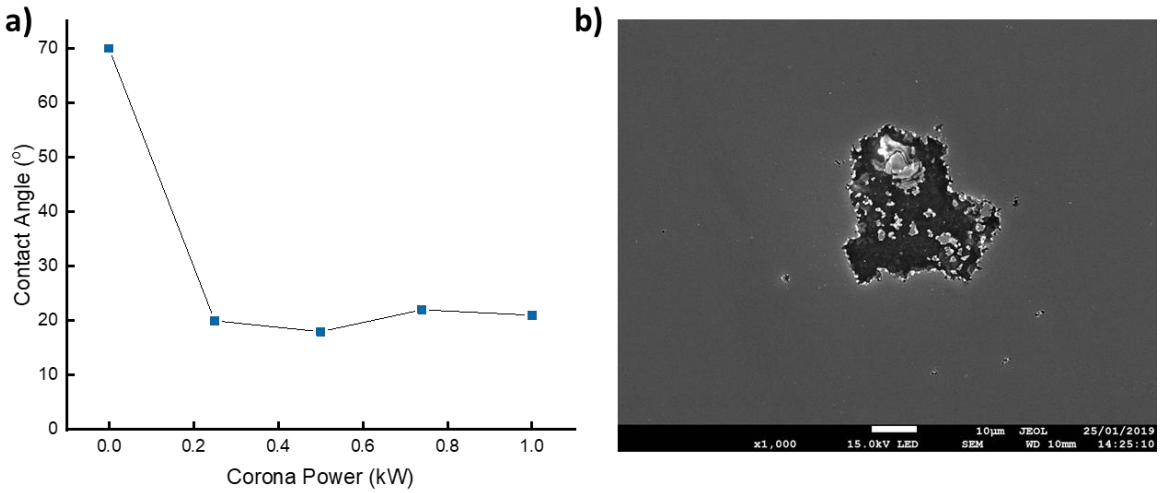

Figure 3. 5 (a) Contact angle of water on ITO-PET at a range of corona power. (b) SEM image of damaged ITO at 1kW.

Also, there is less interfacial charging recombination at electrodes resulting in improved device performance.[28] For the surface treatment of the ITO-PET substrates, an inline corona unit was used. First, the wetting effect of corona treatment was investigated by measuring the contact angle on the treated substrate upon changing the power. The web was passed through the corona unit at speed of 1 m min^{-1} which is also the coating speed used for slot

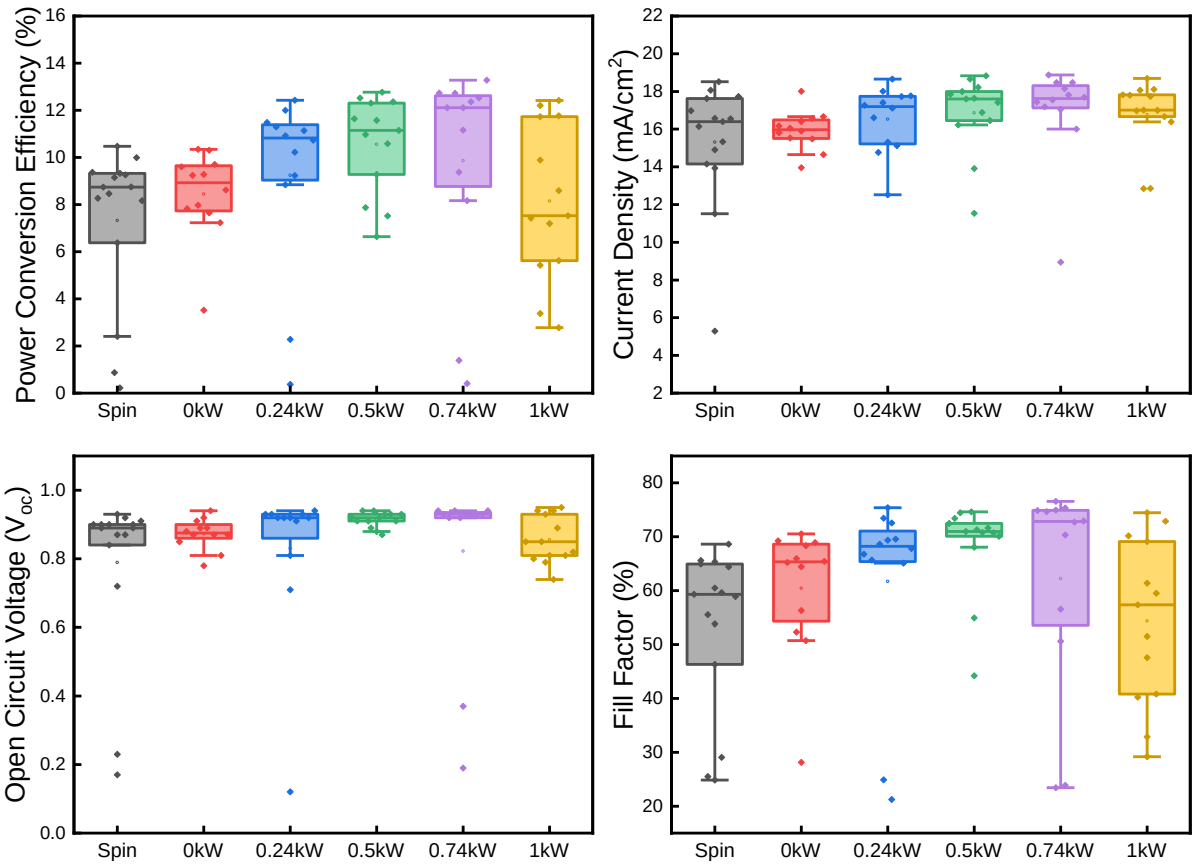

Figure 3. 6 Statistics of JV forward scan parameters of devices made with R2R slot die coating of 1:3 PEDOT:PSS films at corona treatment powers of 0, 0.25, 0.5, 0.74 and 1.0kW and their comparison with spin coated device. For R2R slot-die coated PEDOT:PSS films, rest of the layers were coated by spin coating followed by thermal evaporation of silver contact on the top.

die coating. The corona power was set to 0.25kW, 0.5kW, 0.74kW and 1kW. The contact angle of water on ITO-PET at different power settings was measured and plotted in Figure 3. 5a. As can be noted from the figure, the contact angle sharply falls from 70^o at zero power to around 20^o at 0.2kW power and remains consistent after 0.2kW showing no change in surface energy upon a further increase in power. However higher power (1 kw) caused damage to the substrate which was visible by the naked eye and the damage can be clearly seen in the SEM image shown in Figure 3. 5b. To test the surface treatment effect on the performance, PSCs were fabricated by R2R slot-die coating PEDOT:PSS on the substrates with the same range of corona treatments by adjusting the power of the corona unit. The slot-die settings were the same as used in section 3.3.1. PEDOT:PSS coated films were then sliced into areas of 28x28 mm^2 and the rest of the layers of the architecture was coated by spin coating. For the R2R slot die coating, 1:3 (PEDOT:PSS : IPA) formulation was used. The performance of the resultant

devices is shown in Figure 3. 6. Interestingly an immediate increase in performance is observed at 0.2kW corona compared to no corona. But performance keeps improving till 0.74kW despite no change in contact angle from 0.2 to 0.74kW, suggesting improvement in wetting may not be the core reason for the improvement in performance. Removal of organic contaminants and uniform coating leading to a better shunting barrier seems a more plausible explanation for the improvement in fill factor upon increasing the power of corona. The data suggests the best setting for the surface treatment is with 0.74kW power and the same will be used for all subsequent experiments in this chapter.

3.4 Optimisation of $MAPbI_3$

3.4.1 Ink formulation

Conventional lab scale high-efficiency PSCs are made using high boiling point and polar aprotic solvents like DMF, DMSO, GBL, NMP, or mixtures of them.[29] [30] [31] [32] [33] High boiling point solvents like these have the drawback of requiring films to be heated for extended periods of time after deposition to drive off the excess solvent and induce crystallization of the perovskite film. This leads to poor morphology and rougher films. To mitigate this, anti-solvent quenching was proposed.[29] This strategy involves the dropping of orthogonal solvent on spinning films. Though this method is widely used in the lab-scale fabrication of high-performance PSCs, its viability for the usage in large-scale production is limited. Also, the toxicology and solvent handling concerns that are imposed on factories by regulating agencies for highly toxic, coordinating solvents like DMF are a significant barrier to large-scale manufacturing. To allow industrial scaling of printable perovskite-solar cells, it is necessary to find an alternative solvent blend. One such is using acetonitrile (ACN) wherein methylamine (MA) gas is introduced to increase the precursor's solubility in acetonitrile.[34] Acetonitrile being a volatile low boiling point solvent does not need an additional step of solvent quenching to get uniform defect-free films and hence is more suitable for scale-up manufacturing. Acetonitrile also has a significantly higher work exposure limit (WEL) of 40 PPM than that of DMF (5 PPM) which makes it more interesting from an industrial perspective. Following the first development of the ACN based perovskite formulation, other research groups have made use of it for S2S[35] and R2R[8] slot die coated PSCs showcasing its potential and ease of coating in an industrial scale setup. This work as well will use ACN-MA based $MAPbI_3$ for R2R coated PSCs. The synthesis of this formulation is explained in detail in

experimental methods. Before coating, it is important to determine the rheology of the ink to approximately determine the operating window for slot-die coating without coating defects. The measured surface tension and viscosity are listed in Table 3.1.

Table 3. 1 Viscosity, Surface tension and Capillary number for prepared $MAPbI_3$ formulation.

Formulation	Viscosity (μ) mPa.s	Surface Tension (σ) mNm^{-1}	Capillary Number ($C_a = \frac{\mu V}{\sigma}$) at V = 1$mmin^{-1}$
ACN-MA $MAPbI_3$	0.66	34	$3.23E^{-4}$

Using the capillary number ($\frac{\mu V}{\sigma}$) at 1 m min^{-1} the expected coating window for the stable meniscus can be located from low flow limit[36] plot shown in Figure 3. 7. As can be noted from the plot, maximum dimensionless gap (ratio of the slot-die head gap with substrate

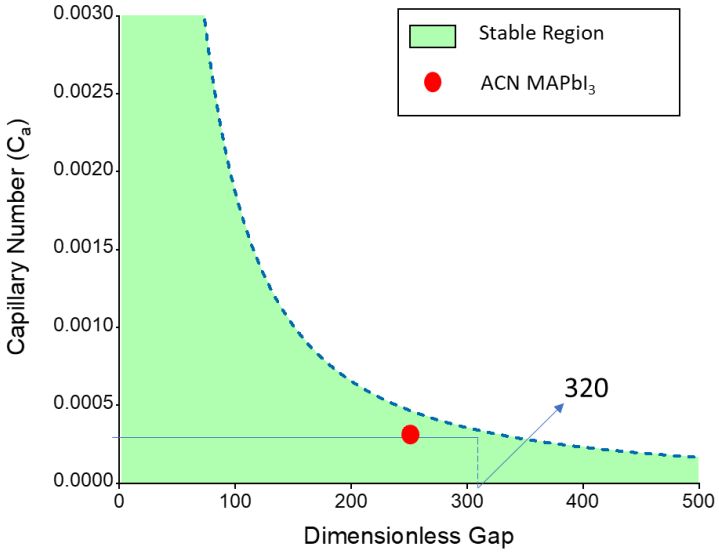

Figure 3. 7 Capillary number vs Dimensionless gap graph for $MAPbI_3$ formulation. Red dot represents the condition used for coating in this work.

and wet film thickness) to get a uniform coating is 320. This implies that for a fixed wet film thickness (WFT) the stable coatings will likely be achieved when the substrate and slot die head gap is below 320*WFT. For instance, a 5 µm WFT will require a substrate to head height in the region of 1600. However, a low viscous ink like the ACN-MA formulation, at a high gap between the substrate and the head, will tend to lose its meniscus, resulting in unstable coatings. To prevent this, a 1000 µm tab length meniscus guide was used. The meniscus was

found to be stable when the gap between the meniscus guide and the substrate was kept close to 100 µm giving us a dimensionless gap of 220, plotted as a red dot in Figure 3. 7 which lies well within the stable region.

3.4.2 R2R Deposition of $MAPbI_3$

In previously reported work from Prof. Trystan Watson's group, the sheet-to-sheet (S2S) coating of ACN-MA based formulation of $MAPbI_3$ was optimized for additive concentration (HCl) and air-knife airflow.[35] An air knife was used to achieve uniform and compact perovskite films[37]. Since this work made use of the same perovskite formulation, the S2S optimisation made previously[35] with air knife settings (50 LPM) was kept the same for the optimisation of R2R deposition for subsequent experiments. However, hotplate drying showcased with the S2S optimisation work cannot be directly implemented on R2R due to considerable difference in drying of hotplate vs inline convection oven in R2R setup. To find out the best drying conditions for the R2R slot-die coated perovskite layer, the perovskite layer was dried under

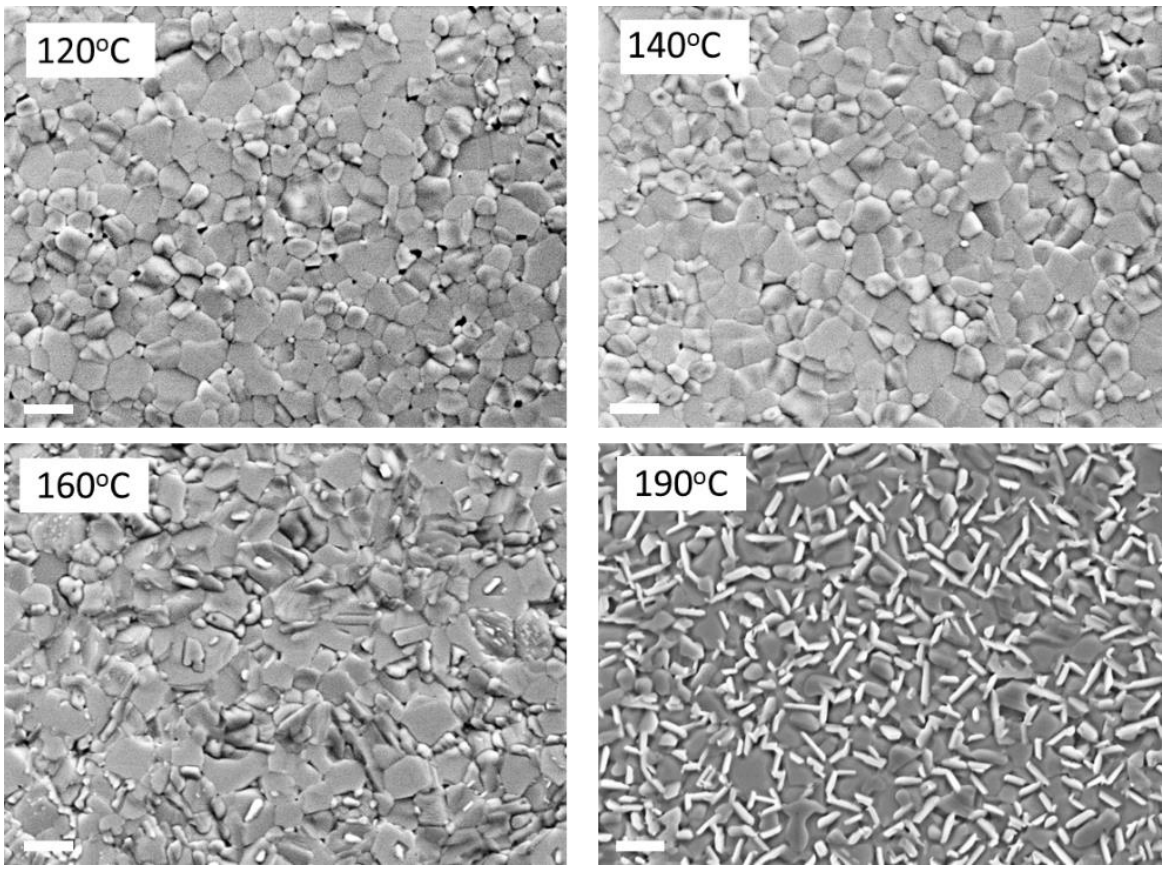

Figure 3. 8 Surface SEM images of R2R slot die coated $MAPbI_3$ on R2R slot die coated PEDOT:PSS dried at 120°C 140°C, 160°C and 190°C oven set points. Scale bar represents 1 µm length.

a range of temperatures. In the inline convection oven, two parameters can be changed to modify the drying. The airflow rate can be increased or decreased to modify the evaporation rate and the temperature. Both can be adjusted simultaneously. Since $MAPbI_3$ is sensitive to crystallisation and drying conditions, it is necessary to optimise and understand the drying of $MAPbI_3$ under the inline convection oven. For the optimisation of drying conditions to be simple, a constant oven flow rate was used (the setting of 50%, which is roughly equivalent to 45 m^3/hour) and varied the oven set point temperature. It was noted that the same set point was used for both the ovens. A coating speed of 1 m min^{-1} was used giving an oven residence time of approximately one minute. To accurately measure the temperature inside the convection oven a thermocouple was placed in oven 1. Temperatures from 120℃ up to

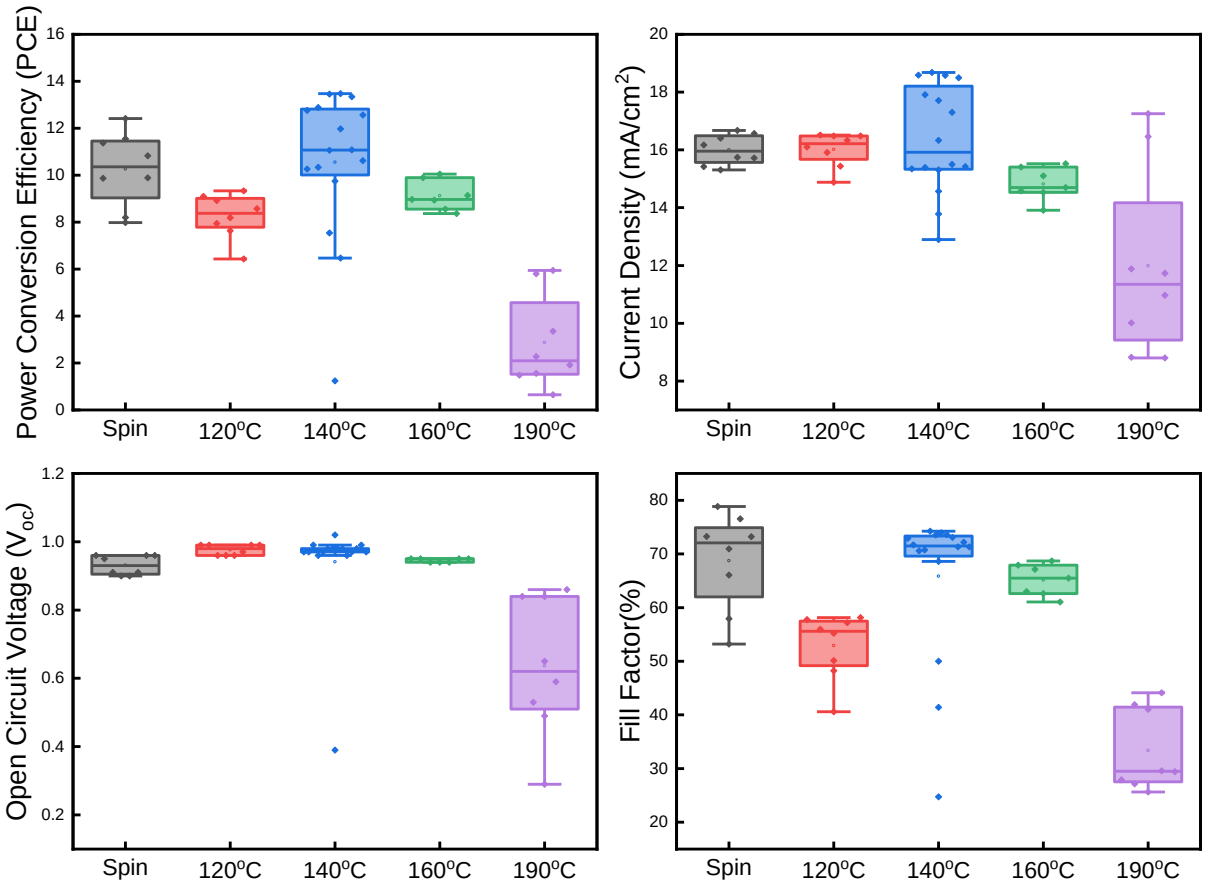

Figure 3. 9 Statistics of JV forward scan parameters of devices made with R2R slot die coating of 1:3 PEDOT:PSS films and 0.5M $MAPbI_3$ dried at set points of 120℃ , 140℃ , 160℃ and 190℃ and their comparison with full spin coated device. For R2R slot-die coated devices, PEDOT:PSS and $MAPbI_3$ were slot-die coated, rest of the layers were coated by spin coating followed by thermal evaporation of silver contact on top.

190°C were used to dry the $MAPbI_3$ film. Though higher temperatures are possible, the instability of PET-ITO at higher temperature restricts its use. The thermocouple placed in the convection oven measured slightly lower temperature than the set temperature i.e., 120°C (106°C) , 140°C (122°C), 160°C(135°C) and 190°C(150°C). This did not have any influence on the drying but was important to note the difference in the set and actual temperature in the oven.

The $MAPbI_3$ films were coated on top of the R2R slot-die coated PEDOT:PSS films as optimised in the last section. The substrate to head gap was kept around 200 µm and the wet film thickness was kept at 5 µm. First, changes in morphology were monitored using scanning electron microscopy (SEM). The images of films dried at each temperature setting are shown in Figure 3. 8. As the temperature increases, tamping of the grains was seen. The grains can be distinctly identified at low temperature, however at 190°C temperature, the grain boundaries disappear, and rod shape structures start to appear. At high temperatures, $MAPbI_3$ degrades into PbI_2 and volatile MA ions. MA being volatile leaves the films while PbI_2 starts aggregating at grain boundaries. The rod-shaped structures present at the grain boundaries are indicative of the presence of PbI_2. Devices were fabricated on top of these films and the corresponding JV statistics are presented in Figure 3. 9. As can be seen from the JV parameters, devices dried at an oven set point of 140°C match the performance of spin coated films quite well while under-annealed (120°C) and over-annealed (190°C) films show significantly lower performance, mainly coming from low fill factor and lower current density compared to the control spin coated device. The drop in fill factor is indicative of extra series resistance present due to less dried films at 120°C while in the case of 190°C drying, the drop is due to the degradation of perovskite into PbI_2 leading to an increase in series resistance and hence the drop in fill factor. The degradation argument can also further be confirmed by a drop in J_{sc} for the degraded films while it stays the same for under annealed films (120°C).

The results show that $MAPbI_3$ films are extremely sensitive to the drying temperature. And thus, to understand the drying dynamics and its effect on the crystallinity and quality of the film, further investigation was done by gathering higher resolution data at the increment of 10°C in oven set points from 120°C to 180°C. The resultant morphology of the films is presented in Figure 3. 10 and shows a similar trend as the earlier batch. The crystal shrinks and the appearance of rod like shape crystals at upwards of 160°C oven set points. These

bright features were attributed to the presence of PbI_2. To confirm this, X-Ray diffraction (XRD) measurement was conducted. The peak around 12.5° corresponds to the 001 face of PbI_2. To compare the PbI_2 peak intensity, the data was normalised by dividing the values by

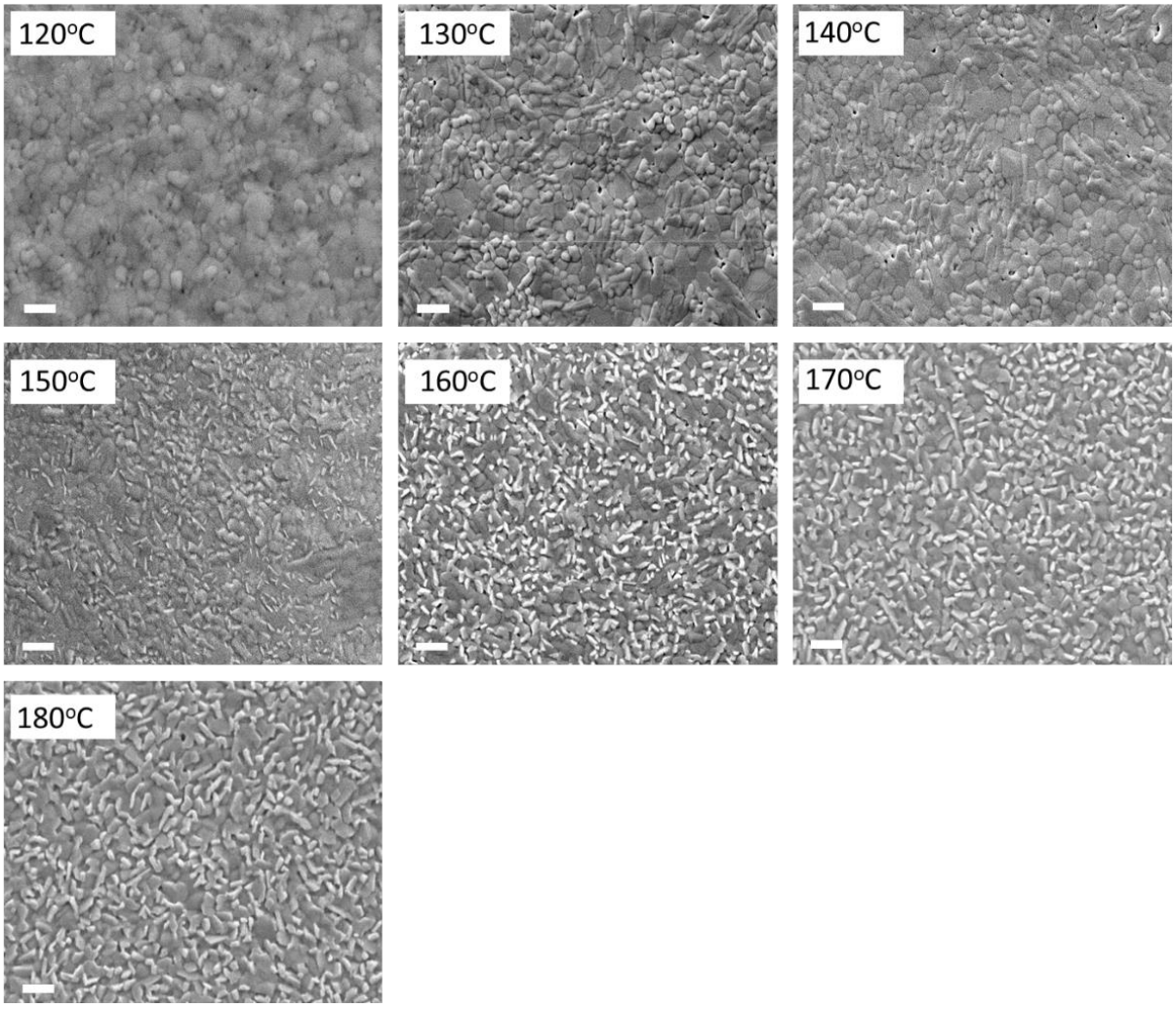

Figure 3. 10 Surface SEM images of R2R slot die coated $MAPbI_3$ on R2R slot die coated PEDOT:PSS dried at 120°C, 130°C 140°C, 150°C, 160°C, 170°C and 180°C oven set points. Scale bar represents 1 µm length.

the maximum. As seen in Figure 3. 11b, the PbI_2 peak intensity increases as drying temperature goes up, confirming the existence of PbI_2 upon thermal degradation of $MAPbI_3$. XRD results also show that the main peak in the region of 13° to 15° which is indicative of perovskite crystal structure is split in the two faces 002 and 110, implying the tetragonal phase of $MAPbI_3$. Gradually as the temperature is increased the 002 face merges into 110 leading to the shift of the peak towards higher angle. This means that as the films are annealed at higher temperature a phase transition happens from tetragonal to cubic.[38]

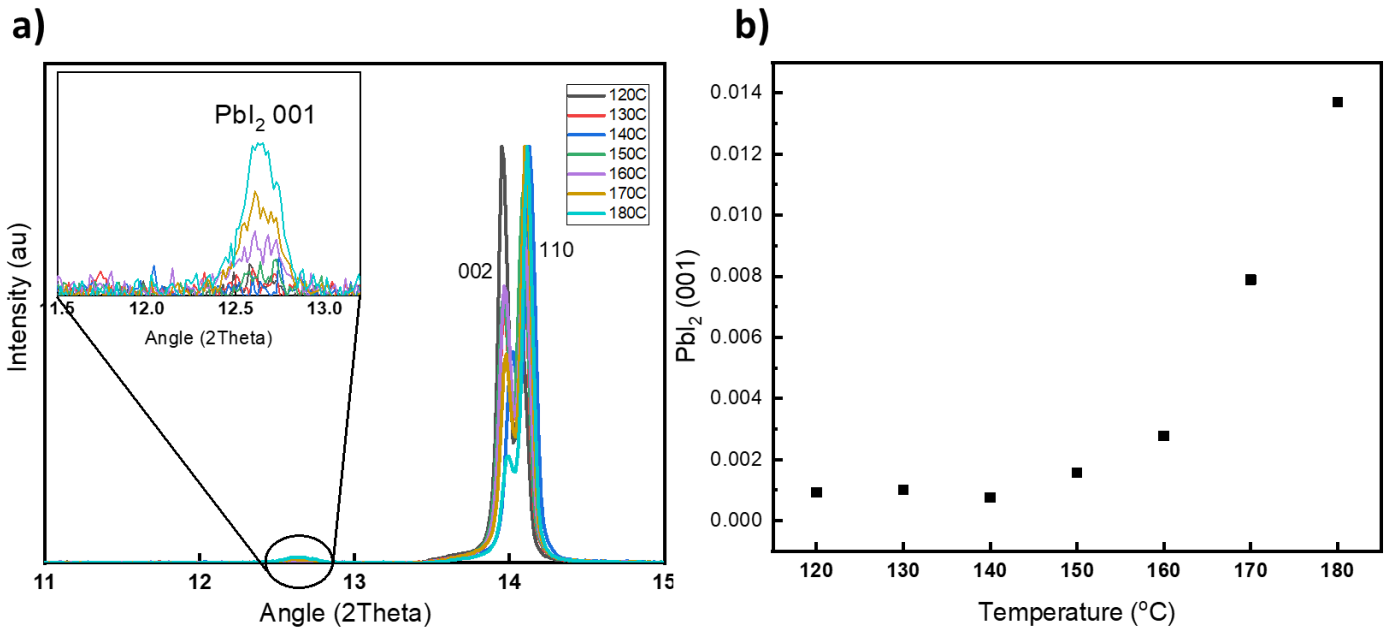

Figure 3. 11 a) XRD spectra of R2R coated $MAPbI_3$ films dried at 120°C, 130°C 140°C, 150°C, 160°C, 170°C and 180°C oven set points. The spectra are normalised by dividing the data points by the maximum value which in this case was the intensity of the peak around 14°. The films were coated on R2R coated PEDOT:PSS films as optimised in previous section. b) scatter plot of PbI_2 001 peak intensity against the temperature.

To further understand the drying effects on the surface of the films and ascertain the thermal degradation, x-ray photoelectron spectroscopy (XPS) was employed. The degradation of $MAPbI_3$ films can also be traced by the presence of Pb^0 $4f_{5/2}$ and $4f_{7/2}$ peaks centred around 141.8 and 136.8 eV respectively.[39] These peaks are located right next to the Pb^{2+} $4f_{5/2}$ and $4f_{7/2}$ centred around 143 and 139 eV respectively which can be seen in zoomed in spectra on the right and left side of Figure 3. 12. Both the Pb^0 peaks are present in the films annealed at 160°C, 170°C and 180°C. This further confirms the degradation of perovskite films dried at higher temperatures. The shift in the Pb^{2+} peaks towards lower energy above 140°C drying temperatures is noted. This may signify lower oxidation as the temperature is increased but could also be due to phase transition from tetragonal to cubic as seen in XRD measurement.[40] Also, another peak was seen in the region of 202-196 eV binding energy (Figure 3. 13a). This was attributed to the merging of the two chloride peaks Cl 2p1/2 and Cl 2p3/2 coming from the HCl additive used for improving film morphology and performance. For device performance and film stability to maximize, it is important that chloride is removed from the

film during drying. A significant amount of chloride is seen in the films dried at a lower temperature as the temperature rises, the intensity of the chloride peak decreases. The

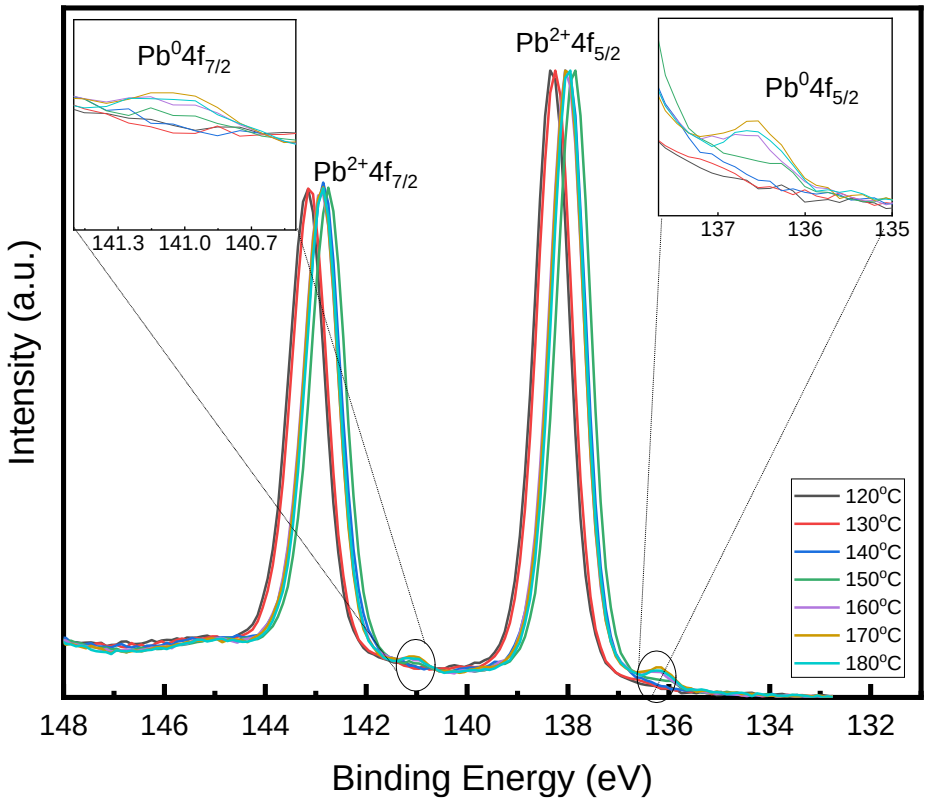

Figure 3. 12 X-ray photoelectron spectroscopy of R2R coated $MAPbI_3$ films dried at 120°C, 130°C 140°C, 150°C, 160°C, 170°C and 180°C oven set points. The spectra are normalised by dividing the data points by the maximum value. The films were coated on R2R coated PEDOT:PSS films as optimised in previous section.

chlorine levels were quantified against the temperature in Figure 3. 13b This confirms the small amount of residual chlorine at and around 150°C and as previously reported, small chlorine content could be beneficial for device performance.[41] Interestingly, the nitrogen atomic percentage falls while the lead percentage remain consistent till 150°C. Here Pb% is total of Pb^0 and Pb^{+2} and N% is total of N^{+3} and N^{+4} coming from methyl ammonium. Beyond 150°C nitrogen falls sharply and lead percentage starts increasing, implying the degradation of perovskite above 150°C. The volatile methyl ammonium ions leave the films upon high thermal stress leading to an increase in the relative Pb% and a decrease in N%. This further confirms the thermal degradation of $MAPbI_3$ films above 150°C as indicated by SEM and XRD. These films were then used for the fabrication of the devices. All the films dried at different temperatures were then chopped into small pieces of 28x28 mm^2 and the rest of the layers

were coated by spin coating. The resultant device data is presented in Figure 3. 14. Though characterisation was done of films dried up to 180°C to understand the effect of temperature

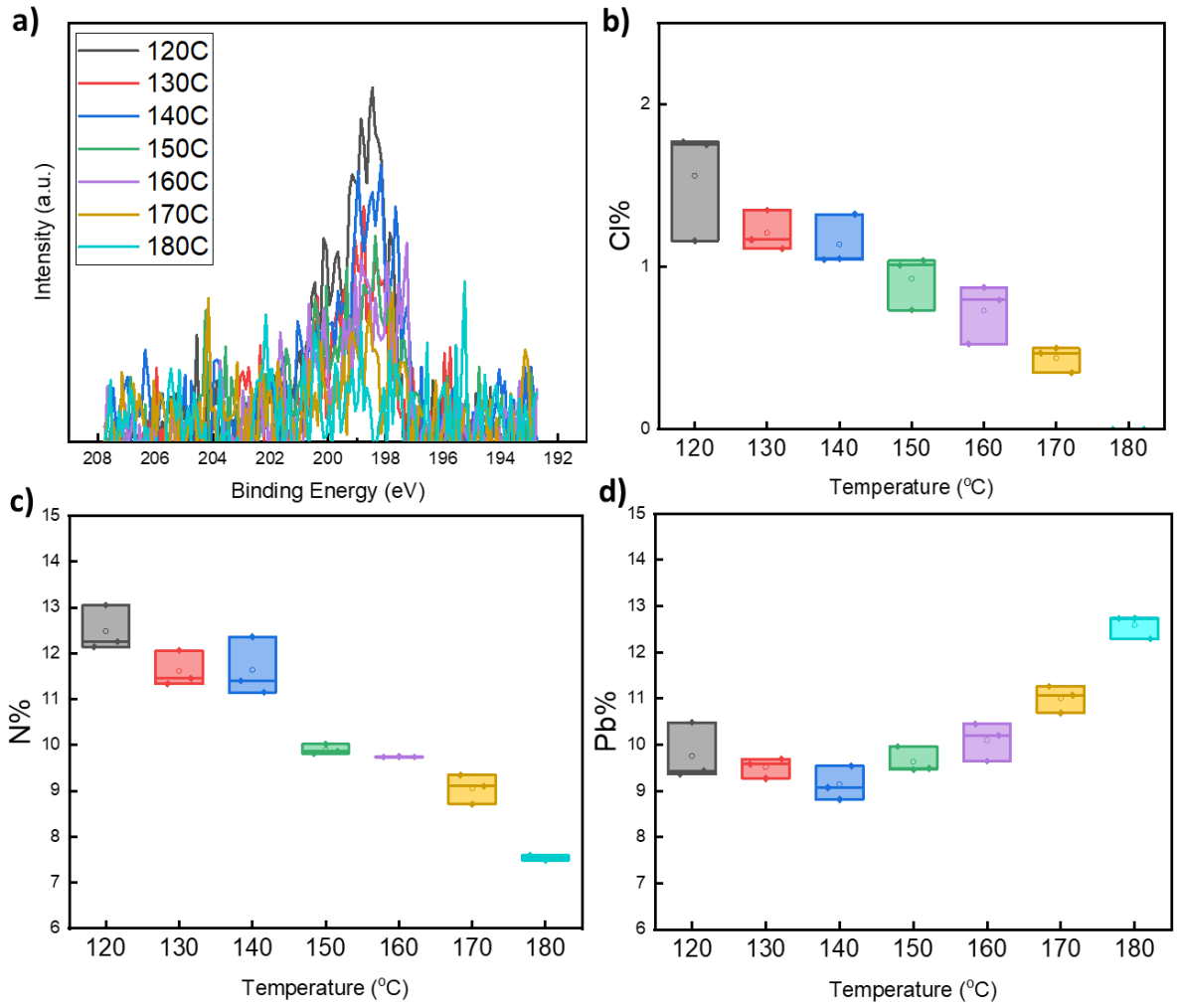

Figure 3. 13 X-ray photoelectron spectroscopy of R2R coated $MAPbI_3$ films dried at 120°C, 130°C 140°C, 150°C, 160°C, 170°C and 180°C oven set points. (a) Cl $2p_{1/2}$ and Cl $2p_{1/2}$ peaks merged into one peak. (b) Atomic percentage of the chlorine present on the surface of the films. (c) Atomic percentage of the nitrogen present on the surface of the films. (d) Atomic percentage of the lead present on the surface of the films

on the morphology and surface chemistry of $MAPbI_3$ films, the devices were only made using films dried up to 160°C. This was because, it was previously noted that the performance saturated around 140°C and dropped at 160°C, and hence the devices were made using R2R coated $MAPbI_3$ dried at oven set points from 120°C to 160°C. The performance showed similar trend and the peak efficiency was achieved at 150°C. The hero cell recorded 11% PCE at 150°C dried films. Though the absolute performance of this batch was quite low compared

to the last one as can be seen by comparing the spin-coated device for both batches. This could be due to batch-to-batch variations, or the room conditions at the time of deposition might have changed due to temperature and humidity in the room as the room conditions were not heavily controlled. In summary, this section focused was towards optimisation of drying parameters for R2R slot die coated $MAPbI_3$. Further, the effect of drying temperatures on surface chemistry was studied by XPS, XRD and SEM. In the next section the remining layers of PCBM and BCP will be optimised for R2R deposition.

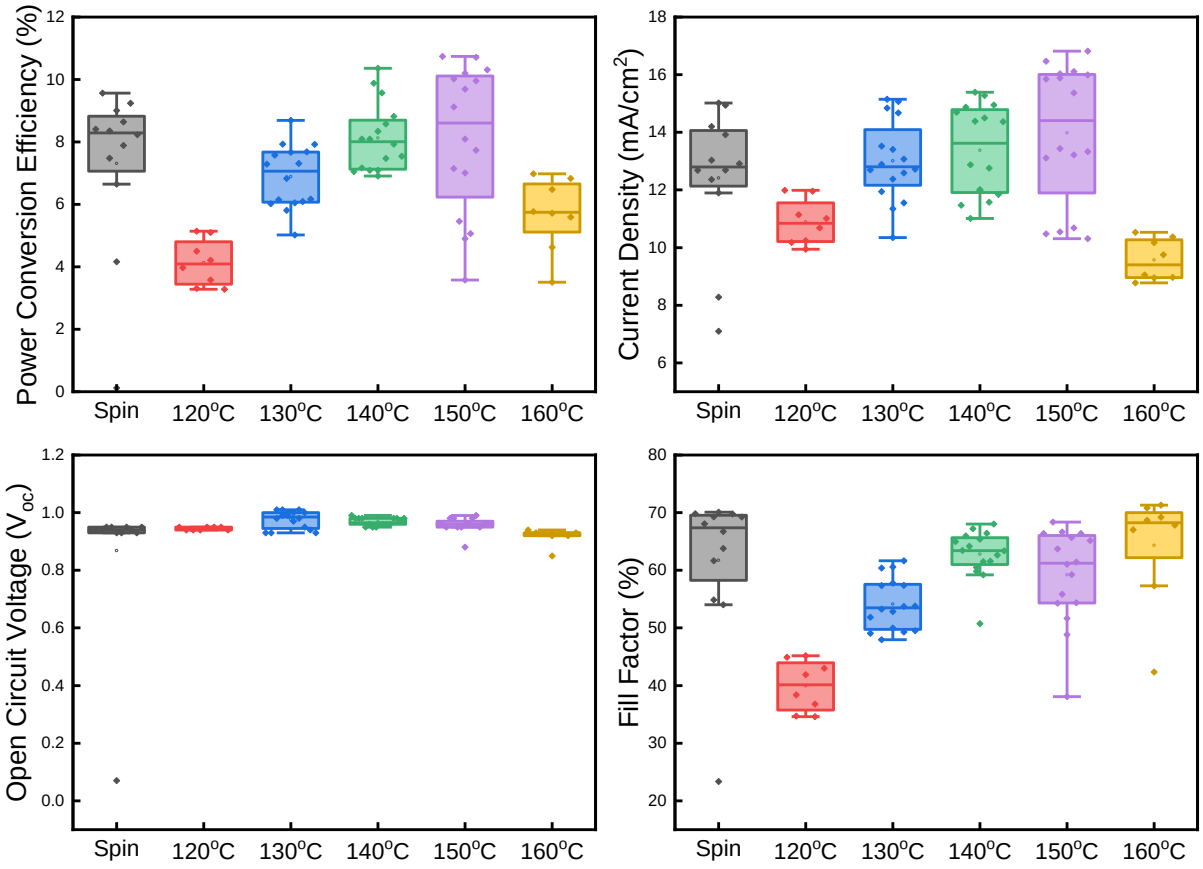

Figure 3. 14 Statistics of JV forward scan parameters of devices made with R2R slot die coating of 1:3 PEDOT:PSS films and 0.5M $MAPbI_3$ dried at set points of 120°C, 130°C, 140°C, 150°C, 160°C and their comparison with full spin coated device. For R2R slot-die coated devices, PEDOT:PSS and $MAPbI_3$ were slot-die coated, rest of the layers were coated by spin coating followed by thermal evaporation of silver contact on top.

3.5 Optimisation of PCBM electron transport layer

Up until this point as the optimisation of PEDOT:PSS and $MAPbI_3$ by R2R was explored with PCBM and BCP being spin coated. Due to the dynamic drying in spin coating and the use of

volatile solvent (chlorobenzene) for dissolution, no external drying was needed for PCBM films, and the solvent was completely removed during the coating itself. Whereas in R2R slot die coating, drying and coatings are two different processes. Therefore, oven drying is needed to remove solvent from the films. PCBM is known to oxidise in presence of light and oxygen.[42] Since in oven drying setup both factors are present, the film could degrade under a large flux of hot air. To check the thermal stability of PCBM films under ambient conditions, PCBM dissolved in chlorobenzene was spin-coated on top of the perovskite layer and put on a hot plate at 60°C, 80°C, 100°C and 120°C for 5 minutes. These were compared with the control films with no drying. No substantial difference was found in the device results shown in Figure 3. 15. All performance parameters remain within the range of the control device (no drying).

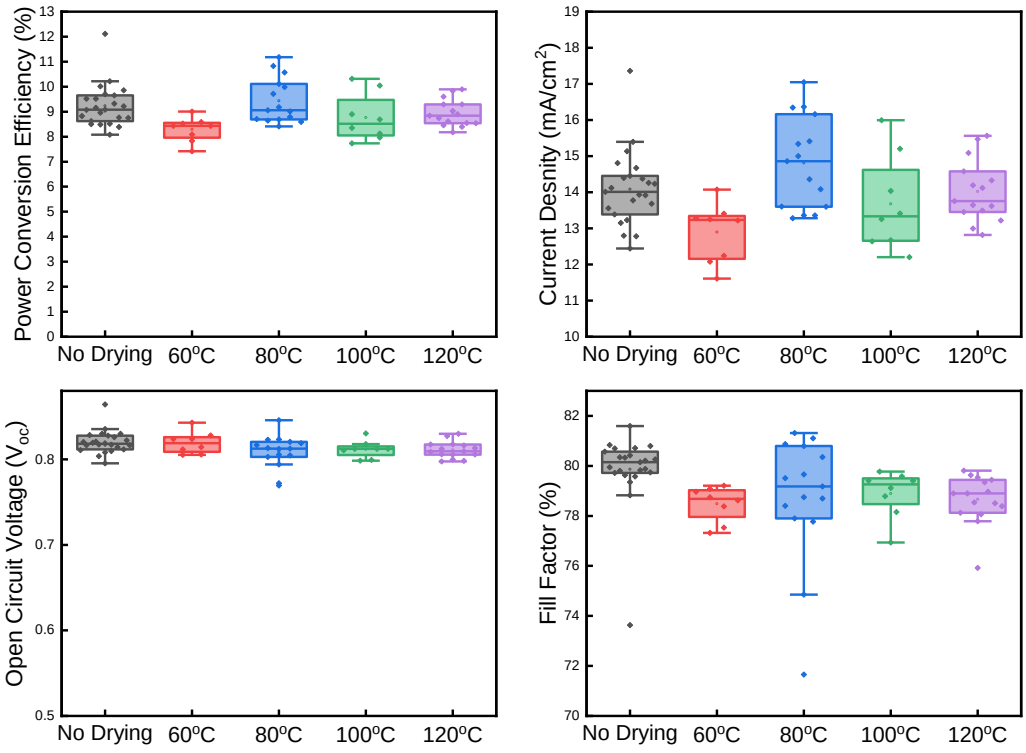

Figure 3. 15 Statistics of JV forward scan parameters of devices made on glass substrate by spin coating PEDOT:PSS, 0.5M $MAPbI_3$, PCBM dried on hot plate at 60°C, 80°C, 100°C, 120°C and their comparison with non-dried PCBM. BCP was spin coated on PCBM followed by thermal evaporation of silver contact on top.

From the data, it can be concluded that the PCBM has not degraded in presence of external heating and therefore should not be too different in the smart coater oven. As a result of the

above experiment, a drying temperature of 90℃ set point was used for drying R2R slot die coated PCBM films which should be enough to get rid of all the solvent from the films.

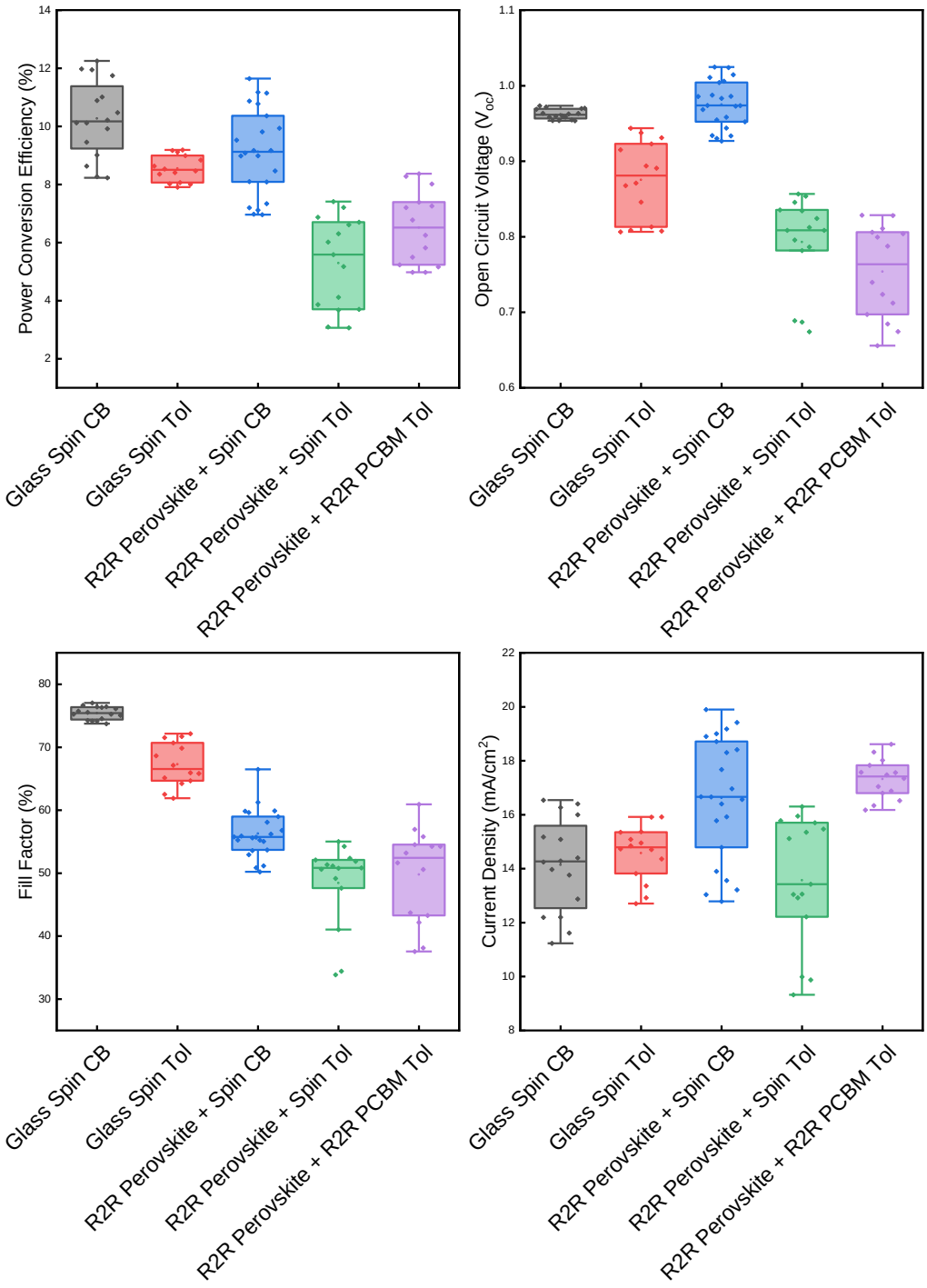

Figure 3. 16 Statistics of JV forward scan parameters of devices made on glass substrate by spin coating with PCBM dissolved in chlorobenzene and toluene compared to that of device made on flex with both the solvents. For flexible devices the bottom two layers were R2R slot-die. For R2R slot die coated PCBM all the layers till PCBM were coated via R2R.

For the above experiment chlorobenzene was used for PCBM dissolution. However, for large scale application chlorobenzene or any halogenated organic solvent are not a good choice since they usually have very low work exposure limits (WEL). Low WEL would mean only small quantity can be used without breaching the safe limit which is 1 PPM time weighted average (TWA) for chlorobenzene, thus reducing the production capacity of the factory. Hence an alternative solvent system is needed for large scale production. First toluene was explored as an option to replace chlorobenzene which has higher WEL TWA of 50 PPM meaning that 50 times more can be used than chlorobenzene in the same facility leading to 50 times higher coating speed given all the other factors remain same. 10 mg ml^{-1} of PCBM was dissolved in toluene. The surface tension of the ink as measured came out to be 28.3 mNm^{-1} and had a viscosity of 0.81 mPa.s. For this ink, a substrate to slot die gap of 200 µm was found to give stable coatings using 1000 µm tab width meniscus guide. Upon coating, due to low solubility of PCBM in toluene, the material aggregated as the films dried and led to poor performance as shown in Figure 3. 16. The impact was observed in FF and V_{oc} while the J_{sc} remains similar. This could be due to poor coverage of the perovskite by PCBM leading to a low shunt resistance. The performance drop was seen with both spin coating as well slot die coating of the PCBM in toluene implying that its likely the drop in performance is not due to the change in deposition technique rather it is the change in the solvent for PCBM that causes the drop in performance.

To understand the morphology of slot die coated PCBM with toluene, PCBM films were slot die coated via benchtop slot-die coater on bare PET films. PET films were cleaned and treated with plasma to clean the surface and increase the wetting property. The optical image of the resultant coating can be seen in Figure 3. 17. From the image, it can be seen that PCBM in toluene tends to aggregate, and lumps of these aggregation are present across the film. This is more clearly visible in optical microscope image taken at 20X magnification. Due to low solubility of PCBM in toluene (~15 mg ml^{-1})[43], as the drying starts, substrates surface energy decreases with increased temperature, leading to quick evaporation of toluene due to its low boiling point which leads to aggregation of PCBM as the solvent evaporates. While PCBM in chlorobenzene is over twice (~39 mg ml^{-1})[43] as soluble, it also has a significantly higher boiling point which leads to slower evaporation resulting in uniform films.

To further understand the drying profile of both the solvent formulations simultaneous thermal analysis (STA) was conducted (see Figure 3. 18). An initial drop of 6% weight is seen with toluene formulation compared to 2% for chlorobenzene, implying rapid toluene removal as predicted before. Also, toluene formulation takes much shorter path indicating faster rate of drying after the initial rapid drop in % weight. The point at which the mass derivative is zero with respect to time is referred as the total evaporation of a solvent. The total

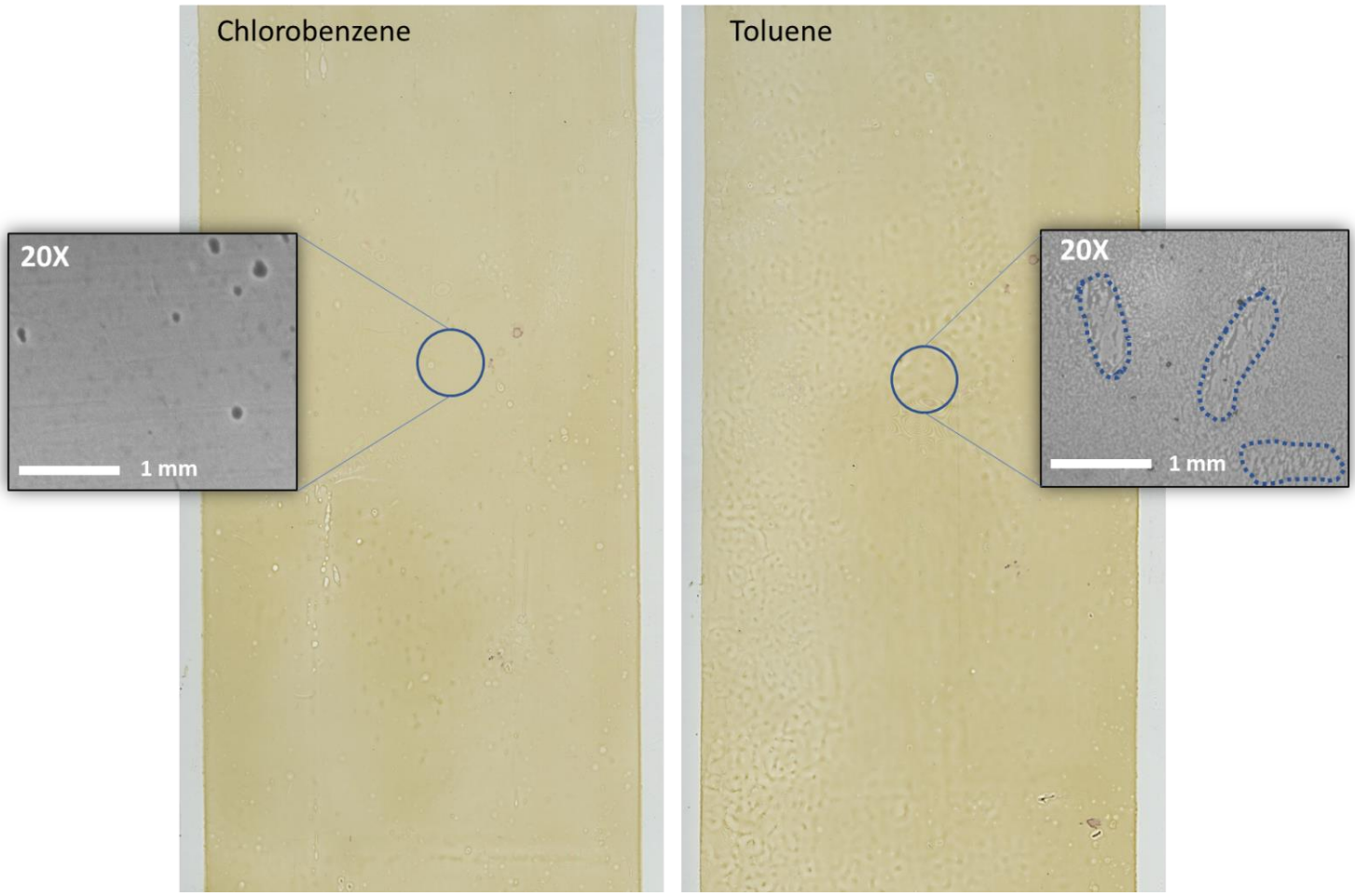

Figure 3. 17 Comparison between benchtop slot-die coated PCBM films dissolved in chlorobenzene and toluene. High magnification image was taken by optical microscope using 20X lens.

evaporation of toluene took place around 83°C while chlorobenzene evaporated completely at 105°C. Two endothermic peaks at 74°C and 102°C can be seen right before these two points of total solvent evaporation. To mimic the drying of the chlorobenzene, solvent engineering was attempted. Several blends of different solvents were made. The strategy was to create a blend with a ladder of increased boiling point and increased solubility of PCBM to

control the removal of solvents in the films mimicking the evaporation of chlorobenzene. O-xylene has been used extensively in organic photovoltaics for polymer dissolution and

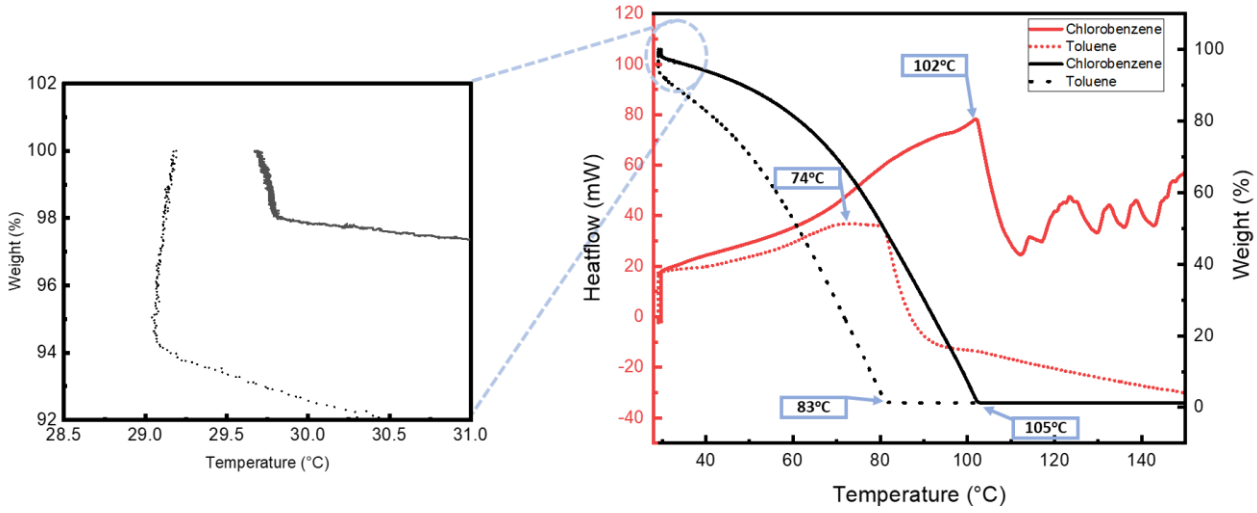

Figure 3. 18 STA Analysis of PCBM formulation in chlorobenzene and toluene

has higher solubility (22.1 mg ml^{-1})[44] than toluene (15.6 mg ml^{-1})[44] and is also less volatile, O-xylene has boiling point of 144℃ and toluene has 110℃. A binary mixture of toluene and o-xylene in the ratio of 7:3 was made (here after referred as Tol:Oxy). The amount of toluene was kept higher to benefit from the fast drying of toluene due to the limited oven residence time. Along with the binary blend of O-xylene and toluene, ternary blends with a higher boiling point and less volatile compounds like cyclohexanone (boiling point 156℃), indane (boiling point 182℃) and 2-methyl anisole(boiling point 171℃) were also prepared by mixing them into the binary mixture. The ternary blend was made by mixing 6 parts of toluene, 2 parts of o-xylene and 1 part of high boiling point solvent. The resultant S2S slot die coated PCBM films on PET films using these different blends are shown in Figure 3. 19. The macro uniformity significantly improves with the binary mixture of Tol:Oxy, and the agglomeration seems to reduce compared to that of toluene. However, it still shows some level of agglomeration visible in higher magnification optical images. But with ternary blends all the films look quite uniform with some difference in morphology as can be seen in higher magnification image of Tol:Oxy:2Ma. PCBM in Tol:Oxy:2Ma optically looks rougher but no patches of agglomeration like films from toluene are seen.

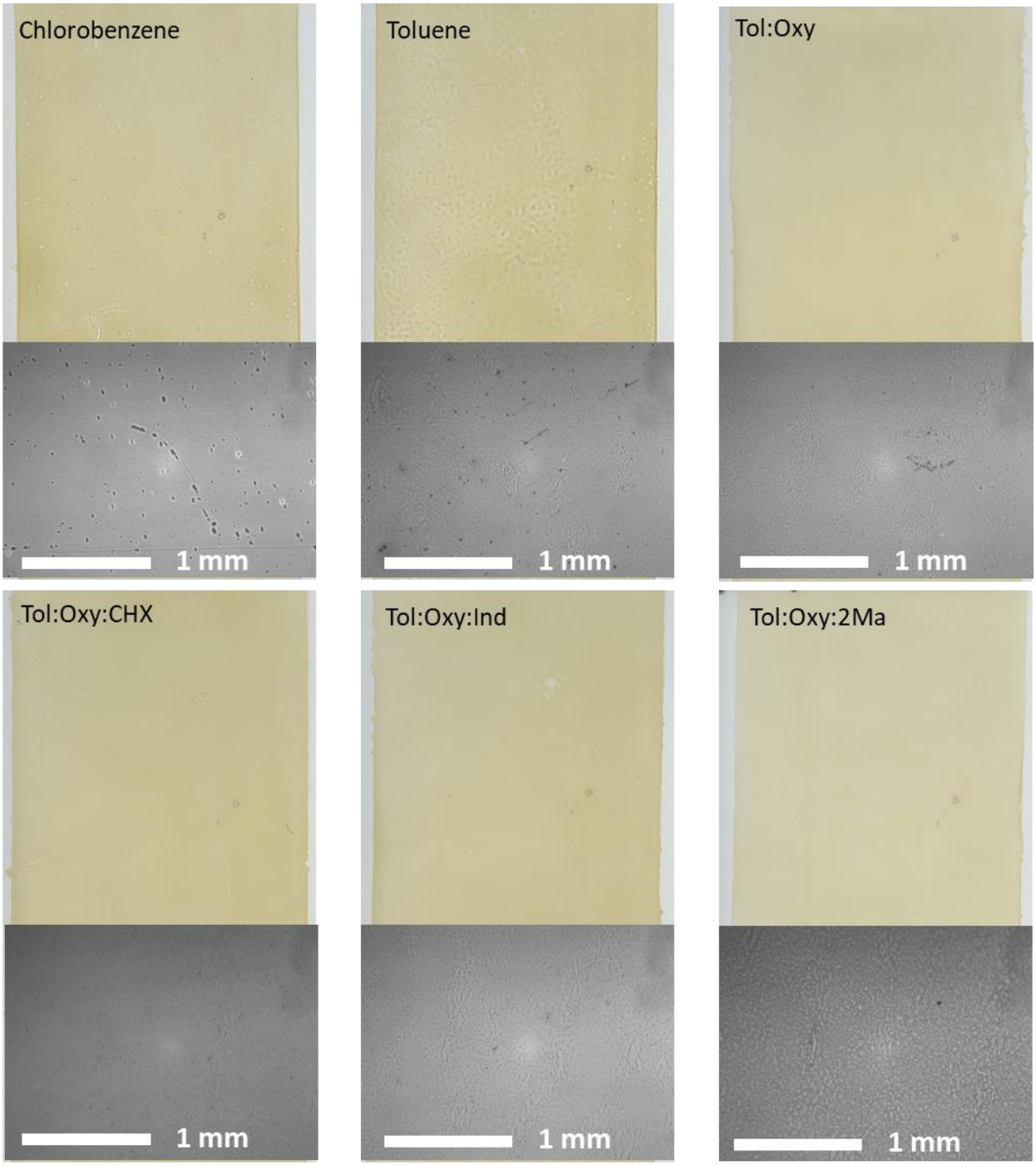

Figure 3. 19 Scanned (beige colour) images and their respective 20X magnification optical microscope images (at the bottom of each scanned image) of S2S slot die coated PCBM films on PET using different solvent blends as solvent for PCBM dissolution. Tol:Oxy is a blend of toluene toluene and O-xylene in 7:3 ratio. Ternary blends represented by Tol:Oxy:X were made in the ratio of 6:3:1, where X is either cyclohexanone (CHX) or Indan (Ind) or 2-Methyl anisole (2Ma).

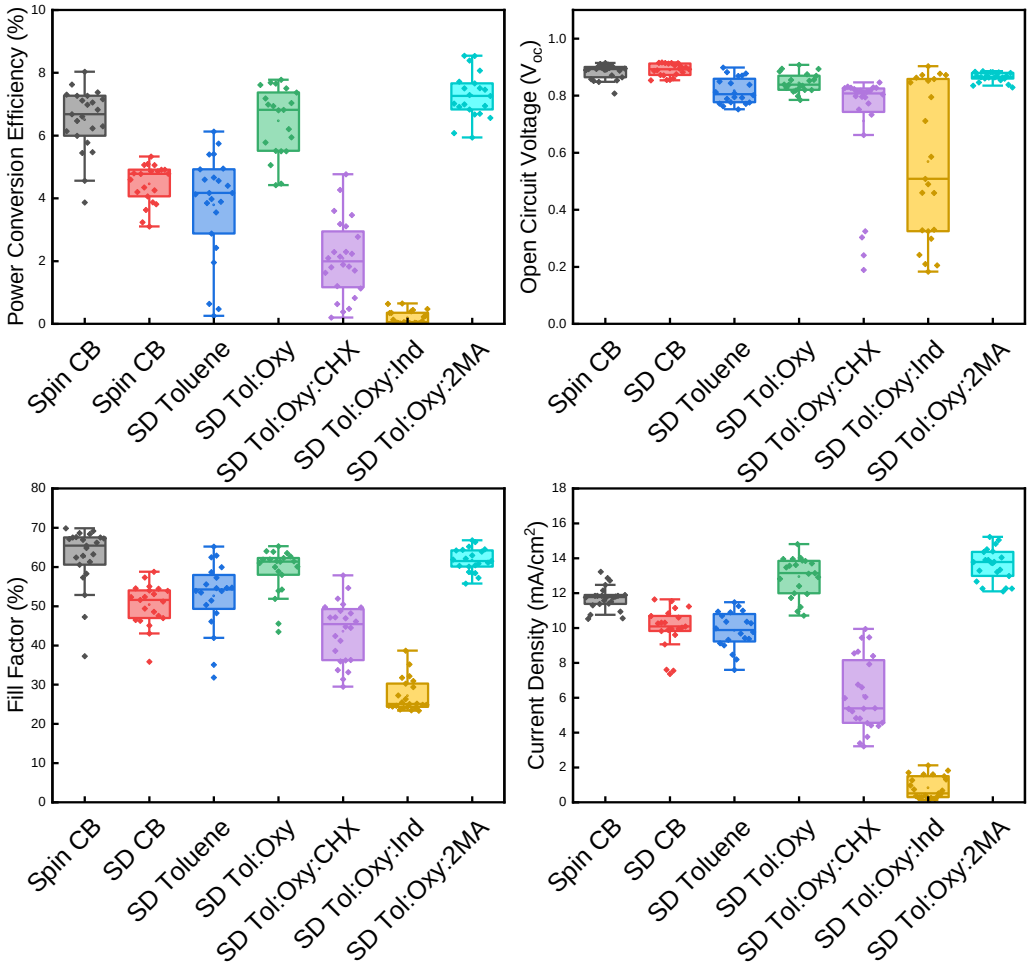

Figure 3. 20 Statistics of JV forward scan parameters of devices made using different solvent blends of PCBM. PCBM was coated via S2S slot-die coater on R2R coated PEDOT:PSS and $MaPbI_3$ films. Device were then chopped into small pieces of 28x28mm and finished with spin coating BCP and Ag thermal evaporation.

All the blends were then used to slot die coat PCBM on R2R coated PEDOT:PSS and $MAPbI_3$. The statistics of the batch are presented in Figure 3. 20. Interestingly addition of O-xylene to the toluene to form binary blend improved the performance. This is due to significant improvement in film uniformity because of controlled evaporation leading to less agglomeration. Contrary to this, though all ternary blend optically looked good, they did not perform well except the one using 2-methyl anisole. Addition of indan and cyclohexanone led to significant drop in performance . The performance drop was mainly due to a drop in J_{sc} and FF. The cause of this is not clear but could possibly be due to the non-favourable interaction of perovskite with indan and cyclohexanone. On the other hand, ternary blend of

2-methyl anisole showed excellent performance matching with the performance of chlorobenzene blend. A step wise drying of solvent and good solubility of PCBM, resulted in low movement of PCBM while drying resulting in uniform film formation. None of the solvents in this ternary blend have WEL over 50, therefore they are a good substitute over

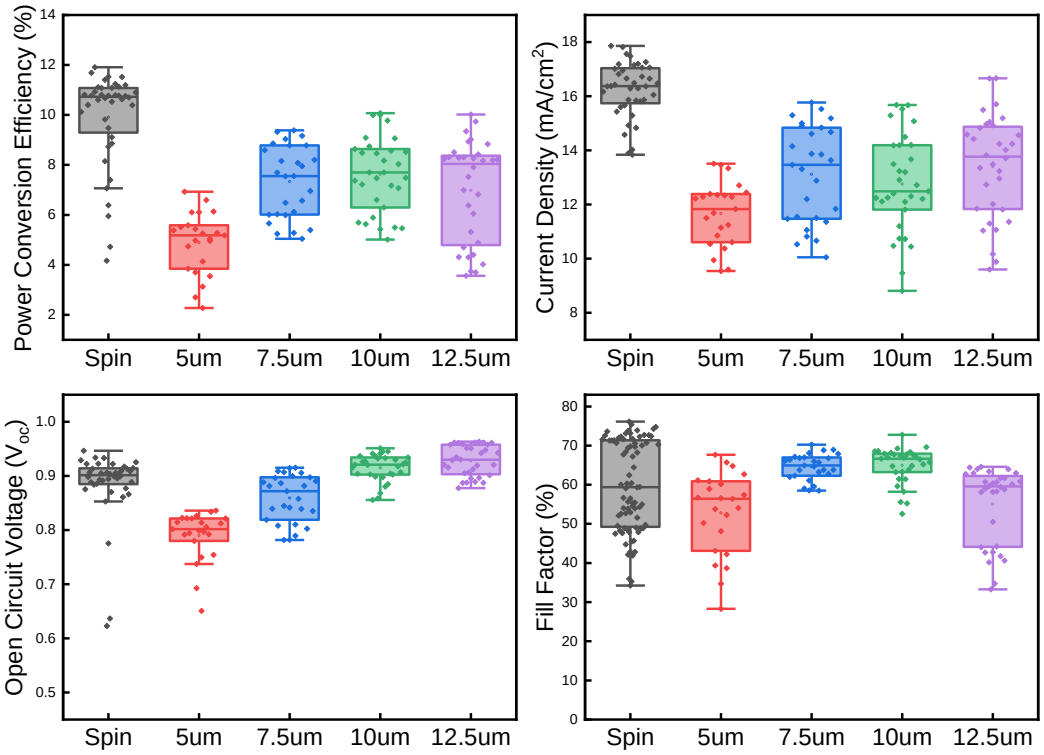

Figure 3. 21 Statistics of JV forward scan parameters of devices made at different wet film thickness of R2R slot die coated PCBM and compared with spin coated device. For R2R slot die coated device, all the layers upto PCBM was slot die coated and the remaning were done by spin coating.

chlorobenzene for high throughput manufacturing of PSCs. After replicating the performance of chlorobenzene over S2S coated PCBM, the implementation of PCBM using R2R was carried out. Due to low viscosity of the inks, a 1000 µm tab length meniscus guide was used. The oven was set at 90°C which corresponded to 84°C of actual temperature measured by thermocouple placed inside the oven. The WFT of PCBM was optimised by coating a 5, 7.5, 10 and 12.5 µm PCBM layer. The performance of the batch is plotted in Figure 3. 21. As the thickness of PCBM increased from 5 to 10 µm WFT, an increase in V_{oc} and FF was observed. This indicates the extent of coverage of perovskite by PCBM. Thicker PCBM increased the perovskite coverage and 10 µm PCBM may have formed a capping layer, avoiding direct contact between perovskite and the top contact. Further increase in thickness led to a drop

in FF coming from increased series resistance of the 12.5 µm PCBM devices. Therefore, 10 µm WFT of PCBM was considered as the optimised value for slot die coating and will be used for as standard for the subsequent experiment. It is to be noted that the overall drop in the performance of R2R slot die coated device compared to spin coated control was not clear however this was recovered in the next experiment.

3.6 Optimisation of Interlayer

As discussed in the introduction chapter BCP improves charge collection and reduces recombination losses in PIN PSCs by forming an ohmic contact between PCBM and silver electrodes. It forms a complex with Ag, aiding charge transfer, and can be applied as a solution-processed or thermally evaporated layer, with the former being more effective for rough perovskite surfaces.[45] [46] [47]

For the optimisation of R2R slot die coated BCP, the WFT was first varied from 5 µm to 15 µm using a 0.5 mg ml^{-1} solution of BCP in ethanol. The surface tension of the ink was found to be 22 mN m and the viscosity 1.28 mPa s. At 1 m min^{-1} coating speed the capillary number is 0.00097. For this capillary number, according to the low flow limit theory, the dimensionless gap must be less than 154. The substrate to head height was adjusted to keep the dimensionless gap close to 150. To dry the as-coated films, the inline convection oven was kept at a 60℃ set point corresponding to 58℃ as measured by the thermocouple placed inside the first oven. However, due to the large flux of air inside the convection oven and extremely low BCP thickness (generally in the range of 5 nm), creating a uniform coating of thin BCP is a challenge. To confirm the presence and uniformity of the BCP layer at various thicknesses, XPS was conducted. The presence of BCP molecule on the surface can be characterised by N1s peak close to 398eV binding energy. [48] Figure 3. 22a shows the XPS spectra of the R2R coated BCP films at various wet film thicknesses. The films were coated on top of the stack of optimised PEDOT:PSS, $MAPbI_3$ and PCBM observed in bare PCBM films with no BCP. These data sets confirm the presence of BCP on PCBM films. To get a deeper understanding of the film, composition analysis of the atomic percentage of all the detected elements on the surface of the BCP and non BCP coated PCBM films was carried out. The resultant data is summarised into a table in Figure 3. 22b.

a)

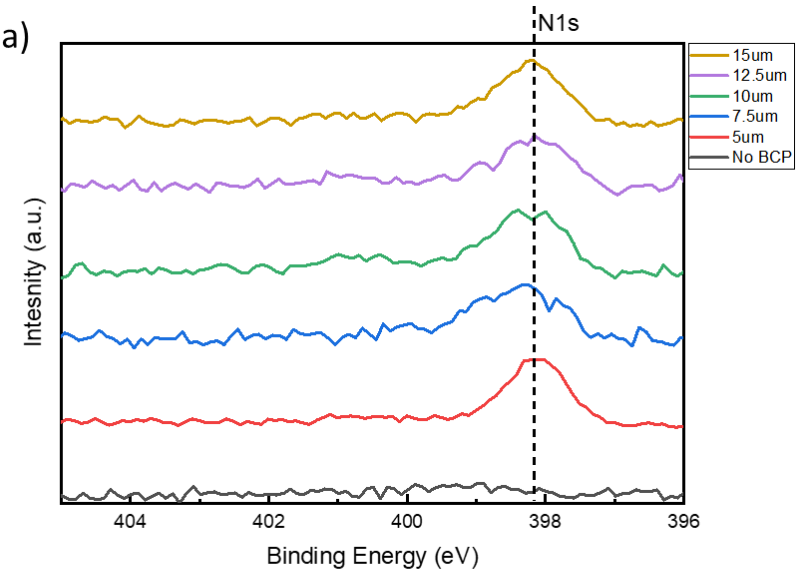

b)

Sample	Carbon	Iodine	Nitrogen	Oxygen	Lead	Silicon
PCBM	94.9	0.05	0.08	4.6	0.02	0.31
BCP 5um WFT	94.8	0.2	0.89	3.8	0.02	0.23
BCP 7.5um WFT	94.4	0.16	0.37	4.9	0.04	0.19
BCP 10um WFT	93.8	0.52	0.68	4.7	0.09	0.26
BCP 12.5um WFT	95.1	0.25	0.47	3.8	0.07	0.30
BCP 15um WFT	94.1	0.32	0.75	4.2	0.08	0.58

Figure 3. 22 a) X-ray photoelectron spectroscopy of R2R coated BCP films of 5 µm, 7.5 µm, 10 µm, 12.5 µm and 15 µm wet film thickness, showcasing the N1s peak close to 398eV representing presence of BCP. The spectra are normalised by dividing the data points by the maximum value. The films were coated on R2R coated PEDOT:PSS, $MAPbI_3$ and PCBM films as optimised in previous section. b) Table of elemental analysis of R2R coated BCP films in atomic percentage.

The atomic percentage of the nitrogen in BCP coated layers is observed in the range of 0.4 to 0.9%. However, the atomic % of nitrogen as calculated from the chemical formula $C_{26}H_{20}N_2$ was 7.1%. It is to be noted that the atomic percentage calculation of nitrogen from the BCP chemical formula is done ignoring H atoms as H atoms are not detectable by XPS. The H atom has only 1 electron which participates in chemical bonding and no core electrons. Any signal from hydrogen could be confused with signals from the excitation of valence electrons from other surface atoms.[49] The wide difference between detected and expected atomic % of nitrogen could be explained by non-uniform and discontinuous formation of BCP layer or that the layer is thinner than the detectable limits of XPS. JV scan statistics with various thickness

of BCP are presented in Figure 3. 23a. With increased thickness from 5 to 7.5 µm, FF and V_{oc} shows improvement leading to improved PCE. Upon further increase of BCP thickness to 10,

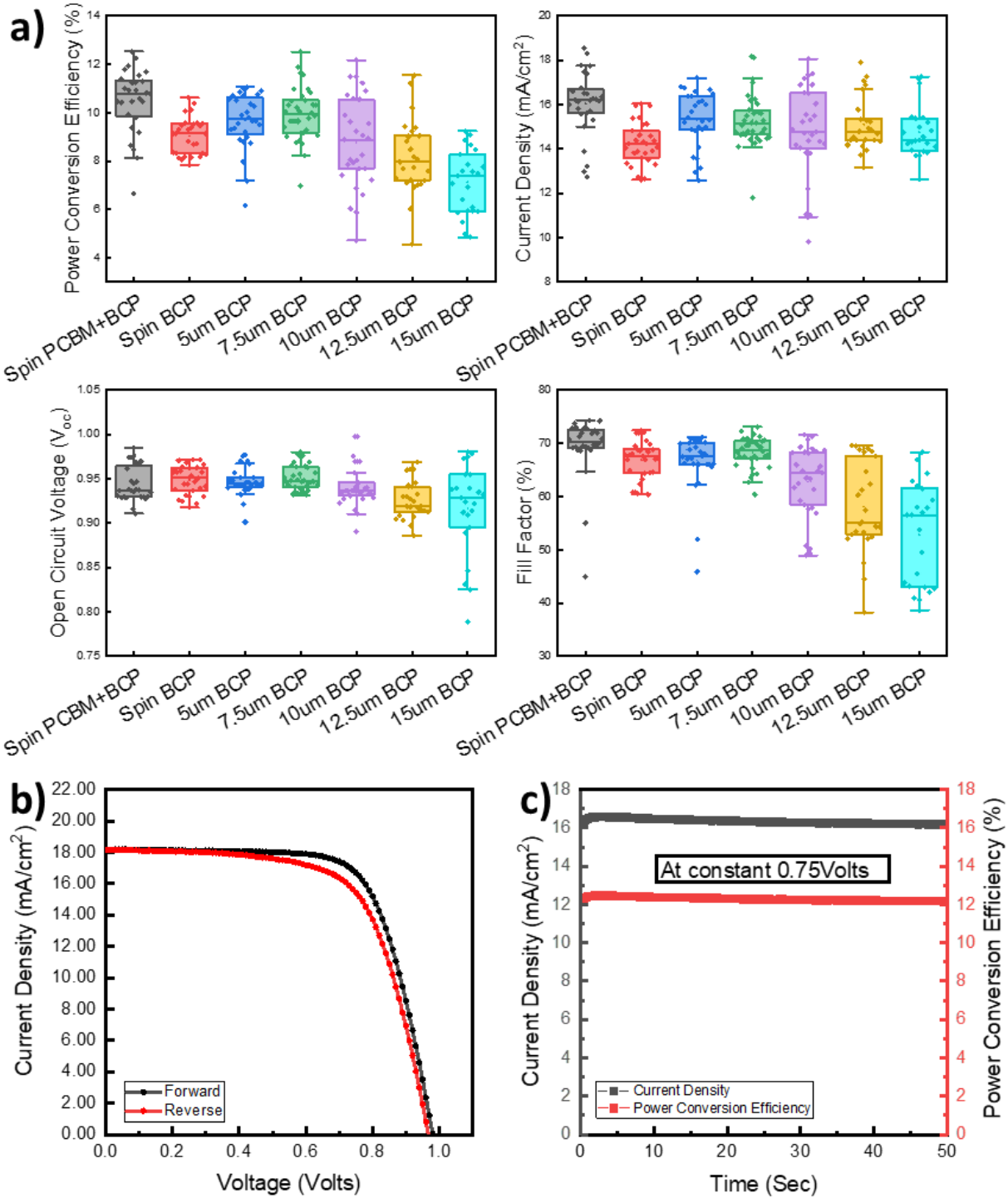

Figure 3. 23 a) Statistics of JV forward scan parameters of devices made at different wet film thickness of R2R slot die coated BCP and compared with spin coated device. b) JV plot of the hero device. c) Stabilised measurement of hero cells done at constant voltage of 0.75V.

12.5 and 15 µm, the FF sharply drops due to increased device resistance caused by the non-conducting nature of BCP. Hence the PCE peaks at 7.5 µm WFT following which the extra series resistance deteriorates the performance. The champion cell recorded J_{sc} of 18.18 mA cm^{-2}, 0.98V V_{oc} and FF of 70.3% resulting in forward scan PCE of 12.52%, respective JV curve is shown in Figure 3. 23 b . A slight hysteresis of 7.5% is recorded for the hero cell. The stabilised power conversion efficiency was also measured by keeping the device at constant voltage (at maximum power point voltage) until the current stabilises (Figure 3. 23c). The measured stabilised PCE over 55 secs stabilisation time was recorded to be 12% which is the highest reported PCE for fully R2R coated PSCs (with the exception of a coated top electrode).

3.7 Stability Measurement

PEDOT:PSS is not known to be a stable HTL material for highly stable PSCs. Due to acidic nature of PSS and hygroscopic nature of the PEDOT:PSS formulation, the interface of PEDOT:PSS degrades at a rapid rate leading to performance degradation over time.[50]

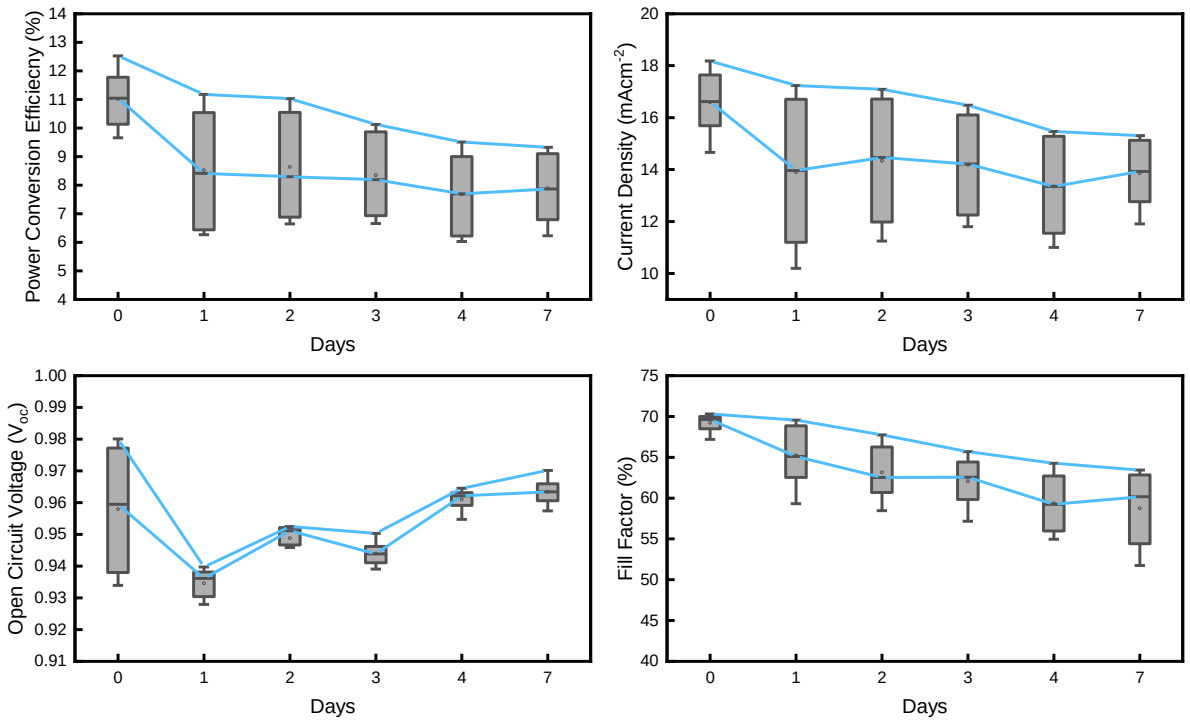

Figure 3. 24 JV statistics of hero batch over 7 days period. The devices were stored in the glove box and were only taken out when measurement was done.

The silver electrode was used as the top contact which again is known to cause instability of PSC by forming silver halide when brought in contact with $MAPbI_3$ if there are pin holes or

due to ion migration.[51] Due to these reasons PSCs with PEDOT:PSS HTL and silver contact suffer from poor stability. To understand the degradation rate of as fabricated R2R coated PSCs the fabricated PSCs were measured over multiple days. The devices were not encapsulated and were kept in glovebox environment and were only taken out to do the measurement. The recorded data over a week is shown in Figure 3. 24. Interestingly, there is a sharp drop in PCE in the first 24 hours and 20% loss of performance from median PCE of 11% on the 1st day to 8.5% median PCE was observed. The major drop in PCE came from the drop in FF and J_{sc}. A deep understanding of the cause of instability is beyond the scope of this work.

3.8 Low toxicity solvent system for R2R slot-die coated $MAPbI_3$

This work shows the coating optimisation of low toxic scalable solvent system for $MAPbI_3$. The ink formulation was developed in MIT, USA and was optimised for R2R setup in Swansea by the author of this thesis. The results of this chapter are published in the following article:

Swartwout, R., **Patidar, R**., Belliveau, E., Dou, B., Beynon, D., Greenwood, P., ... & Bulovic, V. (2022). Predicting Low Toxicity and Scalable Solvent Systems for High-Speed Roll-to-Roll Perovskite Manufacturing. *Solar RRL*, *6*(3), 2100567.[52]

In the work presented, the ACN-MA solvent system has been used for the dissolution of perovskite precursors to slot die coat $MAPbI_3$ films. The low volatile nature of this ink system contributed to the formation of compact films by rapid removal of ACN-MA solvent from the coated wet film. Another reason that motivated the use of ACN-MA system is the low workplace exposure limit (WEL) of ACN (40PPM) compared to DMF (10 PPM) used in highly efficient PSCs. These limits are set by Health and Safety Executive (HSE)[53] in UK and Occupational Safety and Health Administration (OSHA)[54] in the USA. The limits may differ from country to country as they are set by the respective regulatory bodies but are usually in close range as they are based on the academic studies and work histories of industry workers.[55] The limits quantify the amount of the solvent in the air above which it is no longer considered to be safe for workers. It is measured as time weighted average over 8 hours of continuous exposure. Since the ink formulation was developed and optimised at MIT, USA according to the WEL issued by OSHA, the same limits are represented in this work as well. A few commonly used solvents for precursors of $MAPbI_3$ and their WEL as obtained from OSHA is presented in Table 3.2.

In a PSC manufacturing facility, solvent handling will only require post coating of thin films. Drying coated wet films releases solvent vapour. These vapours are then handled by heating, ventilation, and air conditioning systems (HVAC) to avoid solvent build up for toxicity and fire reasons. The higher the speed of the coating for a given wet film thickness, the higher will be the solvent vapour needing extraction. This will require higher amount of air recirculation

Table 3. 2. WEL for commonly used solvents for the dissolution of perovskite precursors.

Solvent System	**WEL (TWA 8hr) PPM**
Dimethylformamide	10
N-Methyl-2-pyrrolidone	10
gamma-Butyrolactone	-
2-Methoxyethanol	25
DMSO	-
Tetrahydrofuran	200
Acetonitrile	40
Methyl Amine	10
Methanol	200

through HVAC system to reduce the vapour from the evaporated solvents in the manufacturing facility. With an increased speed of manufacturing, the incremental cost of capital expenditure and operating expenditure on HVAC system will become high, rendering the product not economical to manufacture. Hence the WEL will have a direct relationship with the upper limit of manufacturing output of a factory. The relationship between the upper limit WEL and coating speed can be derived from the following relation:

First the total usable volume of the room (V_t) can be expressed as the summation of volume of the room and total volume of air extracted by the HVAC system during the day.

$$V_t = V + Q * t \qquad 1$$

where V is the volume of the room in m^3, Q is the air extraction rate of HVAC system in m^3hr^{-1}, and t is time in hrs. t for the purpose of this calculation is fixed at 8 hours as all WEL set by

OSHA is measured over a period of 8 hours. The maximum regulated solvent concentration (C_{max}) in the air can be expressed in g per unit volume by the following equation:

$$C_{max} = WEL * M_w * \frac{P}{RT} \quad (2)$$

Where M_w is the molecular weight of the solvent, P is the pressure of the room, T is the temperature, and R is the constant with value 82.05*10^{-6}m^3 atm mol^{-1} K^{-1}. At standard conditions of 1 atm pressure and 298 K temperature C_{max} in gm^{-3} becomes :

$$C_{max} = 40.89 * WEL * M_w \quad (3)$$

The maximum weight of solvent in g can be calculated by multiplying the maximum gram per unit volume (C_{max}) by the total usable volume (V_t).

$$W_{max} = C_{max} * V_t \quad (4)$$

W_{max} when converted into volume by dividing it by the density of the solvent (ρ) in gml^{-1} gives the maximum solvent in ml ($V_{\max}$) that can be released in air within time t

$$V_{\max} = \frac{40.89 * WEL * M_w * (V + (Q * 8))}{\rho} \quad (5)$$

The volume of solvent released in air by coating a certain wet film thickness of WFT, width of w and length of l per day is given by:

$$V_{coating} = WFT * w * l \quad (5)$$

Therefore, maximum coating that can be done without breaching the safe limit is when $V_{\max}$ is same as $V_{coating}$ given by the following relation.

$$w * l = \frac{40.89 * WEL * M_w * (V + (Q * 8))}{WFT * \rho} \quad (6)$$

The coating area per day, represented by w*s, can be used to calculate the annual maximum capacity of the factory in watts, based on the assumption that the factory operates for a total of 250 days per year, using the following equation:

$$Capacity = \ coating\ area * \eta * I_{1\ Sun} * 250 \qquad 7$$

Where η is the efficiency of the solar cells, and $I_{1\ Sun}$ is the intensity of light incident at AM 1.5. Further combining both equation (6 and 7) gives the capacity as a function of $WEL, V,$ Q by

$$Capacity = \frac{40.89 * WEL * M_w * (\ V + (Q * 8)) * \eta * I_{1\ Sun} * 250}{WFT * \rho} \qquad 8$$

Thus, from the equation 8 it can be concluded that for a given HVAC system (Q) and a given building size (V), using high WEL solvents for coating PSCs is an economical way to boost the output capacity of the factory thus reducing the cost of production. As a solution to this, colleagues at MIT proposed a tetrahydrofuran (THF) based $MAPbI_3$ ink system with WEL of 125PPM. This when compared to DMF (10PPM) and ACN-MA (36 PPM) would increase the capacity over 13-fold against DMF and over 5 time against ACN-MA given the same air exchange rate and the room size. This is a significant increase in the capacity with ideally no extra cost. Furthermore, colleagues at MIT also calculated the additional cost incurred in the solution printing for manufacturing of PSCs. They found an additional cost of ¢0.74/W when DMF is used as the solvent while the same for THF is ¢0.037/W. To add further safety institutes keeps a safety factor of 4X-10X to account for unknown and accidental variables. If a factor of 5X is considered the cost to handle DMF would go up to ¢3.7/W and that for THF would be ¢0.18/W. This is 12% of the cost of current commercial silicon module.

3.8.1 R2R slot die coating of $MAPbI_3$ with THF-MA

The preparation of THF-MA $MAPbI_3$ formulation was done by the recipe received from MIT. Briefly 0.65M precursors of PbI_2 and MAI was weighed and mixed with 35% molar of MACl. The solid precursors were first mixed in 0.5ml of 2M solvent of MA in THF as purchased from Sigma Aldrich. The solution was left till the dissolution of precursors was noted following which 0.5 ml of methanol was mixed into the ink. The rheology of the ink was then measured using viscometer and is presented in Table 3. 3.

The capillary number for this process was similar to the one previously measured for the ACN-MA formulation, so similar slot die coating parameters were used, as optimized in section 3.4.2. The $MAPbI_3$ was coated onto a PEDOT:PSS substrate using a 90mm shim to define the coating width and a 1000 µm tab width meniscus guide. The gap between the substrate and the head was kept at 1100 µm, including a 1000 µm meniscus guide. The coating speed was kept at 1 m min^{-1}, as with all previous coatings. After coating, the wet film of $MAPbI_3$ was

Table 3. 3 Viscosity and surface tension measurement of THF-MA based $MAPbI_3$ ink formulation

Formulation	Viscosity (µ) mPa.s	Surface Tension (σ) mNm^{-1}	Capillary Number ($C_a = \frac{\mu V}{\sigma}$) at V = 1mmin^{-1}
THF-MA $MAPbI_3$	0.93	23.28	$6.6E^{-4}$

partially dried using an air knife at 50 l min^{-1} and then completely dried in a convection oven set at 150℃. Following the coating of $MAPbI_3$, the roll was taken offline, and the coated films were cut into 28x28mm^2 pieces, the remaining layers of PCBM and BCP were spin-coated on

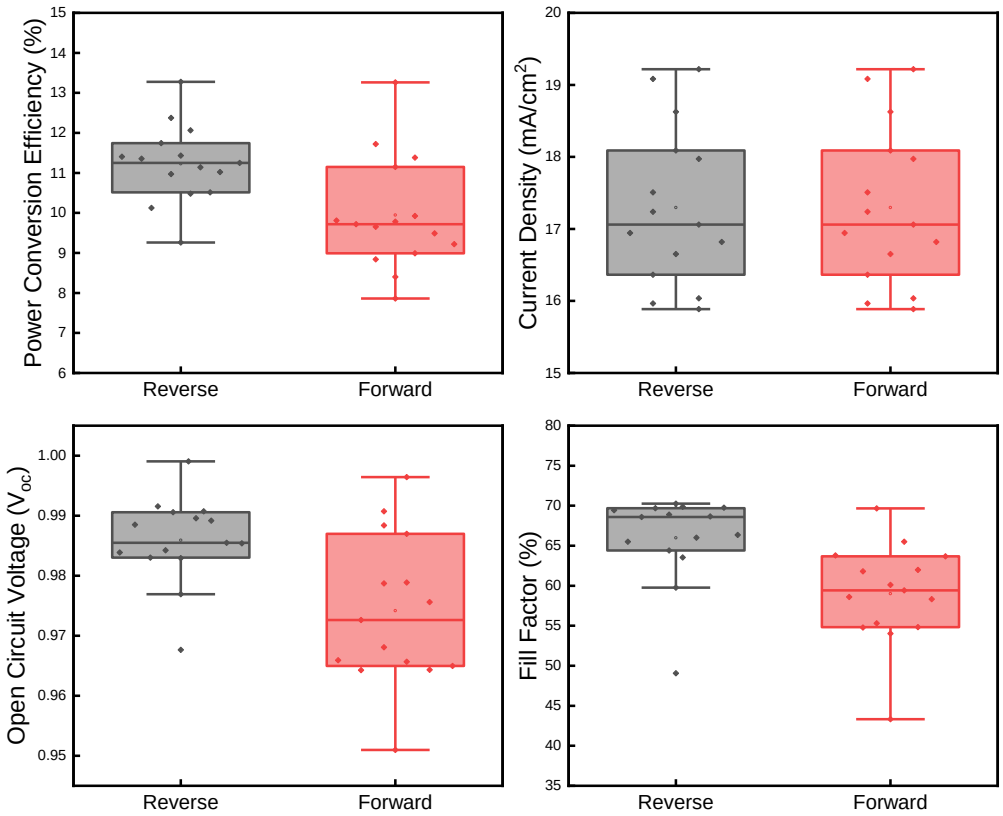

Figure 3. 25 Statistics of JV forward and reverse scan parameters of devices made by R2R slot die coating PEDOT:PSS and THF-MA based $MAPbI_3$.

top of the R2R slot die-coated PEDOT:PSS-$MAPbI_3$ using the standard procedure of optimised spin coated device. The devices were finished by thermally evaporating a silver top contact under vacuum. The JV statistics for this batch are shown in Figure 3. 25. The average PCE measured in the reverse scan was 11.2%, and in the forward scan it was 10%, indicating a small amount of hysteresis in the devices. It is worth noting that the average performance of the R2R slot die-coated THF-MA $MAPbI_3$ matched well with that of the ACN-MA $MAPbI_3$ made in section 3.4.2 (average PCE of 11.5%). The hero cell's PCE was measured to be 13.4%, with a current density of 19 mA/cm^2, an open-circuit voltage of 0.98V, and a fill factor of 71.5%. Due to hysteresis in the device, a more accurate understanding of its performance was obtained by measuring the stabilized PCE at the voltage of the maximum power point (0.73V). The stabilized measurement resulted in a PCE of 13.2%, as shown in Figure 3. 26.

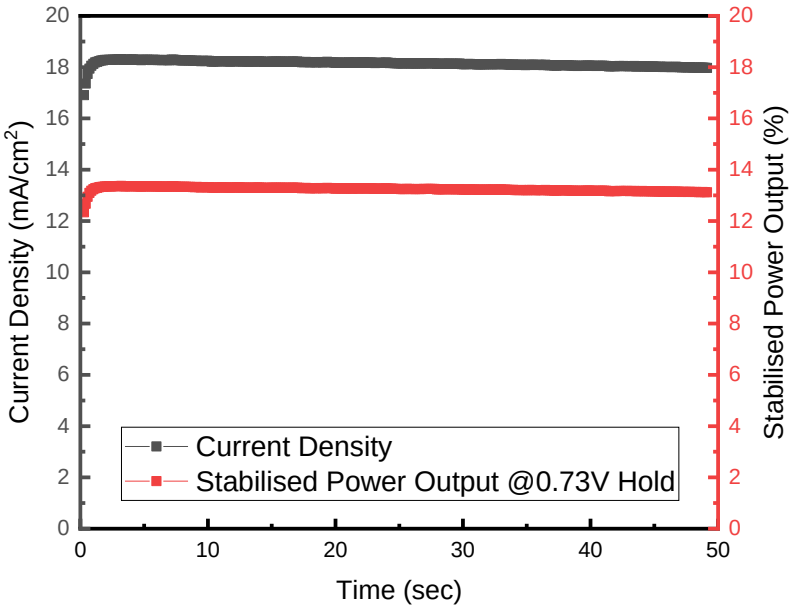

Figure 3. 26 Stabilised measurement of PSC with the R2R slot die coated PEDOT:PSS-$MAPbI_3$. For the coating of $MAPbI_3$ THF-MA based ink formulation was used.

3.9 Conclusion

This work represents a significant body of work to optimise all R2R slot-die coated layers in the PSCs except the electrode. All layers were coated at 1 m min^{-1}, implying that this method can be directly implemented on a continuous R2R line with no significant changes. Moreover, throughout this work, the use of highly toxic solvents was avoided. A PEDOT:PSS layer was optimised by diluting the formulation with IPA to improve the wettability on the surface.

Methyl ammine based ACN solvent system for $MAPbI_3$ dissolution is used as an alternative to toxic solvents like DMF and DMSO. High volatility of MA and ACN helped reduce the drying time and therefore were able to fully dry the films with low oven residence time of 1 min. Oven conditions was found to be critical for the performance and was characterised using XRD, SEM and XPS. A high WEL solvent blend of toluene, O-xylene and 2-methylanisole was used for PCBM coatings as an alternative to the conventionally used chlorobenzene. Finally, BCP layer thickness was optimised by varying WFT and was analysed by XPS. The hero device with all 4 layers R2R coated showed a stabilised PCE of 12% which is the highest value reported in our knowledge for the fully R2R coated PSCs except electrode.

Additionally, the optimisation done for the ACN-MA based solvent system of $MAPbI_3$ was leveraged to coat a less toxic THF-MA based ink formulation. The new formulation showed similar PCE on average basis showcasing the potential of THF for scale up purposes. Though this solvent system is more economical to use and is equally good when compared to ACN-MA solvent system, the THF-MA solvent was not used for the rest of the thesis due to difficulties in sourcing THF-MA of reliable quality from the commercial supplier.

Though relatively low performance was achieved compared to the state-of-the-art device made by conventional laboratory methods such as spin coating, this work demonstrated the potential of high speed continuous R2R manufacturing.

References

1. Best Research-Cell Efficiency Chart | Photovoltaic Research | NREL. https://www.nrel.gov/pv/cell-efficiency.html.

2. Mei, A. *et al.* A hole-conductor-free, fully printable mesoscopic perovskite solar cell with high stability. *Science (1979)* **345**, 295–298 (2014).

3. Patidar, R., Burkitt, D., Hooper, K., Richards, D. & Watson, T. Slot-die coating of perovskite solar cells: An overview. *Mater Today Commun* **22**, 100808 (2020).

4. Kim, Y. Y. *et al.* Gravure-Printed Flexible Perovskite Solar Cells: Toward Roll-to-Roll Manufacturing. *Advanced Science* **6**, 1802094 (2019).

5. Ulična, S. *et al.* Scalable Deposition of High-Efficiency Perovskite Solar Cells by Spray-Coating. *ACS Appl Energy Mater* **1**, 1853–1857 (2018).

6. Mathies, F. *et al.* Inkjet-Printed Triple Cation Perovskite Solar Cells. *ACS Appl Energy Mater* **1**, 1834–1839 (2018).

7. di Giacomo, F. *et al.* Up-scaling perovskite solar cell manufacturing from sheet-to-sheet to roll-to-roll: challenges and solutions. *https://doi.org/10.1117/12.2274438* **10363**, 21–28 (2017).

8. Dou, B. *et al.* Roll-to-Roll Printing of Perovskite Solar Cells. *ACS Energy Lett* **3**, 2558–2565 (2018).

9. Galagan, Y. *et al.* Roll-to-Roll Slot Die Coated Perovskite for Efficient Flexible Solar Cells. *Adv Energy Mater* **8**, 1–7 (2018).

10. Burkitt, D. *et al.* Meniscus Guide Slot-Die Coating For Roll-to-Roll Perovskite Solar Cells. *MRS Adv* **4**, 1399–1407 (2019).

11. Hwang, K. *et al.* Toward large scale roll-to-roll production of fully printed perovskite solar cells. *Advanced Materials* **27**, 1241–1247 (2015).

12. Jakubka, F. *et al.* Determining the coating speed limitations for organic photovoltaic inks. *Solar Energy Materials and Solar Cells* **109**, 120–125 (2013).

13. Heo, Y. J. *et al.* Printing-friendly sequential deposition via intra-additive approach for roll-to-roll process of perovskite solar cells. *Nano Energy* **41**, 443–451 (2017).

14. Kim, J. E. *et al.* Humidity-Tolerant Roll-to-Roll Fabrication of Perovskite Solar Cells via Polymer-Additive-Assisted Hot Slot Die Deposition (SI). *Adv Funct Mater* **29**, 1–9 (2019).

15. Angmo, D. *et al.* A Lab-to-Fab Study toward Roll-to-Roll Fabrication of Reproducible Perovskite Solar Cells under Ambient Room Conditions. *Cell Rep Phys Sci* **2**, 100293 (2021).

16. Troughton, J., Bryant, D., Baker, J. & Watson, T. Efficient, flexible & low temperature perovskite solar cells on industrially applicable metal foils. in *PVSAT-12* (2016).

17. Feleki, B. T., Bouwer, R. K. M., Zardetto, V., Wienk, M. M. & Janssen, R. A. J. p–i–n Perovskite Solar Cells on Steel Substrates. *ACS Appl Energy Mater* (2022) doi:10.1021/ACSAEM.2C00291.

18. Fahlteich, J., Fahland, M., Schönberger, W. & Schiller, N. Permeation barrier properties of thin oxide films on flexible polymer substrates. *Thin Solid Films* **517**, 3075–3080 (2009).

19. Galagan, Y. *et al.* Roll-to-Roll Slot–Die Coated Organic Photovoltaic (OPV) Modules with High Geometrical Fill Factors. *Energy Technology* **3**, 834–842 (2015).

20. Søndergaard, R., Hösel, M., Angmo, D., Larsen-Olsen, T. T. & Krebs, F. C. Roll-to-roll fabrication of polymer solar cells. *Materials Today* **15**, 36–49 (2012).

21. Lin, X. *et al.* Efficiency progress of inverted perovskite solar cells. *Energy Environ Sci* **13**, 3823–3847 (2020).

22. Jeng, J.-Y. *et al.* CH3NH3PbI3 Perovskite/Fullerene Planar-Heterojunction Hybrid Solar Cells. *Advanced Materials* **25**, 3727–3732 (2013).

23. Yuan, D. X. *et al.* A solution-processed bathocuproine cathode interfacial layer for high-performance bromine–iodine perovskite solar cells. *Physical Chemistry Chemical Physics* **17**, 26653–26658 (2015).

24. Chiang, S. E. *et al.* On the role of solution-processed bathocuproine in high-efficiency inverted perovskite solar cells. *Solar Energy* **218**, 142–149 (2021).

25. Sun, K. *et al.* Review on application of PEDOTs and PEDOT:PSS in energy conversion and storage devices. *Journal of Materials Science: Materials in Electronics* **26**, 4438–4462 (2015).

26. Han, W. *et al.* Recent Progress of Inverted Perovskite Solar Cells with a Modified PEDOT:PSS Hole Transport Layer. *ACS Appl Mater Interfaces* **12**, 49297–49322 (2020).

27. Xu, C., Liu, Z. & Lee, E.-C. High-performance metal oxide-free inverted perovskite solar cells using poly(bis(4-phenyl)(2,4,6-trimethylphenyl)amine) as the hole transport layer †. *J. Mater. Chem. C* **6**, 6975 (2018).

28. Remeika, M., Ono, L. K., Maeda, M., Hu, Z. & Qi, Y. High-throughput surface preparation for flexible slot die coated perovskite solar cells. *Org Electron* **54**, 72–79 (2018).

29. Lee, M. M., Teuscher, J., Miyasaka, T., Murakami, T. N. & Snaith, H. J. Efficient Hybrid Solar Cells Based on Meso-Superstructured Organometal Halide Perovskites. *Science (1979)* **338**, 643–647 (2012).

30. Lee, J. W., Kim, H. S. & Park, N. G. Lewis Acid-Base Adduct Approach for High Efficiency Perovskite Solar Cells. *Acc Chem Res* **49**, 311–319 (2016).

31. Mei, A. *et al.* A hole-conductor-free, fully printable mesoscopic perovskite solar cell with high stability. *Science (1979)* **345**, 295–298 (2014).

32. Lee, J. W. *et al.* Tuning Molecular Interactions for Highly Reproducible and Efficient Formamidinium Perovskite Solar Cells via Adduct Approach. *J Am Chem Soc* **140**, 6317–6324 (2018).

33. Jeon, N. J. *et al.* Solvent engineering for high-performance inorganic–organic hybrid perovskite solar cells. *Nature Materials 2014 13:9* **13**, 897–903 (2014).

34. Noel, N. K. *et al.* A low viscosity, low boiling point, clean solvent system for the rapid crystallisation of highly specular perovskite films. *Energy Environ Sci* **10**, 145–152 (2017).

35. Daniel Burkitt *et al.* Acetonitrile based single step slot-die compatible perovskite ink for flexible photovoltaics. *RSC Adv* **9**, 37415–37423 (2019).

36. Carvalho, M. S. & Kheshgi, H. S. Low-flow limit in slot coating: Theory and experiments. *AIChE Journal* **46**, 1907–1917 (2000).

37. Gao, L. L., Li, C. X., Li, C. J. & Yang, G. J. Large-area high-efficiency perovskite solar cells based on perovskite films dried by the multi-flow air knife method in air. *J Mater Chem A Mater* **5**, 1548–1557 (2017).

38. Kavadiya, S., Strzalka, J., Niedzwiedzki, D. M. & Biswas, P. Crystal reorientation in methylammonium lead iodide perovskite thin film with thermal annealing. *J Mater Chem A Mater* **7**, 12790–12799 (2019).

39. McGettrick, J. D. *et al.* Sources of Pb(0) artefacts during XPS analysis of lead halide perovskites. *Mater Lett* **251**, 98–101 (2019).

40. Guo, X. *et al.* Identification and characterization of the intermediate phase in hybrid organic–inorganic MAPbI3 perovskite. *Dalton Transactions* **45**, 3806–3813 (2016).

41. Quarti, C., Mosconi, E., Umari, P. & de Angelis, F. Chlorine Incorporation in the CH3NH3PbI3 Perovskite: Small Concentration, Big Effect. *Inorg Chem* **56**, 74–83 (2017).

42. Perthué, A. *et al.* New insights into polymer solar cells stability: The crucial role of PCBM oxidation. *J Mater Res* **33**, 1868–1878 (2018).

43. 'The Impact of Selective Solvents on the Structure and Function Evoluti' by Sheng Hu. https://trace.tennessee.edu/utk_gradthes/2425/.

44. MacHui, F., Langner, S., Zhu, X., Abbott, S. & Brabec, C. J. Determination of the P3HT:PCBM solubility parameters via a binary solvent gradient method: Impact of solubility on the photovoltaic performance. *Solar Energy Materials and Solar Cells* **100**, 138–146 (2012).

45. Chen, C. *et al.* Effect of BCP buffer layer on eliminating charge accumulation for high performance of inverted perovskite solar cells. *RSC Adv* **7**, 35819–35826 (2017).

46. Yuan, D. X. *et al.* A solution-processed bathocuproine cathode interfacial layer for high-performance bromine–iodine perovskite solar cells. *Physical Chemistry Chemical Physics* **17**, 26653–26658 (2015).

47. Wang, S. *et al.* Favorable electronic structure for organic solar cells induced by strong interaction at interface. *J Appl Phys* **114**, 183707 (2013).

48. Stojilovic, N. Why can't we see hydrogen in X-ray photoelectron spectroscopy? *J Chem Educ* **89**, 1331–1332 (2012).

49. Cameron, J. & Skabara, P. J. The damaging effects of the acidity in PEDOT:PSS on semiconductor device performance and solutions based on non-acidic alternatives. *Mater Horiz* **7**, 1759–1772 (2020).

50. Rivkin, B. *et al.* Effect of Ion Migration-Induced Electrode Degradation on the Operational Stability of Perovskite Solar Cells. *ACS Omega* **3**, 10042–10047 (2018).

51. Swartwout, R. *et al.* Predicting Low Toxicity and Scalable Solvent Systems for High-Speed Roll-to-Roll Perovskite Manufacturing. *Solar RRL* 2100567 (2021) doi:10.1002/SOLR.202100567.

52. Workplace exposure limits - COSHH. https://www.hse.gov.uk/coshh/basics/exposurelimits.htm.

53. 1910.1000 - Air contaminants. | Occupational Safety and Health Administration. https://www.osha.gov/laws-regs/regulations/standardnumber/1910/1910.1000.

54. Oliveira, H. M. de *et al.* Occupational risk assessment of paint industry workers. *Indian J Occup Environ Med* **15**, 52 (2011).

Chapter 4
Towards an efficient roll-to-roll printed hole transport layer for perovskite solar cells via slot die coating

4.1 Introduction

In the previous chapter, we focused on developing a scalable method for R2R deposition of P-I-N PSCs using four slot-die coated layers.[1] However, when compared to the performance of cutting-edge flexible PSCs manufactured using small-scale techniques in research laboratories, where it has been possible to achieve over 20% PCE, the performance was lower.[2] This was also consistent across all investigations that were published where at least the active layer was coated by R2R. All of these articles are summarised in Table 4. 1. At the time of writing this chapter, the highest PCE level obtained using R2R deposition is 13.2% for P-I-N PSCs, where as a minimum the perovskite layer was deposited using a R2R setup.

When considering the devices developed in chapter 3 its likely that the use of poly(3,4-ethylenedioxythiophene)-polystyrenesulfonate (PEDOT:PSS) as the hole transport layer (HTL) was one of the causes of decreased performance in the R2R coated devices due to interfacial recombination at the PEDOT:PSS/perovskite interface. PEDOT:PSS has been the most common, in fact, the only so far to be used as HTL for R2R deposition in P-I-N PSCs. This is because PEDOT:PSS has been effectively optimised in OPVs for R2R deposition and is comparably easier to deposit over a large area. Another reason for this is, it can be deposited with a high thickness on rougher substrates with little to no effect on device series resistance due to its conductive nature. Also, due to this possibility of coating higher thicknesses, the device's performance is not affected by a moderate thickness fluctuation throughout the coating's length and width. This is not the case with other HTLs which might require thickness in nanometres to be effective. However, the PEDOT:PSS interface with perovskite is not highly selective and results in low open circuit voltage(V_{oc}) due to higher non-radiative recombination compared to other HTLs like Spiro-OmeTAD, Poly[bis(4-phenyl)(2,4,6-

trimethylphenyl)amine (PTAA) and poly(3-hexylthiophene-2,5-diyl) (P3HT).[3] This can also be inferred from the data in Table 4. 1, which shows that V_{oc} in P-I-N-based architectures is lower

Table 4. 1 Table showing performance of reported work where in at least layers upto perovskite is R2R

Stack	Substrate	Deposition	HTL	Stabilized PCE	PCE	J_{sc}	V_{oc}	FF	Ref
N-I-P	PET-ITO	Slot Die R2R	Spiro-OMeTAD	13.5	15.2	20.7	1.03	71.5	[4]
N-I-P	PET-ITO	Gravure R2R	P3HT	-	9.7	17.2	0.89	63.1	[5]
P-I-N	PET-ITO	Slot Die R2R	PEDOT:PSS	-	11.16	17.39	0.99	64.82	[6]
P-I-N	PET-Silver Nanowire	Slot Die R2R	PEDOT:PSS	10.5	11	-	-	-	[7]
N-I-P	PET-ITO	Slot Die R2R	Spiro-OMeTAD	12.49	13.41	19.81	0.95	70	[8]
N-I-P		Slot Die R2R	Spiro-OMeTAD	12.6					[9]
P-I-N	PET-ITO	Slot Die R2R	PEDOT:PSS		11.67	21.75	0.98	54.76	[10]
N-I-P	PEN-ITO	Microgravure and Slot Die R2R	Spiro-OMeTAD	9.80	10.57	16.82	0.98	63.99	[11]
N-I-P	Flexible Glass-IZO	Slot Die R2R	Spiro-OMeTAD		14.12	21.24	1.07	61.7	[12]
N-I-P	PET-ITO	Slot Die R2R	P3HT	-	11	19.6	1.04	53.8	[13]
P-I-N	PET-ITO	Slot Die R2R	PEDOT:PSS	13.14	13.27	19.22	0.98	70.26	[14]
P-I-N	PET-ITO	Slot Die R2R	PEDOT:PSS	12	12	-	-	-	[1]

overall than N-I-P-based architectures. It should be noted that PEDOT:PSS is used as the HTL in every P-I-N design stated in Table 4. 1. In this study, we explore an alternative HTL, PTAA that might overcome this loss and show its deposition for the very first time using R2R slot die-coating. PTAA was initially employed in organic light-emitting diodes as a hole injection layer.[15] Because PTAA is also air-stable, it can be coated in an ambient condition, which could result in a low degree of fabrication complexity.[16] Additionally, PTAA exhibits a high resistance to mechanical stress, making it appropriate for flexible PSCs.[17] Further, PTAA highest occupied molecular orbital (HOMO) is closer to $MAPbI_3$ compared to PEDOT:PSS resulting in in better charge extraction. [3] PTAA when utilised as a HTL in P-I-N architecture, is often a very thin layer, in the range of 10-20 nm, in order to eliminate any series resistance losses and maximise performance when it is not doped.[18] The challenge in achieving this deposition at scale

emerges from its application to the indium tin oxide (ITO) layer on PET substrate. ITO applied to a plastic film such as PET can produce a more uneven texture than ITO applied to glass because of the structural and morphological changes created by the polymer substrates during crystal formation during sputtering.[19] Because of the ITO roughness, deposition of ultra thin PTAA yields poor results due to a poor shunt barrier leading to inferior PSCs. A method to overcome this is to boost the conductivity of PTAA by doping allowing a thicker layer however this has been shown to result in less stable PSCs due to ion migration.[20] In order to solve this issue we have employed a bilayer architecture; we first deposited a layer of PEDOT:PSS, which serves as a buffer layer, and then we proceeded to deposit a thin layer of PTAA on top of the PEDOT:PSS. This results in a significant improvement across all performance characteristics of the device, which ultimately leads to improved performance of R2R coated PSCs.

4.2 Experimental Methods

The fabrication of PTAA-based rigid P-I-N PSCs is similar to that of P-I-N-based PSCs in the previous chapter, except that PTAA is substituted for PEDOT:PSS. The optimised concentration used for PTAA deposition is 2.5 mg ml^{-1} in toluene for spin coated devices. PTAA is directly coated on cleaned and plasma treated ITO-glass substrate and spun at 4000RPM speed for 30 sec followed by drying at 100℃ for 10 mins. 0.5M $MAPbI_3$ ink was prepared by mixing 0.5M MAI and 0.53M PbI_2 with 6% Pb excess in acetonitrile. The precursors were then bubbled with methyl amine gas until a transparent pale yellow coloured liquid appeared. The as prepared $MAPbI_3$ ink was spun on the PTAA layer with 2000RPM speed followed by drying for 10 mins at 110℃. This was followed by deposition of the PCBM (40 mg ml^{-1} in chlorobenzene) layer at 3000 RPM for 30 seconds. No drying was required for PCBM films. BCP (0.5 mg ml^{-1} in ethanol) was deposited at 7000 RPM for 10sec. 100 nm of Ag electrode was thermally evaporated post deposition of BCP to complete the device architecture.

For the flexible PSCs prepared by spin coating, a thin layer of PEDOT:PSS was inserted in between PTAA and ITO-PET. This was done by diluting the PEDOT:PSS in 1:6 ratio by IPA. The diluted PEDOT:PSS was then spun with a 2-step spin process, 1000RPM for 5 sec and 5000RPM for 15 sec. The films were then dried at 120℃ for 10 mins. To complete the device the

remaining layer, PTAA-$MAPbI_3$-PCBM-BCP-Ag were coated following the same procedure as optimised for glass based devices.

For R2R slot die coating of PEDOT:PSS, the ink was diluted in 1:6 ratio using IPA. An optimised thickness of 8 µm wet film thickness was coated directly on top of ITO-PET. A gap of approximately 350 µm between the substrate and slot die head was maintained including 250 µm tab width meniscus guide. 90 mm shim was used to define the coating width. The coated wet film of PEDOT:PSS was then dried with 2 inline convection ovens set at 120°C and 140°C respectively. The dried film was collected at the winder and was rewound back to coat PTAA. For PTAA coating a solution, 1 mg ml^{-1} PTAA in toluene was prepared. An optimised 10 µm wet film was coated with 90mm width. The slot die and the substrate gap was kept at approximately 1500 µm including 1000 µm tab width of the meniscus guide used. The wet film of PTAA was dried in two inline convection ovens both set at 120°C. The coated films of bilayer HTL were then taken offline and diced into 28x28mm^2 pieces. To complete the device, $MAPbI_3$, PCBM, BCP and Ag was coated on top of the R2R coated PEDOT:PSS-PTAA following the same spin coating procedure of rigid devices described in the first paragraph.

For S2S slot die coating the same coating parameters were used as R2R except the drying was done on a hot plate with the same conditions as used for drying the spin coated films.

4.3 Optimisation of PTAA based P-I-N PSCs via spin coating on glass substrates

Previous studies on P-I-N PSCs deposition using slot-die coating have predominantly employed PEDOT:PSS as the hole transport layer (HTL). As described in the preceding section, it is prudent to replace PEDOT:PSS cells with PTAA cells in order to increase efficiency. Since the ultimate objective of the project is to use R2R deposition, it is crucial to construct the glass reference device for comparing R2R-deposited PSCs using a PTAA HTL. In establishing the improvement over PEDOT:PSS, a comparison study between the two was necessary. In these preliminary studies spin-coating was used to compare PEDOT:PSS and PTAA before exploring scale-up potential. Therefore, using spin coating, optimisation was carried out on the cell architecture depicted in Figure 4. 1.

The crystallization kinetics and growth of $MAPbI_3$ is likely to be very different on PTAA versus PEDOT:PSS due to their different surface properties. PTAA is a hydrophobic layer and PEDOT:PSS is a hydrophilic layer and will influence the perovskite growth differently. In

chapter 3 we doped 20ulml^{-1} of HCl in $MAPbI_3$ to improve the grain size and crystallinity and it is the intention of this work to continue exploring this composition. The effect of HCl (aq) was studied on ACN-MA based perovskite precursor ink.[21] The results showed the effect of

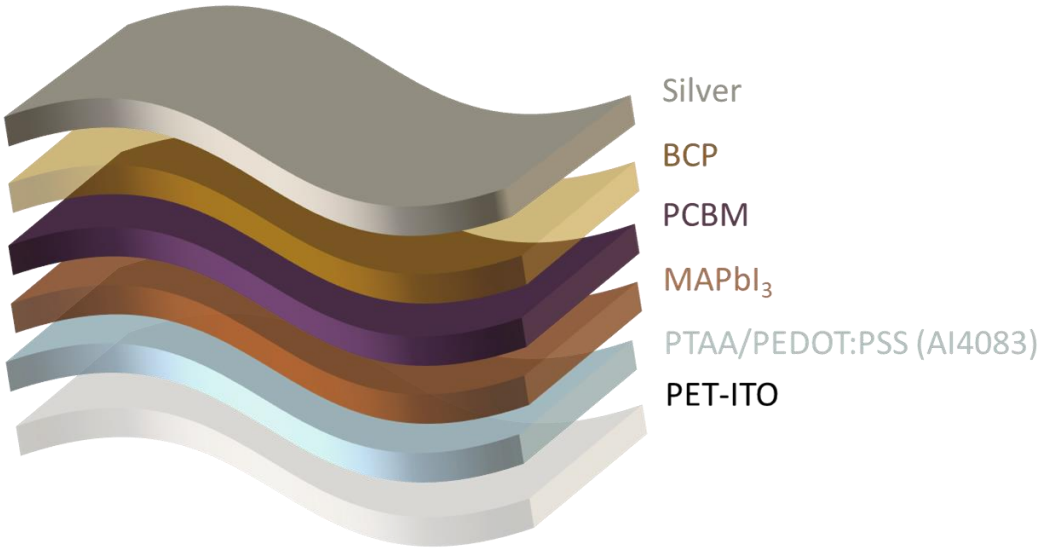

Figure 4. 1 Schematic of P-I-N PSCs fabricated on glass.

HCl on grain growth. Chloride additives are also known for trap passivation and accelerated charge transport and reduced recombination.[22] This approach was compared on both PEDOT:PSS and PTAA to identify if a similar influence occurred. Using scanning electron microscopy (SEM), we first examined the impact HCl addition had on the hydrophobic surface of PTAA. We varied the HCl concentration in 0.5M of $MAPbI_3$ from 10 µl ml^{-1} to 30 µl ml^{-1}. Figure 4. 2 shows a comparison of the morphology of spin-coated films of $MAPbI_3$ on PTAA and PEDOT:PSS films with varying concentrations of HCl. When compared to that of PEDOT:PSS, the morphology on PTAA exhibits striking differences. In both samples, increasing the HCl content results in an increase in the crystal size. With PEDOT:PSS, over 20 µl ml^{-1} HCL, discontinuities between perovskite crystals begin to appear. Chloride additives are known to slow down the crystallisation and formation of nuclei, thus facilitating crystal growth.[23]. Extremely slow crystallisation with higher chloride content may lead to the formation of nuclei at larger distances leading to voids and cracks with big crystals. Interestingly these voids start appearing at a lower HCl concentration on PTAA. The reason for this is unclear, however, it could be because of the hydrophobic nature of PTAA, which has been reported to promote

the growth of larger crystals.[18] Of the films deposited on PTAA, at 10 µl ml^{-1} HCl the growth of large crystal leads to voids in the film.

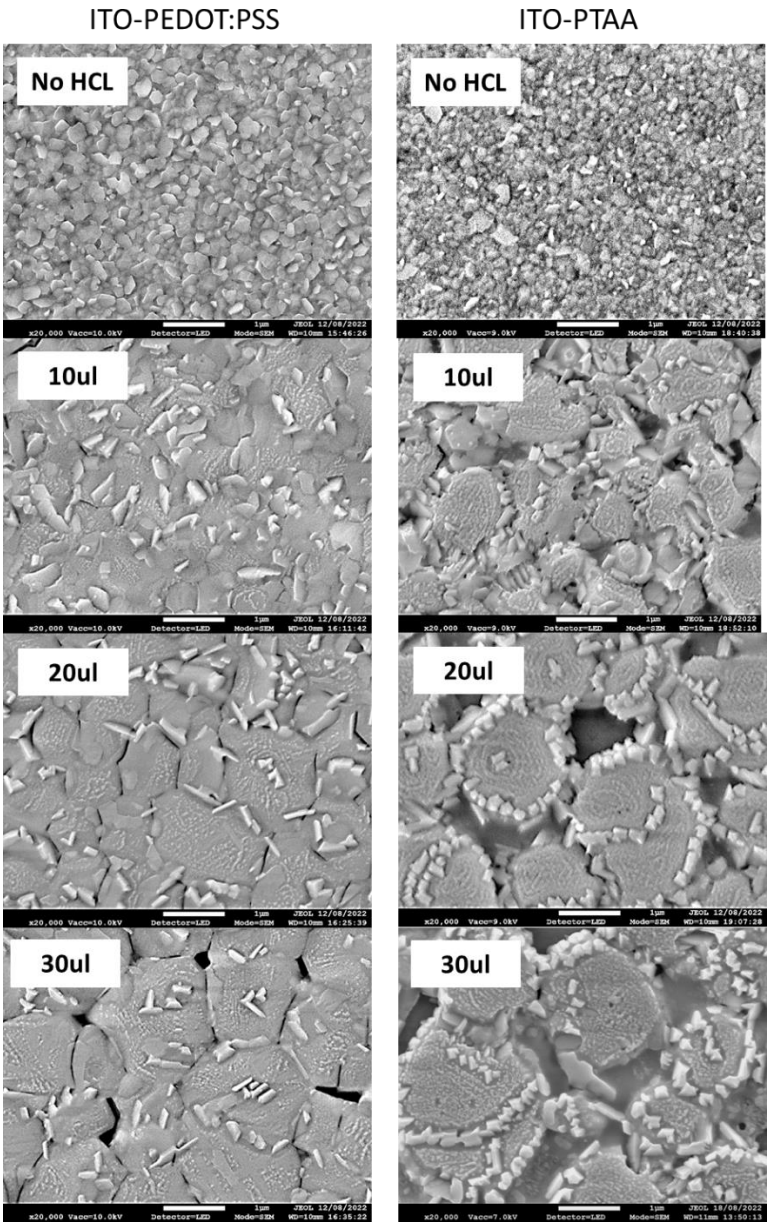

Figure 4. 2 SEM images of $MAPbI_3$ films with 0, 10, 20, 30ulml^{-1} HCl concentration spin-coated on top of ITO-PEDOT:PSS and ITO-PTAA

This result helped narrow the range for optimisation of HCl concentration on PTAA. To find out the optimal concentration for HCL it was varied from 3 µl ml^{-1} to 11 µl ml^{-1}. $MAPbI_3$ films with different HCl concentrations were coated on PTAA. The devices were then completed keeping the remaining layers the same. The performance statistics of the batch are presented in Figure 4. 3. The impact of chloride addition can be seen predominantly on J_{sc}, which steadily

rises as the concentration of HCl in the perovskite increases before beginning to fall and reaching a peak at 7µl of HCl. The increase in J_{sc} is a consequence of bigger crystal sizes and highly crystalline films.[21] Grain size improvement led to a reduction in grain boundaries, which in turn suppressed non-radiative recombination. Consequently, this led to an increase in FF and V_{oc}. Even though the overall performance was poor, the HCl optimization demonstrated a trend with the best PSCs at 7 µl ml^{-1}. This concentration will be used as standard for the remaining experiments in the chapter.

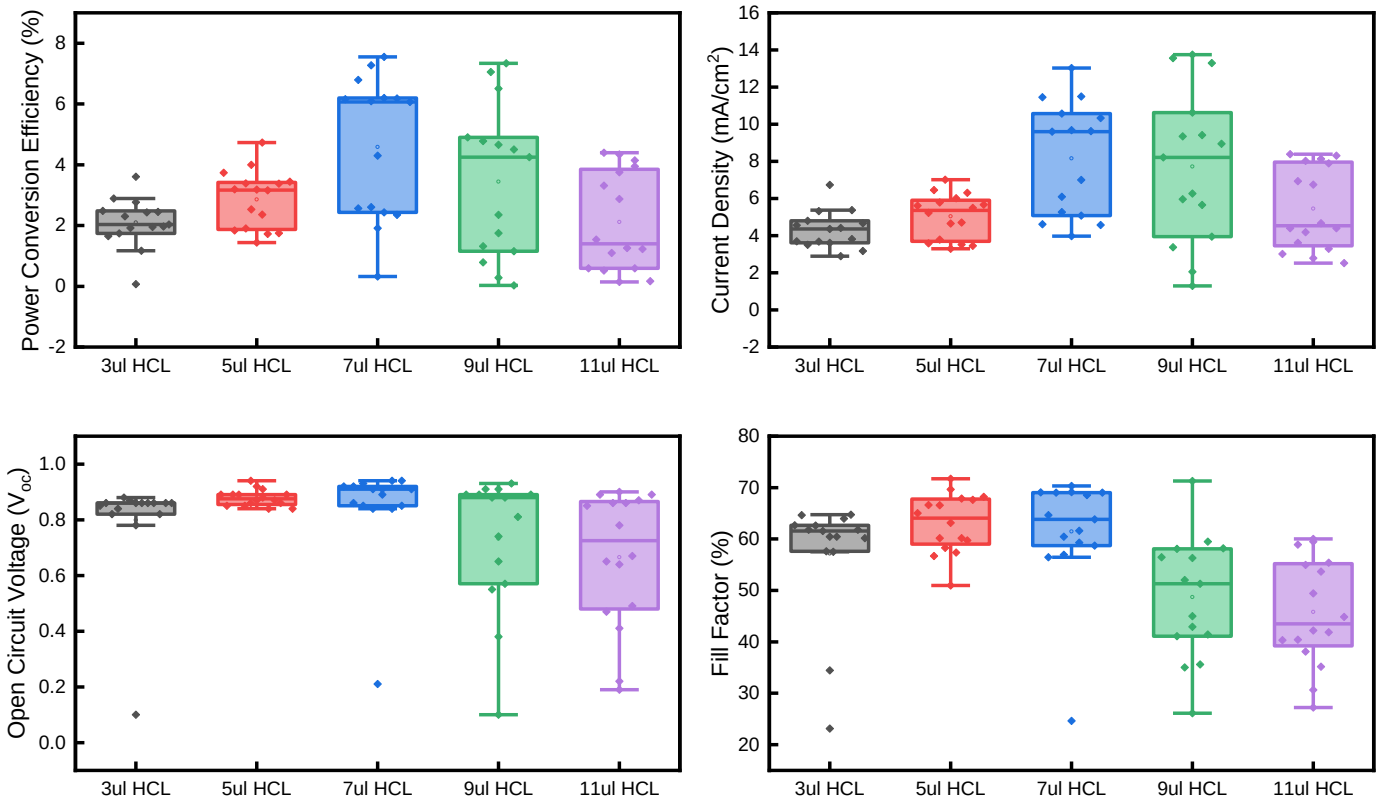

Figure 4. 3 a)Statistics of JV forward scan parameters of devices made with varying concentration of HCL from 3 µl ml^{-1} to 7 µl ml^{-1} using PTAA as HTL. Except for the top silver electrode, which was thermally evaporated, all layers were spin coated.

To deposit PTAA on the first batch of devices, a concentration of 2.5 mg ml^{-1} dissolved in toluene was used. This value was derived after reading many pieces of relevant research.[24,25] It is possible that other laboratories have uniquely optimised conditions for the deposition and characterisation of any given layer within the PSCs stack. These conditions may differ from lab to lab. Both the quality of PTAA and the solvent that is used to dissolve the PTAA could be different because of different suppliers or deposition conditions. Hence, to locate

the optimal PTAA thickness, we experimented with the concentration in steps of 0.5 mg ml^{-1}, ranging from 1 mg ml^{-1} all the way up to 3 mg ml^{-1}. Here the concentration is used as a proxy for layer thickness. The statistical data for this experiment is presented in Figure 4. 4. The data

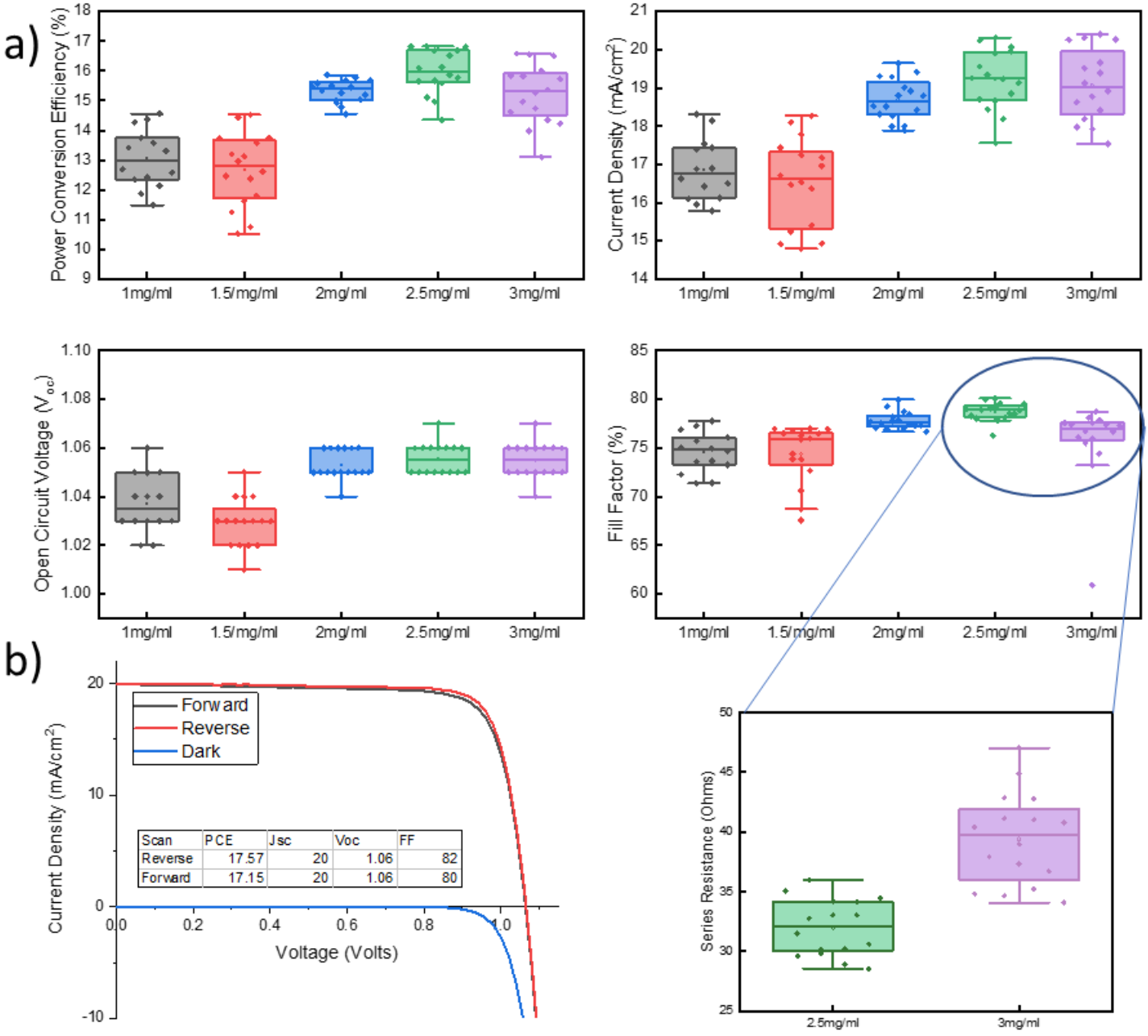

Figure 4. 4 a)Statistics of JV forward scan parameters of devices made with varying concentration of PTAA from 1mg ml^{-1} to 3 mg ml^{-1}l b) Light and dark JV of best performing cell measured by masking 0.09cm^2 corresponding to 2.5 mg ml^{-1}of PTAA concentration.

illustrates a trend in the performance of PSCs with increasing concentrations of PTAA, with the optimum value being at 2.5 mg ml^{-1}. As the concentration of PTAA was increased, an

improvement in J_{sc} and FF was observed. This is because a low concentration of PTAA would likely form a thin layer of PTAA resulting in poor ITO coverage. Any exposed ITO leading to direct contact with the perovskite will cause undesirable current pathways leading to low FF. Upon further increase of the concentration, fill factor reaches its maximum at a concentration of 2.5 mg ml^{-1} and then begins to decrease beyond this point. This is attributed to the reason that a thick layer of PTAA (as a result of higher concentration of PTAA) begins to dominate the device series resistance, which in turn causes the FF to decrease. As can be seen in the series resistance box plot (Figure 4.4) comparing the two, the average series resistance increased to 39 ohms from 33 ohms when the concentration was 2.5 mg ml^{-1}. In the forward scan, the champion device showed an efficiency of 17.57% with 20 $mAcm^{-2}$ J_{sc}, 1.06 V_{oc}, and 82% fill factor.♦ Therefore, 2.5 mg ml^{-1} of PTAA concentration will be used as a standard for spin coated devices. The thickness of a film made from 2.5 mg ml^{-1} of PTAA was hard to accurately measure using a profilometer. However, a film made from 5 mg ml^{-1} of PTAA was found to be about 30-35 nm thick when coated onto glass using a profilometer. As a result, the change in concentration of the PTAA ink will be used as a way to refer the change in the thickness of the film on a spin-coated device for the rest of the work.

4.3.1 PEDOT:PSS Vs PTAA

Following the complete optimisation of PTAA based PSCs, it is essential to evaluate it in comparison to the PEDOT:PSS HTL in order to ascertain the benefits of switching and in order to gain an understanding of the effect that it has on the various parameters of PSCs. To accomplish this, we examined the differences between the two HTLs individually optimised stacks and carried out a number of electrical and optical characterisation measurements. In the previous section we compared the effect of these two HTLs on perovskite film morphology with an HCL additive. Since both HTLs are optimised at a different HCl concentrations, individually optimised HCl concentration was used to make a fair comparison between the two HTLs. For PTAA this concentration was 7 µl ml^{-1} of $MAPbI_3$ precursor ink while for PEDOT:PSS it was 20 µl ml^{-1}. The device statistics between the two different HTLs is presented in Figure 4. 5. The superiority of PTAA is clearly seen in all parameters except FF. J_{sc} and V_{oc}

♦ The discrepancy in performance between the previous and current batches, despite using the same thickness of PTAA, could potentially be attributed to the alteration in laboratory conditions when the cells were fabricated outside of a glove box. Similar variations in performance may also be observed in other experiments as a result.

show a significant improvement over PEDOT:PSS HTL. This is in line with the observations made in literature.[26] The champion PEDOT:PSS device in forward scan had a PCE of 14.16% while that of PTAA reached 16.25%. The drop in fill factor is attributed to poor wettability of perovskite on PTAA due to its hydrophobic nature. This will be discussed in detail in the next chapter. To understand the role of PTAA in improving performance we first examined the quality of the perovskite layer on both PEDOT:PSS and PTAA. This can be done using various optical and electrical measurements. We first compared the absorption of the $MAPbI_3$ layer

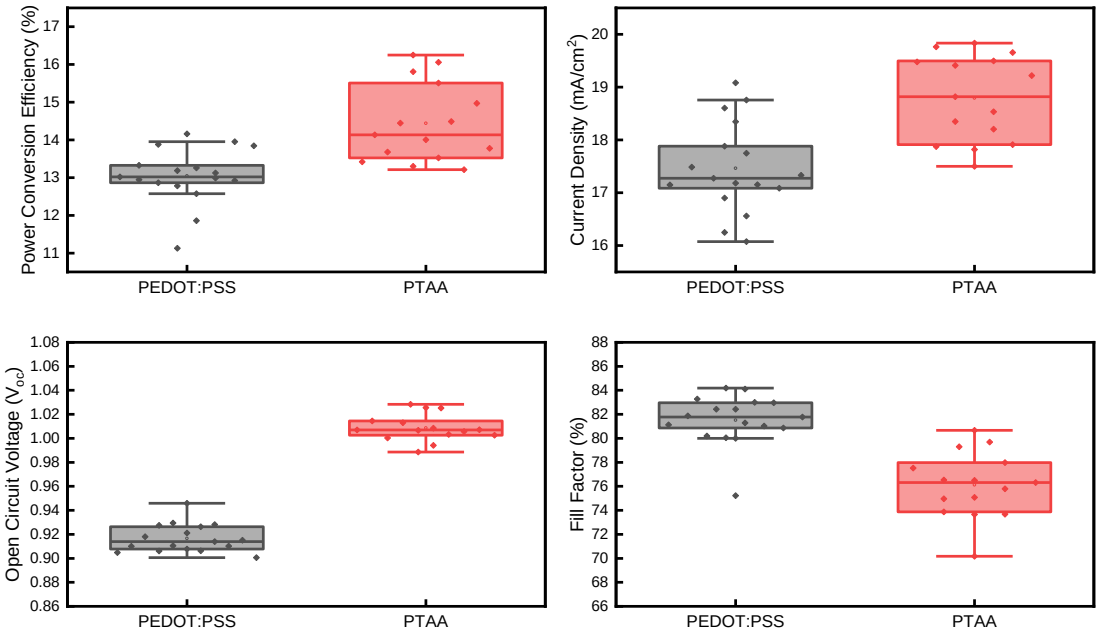

Figure 4. 5 Statistics of JV forward scan parameters of devices comparing PTAA with PEDOT:PSS.

deposited on PTAA and PEDOT:PSS. As can be seen in Figure 4. 6a, the films deposited on PTAA show higher absorption across all wavelengths. This is likely due to change in the properties of $MAPbI_3$ films itself.[27] Increased absorption can result in higher current, which may explain the observed improvement in J_{sc} in PTAA-based devices. A similar trend was also observed in the photoluminescence (PL) measurement represented in Figure 4. 6b. The emission intensity of $MAPbI_3$ coated on glass ITO is plotted against when its coated-on top of PEDOT:PSS and PTAA. $MAPbI_3$ films show significantly higher emission on PTAA, implying the formation of low defect films on PTAA, leading to higher V_{oc} as observed in JV statistics. When the perovskite is coated on top of a charge extraction layer, a phenomenon known as PL quenching occurs where the charge generated in perovskite layer gets extracted to the contact layer. The intensity of the emission decreases as the charge generated in $MAPbI_3$ is

extracted by the HTL. This drop in intensity can be used to determine the efficacy of the HTL charge extraction.[28] In spite of the fact that PTAA performed better in the device stack, we observed less PL quenching with PTAA in comparison to PEDOT:PSS. This is because PL quenching by itself is insufficient to draw any conclusions regarding the charge extraction property of HTLs. Since surface properties of HTLs can influence the growth of the perovskite layer (showed earlier when comparing PEDOT:PSS and PTAA with different HCl), it can

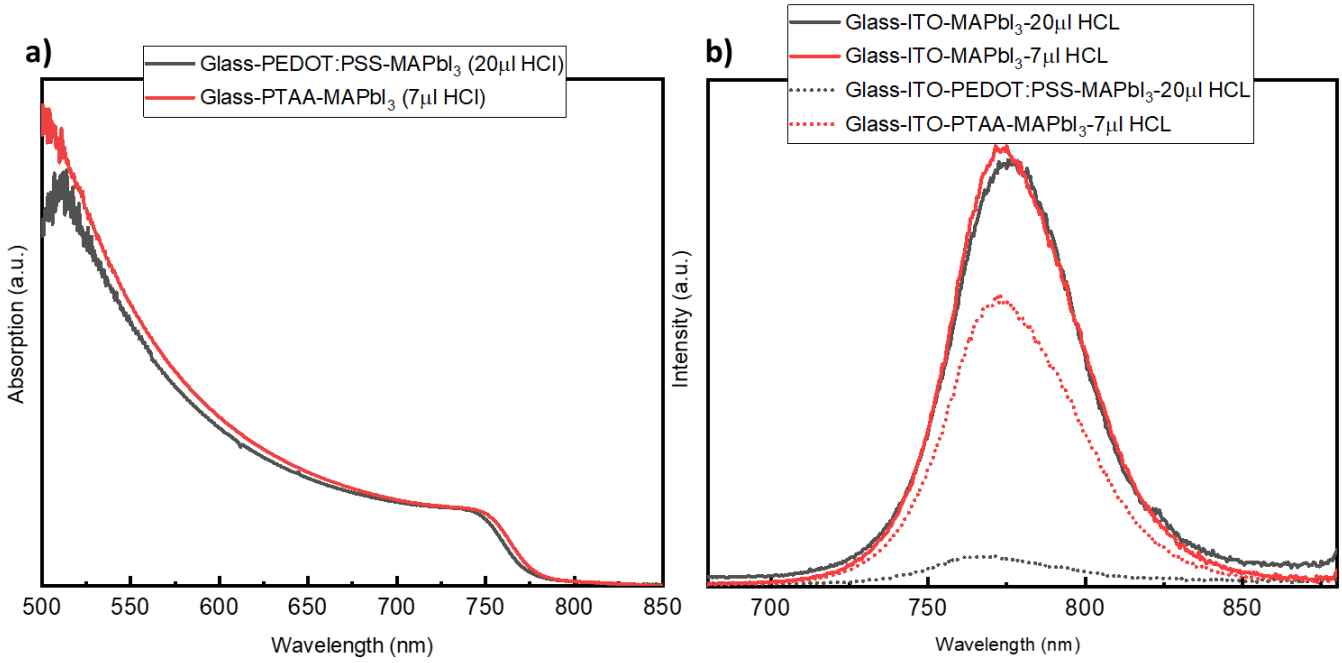

Figure 4. 6 a) UV-Vis absorption plot comparing $MAPbI_3$ absorption when coated on PTAA and PEDOT:PSS b) steady state PL emission of $MAPbI_3$ films on PTAA vs PEDOT:PSS

influence the quality and thus defects in the perovskite layer. Having higher quality of perovskite layer on HTLs will also give higher emission due to suppression of non-radiative defects in the films. This would therefore not give a complete picture about HTLs charge extraction capabilities. Furthermore, PL quenching can occur due to interfacial traps and could explain the reason for low performance of PEDOT:PSS films with high PL quenching. [28]

To understand the PTAA charge extraction capabilities we measured external quantum efficiency (EQE) of perovskite solar cells with both HTLs. The resultant spectra are presented in Figure 4. 7. Because of the suppression of non-radiative recombination at the HTL/perovskite interface and the formation of high quality perovskite layer, the external quantum efficiency across all wavelengths is significantly reduced. Additionally, there is a slight shift in the edge at high wavelength, which is attributed to a modification in the

perovskite layer as a result of PTAA. This demonstrates that for high efficiency PSCs, PTAA is a significantly more effective HTL than PEDOT:PSS due to less interfacial recombination as well as defect suppression in $MAPbI_3$ films.

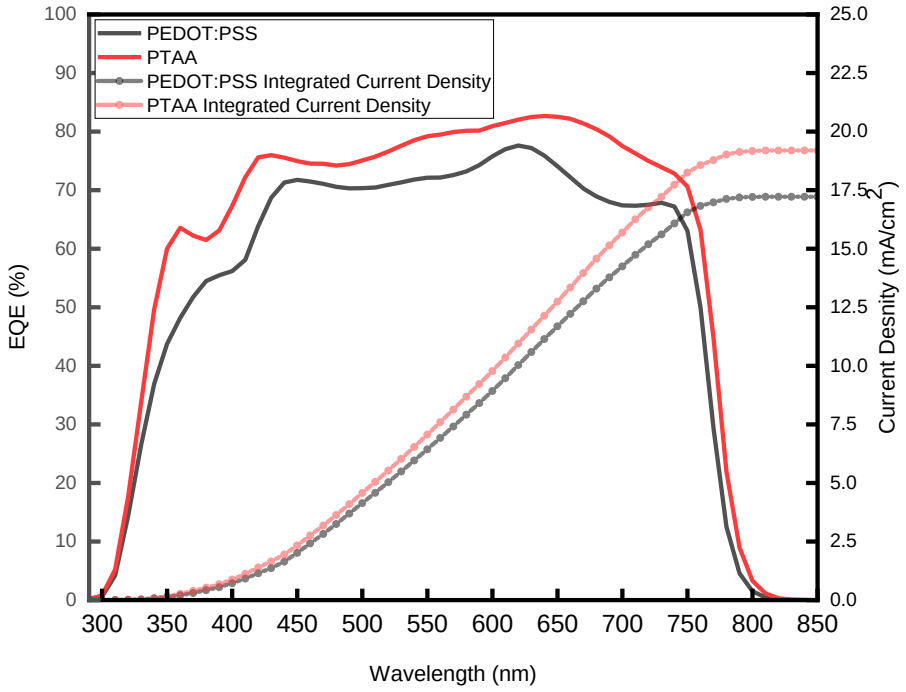

Figure 4. 7 EQE spectra of PSCs with PTAA and PEDOT:PSS as HTL.

4.4 PTAA on flexible P-I-N PSCs

Following the optimisation of PTAA for glass-based devices and establishing its benefits over PEDOT:PSS, its efficacy on flexible PSCs was explored. To achieve this, the same recipe as optimised on glass-based device was used to fabricate the cells on flexible PET-ITO substrate using spin coating. At the same time, we also used a S2S slot die coating technique to deposit PTAA of varying concentrations on PET-ITO to begin the scale up process. The spin-coated flexible devices, to our surprise, did not work, and the majority of them were below 1% PCE. Comparison of JV statistics between the spin coated PTAA and the slot die coated PTAA is shown in Figure 4. 8. SD is the acronym used for slot die coating.

This was a significant disappointment. Nevertheless, slot die coated PTAA did work, but only at higher concentrations, indicating the requirement for a thicker coating for PSCs to work. The same 2.5 mg ml^{-1} concentration of PTAA as optimised for glass-based devices was used to produce the poor performing spin coated flexible ITO-PET devices. This led to high shunts and hence poor performance for spin coated PTAA layer on flexible PSCs. Because the change

of the substrate is the only variable in the transfer from glass to flexible device its likely that the surface morphology of ITO on PET is different than on glass and could be of different roughness. High roughness of ITO would also explain the improvement in performance of slot die coated films as the thickness is increased by increasing the concentration of PTAA.

All the functioning devices had a high series resistance of greater than 125 ohms due to the increased thickness that was required for them to function properly. This had an impact on the overall performance of the PSCs, reducing the maximum efficiency that could be achieved to 12.2%. This is lower than what was achieved with PEDOT:PSS in the previous chapter suggesting that there is an issue in gaining the advantage of using PTAA when a flexible PET-ITO substrate is employed. This was investigated further.

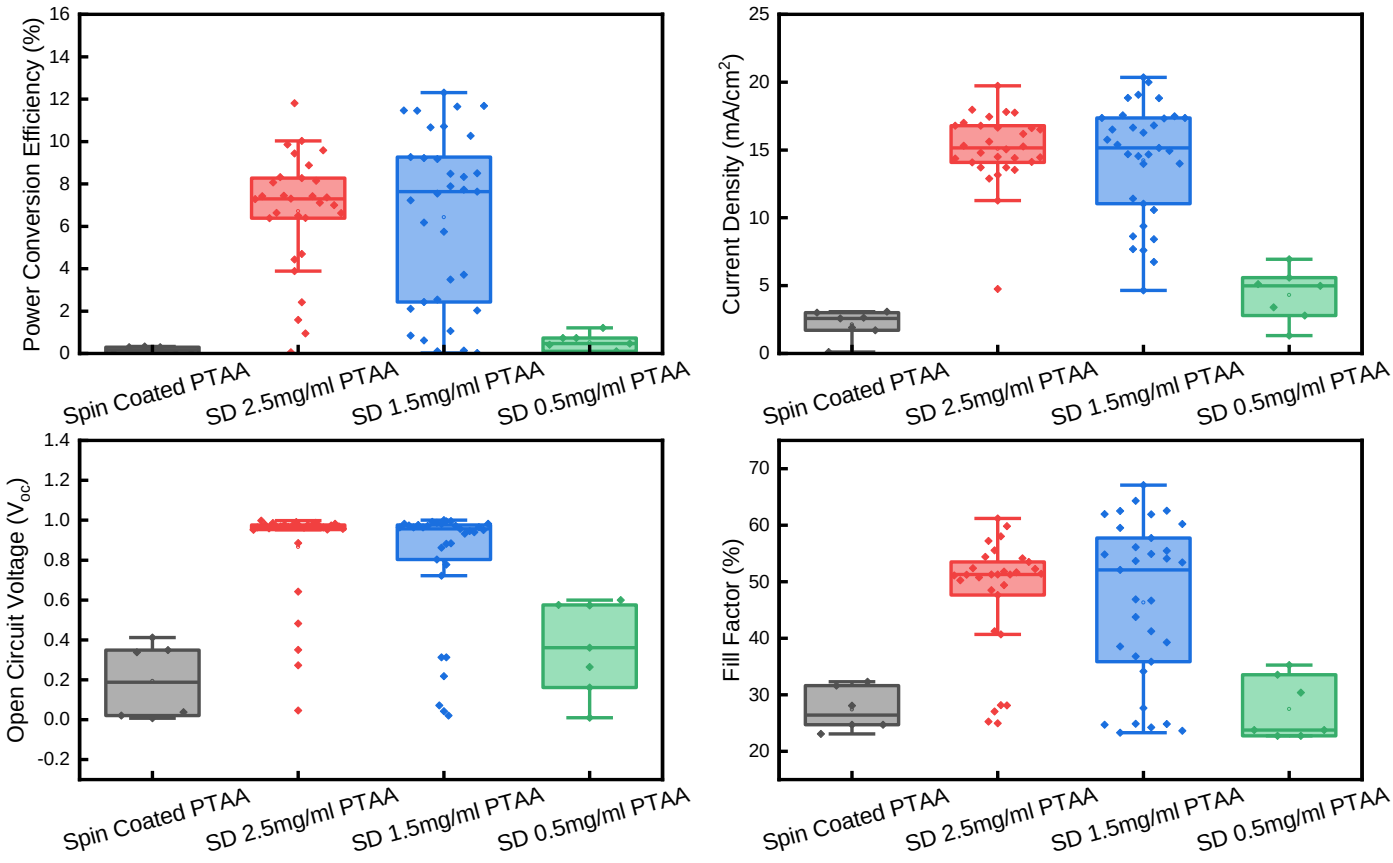

Figure 4. 8 Statistics of JV forward scan parameters of devices made via slot die coating 0.5 mg ml^{-1}, 1.5 mg ml^{-1} and 2.5 mg ml^{-1} PTAA and compared with spin coated PTAA. Slot die coating of PTAA was done using 1000 µm meniscus guide. All the films were coated at a constant wet film thickness of 5 µm. Substrate to slot die head was kept at 300 µm. For spin coating on flexible device 2.5 mg ml^{-1} PTAA was used as optimised for glass based devices in section 4.3

To understand the surface properties of coated PTAA on ITO the coated films were cut into 25x25 mm^2 pieces to characterise using mapping XPS spectroscopy. In order to gather

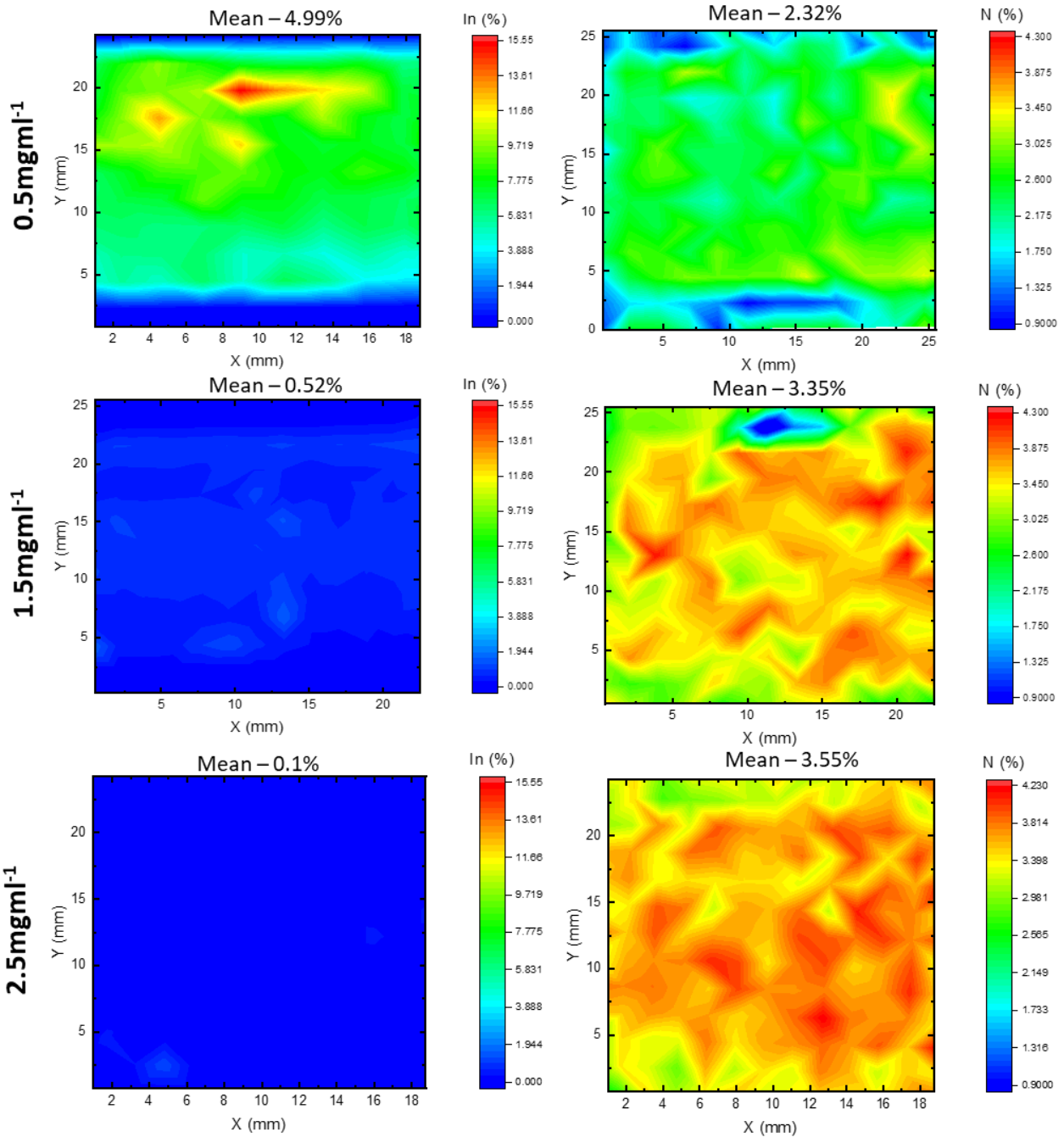

Figure 4. 9 XPS map of In and N atomic percentage on three different layers of slot die coated PTAA using 0.5 mg ml^{-1}, 1.5 mg ml^{-1} and 2.5 mg ml^{-1} concentration.

information regarding the coating's homogeneity, rather than obtaining a spectrum from a single point, an area of roughly 20 millimetres squared was mapped using XPS. XPS has the ability to measure the atomic proportion of elements both on the surface and in the bulk

down to a depth of 10 nm. In order to obtain these maps, the sample stage was moved at intervals of 2 mm while an XPS spectrum was recorded. Each recorded spectrum was then analysed separately at each location to determine the atomic percentages of the constituent elements. The collected data was plotted using a 2D intensity map, and the resultant maps are presented in Figure 4. 9

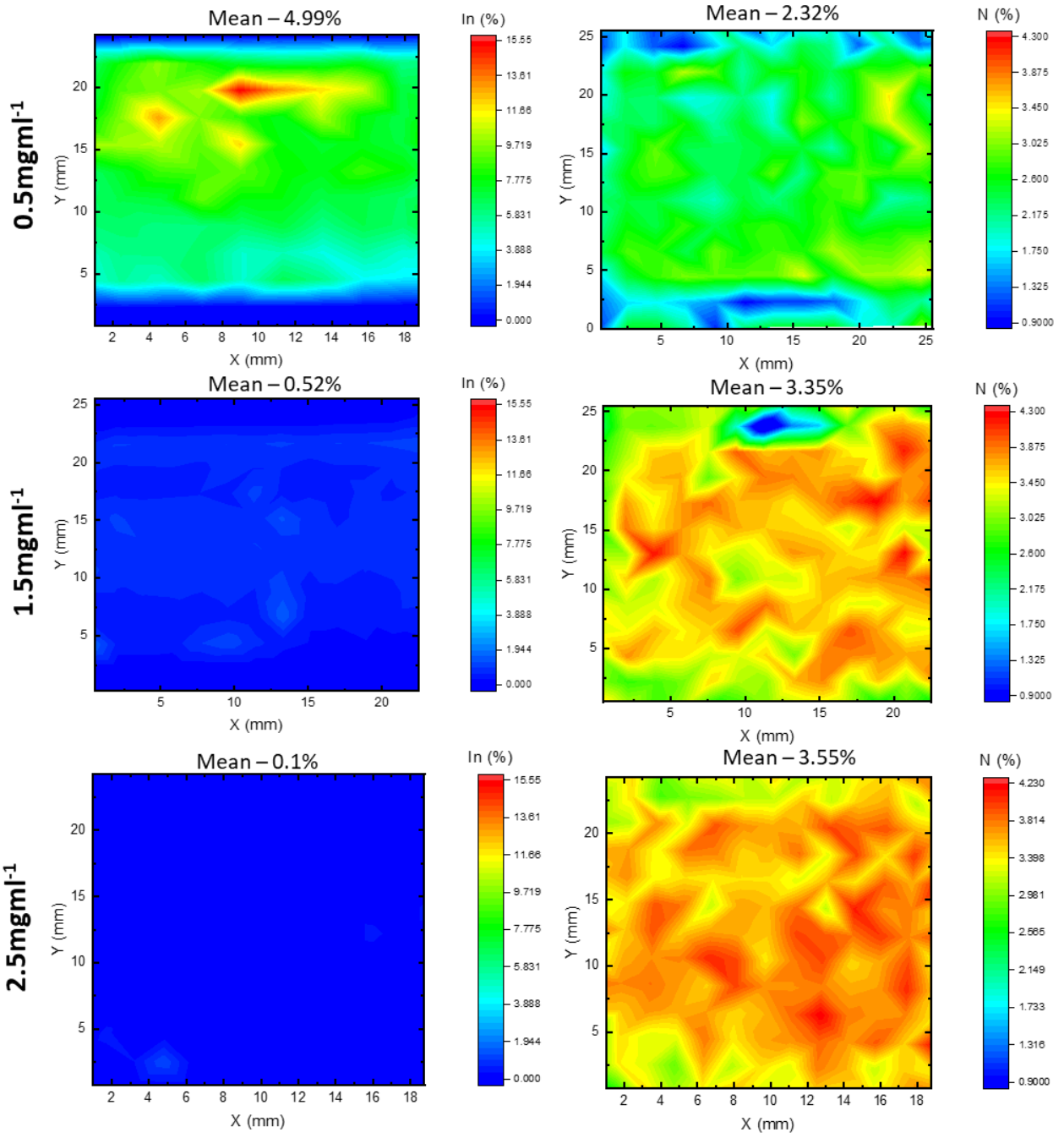

. Since PTAA ($(C_{21}H_{19}N)_n$) is the only source of N atoms on the substrate, the existence of PTAA is confirmed by the nitrogen% (N) detected on the surface of all three slot die coated films.

Quantifying nitrogen at different sites on the same substrate could provide information about the distribution of PTAA over the substrate and thus the homogeneity of the PTAA layer. In an ideal situation, if only the PTAA is present, 4.5% atomic nitrogen will be detected, as determined by the PTAA chemical formula, where one in every 22 atoms is nitrogen (excluding the H atoms, since H atoms are not detected by XPS). Upon analysing the nitrogen map of 0.5 mg ml^{-1} PTAA films, we see the presence of N across the mapped surface with an average 1.97% of N detected. The average N% however increases with increase in the concentration of coated PTAA to 3.35% for 1.5 mg ml^{-1} and 3.55% for 2.5 mg ml^{-1}. Whereas the In map shows the opposite trend with the increment of PTAA concentration. Presence of indium was noticeably higher on the slot die coated PTAA films with a concentration of 0.5 mg ml^{-1} compared to both 1.5 and 2.5 mg ml^{-1}. The In% decreases as the concentration of PTAA is increased to 1.5 and 2.5 mg ml^{-1}. Since the only possible source for the presence of indium on the PTAA film is the ITO substrate present underneath, it is possible to conclude the non-uniform layer of PTAA being coated at lower concentrations of 0.5 mg ml^{-1} leading to poor coverage of ITO. However, there is another possibility that may lead to high level of In detection. If a highly uniform sub 10 nm PTAA film is coated XPS would show high signal of In from ITO present underneath. This would suggest a good coverage of PTAA and no direct contact between ITO and $MAPbI_3$ leading to efficient charge extraction with no undesirable current pathways. However, the JV data presented in Figure 4. 8 show poor performance of 0.5 mg ml^{-1} PTAA films. This suggests, a poor coverage of ITO with low concentration of PTAA. It is also possible to deduce that since the higher concentration of PTAA device shows significantly higher shunt resistance, that ITO, gets adequately covered for PTAA to extract charge from $MAPbI_3$.

Although the XPS result was helpful in understanding the source of shunting on flexible devices, which is inadequate coverage of ITO, it did not provide any information regarding the cause. To understand this, we analysed the surface morphology of PET-ITO using atomic

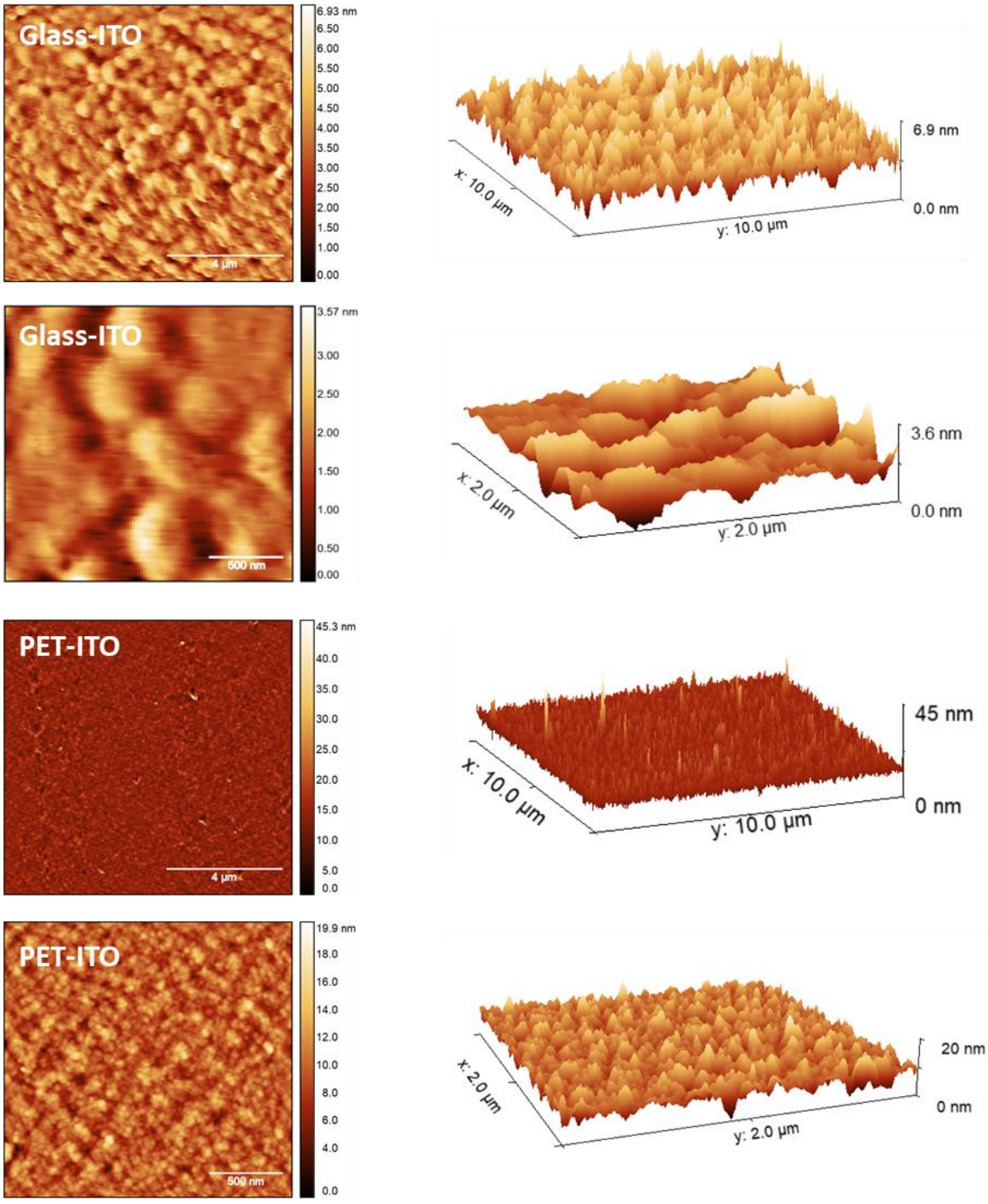

Figure 4. 10 2D and 3D AFM surface analysis of glass and PET-ITO substrate mapping 10x10 and 2x2 μm^2 area.

force microscopy (AFM) and compared them to those of glass-ITO in order to gain insight into the differences between the two. AFM images are shown in Figure 4. 10, it is clear that the surface roughness of ITO on PET is noticeably greater than that on glass. Sharp peaks with heights up to 45 nm can be seen in the ITO that was deposited on a flexible substrate

demonstrating that for devices to perform optimally, the HTL needs to be at least 45nm thick to cover the ITO completely and show high shunt resistance. In addition, the grain size of ITO is significantly larger on glass, as is evident in the 2x2 μm^2 map which shows the variability in the quality of ITO deposited on two different substrates.

Figure 4. 11a explores the AFM data further and illustrates that the average root mean square (RMS) roughness of ITO on glass is 0.81 nm, while the RMS roughness of ITO on PET is 2 nm.

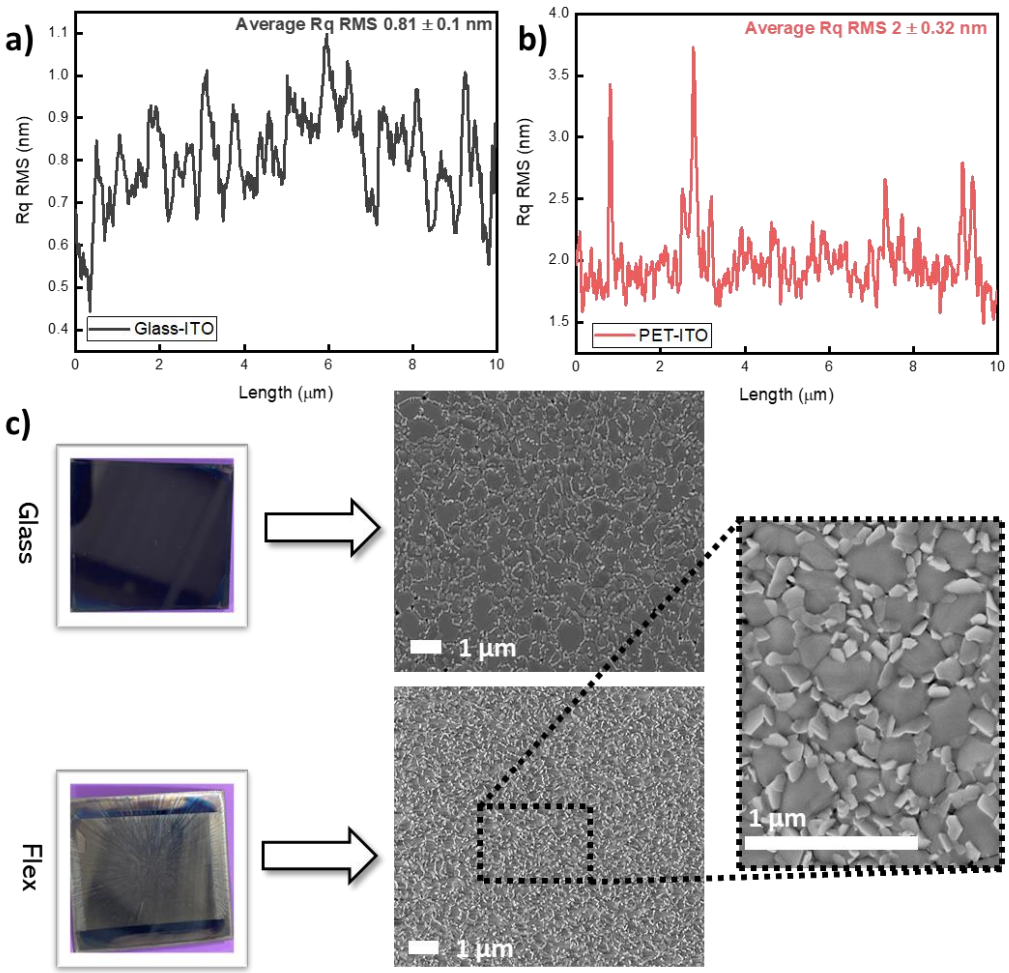

Figure 4. 11 RMS roughness profile across the 10 μm length of the map for a) ITO-Glass and b) ITO-PET. c) Optical images with Glass/PET-PTAA-$MAPbI_3$-PCBM showing the macro defects in perovskite layer coated on thin PTAA layer on different substrate.

The roughness was measured along a length of 10 μm. For undoped PTAA to be efficient, coating of an extremely thin layer of PTAA is required in P-I-N PSCs.[29] If PTAA thickness is reduced a uniform capping layer does not form on rough PET-ITO. This results in a direct contact between the perovskite and the ITO, which causes a loss of charge selectivity and a high level of nonradiative recombination and therefore poor performance. At the time of

fabrication of PSCs for the above experiment, a peculiar difference was noticed between the flexible (spin coated PTAA) and glass-based (spin coated PTAA) devices. The optical image taken during the experiment showing the difference in their appearance is presented in Figure 4. 11c. The figure shows the glass films are shinier and more homogeneous. The spin defects seen in the optical image of flexible device is likely to have emerged due to the application of PCBM to a rough perovskite surface. The spin defects visible following the application of PCBM suggest a significant change in morphology of the perovskite when coated on PET-ITO-PTAA substrates as shown in the SEM images compared in Figure 4. 11c. The grains appeared small on the flexible substrate, and it appeared as though they were protruding from the film in the vertical direction (more clearly visible in zoomed in image). The protrusion of tiny crystals may lead to higher roughness of $MAPbI_3$ films leading to spin defects that became more visible when PCBM was deposited. This shows a complete significant change of crystal growth upon changing the substrate and is attributed to change in surface energy of the substrate leading to change in growth of the $MAPbI_3$ film. [30]

4.5 Using a buffer layer on ITO for the deposition of a thin layer of PTAA

In the previous section, the effect of poor ITO morphology deposited on PET films was found to be the reason for inferior performance of flexible PSCs. Here, the use of a buffer layer to avoid the direct contact between the ITO and perovskite is explored. The coating of a buffer layer on ITO would allow the deposition of PTAA without the need for a thick layer to prevent direct contact between perovskite and ITO. PH1000 was explored for this purpose. PH1000 is a version of the PEDOT:PSS where PEDOT/PSS ratio is increased to improve the conductivity of the film. PH1000 was developed specifically for use in situations requiring both high conductivity and optical transparency. Uses for PEDOT:PSS formulations with high conductivity include serving as replacements for ITO[31,32], providing semi-transparent top electrodes in OPVs[33] and PSCs[34], and acting as a planarization layer on rough surfaces such as metal grids[35] or ITO in this case. With the addition of conductivity enhancement agents like dimethyl sulfoxide (DMSO) and ethylene glycol or by various solvent treatment, the conductive of PH1000 can be further improved.[36]

Returning to PEDOT:PSS (PH1000) may seem a step backwards to the previous chapter, but it's important to realise that the limiting factor in the performance is the PEDOT:PSS/$MAPbI_3$ interface in P-I-N PSCs. This is due to the interfacial recombination at this interface which are

further enhanced by high energy level offset between the perovskite and PEDOT:PSS.[3] In this study, when PH1000 is used as a buffer layer, a stack of PH1000/PTAA/$MAPbI_3$ is produced with PTAA/$MAPbI_3$ interface still in place. The modified device stack is presented in Figure 4. 12a. Charges are effectively extracted by PTAA and transferred to the external contact via PH1000. Thus, leveraging the benefit of PTAA/$MAPbI_3$ interface along with PH1000 buffer layer without compromising the efficient charge extraction at PTAA/$MAPbI_3$.

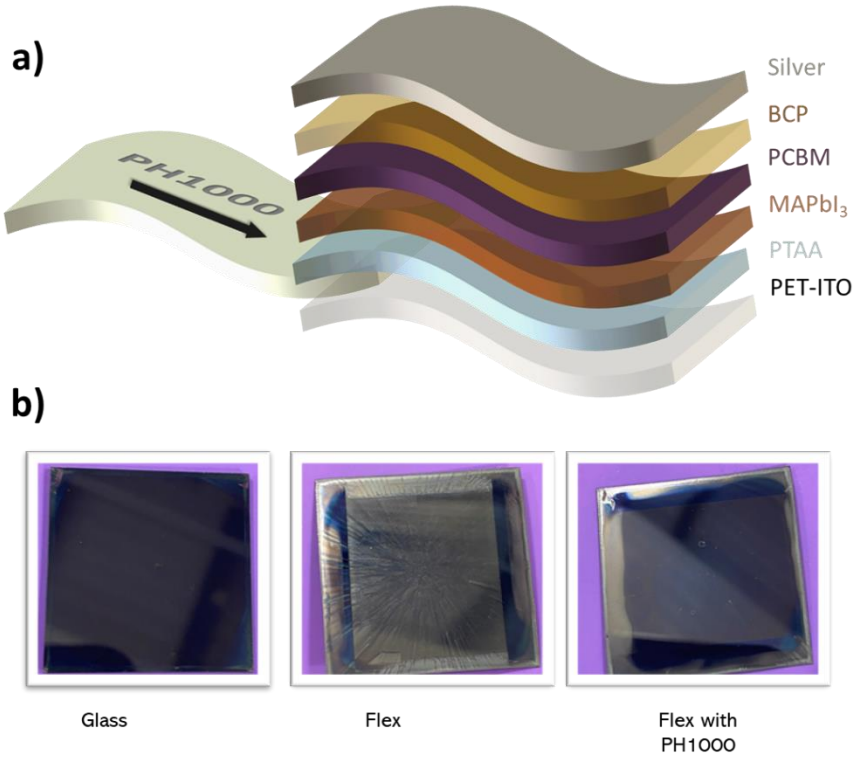

Figure 4. 12 a) Modified device stack showcasing the addition of PH1000 as a buffer layer. b)Optical images of the spin coated films with stack Glass-PTAA-$MAPbI_3$-PCBM, PET-ITO-PTAA-$MAPbI_3$-PCBM and PET-ITO-PH1000-PTAA-$MAPbI_3$-PCBM.

The effect of PH1000 was first tested on spin coated devices by depositing it on PET-ITO with variable thickness. The thickness was controlled by diluting the neat formulation of PH1000 with variable ratio of IPA (0 to 8). Following the PH1000 deposition 2.5 mg ml^{-1} of PTAA (as optimised for glass devices) solution was used to deposit a PTAA layer by spin coating. This is

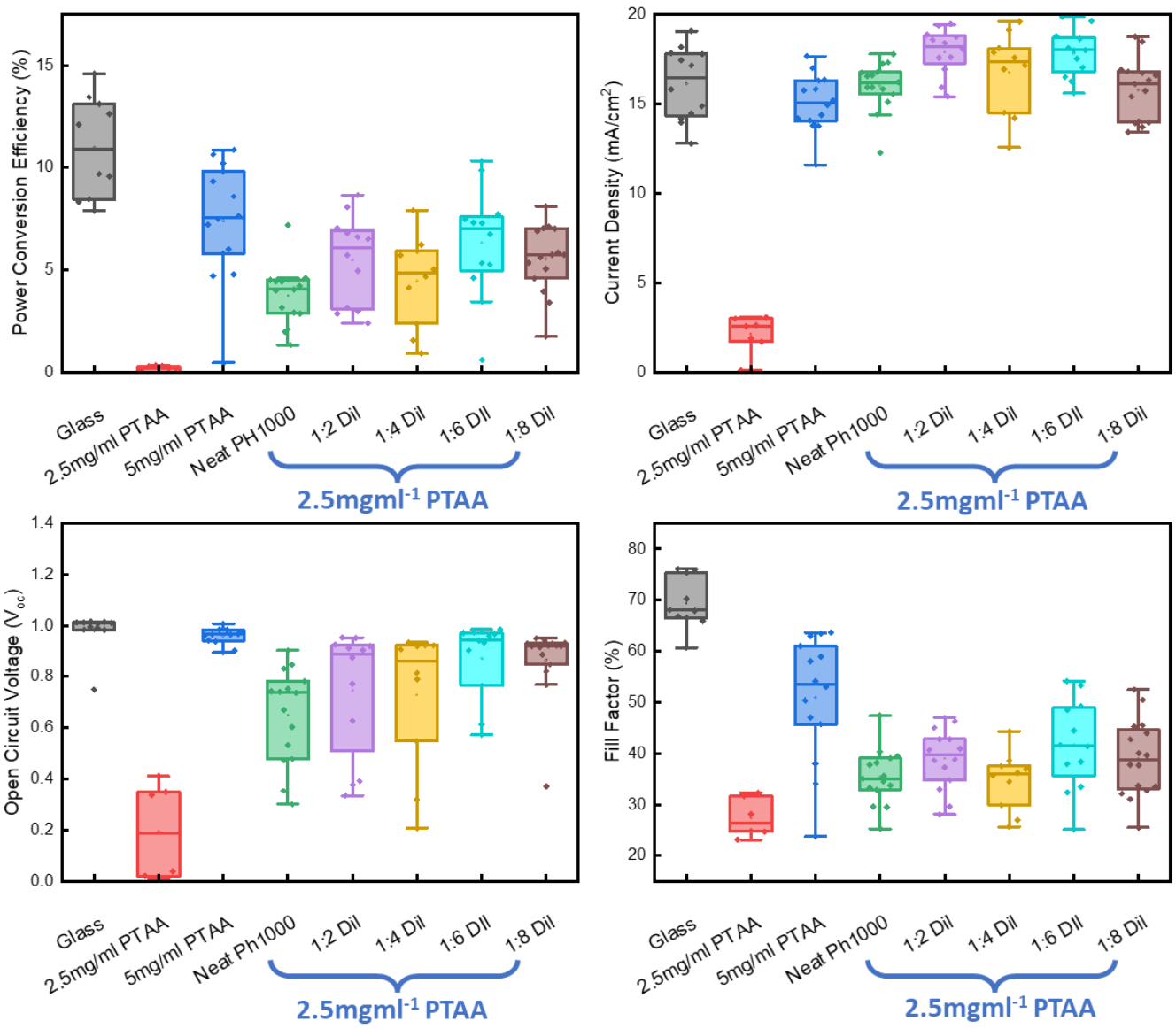

Figure 4. 13 Statistics of the JV forward scan parameters of spin coated device with neat, 1:2, 1:4, 1:6, and 1:8 dilutions of PH1000 with IPA. In addition to that, these are compared with control glass devices that do not contain PH1000 and flexible devices with thicker PTAA of 5 mg ml^{-1} concentration and no PH1000.

then compared with devices with no PH1000. For the devices with no PH1000 two different concentrations of PTAA, 2.5 mg ml^{-1} and 5 mg ml^{-1} were used. 2.5 mg ml^{-1} was used to make a fair comparison between PH1000 and no PH1000, as all the devices containing the buffer layer of PH1000 were coated with 2.5 mg ml^{-1} of PTAA. 5mg ml^{-1} PTAA was coated on a few extra devices to make working devices of PTAA only HTL with no PH1000. This was done to increase the thickness to cover ITO adequately for better performance as discussed in section 4.4. The devices were then completed following the optimised spin coating procedure (of

glass devices) for the rest of the layers as described in the experimental section. Figure 4. 12b shows the visible change that was observed during the experiment. As discussed in the explanation of Figure 4. 11c the change in the appearance of the devices due to change in $MAPbI_3$ roughness was only observed upon coating the PCBM layer. However, with the addition of PH1000 buffer layer, the flexible devices did not show any spin defects upon coating the PCBM layer on $MAPbI_3$ and visibly looked similar to glass-based devices. This suggests some change in the morphology and crystallisation of the $MAPbI_3$ films has occurred due to the insertion of PH1000 buffer layer. The device statistics obtained from the batch are

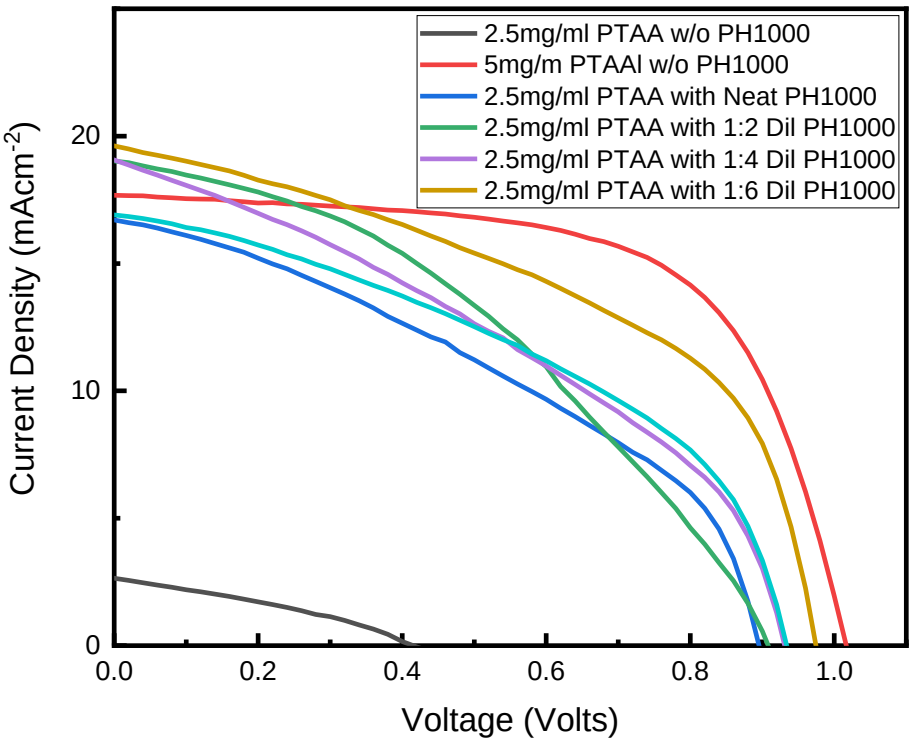

Figure 4. 14 Hero JVs of from each set of device with variable dilution of PH1000 and its comparison with devices with no PH1000.

presented in the box plot in Figure 4. 13. PTAA devices on ITO-PET with no buffer layer of PH1000 showed large performance drop compared to glass devices. This gap was reduced upon using higher concentration of PTAA (5 mg ml^{-1}), in agreement with the results previously seen with S2S slot die coated PTAA layer (Figure 4. 8). Interestingly, the performance drop was also reduced when PH1000 is used as buffer layer without needing to increase the concentration of PTAA solution to 5 mg ml^{-1}. The performance of PSCs with buffer layer of PH1000 increased as the dilution of PH1000 was increased peaking at 1:6 dilution and falling

thereafter. Extremely high thickness of PH1000 (with low dilution) may have caused high parasitic absorption in PH1000 layer resulting in lower J_{sc}. However, no absorption data was available to confirm this. Dilution beyond 1:6 ratio may have led to extremely thin layer of PH1000 thus not covering ITO effectively, leading to direct contact between ITO and $MAPbI_3$. Nonetheless, the application of PH1000 showed, that a thin layer of PTAA can be coated on PET-ITO provided a buffer layer is used in between ITO and PTAA to achieve the same level of ITO coverage as a thick PTAA layer would. Though the idea of using buffer layer made it possible to get functioning devices using 2.5 mg ml^{-1} PTAA, the overall performance of the devices using PH1000 was still relatively low due to a high drop in FF. The reason for this drop was low shunt resistance and can be more clearly observed in JV curves of all the PSCs where PH1000 was used. Figure 4. 14 shows the influence of PH1000 on the JV curve shape of flexible devices. It's likely that this drop in shunt resistance is not due to the shunts due to ITO, because no significant change in the shape of the JV curve at low voltage was seen as the thickness of PH1000 was increased with higher concentration of PH1000. A thicker PH1000 layer would effectively cover ITO and thus avoid any direct contact between ITO and $MAPbI_3$. The drop in FF due to low shunt resistance of the devices when using PH1000 as HTL has been observed in previous reports and is attributed to lower $MAPbI_3$ quality on PH1000 and larger energy band offset with perovskite.[37] If this is assumed to be true in this case, it would suggest PH1000 is taking part in the extraction of holes from $MAPbI_3$ as HTL alongside PTAA. This may be possible if a non-uniform PTAA layer is deposited on PH1000 resulting in extraction of charges by PH1000 from $MAPbI_3$. In this case, holes will be extracted by PH1000 and partly by PTAA. To verify this, the thickness of PTAA coated on top of PH1000 was modified with the assumption that the thicker PTAA would cover the PH1000 layer completely and hence charge must flow from $MAPbI_3$ to PTAA to PH1000. This experiment was conducted on glass devices due to low control on non-optimised reference flexible devices.

One set of devices containing PH1000 with varying thickness of PTAA and the other with PTAA coated directly on ITO was fabricated to compare the effect of increasing PTAA thickness. For the device with PH1000, the thickness of PTAA was increased by changing the concentration of PTAA ink from 2.5 mg ml^{-1} to 5 mg ml^{-1}. Figure 4. 15 presents a comparison of the device JVs in light (a) and dark (b) of the best performing devices from each set. The light JV curve

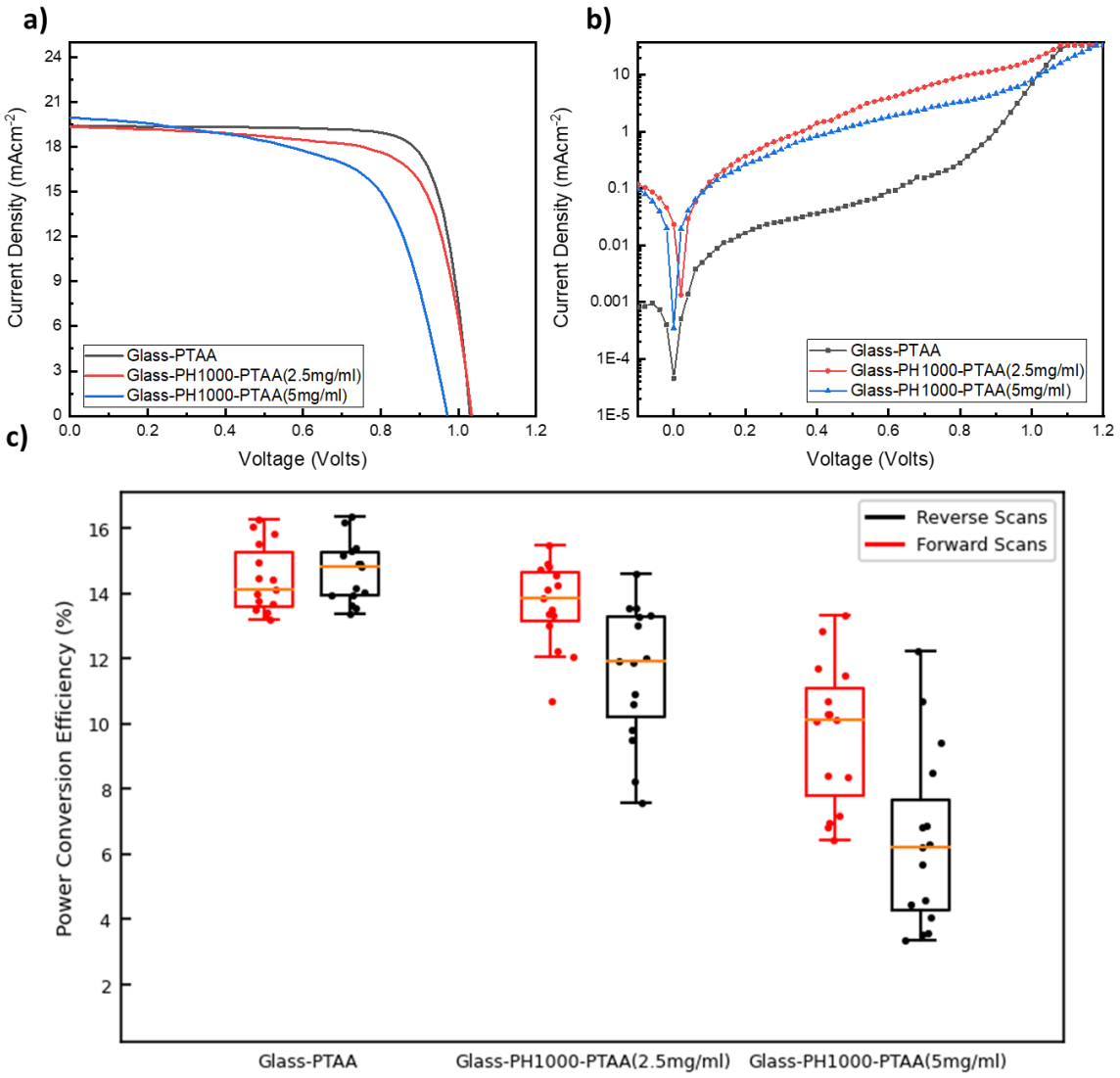

Figure 4. 15 a) Light JV comparison of glass devices in reverse and forward scan with and without PH1000 layer with variable PTAA thickness. b) dark current plotted on logarithimic current axis. c) Statistics of the JV forward scan parameters of glass spin coated device with PH1000 interlayer, comparing two different thickness of PTAA made by changing concentration of PTAA.

shows poor fill factor due to a drop in shunt resistance near J_{sc} upon using PH1000. This is consistent with the previous observation made in flexible devices and can further be confirmed by the dark current measurement compared in Figure 4. 15b. The reverse saturation current is significantly low for devices using PH1000 confirming the current leakage

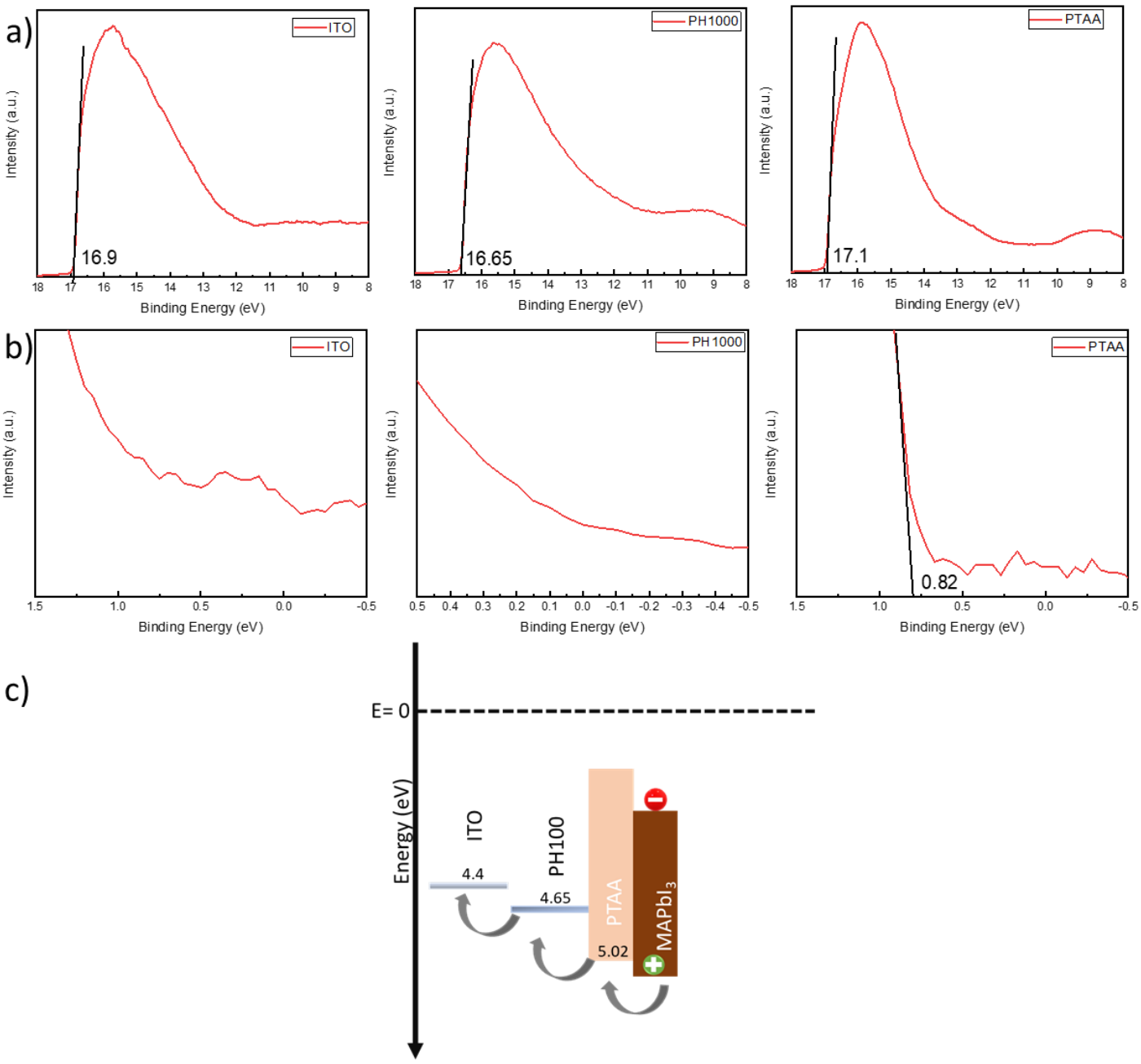

Figure 4. 16 UPS spectra of ITO, PH1000 and PTAA showcasing the position of work function (a) relative to vacuum and valence band (b) maximum relative to fermi level. e) energy band diagram showcasing hole extraction from $MAPbI_3$ plotted using data extracted from the UPS spectra of each layer.

in the device. This current leakage in the opposite direction reduces the total current generated by the device with increment voltage leading to low shunt resistance. Furthermore, the shunt resistance drops further upon increasing the PTAA thickness by changing the concentration of the coated ink. Coating thicker PTAA is likely to reduce direct contact between PH1000 and $MAPbI_3$ effectively reducing direct charge extraction by PH1000

from $MAPbI_3$. Despite this a further drop in shunt resistance was observed. This suggest that it's likely that the direct charge extraction by PH1000 from $MAPbI_3$ is not the only cause of low shunt resistance in the devices using PH1000. However, another conclusion can be drawn from measuring the hysteresis seen in the devices. The boxplot of PCE presented in Figure 4. 15c shows the difference in performance measured under forward (-0.1 to 1.2V) and reverse (1.2 to -0.1V) scan. Devices with no PH1000 show minimal hysteresis with equal performance under both scans. However, the gap between the two scan directions is enhanced when PH1000 is inserted. This further increases with the coating of thicker PTAA. Thicker coating of PTAA would effectively reduce the direct charge extraction by PH1000 from $MAPbI_3$. Thus, charges would likely be extracted by PTAA from $MAPbI_3$ and transferred to ITO via PH1000. Therefore, the increase in hysteresis upon increasing the thickness of PTAA suggests the inefficient charge transfer at the interface between PH1000 and PTAA. This phenomenon, described as inverted hysteresis is caused by unfavourable energy level alignment, ionic accumulation, and space-charge build-up.[38]

To confirm the possibility of poor band alignment, ultraviolet photoelectron spectroscopy (UPS) was used to identify the work function and valence band position of PTAA and PH1000. The UPS spectra shown in Figure 4. 16a,b shows the position of work function and the position of valence band maximum(VB) from the Fermi level. For ITO and PH1000, electron density was detected at the Fermi level , suggesting the work function and ionisation valence band is the same for both the materials which is typically seen in highly conducting materials. However, in the case of PTAA, the position of Fermi level is 0.82eV above the valence band. The spectra-derived value for all three films was then utilised to create a band diagram which is represented in Figure 4. 16c. The band diagram depicts the location of the PH1000 VB between the ITO and the PTAA. According to the band alignment, PH1000 should facilitate the hole transfer to ITO rather than obstructing it. Thus, poor band alignment is also not likely the reason for poor performance of PSCs upon insertion of PH1000. Therefore, the role of PH1000 in causing the current leakage in fabricated PSCs is unclear. A further investigation on understanding its role was not carried out as this would considerably derail progress from the main goal of the work which was to deposit a thin layer of undoped PTAA on flexible PSCs.

The work done thus far demonstrates that the use of PH1000 produced working flexible PSCs with a PTAA HTL which was not otherwise possible while coating the same thickness of PTAA

on flexible substrate as optimised on glass devices. It protected the $MAPbI_3$ from directly contacting ITO. However, its inclusion introduced some new current paths, resulting in a low fill factor. The reason for this is unknown, and it is not the topic of this study. As a result, the full benefits of the buffer layer addition were not realised, and alternative buffer layer will be explored in the next section.

4.5.1 Planarizing PET-ITO using PEDOT:PSS (AI4083)

Utilizing PH1000 assisted in illustrating the problem of rough ITO. However, using PH1000 led to undesirable current pathways resulting in low performance. As a next step, we decided to use the same material that we had previously used for HTL in the previous chapter, AI4083, essentially making a bi-layer HTL. AI4083 has a higher ratio of PSS than PH1000 pushing the VB lower and closer to that of $MAPbI_3$. Thus, it has been more successful as a HTL than PH1000 in extracting of holes from $MAPbI_3$.[37] As described in the previous section, since adding a non or poor HTL material (PH1000) did not work, replacing it with a relatively better HTL material

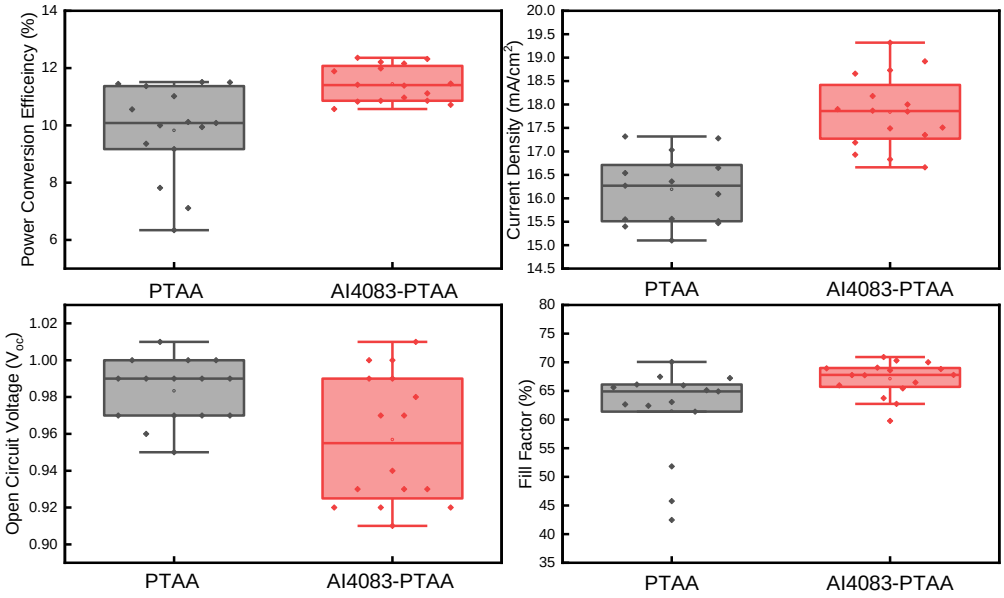

Figure 4. 17 Statistics of the JV forward scan parameters of glass spin coated device comparing glass-ITO-PTAA-$MAPbI_3$-PCBM-BCP-Ag vs glass-ITO-AI4083-PTAA-$MAPbI_3$-PCBM-BCP-Ag.

was the next option. Hence the choice to try AI4083. PTAA and AI4083 both have been successfully used as an HTL individually.[39,40] A combination of them should therefore not show any charge extraction problem. However, the intended use of AI4083 here is to form a buffer layer and enable the deposition of thin PTAA on top of PET-ITO and not to block electrons, as

the PTAA layer deposited on top of AI4083 should do that effectively. The successful use of AI4083 alongside PTAA has also been demonstrated in previous reports.[41,42] This thesis was initially tested on a glass-based device to determine the viability of AI4083 as an adjacent layer to PTAA before using it as buffer layer on PET-ITO. The testing was conducted using the same dilution level that was optimised for PH1000 that is 1:6 with IPA since the solid content of both formulations is similar according to information provided by the material supplier. The device statistics are presented in Figure 4. 17. PSCs that had only PTAA as their HTL demonstrated inferior performance when compared to those that contained AI4083 as an interlayer in between PTAA and ITO. Every parameter, except for V_{oc}, showed improvement. This may simply be the result of a non-optimised thickness of AI4083 for glass devices. Despite this, there was no evidence of reduction in fill factor due to current leakage, which was the case with PH1000. Instead, AI4083 resulted in an increase in the fill factor, suggesting an improved electron blocking behaviour of the combined HTL which is in agreement with previously reported results[41,42]. The complete discussion of the role of AI4083 will be discussed in later sections. Furthermore, the same experiment was repeated on flexible substrates to test the AI4083 ability to protect the direct contact of $MAPbI_3$ with rough ITO on PET. Previously it was shown (Figure 4. 4 a)Statistics of JV forward scan parameters of devices made with varying concentration of PTAA from 1mg ml^{-1} to 3 mg ml^{-1}l b) Light and dark JV of best performing cell measured by masking 0.09cm^2 corresponding to 2.5 mg $ml^{-1}$of PTAA concentration.Figure 4. 4a) that the optimised concentration of PTAA when deposited on glass is 2.5 mg ml^{-1} but when the same is done on flexible cells 5 mg ml^{-1} concentration was required i.e., thicker PTAA for functioning device. This was due to change in ITO roughness. For flexible devices with AI4083 two concentrations of PTAA 2.5 mg ml^{-1} and 5 mg ml^{-1} was used. With AI4083 layer stack, 2.5 mg ml^{-1} of PTAA was used to check if the same thickness of PTAA can be coated on PET-ITO with AI4083 as used on glass-ITO. In addition, 5 mg ml^{-1} was used to compare the devices with and without AI4083 layer on PET-ITO keeping the PTAA thickness same. The remaining layers were coated using standard spin coating conditions as optimised for glass devices. The performance data obtained is presented in Figure 4. 18. This data is very informative about the role AI4083 plays in improving the performance of PTAA based flexible PSCs. The box plot shows AI4083 does not have much effect on improving the performance when the thickness of PTAA is kept the same. However, its only when we decrease the PTAA thickness by reducing the concentration of PTAA ink to 2.5 mg ml^{-1} (optimised concentration

on glass devices) we see major increase in performance mainly due to significantly higher fill factor. This reduction of PTAA thickness

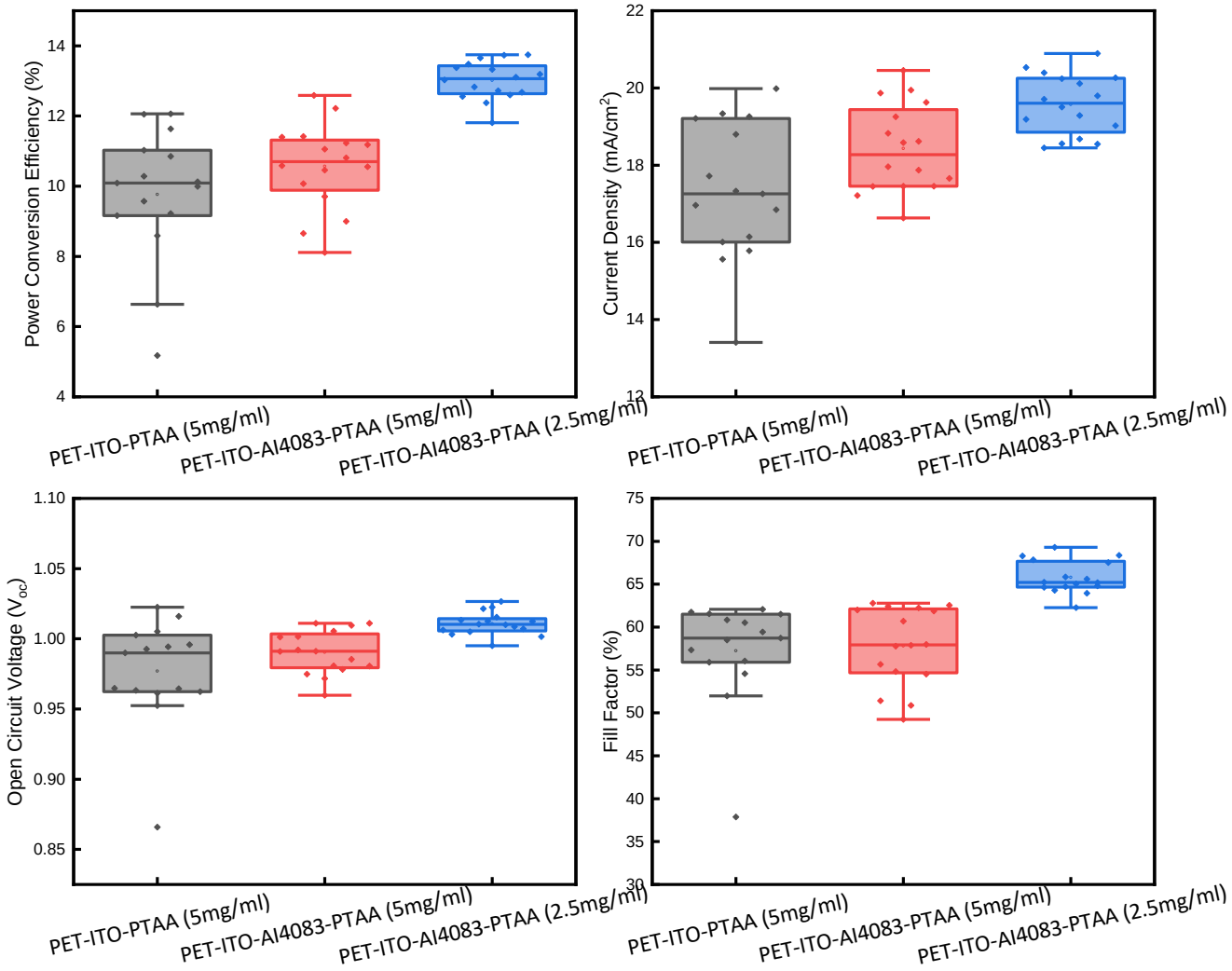

Figure 4. 18 Statistics of the JV forward scan parameters of flex spin coated device comparing the effect of AI4083 interlayer on thick (5 mg ml^{-1}) and thin PTAA (2.5 mg ml^{-1}).

is only possible when AI4083 is deposited first onto ITO. This again proves that the major factor which led to inferior PTAA based flexible device is thickness of PTAA which if reduced leads to poor PTAA coating due to rougher ITO and hence significantly lower performance. This indicates that the AI4083 role here is to enable coating of thin PTAA films which otherwise is not possible. The flexible device with AI4083 and 2.5 mg ml^{-1} PTAA resulted in an average PCE of 13% which was close to zero using the same thickness of PTAA without AI4083 buffer layer. For the next set of work, the device made in this experiment with PET-

ITO-AI4083-PTAA-$MAPbI_3$-PCBM-Ag stack using spin coating will be used as a control device to optimise the same device stack of HTL using R2R slot die coating.

4.6 Roll to Roll Optimisation of AI4083-PTAA Bi-Layer HTL

After confirming the contribution of AI4083 to the enhancement of PTAA deposition on PET-ITO substrate, the R2R optimization of both layers was conducted. For the coating of AI4083 layer, a diluted AI4083 (1:6 in IPA) was used and for the coating of PTAA an initial unoptimized concentration of 1 mg ml^{-1} in toluene was used.

For the optimisation of AI4083 layer, the previous experience (in chapter 3) of R2R slot die coating was found useful. For its use as HTL in P-I-N PSCs in the previous chapter, it was diluted in 1:3 ratio with IPA. In this work, the dilution was done in 1:6 ratio to coat a thinner layer. Higher dilution with IPA changed the viscosity of the AI4083 formulation to 5.3 mPa.s from 22.7 mPa.s for 1:3 dilution used in the previous chapter. The viscosity measurement was done by rheology meter and an average of five measurements were taken as a final value for the viscosity of the measured ink. For coating a low viscosity formulation, a meniscus guide of 250 µm was introduced. The total slot-die to substrate gap was kept at 350 µm (including 250 µm tab width of meniscus guide) for a stable meniscus to form. The drying temperature of the AI4083 coating was kept the same at 120℃ and 140℃ for the two ovens respectively. The coating width was defined by 90mm shim used alongside the meniscus guide. To optimise the thickness of 1:6 diluted ink of AI4083, WFT was varied by changing the ink flow rate to the slot die head. Figure 4. 19 shows the device statistics made using R2R slot die coated AI4083 films with WFT from 6 µm to 14 µm . The remaining layers (PTAA-$MAPbI_3$-PCBM-BCP) post slot die coating of AI4083 were deposited by spin coating following the optimised spin coating procedure mentioned in the experimental section. The data shows peak performance at 8 µm WFT of AI4083. Interestingly performance starts dropping if thickness is increased further with decrease in FF and J_{sc}. The effect of J_{sc} with change in thickness can be attributed to both absorption as well as reflectance losses. Due to higher thickness parasitic absorption may incur before the light reaches the absorber layer reducing the current generation by PSC. On the other hand, the reflection losses may originate from thin-film interference in the layered stack, which can cause near negligible reflectance at certain wavelengths but higher reflectance at other wavelengths.[43] The drop in FF could be due to series resistance losses. A lower than 8

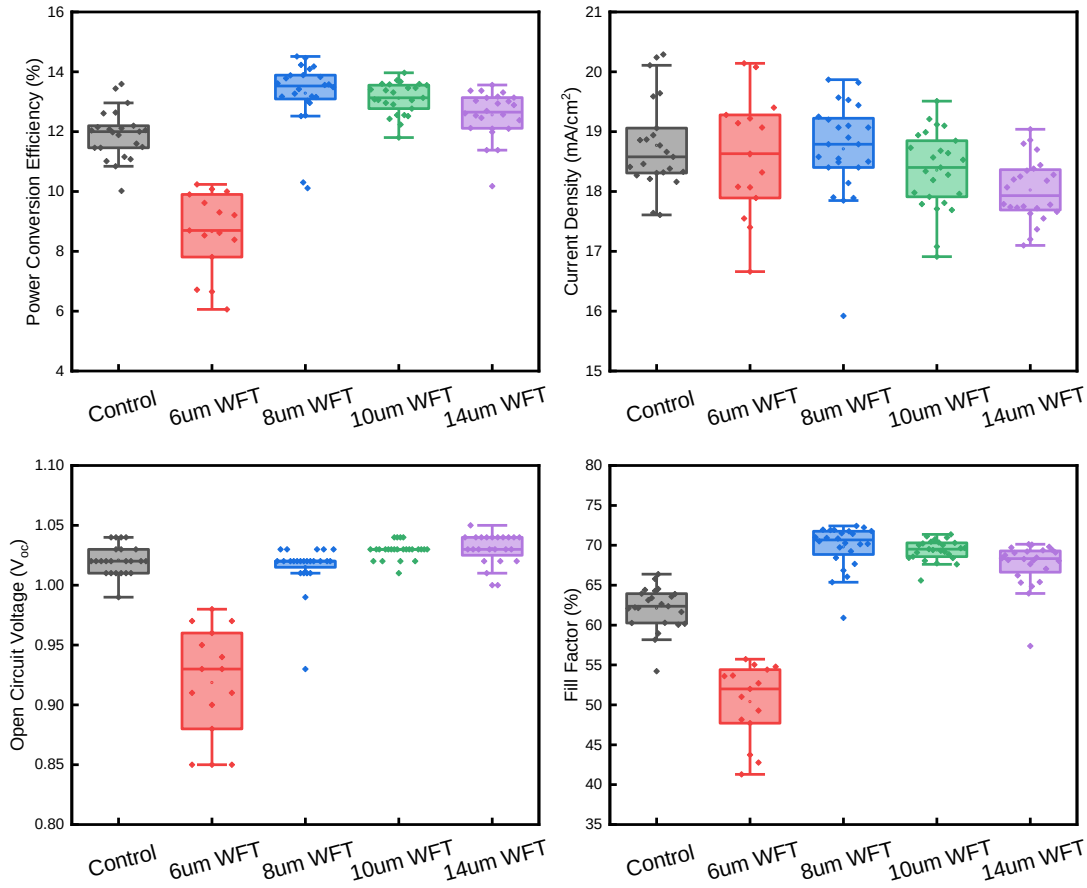

Figure 4. 19 Statistics of the JV forward scan parameters of flexible PSCs fabricated for the thickness optmisation of R2R slot die coated AI4083. The R2R coated films were then chopped into 28x28mm^2 pieces and the rest of the device layers were completed by spin coating to complete the device stack. The control device in this data is all spin coated device with AI4083 as planarisation layer.

µm WFT coated film may not have covered the ITO sufficiently to avoid shunts due to rough ITO which is evident by significantly low FF for 6 µm coated AI4083 film. AI4083 with 8 µm WFT worked best covering the ITO adequately for PTAA to be coated on top and not thick enough to induce extra series resistance and optical losses. As such, optimised 8 µm WFT will be used as a standard thickness of R2R slot die coated AI4083 buffer layer for subsequent experiments. Next, following the finding of optimal AI4083 thickness R2R slot die coating optimisation of PTAA was carried. Again, to find an optimal thickness of PTAA for best performance we varied the WFT of PTAA by increasing the flow rate of PTAA formulation into the slot die head. The WFT was varied from 6 µm WFT to 14 µm WFT in increments of 2 µm . The JV data obtained post finishing the rest of the device with spin coating is presented in

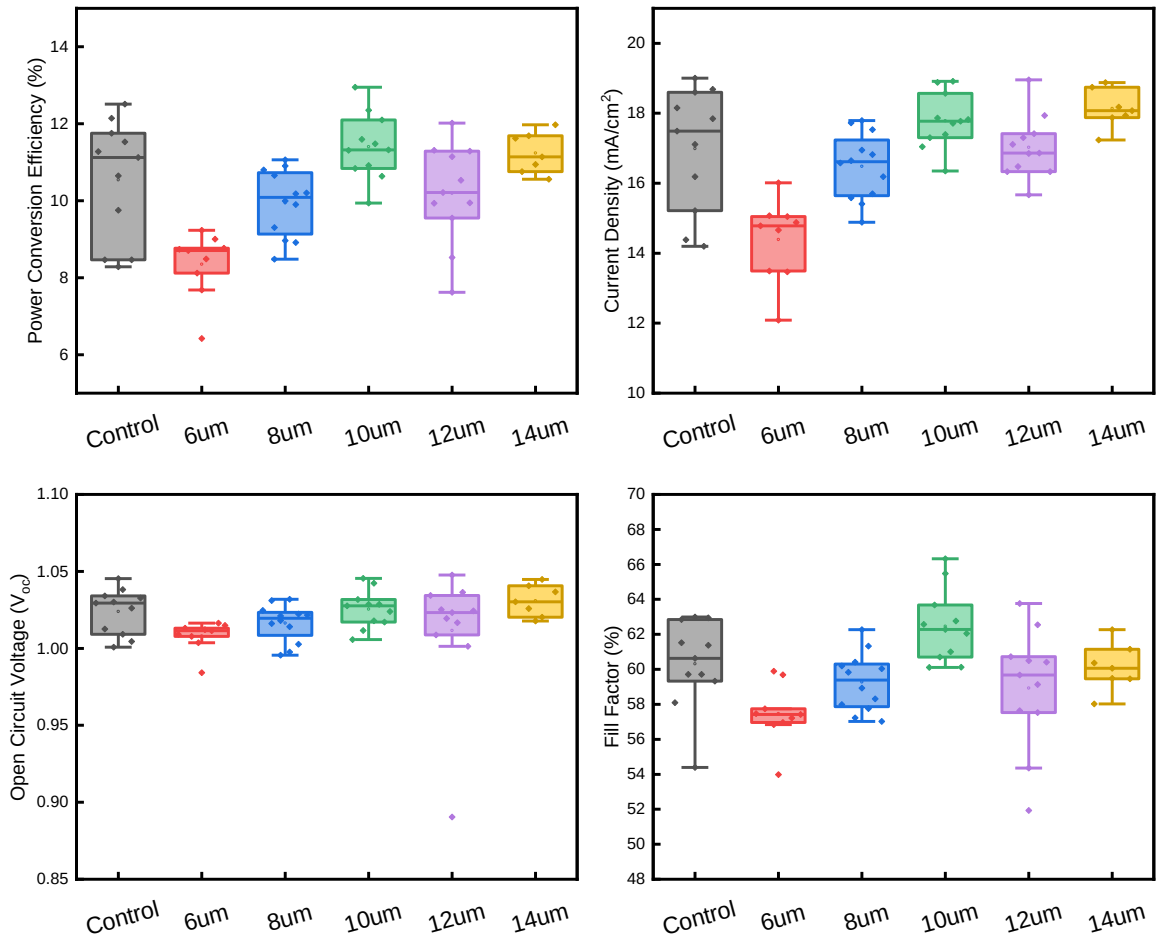

Figure 4. 20 Statistics of the JV forward scan parameters of flexible PSCs fabricated for the thickness optmisation of R2R slot die coated 1 mg ml^{-1} PTAA formulation. PTAA was coated on top of R2R slot diec coated AI4083 layer as optmised in the previous experiment. The R2R coated films were then chopped into 28x28mm^2 pieces and the remaining device layers were finished by spin coating. The control device in this data is all spin coated flexible device with AI4083 as planarisation layer.

Figure 4. 20. As the WFT increases, the statistics reveal a trend in performance. PCE steadily increases when the thickness is increased up to 10 µm WFT, after which it begins to decline. The decrease in performance above 10 µm WFT is mainly due to low FF which can be attributed to increase in device series resistance due to thicker PTAA layer. The data suggests the optimal thickness of PTAA for best performing PSCs is 10 µm WFT which matched well with the performance of control spin coated flexible devices with an AI4083 buffer layer. The R2R coated AI4083-PTAA layer with optimised layer thickness resulted in an average PCE of 11.8%.

To understand the extent of ITO coverage obtained by coating optimised 8 μm WFT of AI4083 buffer layer, XPS mapping was conducted. In this instance, the resolution was improved by reducing the mapping area and bringing the step size down from 2 millimetres (as was used in the maps shown in Figure 4. 9**Error! Reference source not found.**) to 0.75 millimetres. The mapping was completed on an area measuring 25.5 x 8.25 mm^2. A spectra was recorded at each point and the atomic percentage of elements was calculated from every spectrum. The atomic percent at each point is plotted in a 2d intensity map and is shown in Figure 4. 21a. We first ran the XPS map on an R2R coated 8 μm WFT AI4083 that had been optimised in a prior experiment and performed the best. The sulphur detected on the films confirms (on maps shown on the right side) the presence of AI4083. The sulphur % used for the S map is a total of the sulphonate from PSS and thiophene from PEDOT. A uniform signal of sulphur across the mapped area as seen in the right side of Figure 4. 21 shows a uniform deposition of AI4083 on ITO while the In map shows non uniformity in In detected on AI4083 film. However due to different scales in the map, it is a likely that the non-homogeneity is not seen at the larger scale of S in AI4083 map. To check the variation of S relative to In, the respective values of the two are plotted in a 2D scatter plot with In on Y axis and S on X axis. The scatter plot presented in Figure 4. 21b shows that the presence of In and S is bound in a region with both of them located in the same region. This suggests wherever there is higher Indium present, S is higher as well, but more importantly the variation is minimal in both S and In. A possible scenario to explain this is that the AI4083 is not planarising the ITO surface rather it is following the topography of ITO leading to a similar roughness of ITO. This is demonstrated in the picture on the right side of Figure 4. 21a. This coating morphology would coat AI4083 uniformly across the ITO, thus explaining the low variation seen in ITO as well as AI4083. However, XPS map alone is not sufficient to make this conclusion and AFM analysis will be done in later sections to verify this possibility. Further PTAA layer deposited via slot die coating (10 μm WFT coated with 1 mg ml^{-1} PTAA solution in toluene) on top of the PET-ITO was analysed by monitoring In and N atomic %. The In map of PTAA shows significantly higher variation along with higher In detected across the mapped area than was seen with AI4083. This is likely due to the thickness difference between the two. However, this once again shows why coating the same thickness of PTAA on ITO does not work but works when AI4083 layer is coated underneath it. N%, which is being used as a proxy to confirm the presence of PTAA,

is also non uniformly present across the mapped area of PTAA. To further check the variation relative to each other,

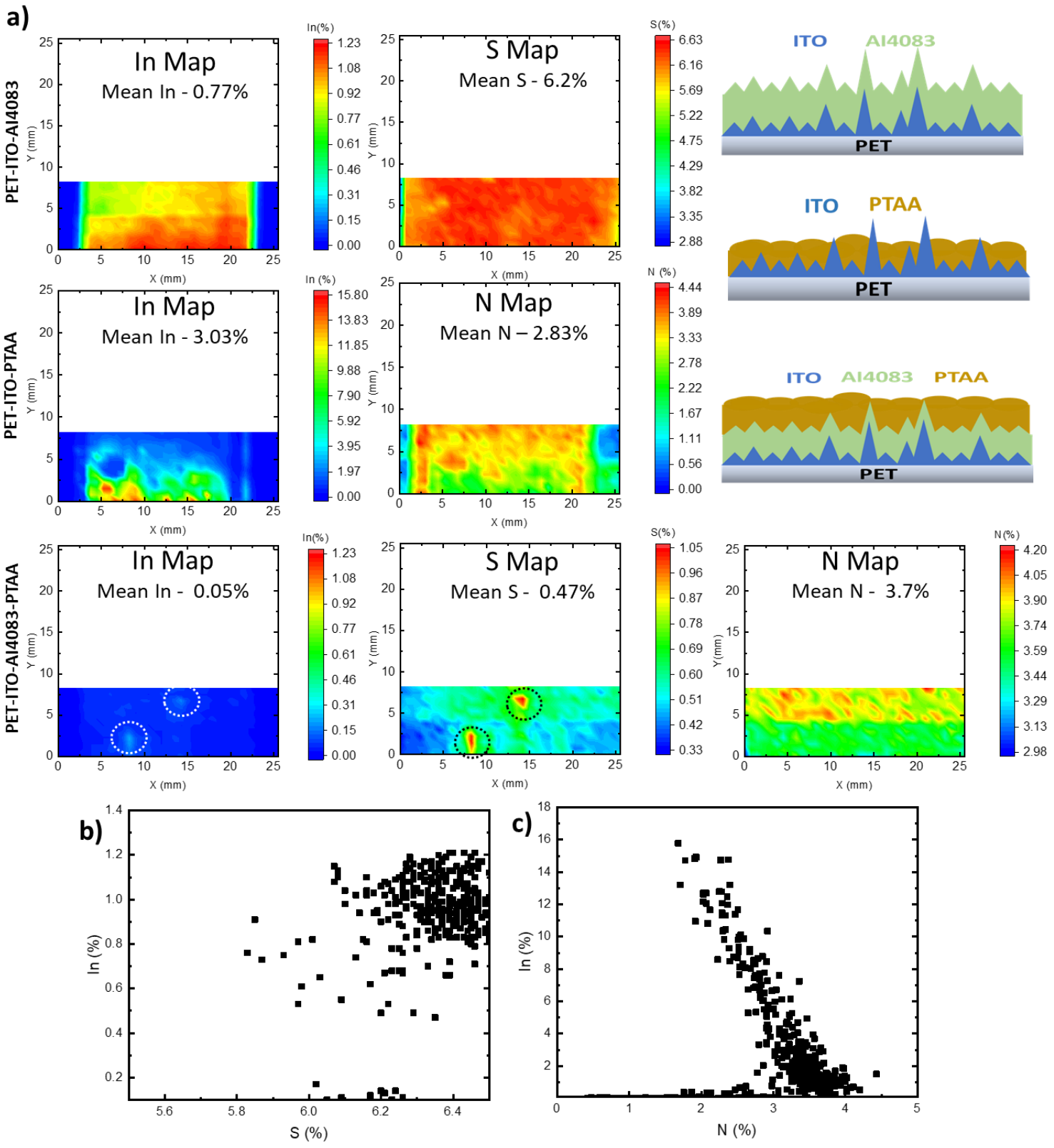

Figure 4. 21 a) XPS atomic% map of R2R slot-die coated AI4083, PTAA, AI4083-PTAA on PET ITO. b) Variation of S against In in slot die coated AI4083 on PET-ITO. c) Variation of N against In in slot die coated PTAA on PET-ITO.

a scattered 2D plot of In vs N is presented in Figure 4. 21c. This graph shows a different pattern than was seen with In vs S of AI4083 map. In PTAA coating the low In is detected wherever high N is present, suggesting a non-uniform coating of PTAA. This non uniformity suggest an uneven amount of PTAA present in the film. At places where there is higher indium, possibly due to high roughness in the region, there is low presence of PTAA and vice versa. This type

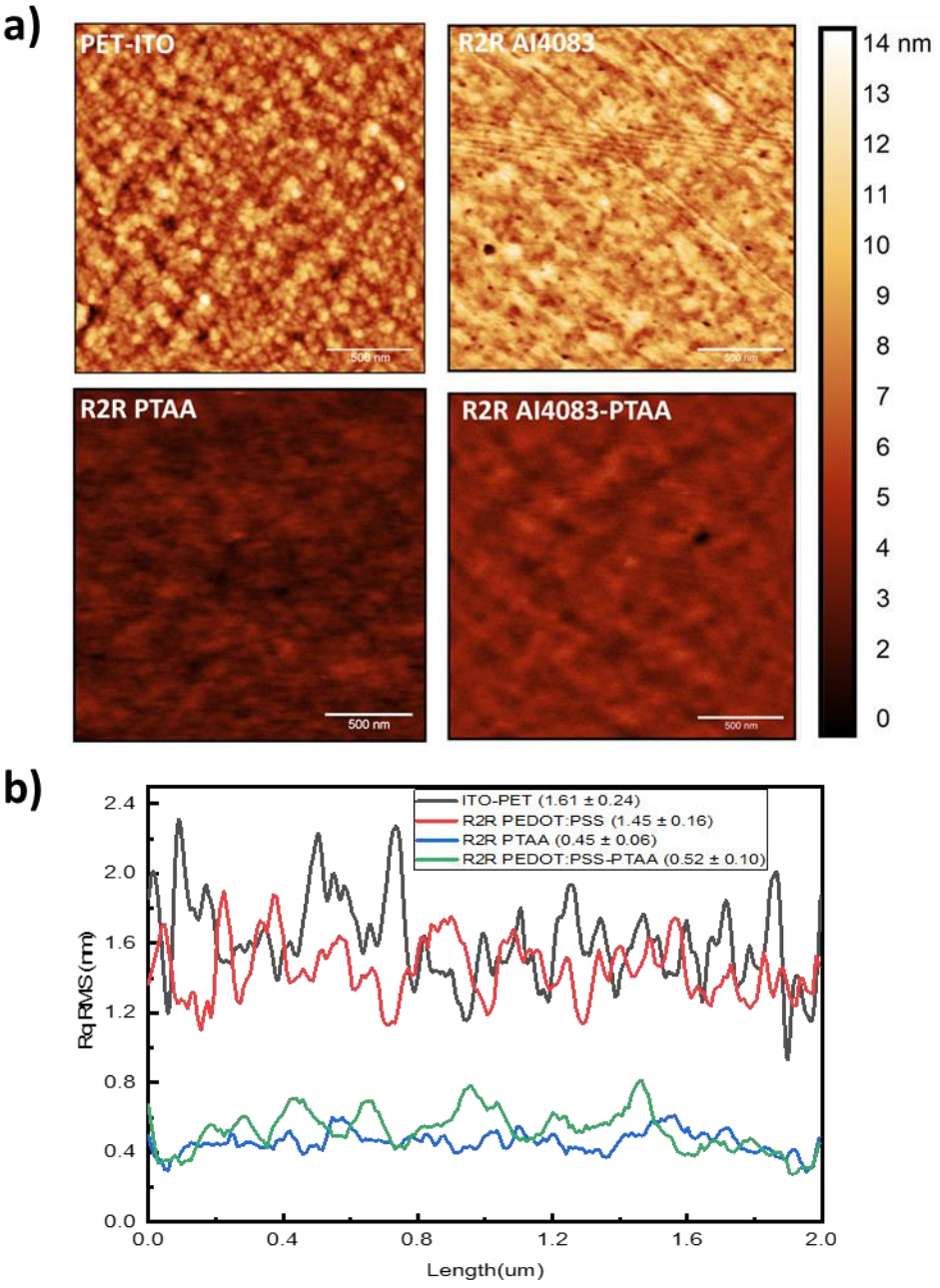

Figure 4. 22 a) AFM images of ITO-PET, as optimised R2R deposited AI4083 on ITO-PET, as optimised PTAA deposited on ITO-PET, as optimised AI4083-PTAA deposited on ITO-PET. b) Root mean square roughness (Rq RMS) profile along the length of the respective films.

of coating should planarise the ITO. A pictorial representation of this is presented in Figure 4. 21a on right side of the ITO-PTAA maps. This again will be confirmed by AFM in the later section. Next, the combination of these two layers, PET-ITO-AI4083-PTAA was mapped. The average detected In % falls to 0.05%, showing that a complete coverage of ITO was achieved with bi-layer HTL. Interestingly in ITO-AI4083-PTAA maps, two defects were noticed which are seen in both maps of In and S and are shown by dotted circles in Figure 4. 21a. At these defects the intensity of In as well S is significantly higher than their respective average. This again confirms that the AI4083 layer is likely following the topography of ITO layer underneath it.

To further confirm the behaviour of PTAA and AI4083 films, the same films were analysed using AFM, and the results were compared in order to interpret the changes in morphology and surface roughness. A 2x2 μm^2 map of as optimised AI4083 only, PTAA only and AI4083-PTAA layer along with PET-ITO is shown in Figure 4. 22a. A change in morphology of the substrate upon the deposition of AI4083 and PTAA is clearly observed. After the deposition of AI4083 and PTAA, the sharp grains of ITO that were evident before deposition become blurred. Optical images, on the other hand, did not provide a great deal of information as the definite grains are not visible in the coated layers. Therefore, the root mean square roughness of the 4 images is compared in Figure 4. 22b. Interestingly, the deposition of AI4083 did not significantly alter the roughness of the ITO confirming the initial theory. The surface roughness however is noticeably improved after the deposition of PTAA on top of the PET-ITO and AI4083 layers. When PTAA is deposited directly on ITO it formed a layer with average RMS roughness of 0.45 nm but when deposited on ITO-AI4083 layer, the roughness is slightly higher, 0.52 nm. This can also be seen in the colour intensity change on the bottom two image of Figure 4. 22a.

The data gathered so far suggests that the role of AI4083 is not to planarize the ITO, but rather to establish a buffer layer in between the PTAA and the ITO to protect any direct contact between the perovskite and the ITO, which ultimately results in a stronger rectifying junction. PTAA on the other hand does planarise the surface and the extent of this planarisation

depends on the surface PTAA is coated upon. When coated on ITO, the planarisation effect is high, but when coated on AI4083 its relatively lower as shown by AFM measurement.

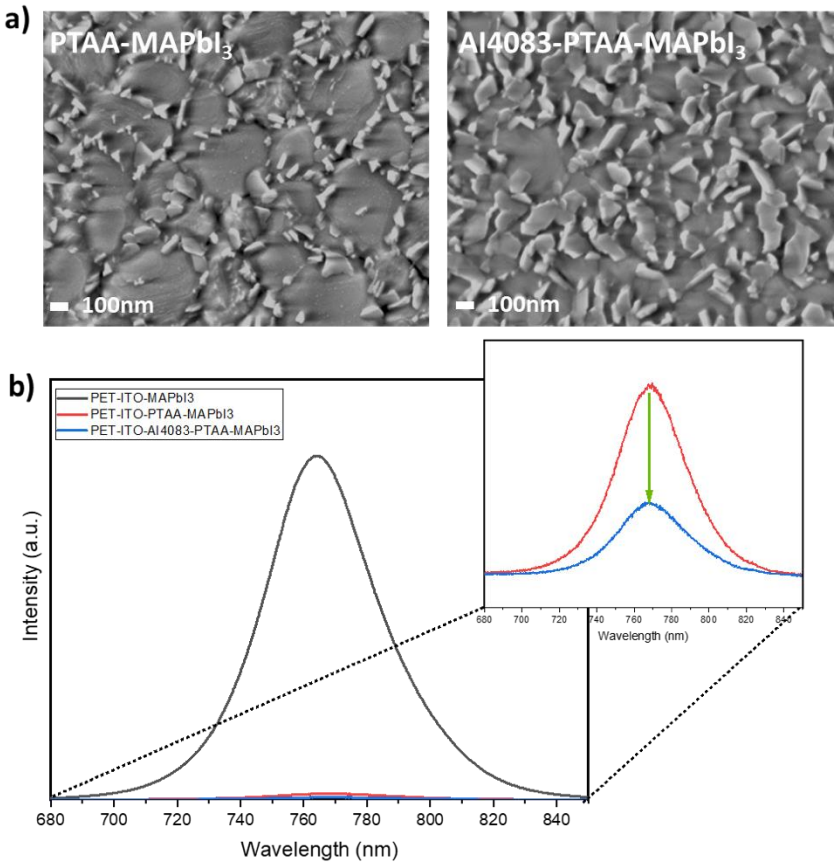

Figure 4. 23 a) SEM image of $MAPbI_3$ deposited on top of R2R coated PTAA and R2R coated AI4083-PTAA bilayer. b) PL spectra of $MAPbI_3$ deposited on bare ITO-PET and on top of HTLs.

To check the influence of bi-layer HTL (AI403-PTAA) on the $MAPbI_3$ morphology, we conducted SEM analysis on spin-coated $MAPbI_3$ that was deposited on top of R2R-coated PTAA and R2R-coated AI4083-PTAA. The images obtained are presented in Figure 4. 23a. Alongside this, we also carried out the steady state PL measurement to investigate the quality of the $MAPbI_3$ layer coated under the two circumstances and compare the hole extraction capabilities and the same is presented in Figure 4. 23b. When the underlying layers are changed, the morphology of $MAPbI_3$ as can be seen by SEM images shows a slight change at the grain boundaries. When $MAPbI_3$ is deposited on top of PET-ITO-PTAA, there is a slight disintegration between the grain boundaries, but when it is deposited over PET-ITO-AI4083-PTAA bilayer, the grains appear to have fully fused together and the grain boundaries are hard to distinguish. The bright flakes seen around and over the $MAPbI_3$ crystals is attributed to PbI_2

crystals originating from 6% excess PbI_2 used in the ink formulation. Furthermore, PL measurement shown in Figure 4. 23b shows a significant quenching of the intensity by the bilayer HTL compared to that of only PTAA layer with respect to only $MAPbI_3$ layer. PL quenching refers to decrease in PL intensity due to charge extraction by adjacent contact layer.[28] Thus, the higher the charge extraction (which is a feature of a good charge extracting layer), the higher will be the quenching. This combined with the JV data previously compared shows that the bilayer of AI4083 and PTAA is significantly more efficient in hole extraction than a single layer of PTAA.

In order to further investigate the impact of the bilayer on the complete device, we carried out several electrical characterizations on the finished device (AI4083 and PTAA were R2R slot die coated and the remaining layers were coated by spin coating). First the JV measurement in reverse scan is plotted in Figure 4. 24a. The hero cells without AI4083 could only achieve a maximum of 12.6% PCE with J_{sc} 19.94 mA/cm^2, V_{oc} 1 V and FF 63.39% in reverse scan. However, when AI4083 is inserted as a buffer layer to protect direct contact between perovskite and ITO, the PCE jumps to maximum of 15.2% with J_{sc} 20.7 mA/cm^2, V_{oc} 1.07 volts and FF 69.26%. The dark current comparison shows the significantly better rectification happening with AI4083 than just PTAA layer leading to higher turn on voltage. The jump in fill factor and V_{oc} seen upon using AI4083 buffer layer can be explained by the light dependent intensity measurement done to calculate the ideality factor of the device (Figure 4. 24b). The device using AI4083 as a buffer layer has an ideality factor of 1.09 calculated by the slope of the linear fit while only PTAA device showed an ideality factor of 1.44. In most cases, the ideality factor of PSCs falls somewhere between 1 and 2. Devices with an ideality factor of 1 are thought to be dominated by second-order bimolecular radiative recombination, whereas devices with an ideality factor of 2 are thought to be dominated by first-order monomolecular non-radiative recombination, which is essentially trap-assisted recombination.[44] Ideality factor of 1.44 for PSC without AI4083 suggest a high amount of non-radiative recombination compared to 1.09 for the device with AI4083. Combining this with the results of the XPS mapping, the likely cause of the inadequate coverage of ITO by PTAA layer leads to higher non radiative recombination at this interface. This was verified further by measuring the electroluminescence of the entire device both with and without a AI4083 buffer layer (see

Figure 4. 24c). A Keithley source meter was used to apply the external voltage of 1.2 Volts, and an integrating sphere was used to measure the emission of the device. The device that

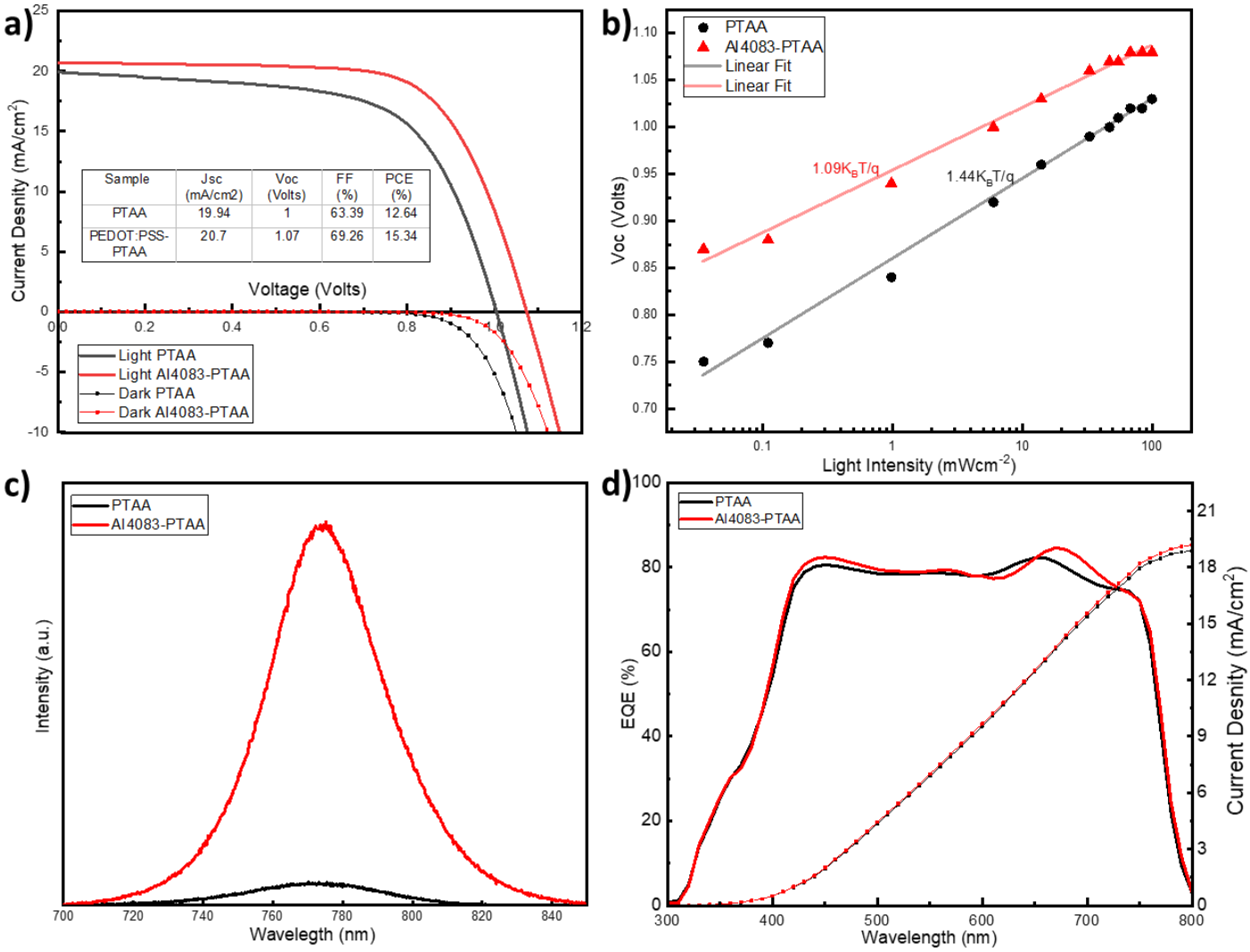

Figure 4. 24 a) Light and dark JV reverse scan of hero cells with and without AI4083 layer. b) Light intensity dependent V_{oc} measurement plotted on log scale of the hero cells. c) Electroluminescence spectra of the hero cells. d) EQE of both the hero cells.

only contained the PTAA layer showed much reduced emission, which suggests the presence of higher levels of non-radiative recombination. Since the only interface that was altered in this comparative investigation was the one between the perovskite and the hole transport layer, it is highly likely that any decrease in emission only occurs as a result of the non-radiative recombination at this interface.

EQE spectra of the same two devices were also compared and are shown in Figure 4. 24d. When AI4083 is not present, there is a minor decrease in the quantum efficiency at shorter

wavelengths, which suggests that there is a loss of carriers at the HTL/perovskite interface. This also supports the EL and ideality factor measurement made previously. Also, the J_{sc} calculated by EQE was 19.27 mA/cm^2 with AI4083 and 18.95 mA/cm^2 without AI4083. These values are comparable to the value that was obtained by JV measurement, which suggests that JV measurement is accurate.

Overall, the electrical characterisations on completed PSCs suggest that the insertion of a AI4083 buffer layer has considerably suppressed the non-radiative recombination at the PTAA/$MAPbI_3$ interface and is the reason for improvement in performance.

4.7 Conclusion

In this study, a R2R fabrication technique for the deposition of PTAA in P–I–N stack perovskite solar cells was demonstrated. This was achieved by putting an AI4083 layer in between the ITO and PTAA to solve the problem of rough ITO on PET substrates. The AI4083 layer effectively worked as a buffer layer allowing a thin PTTA layer to be coated on top of it without needing to dope it to enhance the conductivity. The use of AI4083 was found critical to improve the performance of P-I-N stack. This bi-layer HTL architecture when deposited via R2R slot die coating recorded the best efficiency at 15.2% which is much higher compared to the work done in previous chapter where only AI4083 was used as HTL. The role of AI4083 to improve the performance was characterised by AFM, XPS, EL, PL and SEM . The combination of these techniques helped determine the impact of AI4083 had on reducing the non-radiative recombination at the PTAA/Perovskite interface.

References

1. Burkitt, D. *et al.* Roll-to-roll slot-die coated P–I–N perovskite solar cells using acetonitrile based single step perovskite solvent system. *Sustain Energy Fuels* **4**, 3340–3351 (2020).

2. Dong, Q. *et al.* Flexible perovskite solar cells with simultaneously improved efficiency, operational stability, and mechanical reliability. *Joule* **5**, 1587–1601 (2021).

3. Stolterfoht, M. *et al.* The impact of energy alignment and interfacial recombination on the internal and external open-circuit voltage of perovskite solar cells. *Energy Environ Sci* **12**, 2778–2788 (2019).

4. Galagan, Y. *et al.* Roll-to-Roll Slot Die Coated Perovskite for Efficient Flexible Solar Cells. *Adv Energy Mater* **8**, 1–7 (2018).

5. Kim, Y. Y. *et al.* Gravure-Printed Flexible Perovskite Solar Cells: Toward Roll-to-Roll Manufacturing. *Advanced Science* **6**, 1802094 (2019).

6. Zuo, C., Vak, D., Angmo, D., Ding, L. & Gao, M. One-step roll-to-roll air processed high efficiency perovskite solar cells. *Nano Energy* **46**, 185–192 (2018).

7. Sears, K. K. *et al.* ITO-Free Flexible Perovskite Solar Cells Based on Roll-to-Roll, Slot-Die Coated Silver Nanowire Electrodes. *Solar RRL* **1**, (2017).

8. Ham, D. S. *et al.* Influence of Drying Conditions on Device Performances of Antisolvent-Assisted Roll-To-Roll Slot Die-Coated Perovskite Solar Cells. *ACS Appl Energy Mater* **4**, 7611–7621 (2021).

9. di Giacomo, F. *et al.* Up-scaling perovskite solar cell manufacturing from sheet-to-sheet to roll-to-roll: challenges and solutions. *https://doi.org/10.1117/12.2274438* **10363**, 21–28 (2017).

10. Kim, J. E. *et al.* Humidity-Tolerant Roll-to-Roll Fabrication of Perovskite Solar Cells via Polymer-Additive-Assisted Hot Slot Die Deposition (SI). *Adv Funct Mater* **29**, 1–9 (2019).

11. Gong, C. *et al.* Flexible Planar Heterojunction Perovskite Solar Cells Fabricated via Sequential Roll-to-Roll Microgravure Printing and Slot-Die Coating Deposition. *Solar RRL* **4**, 1900204 (2020).

12. Dou, B. *et al.* Roll-to-Roll Printing of Perovskite Solar Cells. *ACS Energy Lett* **3**, 2558–2565 (2018).

13. Heo, Y. J. *et al.* Printing-friendly sequential deposition via intra-additive approach for roll-to-roll process of perovskite solar cells. *Nano Energy* **41**, 443–451 (2017).

14. Swartwout, R. *et al.* Predicting Low Toxicity and Scalable Solvent Systems for High-Speed Roll-to-Roll Perovskite Manufacturing. *Solar RRL* 2100567 (2021) doi:10.1002/SOLR.202100567.

15. Liu, S., Jiang, X., Ma, H., Liu, M. S. & Jen, A. K. Y. Triarylamine-containing poly(perfluorocyclobutane) as hole-transporting material for polymer light-emitting diodes. *Macromolecules* **33**, 3514–3517 (2000).

16. Zhang, W. *et al.* Systematic improvement in charge carrier mobility of air stable triarylamine copolymers. *J Am Chem Soc* **131**, 10814–10815 (2009).

17. Lee, I., Rolston, N., Brunner, P. L. & Dauskardt, R. H. Hole-Transport Layer Molecular Weight and Doping Effects on Perovskite Solar Cell Efficiency and Mechanical Behavior. *ACS Appl Mater Interfaces* **11**, 23757–23764 (2019).

18. Wang, Q., Bi, C. & Huang, J. Doped hole transport layer for efficiency enhancement in planar heterojunction organolead trihalide perovskite solar cells. *Nano Energy* **15**, 275–280 (2015).

19. Guillén, C. & Herrero, J. Comparison study of ITO thin films deposited by sputtering at room temperature onto polymer and glass substrates. *Thin Solid Films* **480–481**, 129–132 (2005).

20. Li, Z. *et al.* Extrinsic ion migration in perovskite solar cells. *Energy Environ Sci* **10**, 1234–1242 (2017).

21. Daniel Burkitt *et al.* Acetonitrile based single step slot-die compatible perovskite ink for flexible photovoltaics. *RSC Adv* **9**, 37415–37423 (2019).

22. Guo, Y. *et al.* Influence of the MACl additive on grain boundaries, trap-state properties, and charge dynamics in perovskite solar cells. *Physical Chemistry Chemical Physics* **23**, 6162–6170 (2021).

23. Odysseas Kosmatos, K. *et al.* Methylammonium Chloride: A Key Additive for Highly Efficient, Stable, and Up-Scalable Perovskite Solar Cells. *Energy & Environmental Materials* **2**, 79–92 (2019).

24. Xu, W. *et al.* Suppressing Defects-Induced Nonradiative Recombination for Efficient Perovskite Solar Cells through Green Antisolvent Engineering. *Advanced Materials* **32**, 2003965 (2020).

25. Wang, H. *et al.* Reducing photovoltage loss at the anode contact of methylammonium-free inverted perovskite solar cells by conjugated polyelectrolyte doping. *J Mater Chem A Mater* **8**, 7309–7316 (2020).

26. Khadka, D. B., Shirai, Y., Yanagida, M., Ryan, J. W. & Miyano, K. Exploring the effects of interfacial carrier transport layers on device performance and optoelectronic properties of planar perovskite solar cells. *J Mater Chem C Mater* **5**, 8819–8827 (2017).

27. Kim, J. *et al.* Excitation Density Dependent Photoluminescence Quenching and Charge Transfer Efficiencies in Hybrid Perovskite/Organic Semiconductor Bilayers. *Adv Energy Mater* **8**, 1802474 (2018).

28. Zhao, Q. *et al.* Achieving efficient inverted planar perovskite solar cells with nondoped PTAA as a hole transport layer. *Org Electron* **71**, 106–112 (2019).

29. Fang, Z. *et al.* Modulating preferred crystal orientation for efficient and stable perovskite solar cells—From progress to perspectives. *InfoMat* **4**, e12369 (2022).

30. Liu, T. *et al.* Low temperature processed ITO-free perovskite solar cells without a hole transport layer. *RSC Adv* **5**, 94752–94758 (2015).

31. Kim, Y. H. *et al.* Highly Conductive PEDOT:PSS Electrode with Optimized Solvent and Thermal Post-Treatment for ITO-Free Organic Solar Cells. *Adv Funct Mater* **21**, 1076–1081 (2011).

32. Zhou, Y. *et al.* Indium tin oxide-free and metal-free semitransparent organic solar cells. *Appl Phys Lett* **97**, 153304 (2010).

33. Bu, L. *et al.* Semitransparent Fully Air Processed Perovskite Solar Cells. *ACS Appl Mater Interfaces* **7**, 17776–17781 (2015).

34. Muhsin, B., Roesch, R., Gobsch, G. & Hoppe, H. Flexible ITO-free polymer solar cells based on highly conductive PEDOT:PSS and a printed silver grid. *Solar Energy Materials and Solar Cells* **130**, 551–554 (2014).

35. Shahrim, N. A., Ahmad, Z., Wong Azman, A., Fachmi Buys, Y. & Sarifuddin, N. Mechanisms for doped PEDOT:PSS electrical conductivity improvement. *Mater Adv* **2**, 7118–7138 (2021).

36. Gebremichael, Z. T. *et al.* How varying surface wettability of different PEDOT:PSS formulations and their mixtures affects perovskite crystallization and the efficiency of inverted perovskite solar cells. *RSC Adv* **12**, 25593–25604 (2022).

37. Wu, F. *et al.* Inverted Current-Voltage Hysteresis in Perovskite Solar Cells. *ACS Energy Lett* **3**, 2457–2460 (2018).

38. Li, S., Cao, Y. L., Li, W. H. & Bo, Z. S. A brief review of hole transporting materials commonly used in perovskite solar cells. *Rare Metals* **40**, 2712–2729 (2021).

39. Ke, Q. bin, Wu, J. R., Lin, C. C. & Chang, S. H. Understanding the PEDOT:PSS, PTAA and P3CT-X Hole-Transport-Layer-Based Inverted Perovskite Solar Cells. *Polymers 2022, Vol. 14, Page 823* **14**, 823 (2022).

40. Wang, M. *et al.* Defect passivation using ultrathin PTAA layers for efficient and stable perovskite solar cells with a high fill factor and eliminated hysteresis. *J Mater Chem A Mater* **7**, 26421–26428 (2019).

41. Wang, Z. *et al.* Rational Interface Design and Morphology Control for Blade-Coating Efficient Flexible Perovskite Solar Cells with a Record Fill Factor of 81%. *Adv Funct Mater* **30**, 2001240 (2020).

42. Caprioglio, P. *et al.* On the Origin of the Ideality Factor in Perovskite Solar Cells. *Adv Energy Mater* **10**, 2000502 (2020).

Chapter 5
Optimisation of Roll-to-Roll Slot Die Coated $MAPbI_3$ on PTAA layer for efficient Perovskite Solar Cells

5.1 Introduction

In the previous two chapters, a method to print all the layers of P-I-N PSCs (except metal contact) via R2R slot die coating was developed. Later, for the same architecture a more efficient HTL system was developed in chapter 3. It consisted of a combination of PEDOT:PSS(AI4083)♦ and PTAA. PTAA was chosen to improve the efficiency as it has favourable band alignment with $MAPbI_3$ than PEDOT:PSS. Furthermore, the acidic nature of PEDOT:PSS contributes to the degradation of the HTL/$MAPbI_3$ interface, resulting in less stable PSCs.[1] Though PTAA is a highly efficient layer as showed in the last chapter compared to PEDOT:PSS, it has several challenges. A quite commonly faced problem is the hydrophobic surface of PTAA which makes difficult to coat a uniform defect free $MAPbI_3$ layer on top of it. This is a significant issue specially with large area coatings more so than coating of perovskite layer via spin coating which was shown successfully in the previous chapter. To overcome the problem, solutions like the use of a surfactant[2,3], solvent treatment[4] and the use of an interface layer[5,6] have been demonstrated in the literature. For large area coatings, $MAPbI_3$ deposition on PTAA has been done via blade and slot die coating in a S2S system[7], but no reports are yet available showcasing the R2R deposition of $MAPbI_3$ on PTAA. This is likely because S2S systems are more flexible than R2R system. Processing conditions such as substrate heating, vacuum drying, are possible on S2S system but they are not trivial to carry out on R2R setup. Thus, R2R coating requires different engineering to achieve the same results.

The previous work achieved an efficiency of up to 15.2% by spin coating the $MAPbI_3$ layer on top of R2R slot die coated PEDOT:PSS-PTAA bilayer. In this work, efforts will be made to

♦ Unless otherwise specified, the PEDOT:PSS discussed in this chapter is AI4083 grade which is a common HTL material used in PSCs

optimise the R2R slot die coating of $MAPbI_3$ onto R2R coated PEDOT:PSS-PTAA, with the goal of minimising the performance loss that results from the transfer of the process from spin coating to R2R slot die coating. The challenge with this process transfer will be discussed and characterised to find the appropriate solution.•

5.3 Experimental Methods

For the optimisation of R2R slot die coated $MAPbI_3$ layer on PEDOT:PSS-PTAA bilayer HTL, the control device in this work was fabricated on top of R2R coated PEDOT:PSS-PTAA as optimised in the previous chapter to make a fair comparison between the R2R slot die vs spin coated $MAPbI_3$. This will be true for all the experiments unless otherwise stated. The rest of the fabrication process of the device was done using spin coating to complete the stack of PET-ITO-PEDOT:PSS-PTAA-$MAPbI_3$-PCBM-BCP. The procedure for this deposition was kept the same as chapter 3 and chapter 4. Next, silver was thermally evaporated using a bell jar to complete the device.

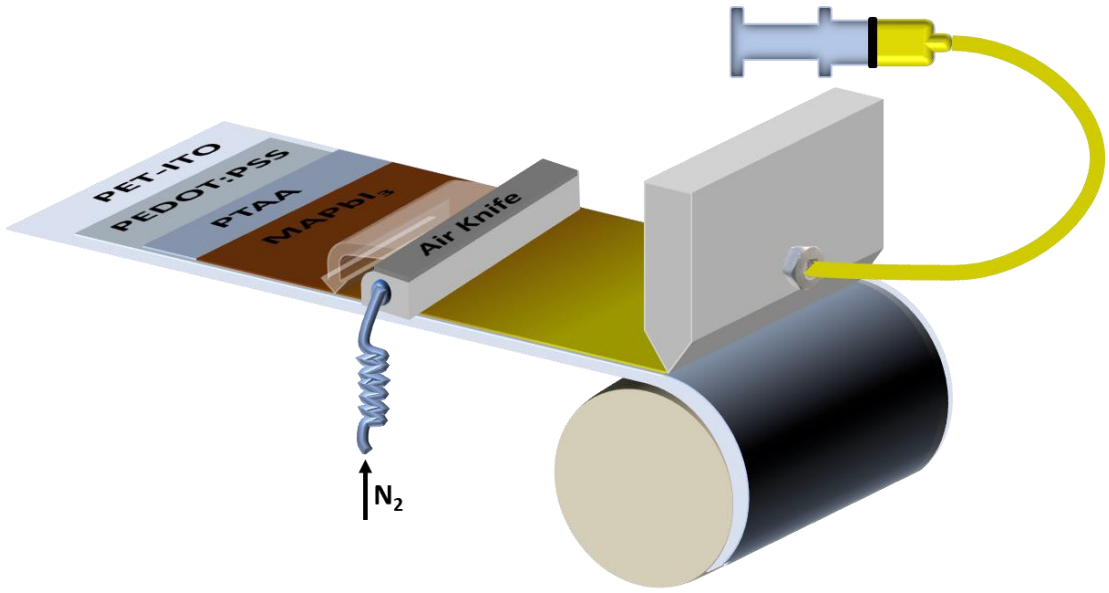

Figure 5. 1 Schematic representation of R2R slot die coating of $MAPbI_3$ on R2R slot die coated PEDOT:PSS-PTAA on PET-ITO substrate.

For the R2R slot die coating of $MAPbI_3$ on PEDOT:PSS-PTAA, previous experience gathered in chapter 3 when depositing $MAPbI_3$ on PEDOT:PSS was leveraged. This was possible because

•At the time this work was carried out, there was limited availability of PET-ITO substrate. Therefore, the experiments were designed to make the efficient use of substrate which meant limiting the number of experiments to optimise the slot die coating of $MAPbI_3$ on PEDOT:PSS-PTAA.

no major changes were made in the $MAPbI_3$ precursor ink, and the core solvent system of ACN-MA was kept the same. For R2R slot die coating of $MAPbI_3$, a 90mm coating width was defined by a shim integrated in to the slot die head. Along with the shim a 1000 µm tab width meniscus guide was also used to control the meniscus. A gap of 1100 µm (including 1000 µm meniscus guide) was kept between the slot die head and the substrate. The coating was applied at 1 m min^{-1} web speed which was intentionally kept the same as the rest of the layers so that the work developed in this chapter can be directly used in a pilot scale R2R system with multiple coating stations. The as prepared $MAPbI_3$ ink was slot die coated onto PET-ITO-PEDOT:PSS-PTAA (optimised in chapter 4) followed by drying with N_2 air knife. The films were then annealed using two inline convection ovens set at 150℃. The schematic of the process is presented in Figure 5. 1. Preparation of the $MAPbI_3$ ink will be discussed in the next section. The remaining layers (PCBM-BCP-Ag) post the deposition of $MAPbI_3$ was done following the standard procedure of control device via spin coating and thermal evaporation.

5.2 Ink formulation

Up until this point, the ink that was utilised for perovskite deposition (for spin coating as well as slot-die coating) was based on the bubbling process developed by another group[8] and is discussed in the materials and methods section. This procedure is not only laborious and time consuming, but it also relies on manual identification of the stop point as soon as the PbI_2 and MAI precursor dissolves in ACN, forming a translucent pale-yellow liquid. Because of this, the amount of methylamine that is dissolved in the formulation is less certain, and the amount that is dissolved may be different from one experiment to the next.

At the time of starting this work, a commercial alternative was made available by TCI chemicals. It consisted of methylamine dissolved in acetonitrile at a concentration of 9% w/w. It is easier and more time efficient to prepare perovskite formulation using this solvent in a standard approach of mixing all of them together. However, before completely switching to it, it was essential to evaluate its performance in comparison to the formulation that was prepared using the bubbling approach. In order to verify this, two separate solutions were made by using the same precursors in distinct solvent system. In the first formulation, methylamine gas was bubbled in the mixture of precursors and neat acetonitrile solvent to dissolve the precursors, whereas in the second formulation, the precursors were directly mixed with methyl amine dissolved ACN at a concentration of 9% w/w. These two solutions

were then used to make P-I-N PSC. The architecture consisted of ITO-PEDOT:PSS-PTAA-$MAPbI_3$-PCBM-BCP-Ag. For this R2R printed PEDOT:PSS-PTAA substrates prepared in the last chapter was used and the rest of the layer including perovskite were all spin coated. The devices were then measured under 1 Sun to assess their performance. The performance parameters of both the sets of devices are compared in a box plot in Figure 5. 2. The data shows comparable performance of both the sets of perovskite formulation. This collection of

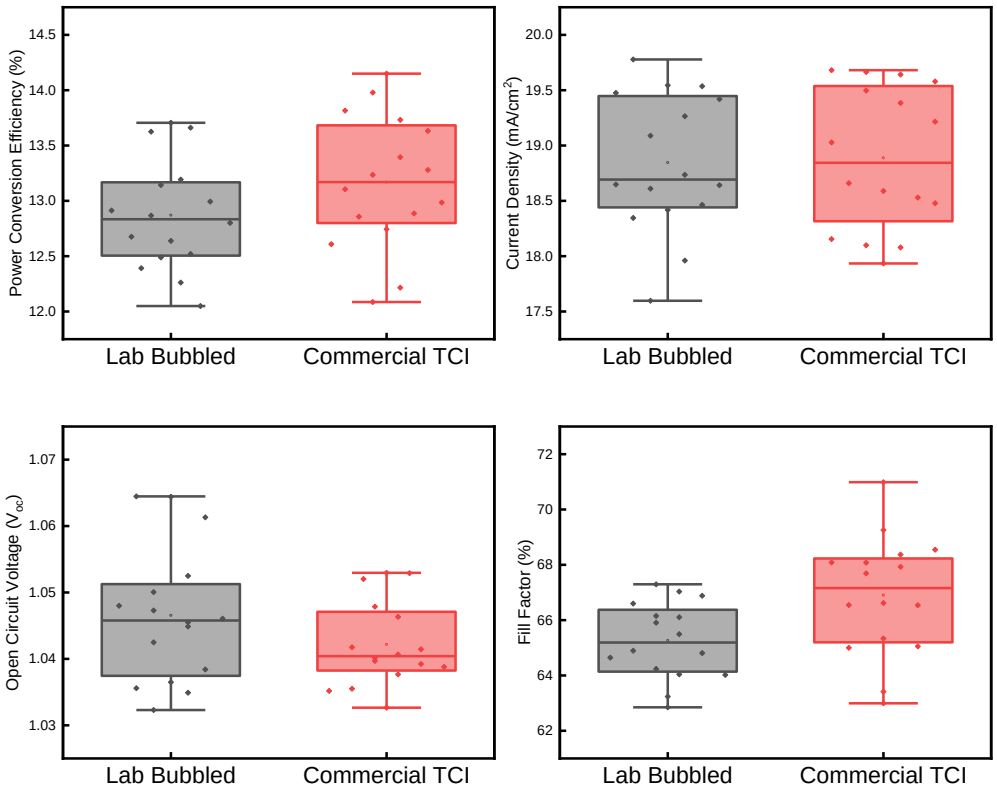

Figure 5. 2 Statistics of JV forward scan parameters of two sets of devices made using bubbling method labelled as Lab bubbled and solvent obtained commercially from TCI labelled as commercial TCI. All the layers in the stack of PET-ITO-PEDOT:PSS-PTAA-$MAPbI_3$-PCBM-BCP were spin coated followed by thermal evaporation of silver contact.

findings is significant since the commercial mixture of methyl amine in acetonitrile (ACN) enables a sizeable cut in the amount of time required for the preparation of ink formulation, in addition to being less variable. Hence for the rest of coatings in this work, the commercial ACN solvent was used for the preparation of $MAPbI_3$ ink.

5.3 R2R Slot Die Coating of $MAPbI_3$ on PTAA

A R2R slot die coating method for the deposition of $MAPbI_3$ layer in the P-I-N stack with PEDOT:PSS as HTL was developed and optimised in chapter 3. For the optimisation in this

work, we used the same drying and coating parameters as optimised previously. Briefly, the coating was applied at 1 m min^{-1} speed and the films were dried at 150℃ set points for both the convection oven. Because the ACN-based perovskite ink has a low viscosity, a meniscus guide with a tab width of 1000 µm was utilised, and a space of 100 µm maintained between the substrate and the meniscus guide while coating. A 5 µm wet film thickness (WFT) using

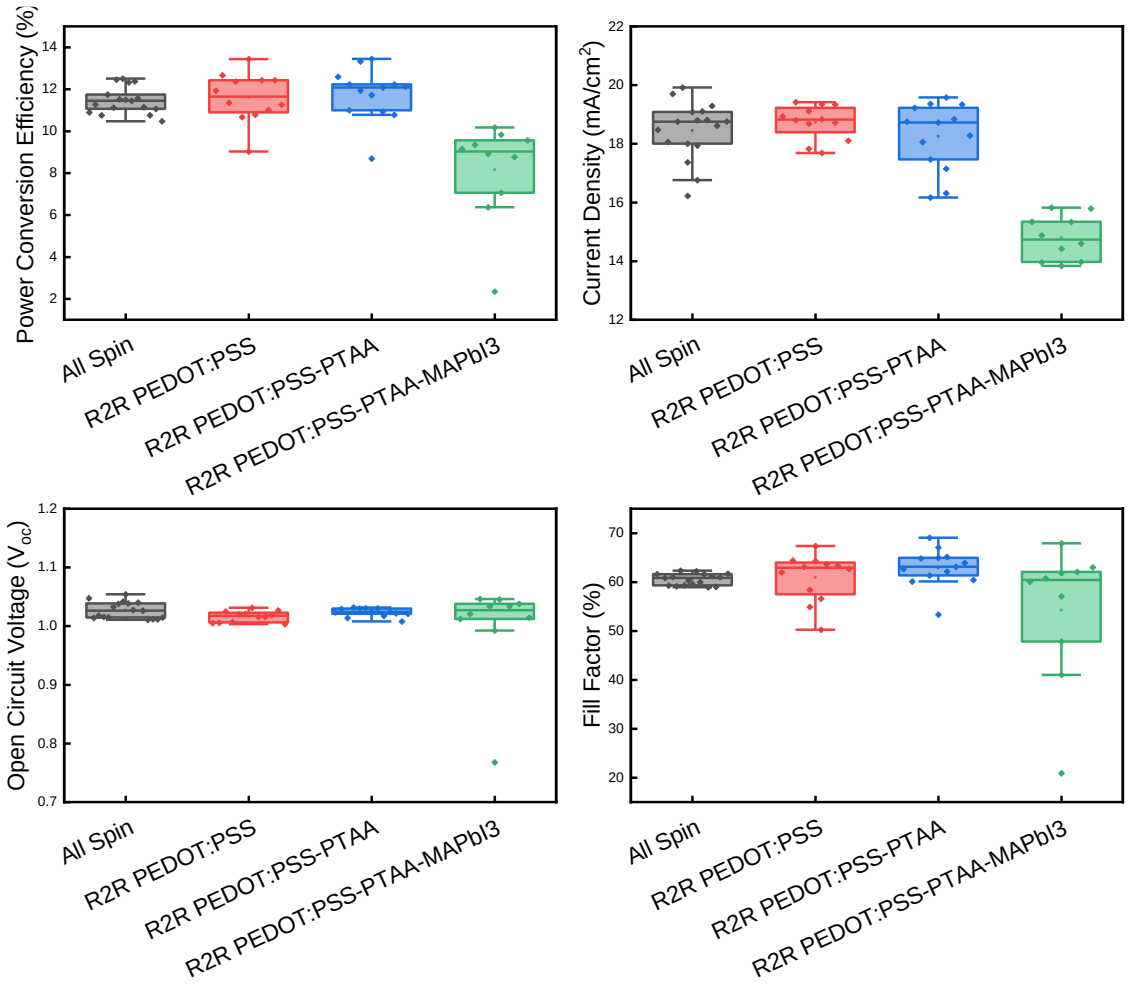

Figure 5. 3 Statistics of JV forward scan parameters of device with partially R2R slot die coated layer and its comparison with all spin coated device with stack of PET-ITO-PEDOT:PSS-PTAA-$MAPbI_3$-PCBM-BCP-Ag.

0.5M perovskite solution was coated on top of R2R slot die coated PEDOT:PSS-PTAA films optimised in the previous chapter. To fabricate the complete device, the coated substrate was chopped into smaller size of 28x28 mm^2 and the rest of the layers were spin coated on top of it. In this experiment four batches of devices were fabricated. The experiment was designed to slot die coat in a staggard manner to probe the quality of each layer. To establish

a control, in the first batch of devices, all the layer in the architecture were coated via spin coating. For the second batch to verify the quality of PEDOT:PSS coating, only PEDOT:PSS was R2R slot-die coated, and the rest of the device was completed by spin coating. In the third batch, two layers, PEDOT:PSS and PTAA were slot-die coated and everything else including perovskite was spin coated. While in the fourth and final batch, three layers, PEDOT:PSS-PTAA-$MAPbI_3$ were R2R slot die coated, and the rest were done by spin coating. The comparison of R2R coated $MAPbI_3$ and spin coated $MAPbI_3$ is made in the box plot form in Figure 5. 3. Interestingly, the performance of R2R coated PEDOT:PSS and R2R coated PEDOT:PSS-PTAA is comparable to that of spin coating. Performance suffers greatly when $MAPbI_3$ is slot die coated on top of PTAA. The PCE decreases from an average of 12% to less than 10%. As can be seen in Figure 5. 3, the decrease in short circuit current density and a small drop in fill factor are the main causes of this decline while no change in V_{oc} was noted. To probe into the reasons for this drop, we first looked at the morphology of R2R slot die

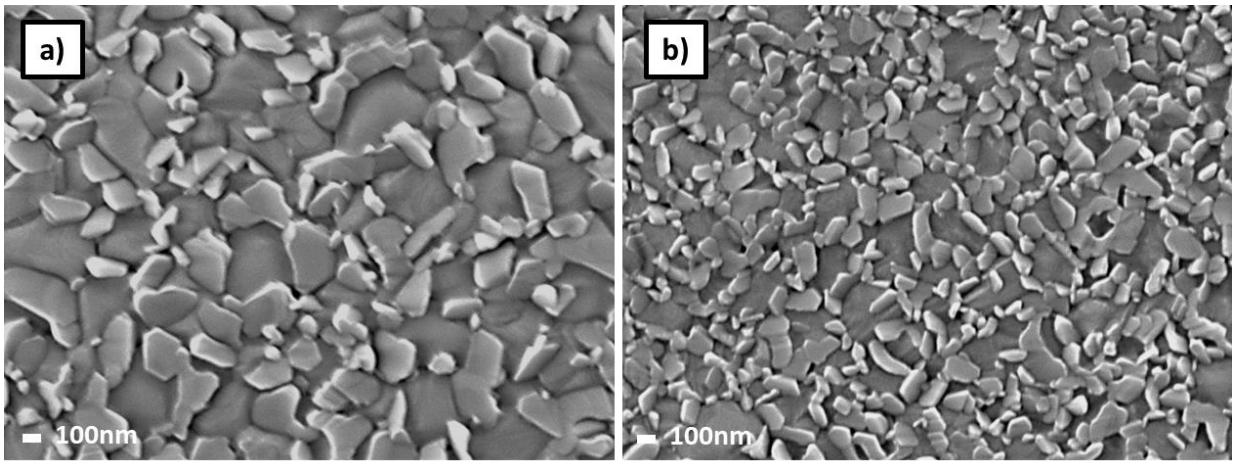

Figure 5. 4 SEM images of $MAPbI_3$ films coated on R2R slot die coated PEDOT:PSS-PTAA via a) Spin Coating b) R2R slot die coating.

coated films under SEM and compared that to the spin coated films. As can be seen in Figure 5. 4 the morphology of the $MAPbI_3$ film that is coated using spin coating is very different from the morphology of the R2R slot die coated films. The crystals vary in size, and the grains are scattered in different patterns across the surface. The slot die coated film contains tiny grains, and these grains do not seem to have a preferable orientation. In contrast, the spin coated films, which have bigger grains, and are relatively oriented in the same direction. This can further be seen in XRD spectra shown in Figure 5. 5a. The $MAPbI_3$ characteristic peak (110) at

14° is twice as intense of the spin coated $MAPbI_3$ films compared to R2R slot die coating confirming higher preferred orientation of $MAPbI_3$ crystals upon spin coating. The additional peak seen around 26° originates from the substrate as shown by the black XRD spectra. This peak will, therefore, appear in all subsequent XRD done on layers coated on ITO-PET substrates. Furthermore, the quality of the spin coated, and slot die coated films were probed by UV-Vis spectroscopy. The two spectra as illustrated in Figure 5. 5b shows an interesting trend. The R2R coated film absorbs much less light compared to the spin coated $MAPbI_3$ films across the measured wavelength. This could be due to thickness difference between the two meaning the R2R slot die coated films are relatively thinner than spin coated films, leading to low absorption of incident photons which could be another reason for low J_{sc} exhibited by PSCs

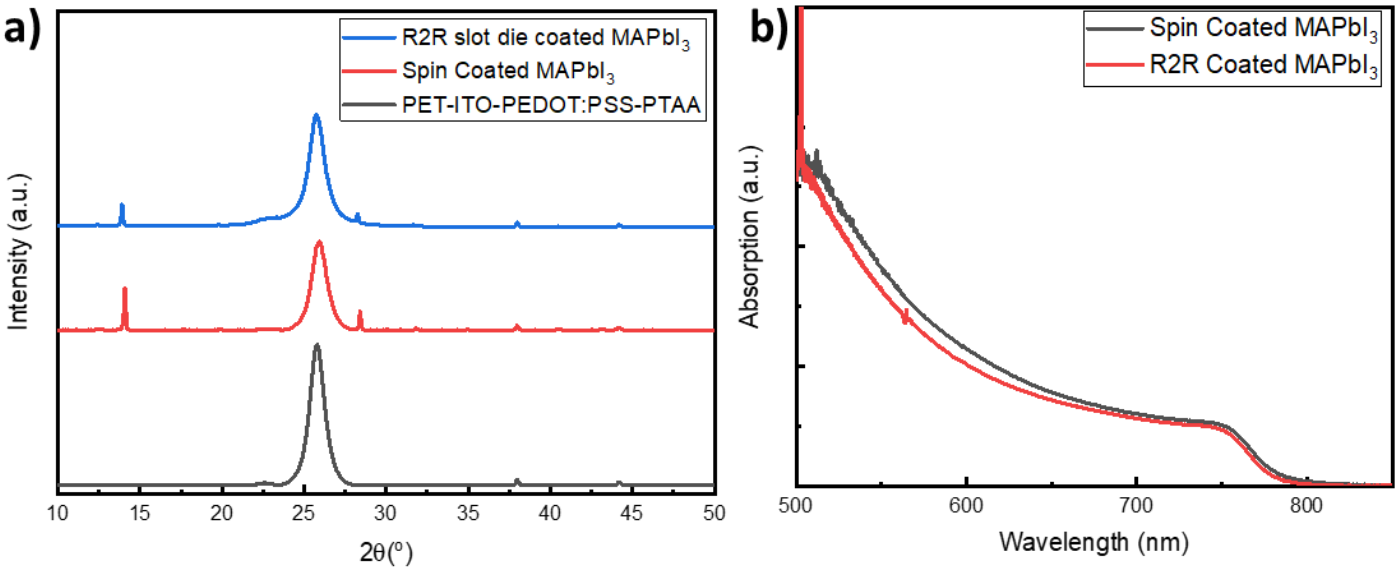

Figure 5. 5 a) XRD spectra of $MAPbI_3$ films comparing spin coating and R2R slot die coating on R2R slot die coated PEDOT:PSS-PTAA layer on ITO-PET. b) UV-Vis absorption spectra of $MAPbI_3$ films coated on R2R slot die coated PEDOT:PSS-PTAA films. The comparison is made between the spin coated $MAPbI_3$ films and R2R slot die coated films.

fabricated via R2R coating of $MAPbI_3$ films. Or low absorption in $MAPbI_3$ can also be caused by inherent change in the $MAPbI_3$ film itself.

To rule out the possibility of thinner films being coated via slot die coating compared to spin coated films, film thickness need to be determined precisely. Due to the fragile nature of PET substrate, which bends as a result of the stylus pressure exerted during measuring the

thickness using profilometer, it was challenging to precisely measure thickness on flexible substrate. Calculating the dry film thickness from the wet film thickness is another way to estimate the thickness. However, the density of the films must be determined for it to work. Typically, it is assumed that the spin coated film density is the same as the slot die coated film density, and the dry film thickness is determined using the spin coated film density. However, this assumption may not be valid for films which are sensitive to coating and drying methods leading to change in the density of films. As a result, in order to confirm the thickness's influence on the absorption and performance of slot die coated $MAPbI_3$ films, we adjusted the wet film thickness from 5 µm, which is the value that was used for the previous experiment, to 7 µm. Along with the WFT, oven temperature set for drying the film was also varied from 130℃ to 150℃ to understand the influence it had if any on the performance of the R2R slot die coated $MAPbI_3$.

The SEM images of the $MAPbI_3$ films of different thickness and dried at different temperature is presented in Figure 5. 6. No obvious change in morphology was seen when thickness is varied. A more prominent change in morphology is observed with increasing temperature. Films dried at 150℃ appears to have sharper features while the films dried at 140℃ and 130℃ appears to be relatively more compact. However, all the films showed small crystal size consistent with previous observation made in Figure 5. 4. Furthermore, Figure 5. 7 illustrates a comparison of the absorption spectra of spin-coated films and R2R slot-die coated films with varying wet film thicknesses of 5 µm, 6 µm, and 7 µm at three different oven set temperature for both the ovens (130℃ , 140℃ and 150℃). The PL spectra of the same films are shown on the right side of the figure. The temperature change is colour coded with 130℃ represented by red, 140℃ represented by blue and 150℃ represented by green. In comparison to 5 µm thick films, there was no discernible difference in the absorption of 6 µm thick films for all three temperatures, and still showed much less absorption than spin coated film. The 7 µm thick films demonstrated equivalent absorption to that of spin coated film at all three drying temperatures. However, absorption of films alone, does not lead to better devices. The light being absorbed must be converted into electrons and holes and these charges must be extracted with similar efficiency for the device to match the performance.

PL spectra plotted on the right side of the Figure 5. 7 shows the difference in PL quenching quench (decrease in PL intensity when coated upon charge extraction layer). $MAPbI_3$ films

when coated on PEDOT:PSS-PTAA HTL, charge transfer would take place from $MAPbI_3$ to HTL

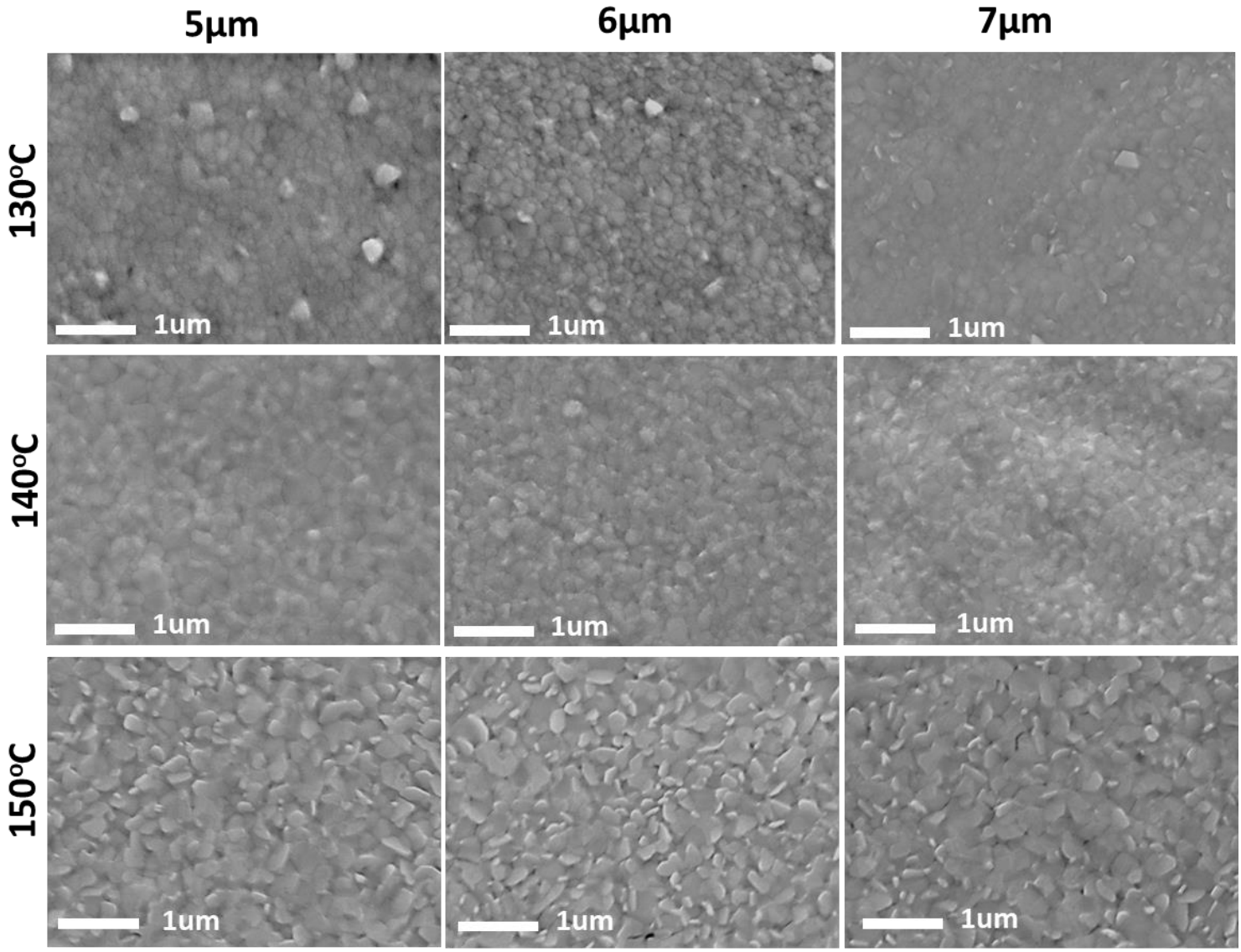

Figure 5. 6 SEM images of R2R coated $MAPbI_3$ films with 5, 6 and 7 µm WFT and dried at 130, 140 and 150°C oven set points. The $MAPbI_3$ films were coated on R2R slot die coated PEDOT:PSS-PTAA as optimised in the last chapter.

resulting in reduction of PL intensity relative to when coated on PET-ITO as shown in Figure 5. 7f. Interestingly PL quenching is relatively low in R2R coated $MAPbI_3$ films compared to spin coated $MAPbI_3$ film. The relative quenching was only compared for one set of variables (5 µm WFT and 150°C drying temperatures as shown in Figure 5. 7f). This was because coating $MAPbI_3$ on PET-ITO with all three WFT and oven temperature drying would have consumed large amount of PET-ITO substrate which was available in limited amount. The low PL quench

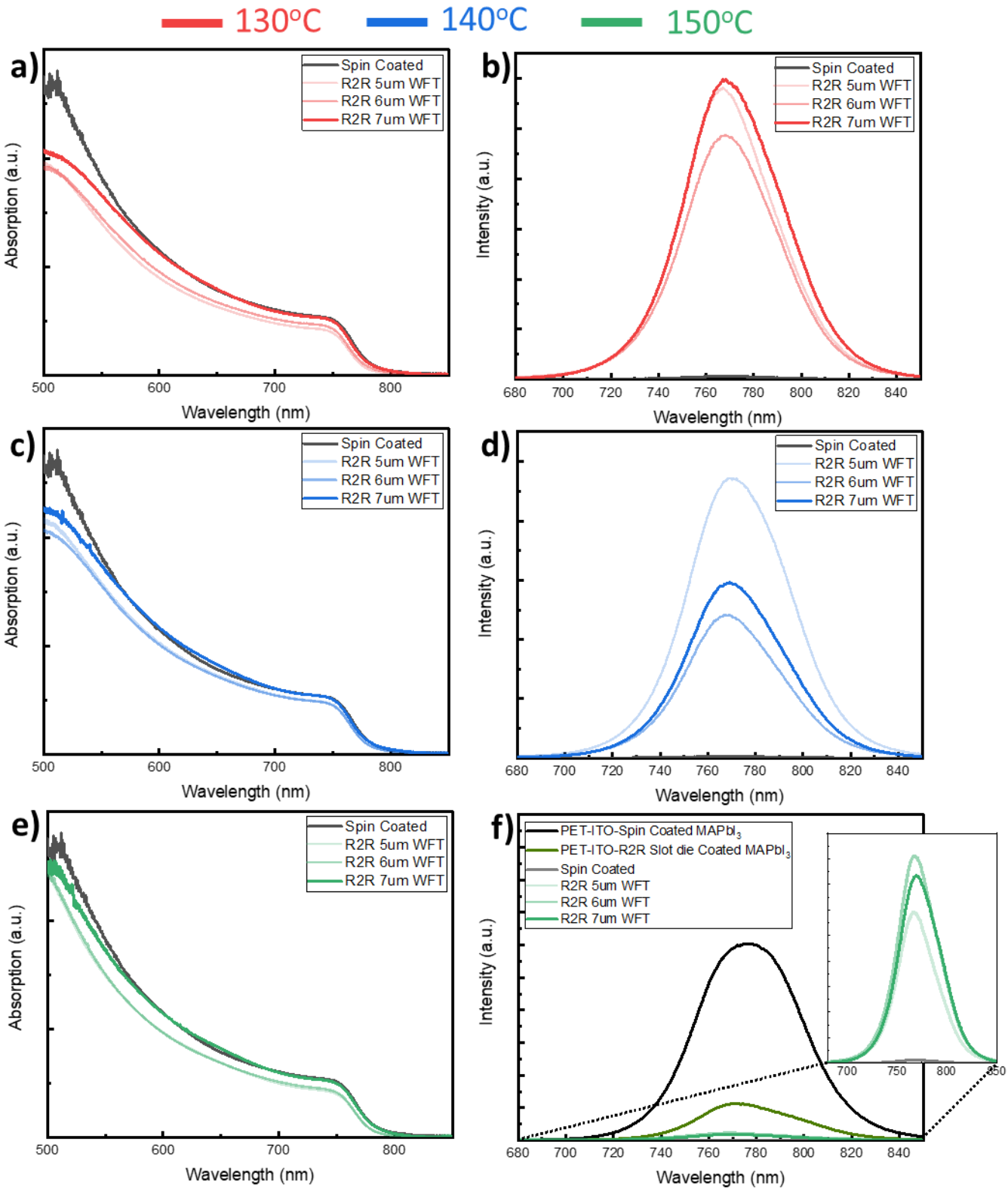

Figure 5. 7 UV-Vis absorption (a,c and e) and photoluminescence spectra (b,d and f) of $MAPbI_3$ films coated on R2R slot die coated PEDOT:PSS-PTAA films. Unless otherwise stated in the legend of each sub figures, all the $MAPbI_3$ films are R2R slot die coated, or spin coated on R2R slot die coated PEDOT:PSS-PTAA.

with R2R slot die coated films could mean two things; the slot die coated films are of high quality and have significantly lesser defects than spin coated films leading to higher PL emission. And secondly that the interface of perovskite and HTL is acting as a non-selective

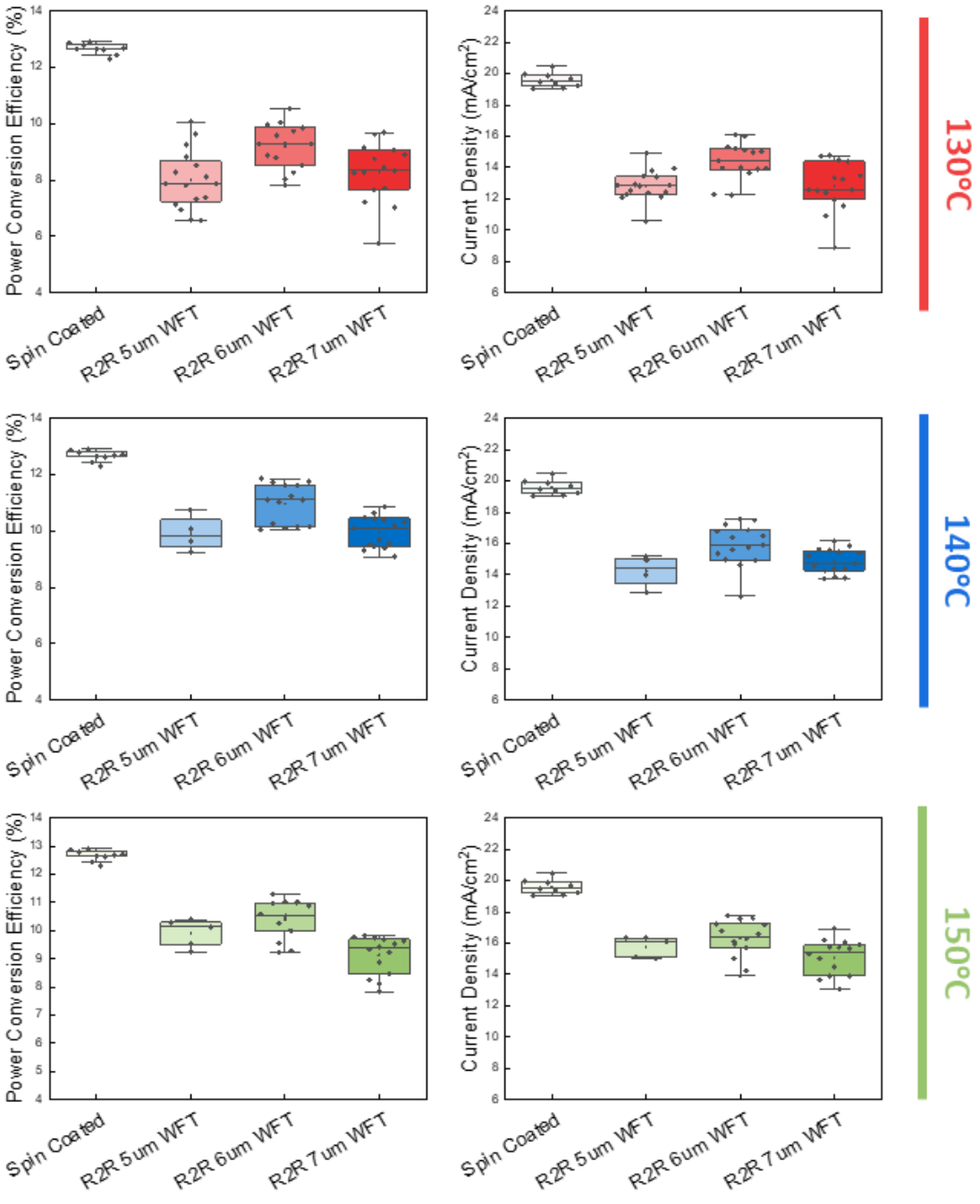

Figure 5. 8 Statistics of JV forward scan parameters of device with R2R slot die coated PEDOT:PSS-PTAA-$MAPbI_3$ at variable wet film thickness of 5 µm, 6 µm and 7 µm and oven drying at 130°C , 140°C and 150°C of $MAPbI_3$ films and its comparison with spin coated device. It is to be noted that spin coated device were fabricated on R2R coated PEDOT:PSS-PTAA substrate with $MAPbI_3$ and the rest of the layers were spin coated.

interface due to poor physical contact and no charge transfer is taking place in between the two-layers and all the charges are recombining radiatively leading to higher PL emission. To confirm this theory, we fabricated the PSCs using the same films and spin coating the remaining layers to complete the device stack.

The fabricated devices having different wet film thickness and different drying temperature were then characterised using JV measurement. The J_{sc} and PCE obtained from the JV measurement are plotted in the box plot form in

Figure 5. 8. The data is separated into three box plots each containing devices made with 5 µm, 6 µm and 7 µm wet film thickness of perovskite at each drying temperature and their comparison with devices made by spin coating a $MAPbI_3$ layer. For all three sets of data, a similar trend is seen in the J_{sc}. Every variable resulted in lower J_{sc} than the spin coated control. This combined with the PL analysis suggest the poor charge extraction in devices made using slot die coated $MAPbI_3$ films . The data show that, although having the same absorption as a spin-coated device (for a WFT of 7 µm as shown above), increasing thickness by increasing WFT has no effect on the photocurrent produced by the device. This suggests that the issue is with the charge collection rather than the thickness of the films. This could be due to two reasons. One, a high amount of interface defects would lead to low charge collection and higher non radiative recombination at the interface . This however is less likely considering no drop in V_{oc} (see Figure 5. 8) was observed in devices made via R2R slot die coating $MAPbI_3$ films. Also, interfacial non radiative recombination would quench PL emission which again was not observed with R2R coated films.[9] This leads us to the second reason, poor interface contacts between PEDOT:PSS-PTAA layer and R2R coated $MAPbI_3$ layer. An inferior physical contact would reduce the charge extraction and would also explain the higher PL emission seen in R2R slot die coated $MAPbI_3$ films. A plausible reason for poor interface contact can be disoriented crystals with less preferred orientation leading to gaps at the interface of $MAPbI_3$ and PEDOT:PSS-PTAA layer. Further, XRD spectra shown previously in Figure 5. 5 is clear evidence for the low crystalline R2R slot die coated $MAPbI_3$ films compared to spin coated $MAPbI_3$ films.

To understand the cause of this change in crystallisation, a comparison can be made with the slot die coating optimisation of the $MAPbI_3$ films done in chapter 3 on PEDOT:PSS layer with architecture PET-ITO-PEDOT:PSS-$MAPbI_3$-PCBM-BCP-Ag. There are two major differences

that can be noted in deposition of $MAPbI_3$ films on PEDOT:PSS as done in chapter 3 vs on PTAA being done in this work. One, PEDOT:PSS layer is hydrophilic while the PTAA layer is hydrophobic leading to different surface energy and different nucleation dynamics.[10] Second, the optimised HCl concentration used to dope the $MAPbI_3$ for coating on PEDOT:PSS is 20 µl ml^{-1} and that on PTAA is 5 µl ml^{-1}. This is an important distinction as chloride additives have been known to promote preferentially oriented growth and higher crystalline films by slowing down the nucleation.[11] Hence, the low amount of chloride present in $MAPbI_3$ films on PTAA could also explain the significantly low crystalline slot-die coated $MAPbI_3$ films on PTAA. To ascertain the cause of this a test of both the theories was conducted and will be discussed in the following sections.

5.3.1 Modification of the surface energy via solvent treatment

In coating processes, the surface energy of the substrate can affect the wetting and adhesion of the coating material. Films with high surface energy are wet easily by the coating material, which can improve the uniformity of the coating. Films with low surface energy, on the other hand, can be more difficult to wet and may produce uneven or incomplete coatings. Surface energy also has an effect on nucleation and crystal growth by inducing homogeneous or heterogenous nucleation.[10]

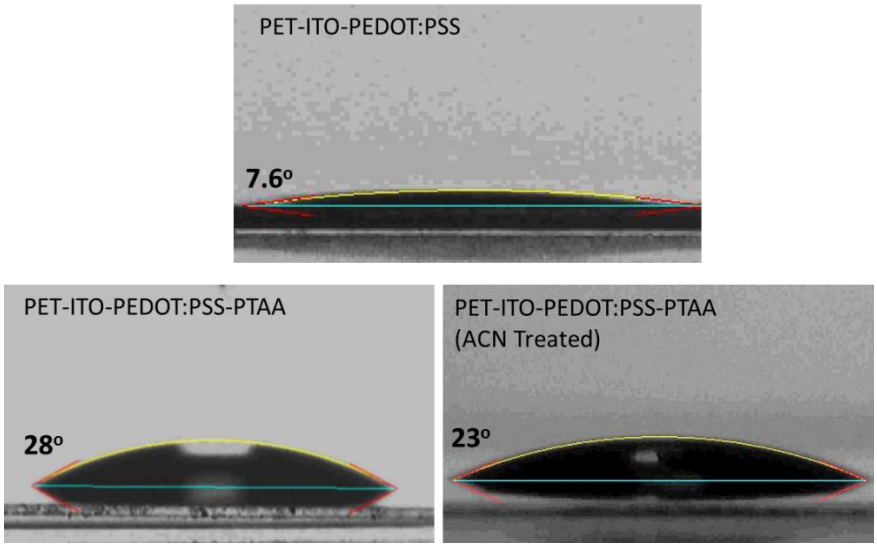

Figure 5. 9 Contact Angle measurement on R2R prepared PET-ITO-PEDOT:PSS, R2R prepared PET-ITO-PEDOT:PSS-PTAA with no ACN treatment and with ACN treatment done by spin coating.

It was noted in the preceding section that the $MAPbI_3$ layer deposited via R2R slot die coating had poor physical interface contact with the PTAA layer, resulting in poor charge extraction

(it should be noted that the dynamic drying in spin coated $MAPbI_3$ films is likely the reason for better interface contact with PTAA resulting in better performance).

The low surface energy of the PTAA layer, which results in poor wetting of the coated ink, could be the one of the reasons for this poor interface. To verify this possibility, wetting on PTAA needs to be improved. Various methods have been reported in the literature like the use of surfactants[3], interface layers[6] ,plasma treatments[12] and solvent treatments[4]. All these techniques have proven effective in improving $MAPbI_3$ ink wetting on PTAA. For the R2R setup, prewetting PTAA with solvent treatment was the quickest method to test the

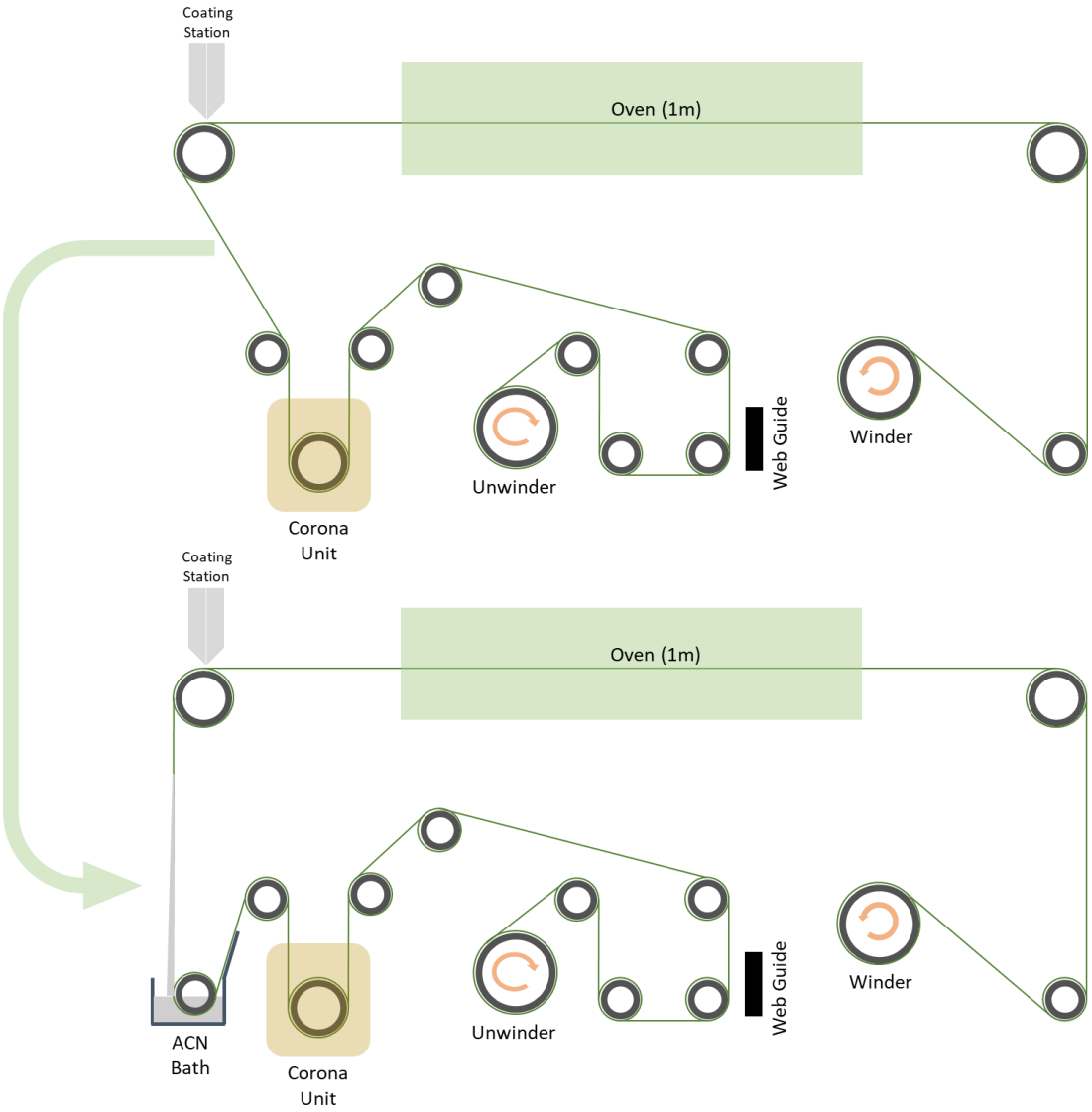

Figure 5. 10 Schematic of R2R web line before and after the ACN bath insertion.

hypothesis for enhancing the wetting at the PTAA surface. Prewetting often involves using the same solvent that is used for dissolution of $MAPbI_3$ precursors. In this case the solvent is acetonitrile (ACN). We first tested the effect of ACN on improving the wetting via spin coating ACN on R2R slot die prepared ITO- PET-PEDOT:PSS-PTAA. The substrate was characterised by contact angle measurement done pre and post wetting with ACN. For contact angle measurement we dropped $5\mu l$ of ACN-MA $MAPbI_3$ ink on ACN treated (spin coating) R2R slot die prepared ITO-PET-PEDOT:PSS-PTAA. The resultant measurements are presented in Figure 5. 9 showing the difference prewetting of ACN makes by decreasing the contact angle from 28^o to 23^o. Though not close to the wetting behaviour of PEDOT:PSS (also shown in the Figure 5. 9), it is significant enough to check the surface energy effect on R2R coated $MAPbI_3$ films. To do an ACN treatment in R2R setup, before the coating of $MAPbI_3$ layer, the web path was modified to insert an ACN bath as shown in Figure 5. 10. and is situated approximately 0.5 metres before the coating head. The web consisting of ITO-PET-PEDOT:PSS-PTAA is passed through the ACN bath coating applying a thin film of ACN which then readily dries before

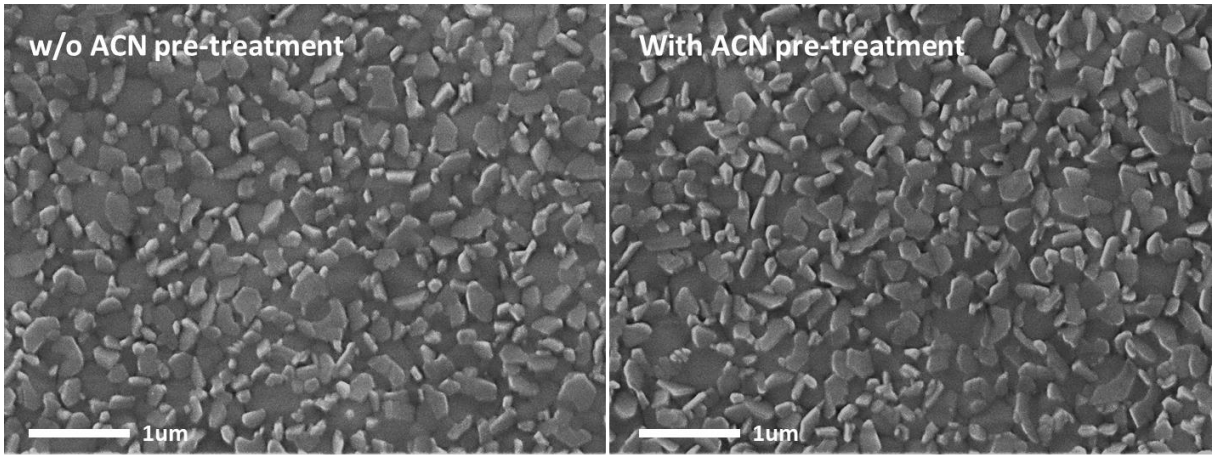

Figure 5. 11 SEM images of R2R slot die coated $MAPbI_3$ films on R2R coated PEDOT:PSS-PTAA on ITO-PET substrates with and without pre-treatment of ACN using ACN bath.

reaching the coating head due to the volatile nature of ACN at room temperature. No additional drying was done to remove the ACN. The as coated $MAPbI_3$ films were then characterised using multiple characterisation techniques to understand the effect of surface energy change on the optical and electrical properties of $MAPbI_3$ films. The SEM image of the R2R slot die coated $MAPbI_3$ films with and without ACN treatment is presented in Figure 5. 11. No significant change can be observed with the films and the same morphology with

randomly oriented grains is visible in both the picture. Furthermore, XRD was used to check

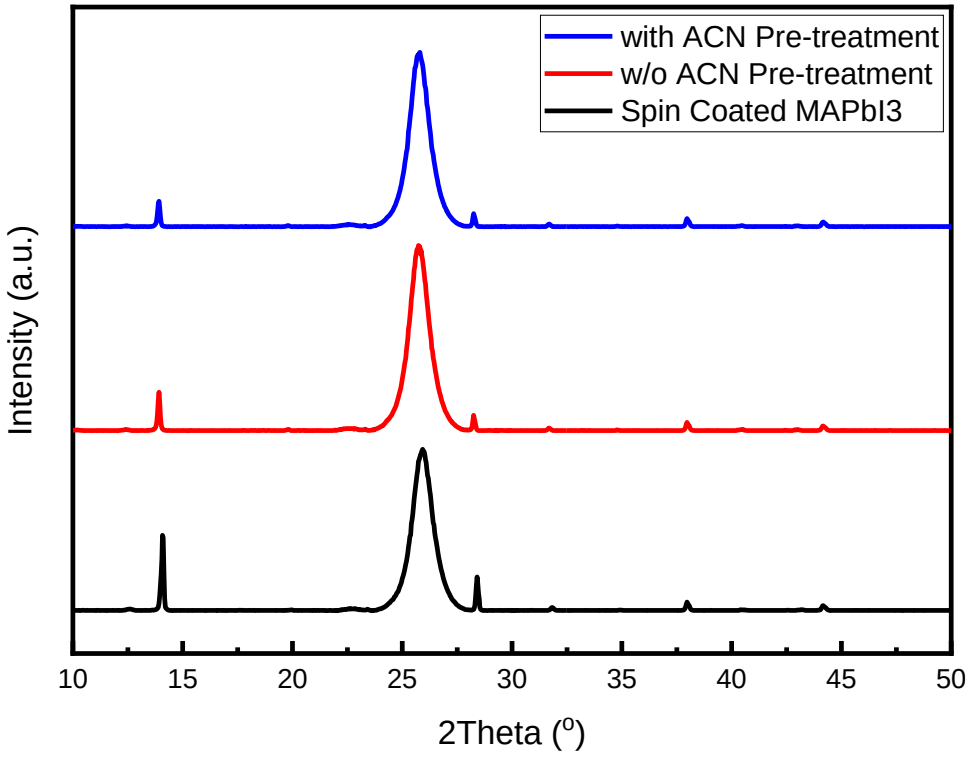

Figure 5. 12 XRD Spectra of R2R slot die coated and spin coated $MAPbI_3$ films on R2R coated PEDOT:PSS-PTAA on ITO-PET substrates with and without pre-treatment of ACN using ACN bath.

the relative crystallinity of the films and preferential orientation. The XRD spectra compared in Figure 5. 12 shows the characteristic 110 peak (at 14°) of R2R and spin coated $MAPbI_3$. The R2R coated films including the film with ACN pre wetting treatment showed low intensity peak compared to a spin coated film confirming no significant improvement in preferential crystal growth due to ACN treatment. This suggests the change in wetting behaviour of $MAPbI_3$ ink on hydrophobic PTAA surface did not have the anticipated effect on crystallisation of R2R slot die coating of $MAPbI_3$ films and that the randomly oriented crystals may still be causing a poor interface. To further confirm its effect on device performance, we fabricated PSCs using the same films to compare the device charge extraction capabilities upon ACN pre wetting treatment. To complete the device, R2R prepared PET-ITO-PEDOT:PSS-PTAA-$MAPbI_3$ (with and without ACN pre wetting treatment) films were diced into 28x28 mm^2 pieces and rest of the layer were done by spin coating PCBM, BCP and thermal evaporation of Ag contact. The resultant performance parameter obtained by running the JV measurement on completed device is plotted in Figure 5. 13. An immediate drop in photocurrent is noted with

the devices made by slot die coating $MAPbI_3$ layer compared to spin coating which is consistent with previous result (Figure 5. 3). However, an improvement in fill factor is noted upon prewetting the substrate with ACN before coating the $MAPbI_3$ layer. Though no improvement in film crystallinity and morphology was observed, the improvement in FF is likely caused by more uniform deposition due to increased wetting with ACN treatment. The

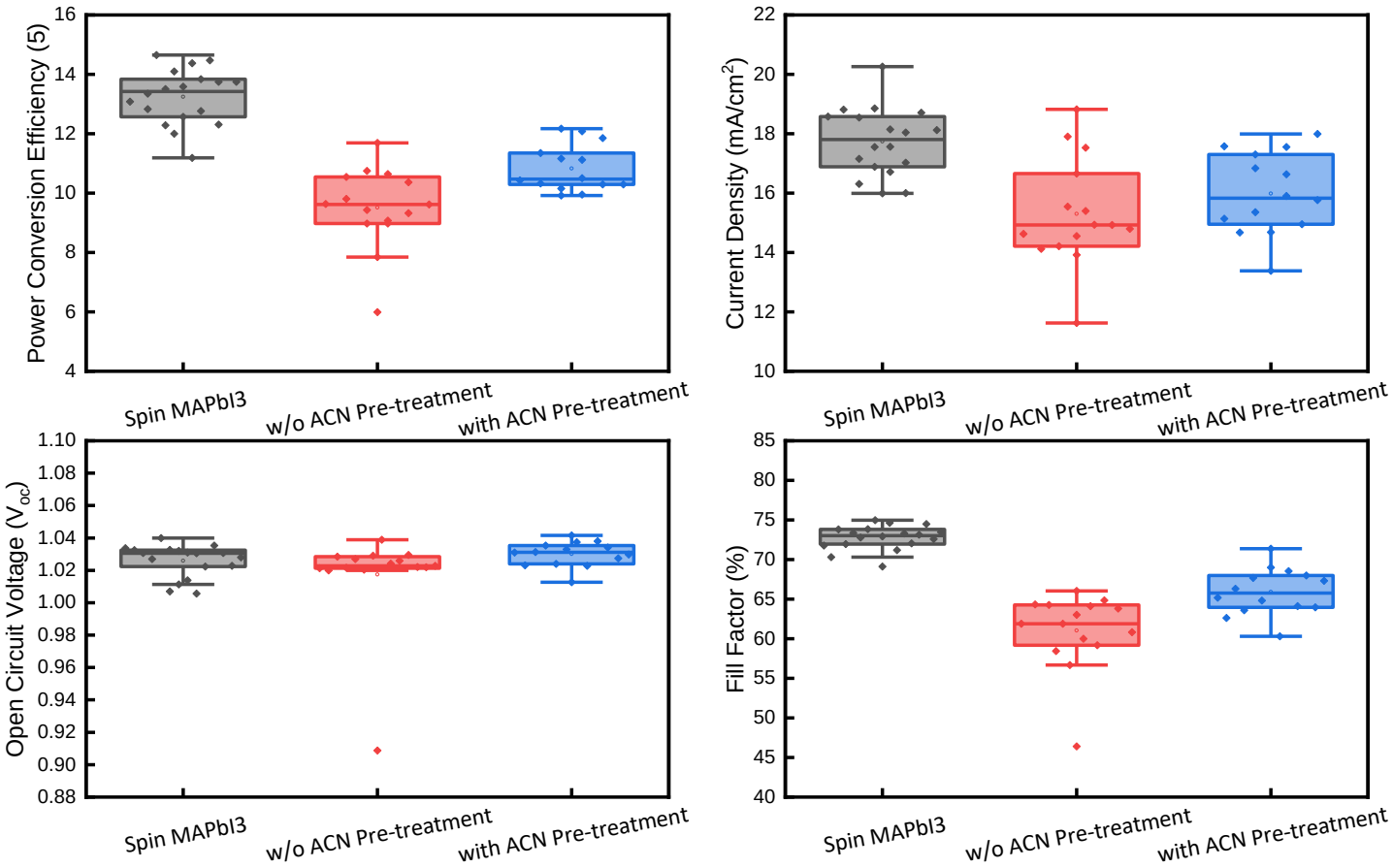

Figure 5. 13 Statistics of JV forward scan parameters of device with R2R slot die coated PEDOT:PSS-PTAA-$MAPbI_3$ on ITO-PET substrates. The comparison is made between the ACN treatment (and no ACN treatment) done before slot die coating of $MAPbI_3$ films and the two are then compared with spin coated $MAPbI_3$ films on R2R slot die coated PEDOT:PSS-PTAA.

uniform coating also leads to less variation in performance as evidenced by lower spread in the PCE. Although, a slight improvement in performance is noted, the drop in J_{sc} compared to the spin coated device could not be improved by improving the surface wetting of PTAA layer. This suggests, the poor interface of $MAPbI_3$ layer with PTAA still exists hindering the charge extraction by PTAA. This again is due to relatively random oriented $MAPbI_3$ crystals in the slot die coated film as confirmed by XRD (Figure 5. 12). Additionally, lower uniformity in crystal

orientation may also be caused by the low chloride additive in $MAPbI_3$ as explained earlier. The next section will explore the role of changing the crystallisation kinetics by additive and ink engineering to enhance the PTAA interface by inducing preferential crystal growth of the $MAPbI_3$ films .

5.3.2 Ink engineering to enhance the preferential growth of slot die coated $MAPbI_3$ film

In the previous section we established that the surface wetting is likely not causing the formation of less orientated $MAPbI_3$ crystals in slot die coated films. As was previously mentioned, another difference between the optimisation done in chapter of R2R slot die coating was different amount of chloride additive. For the deposition of $MAPbI_3$ on PEDOT:PSS as optimised in chapter 3, a higher amount of HCl (20 $\mu l\ ml^{-1}$) was used. While, for the deposition of $MAPbI_3$ on PTAA, a low concentration (5$\mu l\ ml^{-1}$) of HCl(aq) is used because any higher amount led to growth of disintegrated crystals as described in chapter 4 section 4.3. This however was seen for spin coated $MAPbI_3$ films and no experiment yet was

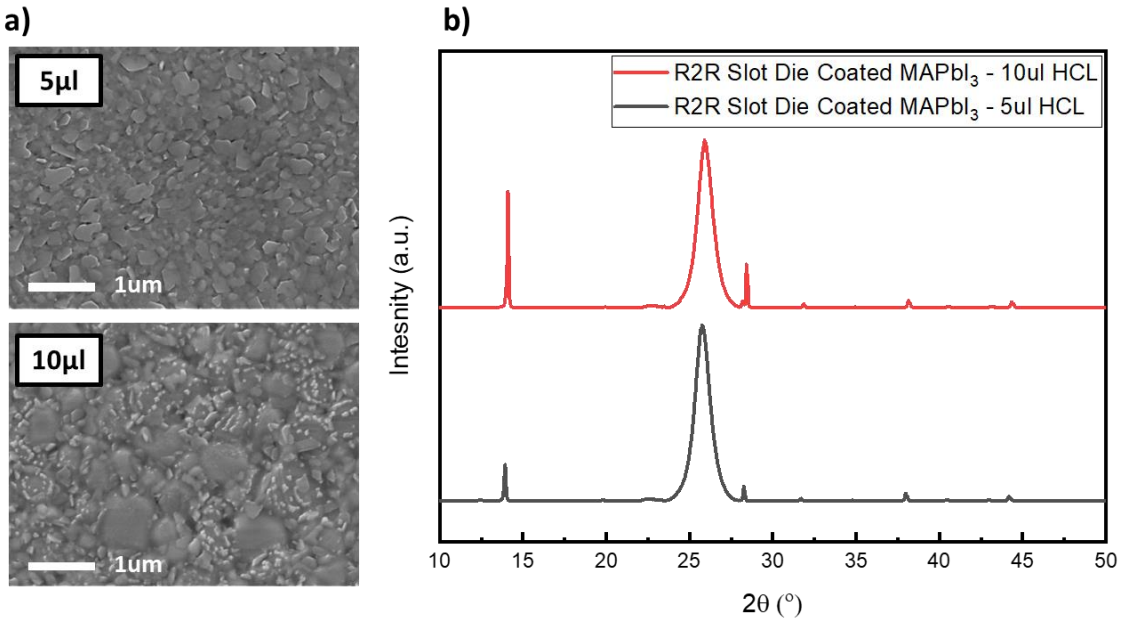

Figure 5. 14 SEM images (a) and XRD Spectra (b) of R2R slot die coated $MAPbI_3$ with 5 µl ml^{-1} and 10 µl ml^{-1} HCl doping. The $MAPbI_3$ films were coated on R2R slot die coated PEDOT:PSS-PTAA.

done to confirm if higher HCl can be added in $MAPbI_3$ for slot die coating with no negative effect on morphology of the film. Chloride doping strongly influences the crystal size and

orientation, higher chloride leads to highly oriented crystal growth.[12] Therefore, to ascertain that no additional HCl can be used than already optimised for spin coating of $MAPbI_3$, a R2R experiment was carried out. $MAPbI_3$ with increased amount of HCl (10 µl ml^{-1}) was R2R slot die coated and compared with the concentration been used thus far (5 µl ml^{-1}). SEM images of coated films are presented in

Figure 5. 14a. Though adding 10 µl ml^{-1} HCl resulted in higher crystal size, it showed a similar change in the morphology as was observed with spin coating upon using higher amount of HCl. The film looked rough due to gaps being created between the crystals. This is likely to give inferior performance with poor fill factor. On the other hand,

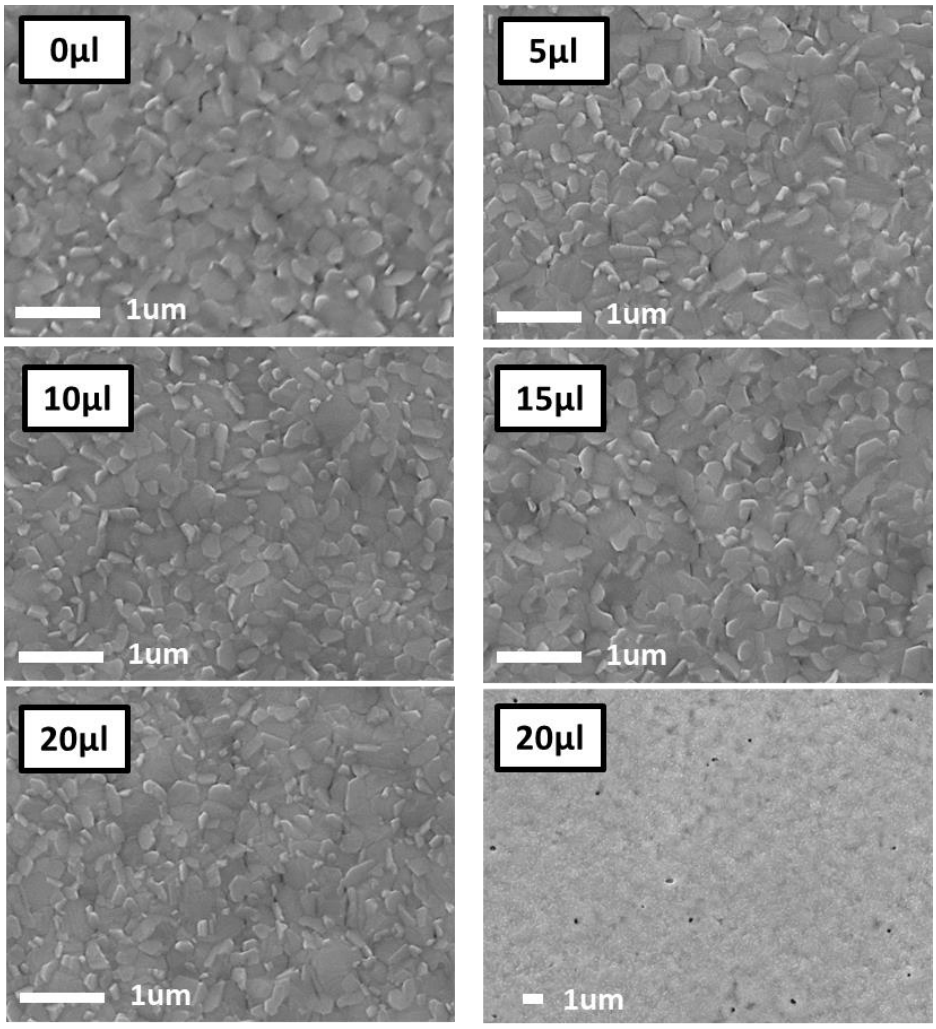

Figure 5. 15 SEM images of the R2R slot die coated $MAPbI_3$ films with varying amount of DMSO (0, 5, 10, 15 and 20 µl ml^{-1}). All the $MAPbI_3$ films were coated on R2R slot die coated PEDOT:PSS-PTAA layer. The right bottom image of $MAPbI_3$ with 20 µl ml^{-1} DMSO is at the 5K magnification while other are taken at 30K magnification.

as anticipated higher HCl led to significant enhancement in oriented growth leading to higher crystallinity of the films as evidenced by the XRD spectra in

Figure 5. 14. The characteristic peak of $MAPbI_3$ at 14° is much more intense when using 10 µl ml^{-1} compared to 5 µl ml^{-1} HCl. Figure 5. 6. Because no additional chloride could be added to increase preferred growth when deposition on PTAA due to deterioration in the morphology, another additive was investigated, di-methyl sulfoxide (DMSO).

DMSO has been frequently used to control crystallisation via the creation of a strong PbI_2-DMSO adduct.[13] It has also been employed in a volatile solvent mixture of 2-methoxy ethanol and acetonitrile to increase crystal size and to improve physical contact with PTAA underneath.[14] DMSO, due to its high boiling point, low volatile nature, and its strong bonding with PbI_2 slows down the formation of nuclei thus giving more time for the created nuclei to grow larger and form bigger crystals rather than generating new nuclei. This control over the crystal growth should enhance the crystal size and help form highly oriented crystals as has been reported previously. [14] To test this theory, we doped the 0.5M $MAPbI_3$ ink with small amounts of DMSO in varying concentration (5, 10, 15, 20 µl ml^{-1}) and slot die coated the $MAPbI_3$ films with 6 µm WFT on R2R slot die coated PEDOT:PSS-PTAA. The change in

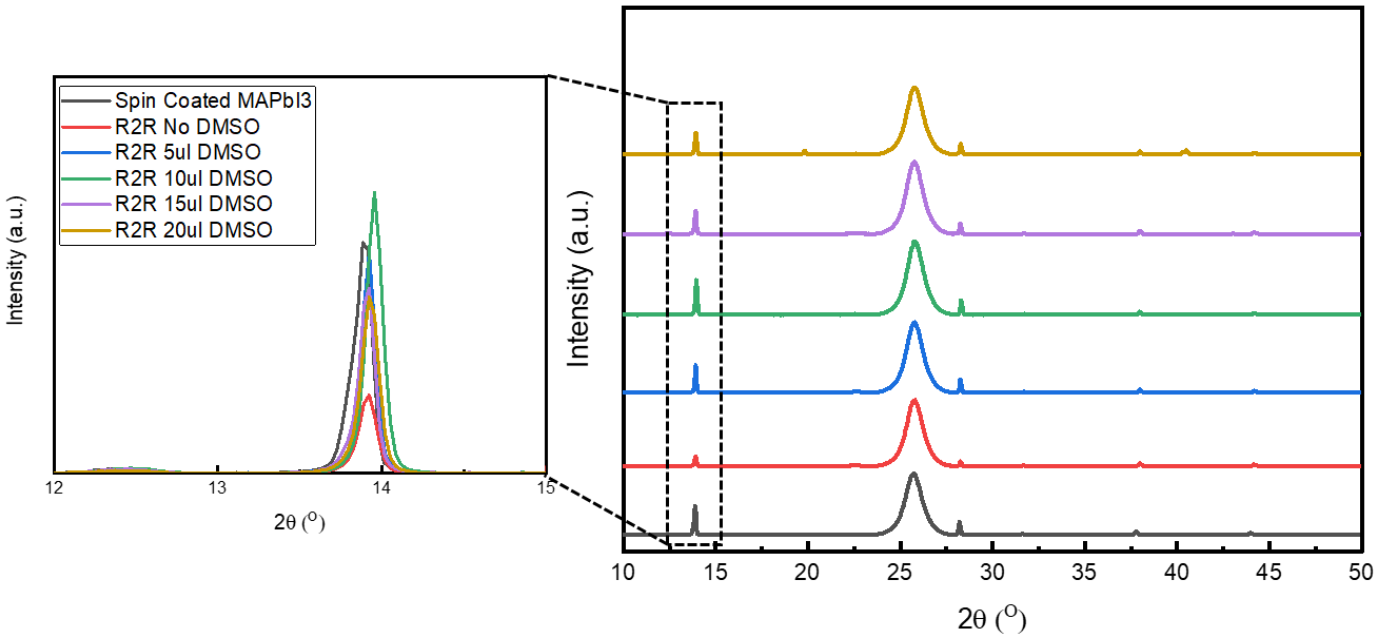

Figure 5. 16 XRD spectra of the R2R slot die coated $MAPbI_3$ films with varying amount of DMSO (0, 5, 10, 15 and 20 µl ml^{-1}). All the $MAPbI_3$ films were coated on R2R slot die coated PEDOT:PSS-PTAA layer. All the R2R slot die coated films are then compared with spin coated $MAPbI_3$ films on R2R slot die

coated PEDOT:PSS-PTAA.

morphology upon addition of DMSO was characterised by SEM and the images are compared in Figure 5. 15. As can be seen there is a slight change in the morphology upon addition of DMSO. However no further change is observed upon increasing the amount of DMSO till 15 µl ml^{-1}. Unlike previously observed, no significant change in crystal size was seen.[14] This will be further discussed later in the section. At 20 µl ml^{-1} DMSO however, pin holes start to

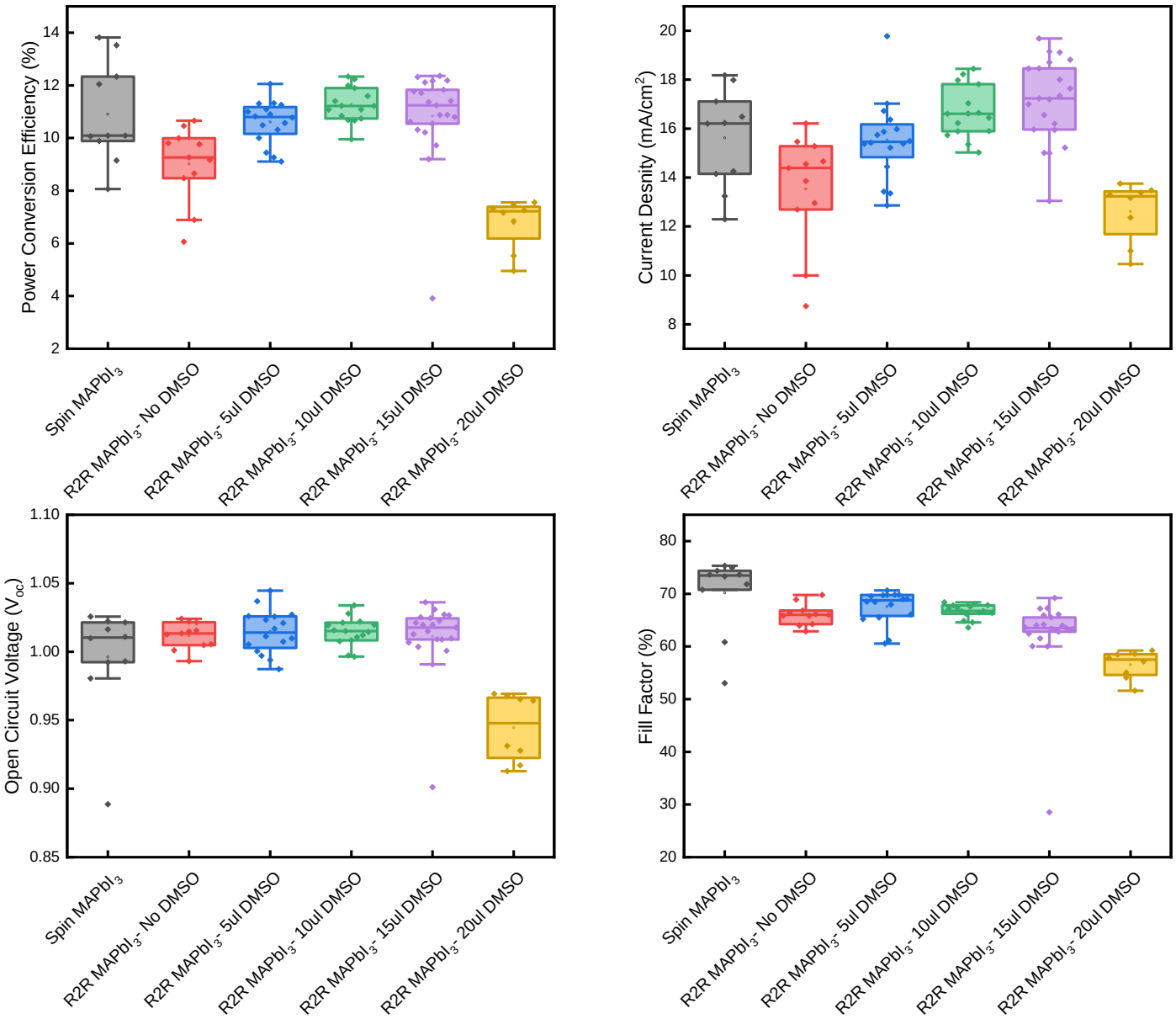

Figure 5. 17 Statistics of JV forward scan parameters of device with R2R slot die coated PEDOT:PSS-PTAA-$MAPbI_3$ with varying amount of DMSO (0, 5, 10, 15, 20 µl ml^{-1}). The comparison is made between the ACN treatment (and no ACN treatment) done before slot die coating of $MAPbI_3$ films and the two are then compared with spin coated $MAPbI_3$ films on R2R slot die coated PEDOT:PSS-PTAA.

appear which can be seen in the bottom right image taken at low magnification. This is likely due to extremely slow drying induced by the high amount of DMSO leading to disconnects between the crystals. Further, to check the effect of DMSO addition on crystal orientation XRD spectroscopy was done on the same films and the results of it are presented in Figure 5. 16. The spectra compare the intensity of the characteristic peak of $MAPbI_3$ 110 peak located close to 14°. As anticipated, the crystal orientation in 110, direction improved considerably (as seen with the improvement in the intensity of the 110 peak) with the addition of DMSO and matched with the spin coated films. This suggest that controlling the nucleation by introduction of non-volatile DMSO have helped increase the relative orientation of the $MAPbI_3$ crystals in agreement with the literature. [14] However unlike what was seen previously

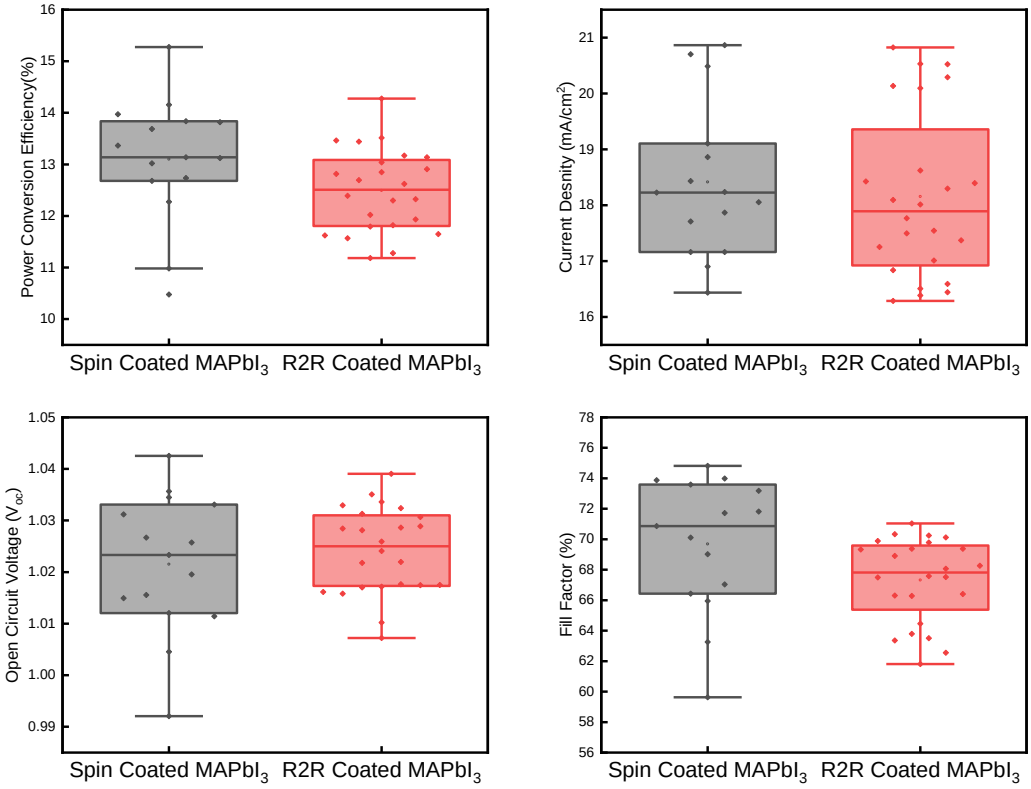

Figure 5. 18 Statistics of JV forward scan parameters of device with R2R slot die coated PEDOT:PSS-PTAA-$MAPbI_3$ compared with spin coated $MAPbI_3$ on R2R coated PEDOT:PSS-PTAA. For both the sets of devices, the remaining layers of PCBM-BCP were spin coated followed by thermal evaporation of the silver contact to complete the device stack.

in the literature, the grain growth did not take place as evident by SEM images in Figure 5. 15. Next, to check the effect of the crystal orientation on the performance of PSCs, we completed the devices by spin coating (PCBM-BCP) on all the R2R slot die coated $MAPbI_3$ films

followed by thermal evaporation of silver contacts. The devices were then measured under a 1sun light source to get the JV curve. The parameters extracted from the JV curve of each device are plotted in Figure 5. 17. On average performance seems to improve upon the addition of DMSO up until 15 µl ml^{-1} concentration. After which it drops suddenly, which is likely the result of pin holes in the films when excessive DMSO was used as previously presented in Figure 5. 15. The average performance increase is led by average increase in J_{sc} with the increased addition of DMSO. However due to large standard deviation seen in the data no conclusion can be drawn definitively.

The experiment was repeated by slot die coating $MAPbI_3$ formulation with 10 µl ml^{-1} (as found to be the optimal concentration from the previous experiment) DMSO and a comparison was made by spin coating the same $MAPbI_3$ formulation. The box plot of performance parameters obtained from the JV scan is presented in Figure 5. 18. The device fabricated by slot die coating three layers (PEDOT:PSS, PTAA and $MAPbI_3$) performed closely to that of spin coated $MAPbI_3$. The J_{sc} which had been lower for slot die coated $MAPbI_3$ on PTAA matched with that obtained by spin coating. The average PCE recorded for R2R slot die coated $MAPbI_3$ was 12.9% with champion device recording 14.5% stabilised PCE (Figure 5. 19) which is highest amongst any reported work on R2R fabrication of P-I-N PSCs.

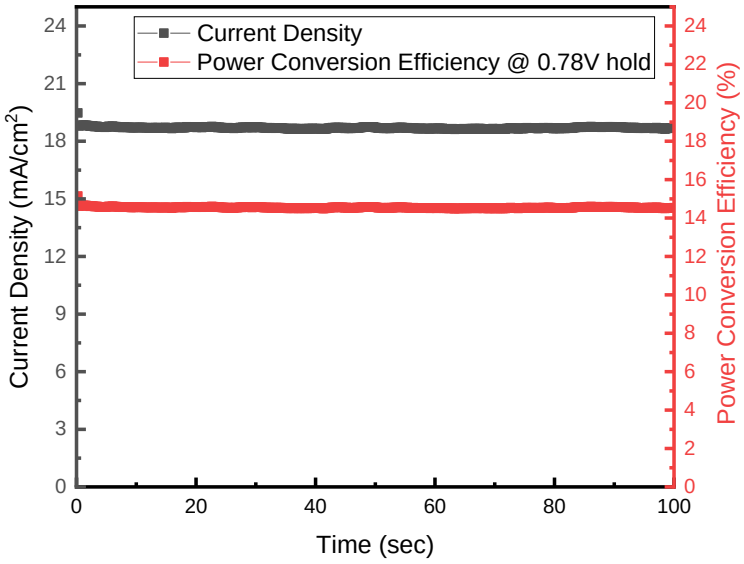

Figure 5. 19 Stabilised power conversion efficiency of best performing PSC (held at maximum power point voltage) fabricated by R2R slot die coating PEDOT:PSS, PTAA and $MAPbI_3$.

However, it is important to note that the conclusion regarding the improvement in crystal

orientation (as depicted in Figure 5. 16) as the sole cause for the observed average improvement in J_{sc} cannot be definitively established at this point. This is primarily due to the the absence of additional supporting data to validate the hypothesis. Further investigations are necessary to establish a more conclusive relationship between the improved crystal orientation and the observed average improvement in J_{sc}.

To anticipate the role of DMSO, it's important to understand the growth of the film. The LaMer curve have been extensively used to predict the nucleation and crystallisation kinetics.[15,16] This model describes nucleation and crystal growth in three phases and is represented in Figure 5. 20. Phase 1 is the pre nucleation stage where the monomeric particles or colloids are accumulating as the solvent dries from the film. Upon further removal of solvents, nucleation of the film starts as the concentration of the film crosses the supersaturation point (C_{min}) which is the beginning of phase 2. In phase 2 rapid nucleation happens along with the growth of the nuclei. The growth and the creation of the nuclei is controlled by the concentration of the film. If the concentration is above $C_{min,}$ nucleation is faster than growth while growth dominates when the concentration drops below $C_{min.}$ Thereafter, the concentration drops due to solute consumption by nucleation and crystal growth and falls below C_{min} and phase 3 begins. In phase 3, no further nucleation happens as the concentration of the film is below $C_{min.}$ Therefore, in Phase 3 the created nuclei and crystal grows further by diffusion.

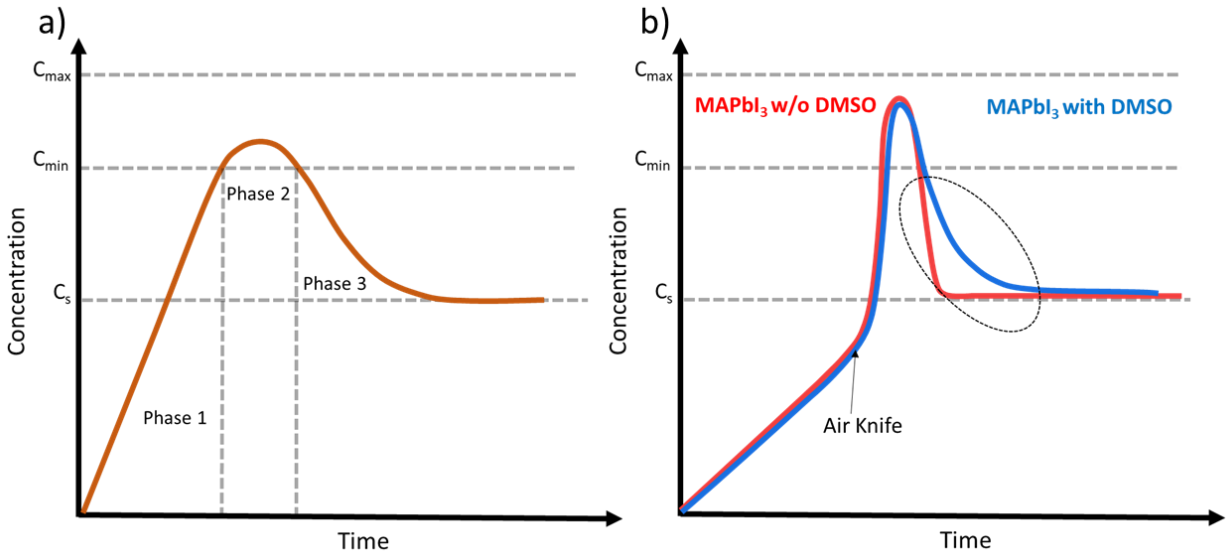

Figure 5. 20 The La Mer curve used for the description of nucleation and crystal growth and its

relationship with the solution concentration.

In the case of a standard DMF/DMSO-based perovskite formulation, the nucleation process begins when the film is washed with antisolvent[17], and these nuclei expand and fuse during drying to produce a compact film. Anti-solvent washing is not necessary in the case of ACN-MA ink composition due to fast quenching upon release of volatile ACN-MA. A few reports have also showed that these films do not require drying on hot plate.[8,18] This suggests, that both the nucleation and growth of the films happens during the spin coating process itself. In the case of spin coating the ACN-MA based perovskite films , the film reaches supersaturation as its spinning due to drying by centrifugal force, followed by which nucleation happens along with growth of the nuclei as drying continues due to spinning. The LaMer curve for this way of drying would look like Figure 5. 20a. However, for large area air knife assisted coating the supersaturation occurs only when the film passes under the knife and not during the coating. At the time of air knife quenching, the concentration of ink increases sharply leading to rapid nucleation and crystal growth. This type of drying procedure would closely follow the LaMer curve shown in Figure 5. 20b. Due to this fast nucleation and growth, crystals remain smaller in the final film compared to spin coated film as was the case throughout this work. Crystal size is directly proportional to nucleation density in phase 2. [19] Volatile solvent systems tend to form small crystals due to high nucleation caused by rapid removal of the solvent [20] and even smaller crystals are formed with air knife for the same reason. After the addition of DMSO the nucleation should slow down, and crystal growth should dominate over new nucleation leading to higher crystal size.[14] However, this was not observed with the slot die coated $MAPbI_3$ films as evident from the SEM images in Figure 5. 15. This can be explained by the LaMer diagram in Figure 5. 20b. The nucleation density is likely to be similar with and without DMSO when using air knife quenching, suggesting that the low volatility induced by DMSO may be suppressed by the high pressure exerted by the air knife. A similar nucleation density with and without DMSO would explain no observed change in the crystal size. However, there was an improvement in the relative orientation as observed in XRD measurement (see Figure 5. 16) which led to better performance. This is likely due to slow diffusion growth of the crystals when the film is below $C_{min.}$(shown by the dotted ellipse in Figure 5. 20b). The decreased crystal growth rate increases the likelihood of oriented growth, which could explain the relatively higher occurrence of oriented crystals in the presence of

DMSO compared to its absence.

5.4 Conclusion

This work illustrated the challenges in the process transfer from spin coating to R2R slot die coating of $MAPbI_3$ on PTAA. XRD, PL SEM and UV-Vis measurements were undertaken to understand the loss of performance occurred during this transfer. This characterisation showed that slot die coated films were of low crystallinity compared to spin coated $MAPbI_3$ films. This low crystalline film deposited by slot die coating may have been the reason for lower short circuit current and hence lower PCE. To address this issue, surface treatment and ink engineering strategies were employed. Among these approaches, ink engineering involving the addition of DMSO was found to be more effective. Although the addition of DMSO did not alter the grain size of the R2R slot die coated MAPbI3 films, it likely facilitated an improvement in crystal orientation by controlling the diffusion growth of nuclei. Consequently, this resulted in improvement in PCE with the best cell showcasing 14.6% PCE. However, a definitive conclusion regarding the relationship between oriented film growth and short-circuit current (J_{sc}) could not be established definitively. Further investigations are required to provide a comprehensive understanding of the role of oriented film growth in J_{sc} enhancement.

Reference:

1. Cameron, J. & Skabara, P. J. The damaging effects of the acidity in PEDOT:PSS on semiconductor device performance and solutions based on non-acidic alternatives. *Mater Horiz* **7**, 1759–1772 (2020).

2. Liu, K. *et al.* Zwitterionic-Surfactant-Assisted Room-Temperature Coating of Efficient Perovskite Solar Cells. *Joule* **4**, 2404–2425 (2020).

3. Deng, Y. *et al.* Surfactant-controlled ink drying enables high-speed deposition of perovskite films for efficient photovoltaic modules. *Nature Energy 2018 3:7* **3**, 560–566 (2018).

4. Li, Y. *et al.* Two-step solvent post-treatment on PTAA for highly efficient and stable inverted perovskite solar cells. *Photonics Research, Vol. 8, Issue 10, pp. A39-A49* **8**, A39–A49 (2020).

5. Li, Y. *et al.* Interfacial Engineering of PTAA/Perovskites for Improved Crystallinity and Hole Extraction in Inverted Perovskite Solar Cells. *ACS Appl Mater Interfaces* **14**, 3284–3292 (2022).

6. Xu, J. *et al.* Surface-tension release in PTAA-based inverted perovskite solar cells. *Org Electron* **100**, 106378 (2022).

7. Subbiah, A. S. *et al.* High-Performance Perovskite Single-Junction and Textured Perovskite/Silicon Tandem Solar Cells via Slot-Die Coating. *ACS Energy Lett* acsenergylett.0c01297 (2020) doi:10.1021/acsenergylett.0c01297.

8. Noel, N. K. *et al.* A low viscosity, low boiling point, clean solvent system for the rapid crystallisation of highly specular perovskite films. *Energy Environ Sci* **10**, 145–152 (2017).

9. Kim, J. *et al.* Excitation Density Dependent Photoluminescence Quenching and Charge Transfer Efficiencies in Hybrid Perovskite/Organic Semiconductor Bilayers. *Adv Energy Mater* **8**, 1802474 (2018).

10. Kumar, J., Srivastava, P. & Bag, M. Advanced Strategies to Tailor the Nucleation and Crystal Growth in Hybrid Halide Perovskite Thin Films. *Front Chem* **10**, 330 (2022).

11. Chen, A. Z. *et al.* Crystallographic orientation propagation in metal halide perovskite thin films. *J Mater Chem A Mater* **5**, 7796–7800 (2017).

12. Daniel Burkitt *et al.* Acetonitrile based single step slot-die compatible perovskite ink for flexible photovoltaics. *RSC Adv* **9**, 37415–37423 (2019).

13. Lee, J. W., Kim, H. S. & Park, N. G. Lewis Acid-Base Adduct Approach for High Efficiency Perovskite Solar Cells. *Acc Chem Res* **49**, 311–319 (2016).

14. Deng, Y. *et al.* Tailoring solvent coordination for high-speed, room-temperature blading of perovskite photovoltaic films. *Sci Adv* **5**, (2019).

15. Pascoe, A. R. *et al.* Directing nucleation and growth kinetics in solution-processed hybrid perovskite thin-films. *Science China Materials 2017 60:7* **60**, 617–628 (2017).

16. Pound, G. M. & Mer, V. K. L. Kinetics of Crystalline Nucleus Formation in Supercooled Liquid Tin. *J Am Chem Soc* **74**, 2323–2332 (1952).

17. Jeon, N. J. *et al.* Solvent engineering for high-performance inorganic–organic hybrid perovskite solar cells. *Nature Materials 2014 13:9* **13**, 897–903 (2014).

18. Wang, K. *et al.* Isothermally Crystallize Perovskites at Room-Temperature.

19. McGinty, J., Yazdanpanah, N., Price, C., Horst, J. H. ter & Sefcik, J. CHAPTER 1 Nucleation and Crystal Growth in Continuous Crystallization. *The Handbook of Continuous Crystallization* 1–50 (2020) doi:10.1039/9781788013581-00001.

20. Wu, C. *et al.* Volatile solution: the way toward scalable fabrication of perovskite solar cells? *Matter* **4**, 775–793 (2021).

Chapter 6
Conclusions

The culmination of this work in the three research chapters signifies progress in the development of the Roll-to-Roll (R2R) slot-die coated perovskite solar cells (PSCs). In this exploration, the emphasis was made on the optimisation of each layer avoiding the use of highly toxic solvents.

In Chapter 1, all R2R slot-die coated layers in the PSCs, excluding the electrode was optimised. This process was executed at a rate of 1 m min^{-1}, showcasing its feasibility for a continuous R2R line with no significant adjustments. Safer solvent alternatives, such as a methyl ammine-based ACN solvent system and a high WEL solvent blend of toluene, O-xylene, and 2-methylanisole was introduced, which replaced hazardous solvents like DMF and DMSO and chlorobenzene. While the resulting PCEs were lower than those produced by conventional laboratory methods, the findings evidenced the viability of our eco-friendly approach for future development.

To further improve the efficiency of R2R coated PSCs, chapter 2 revealed the successful implementation of a R2R fabrication technique for depositing PTAA in P–I–N stack perovskite solar cells. The inclusion of an AI4083 buffer layer rectified the rough ITO on PET substrates issue, enabling us to coat a thin PTTA layer. This resulted in an improved performance, evidenced by an achieved efficiency of 15.2%.

In Chapter 3, the challenges faced during the transition from spin coating to R2R slot die coating of $MAPbI_3$ on PTAA was addressed. The difficulties stemmed from low crystalline slot die coated $MAPbI_3$ films on, leading to decreased performance. To tackle this, surface treatment and ink engineering were employed. The latter, involving DMSO addition, was found to be more effective, resulting in improved crystal orientation, and subsequently, increased PCE to 14.6%.

Overall, this research work showcases the promise of eco-friendly, scalable R2R fabrication techniques for PSCs. These findings represent significant strides towards more efficient, cost-effective, and environmentally friendly solar cell technologies. Despite achieving relatively lower PCEs than state-of-the-art devices produced via conventional methods, this work

underscores the potential of scalable R2R methods and sustainable solvents for the future of PSCs. The presented research stands as a stepping-stone towards the next wave of green energy solutions, underscoring the profound potential that lies within eco-conscious solar cell manufacturing.